On-line signal analysis of partial discharges in medium-voltage power cables

Veen, J.

DOI:
10.6100/IR586076

Published: 01/01/2005

Document Version
Publisher's PDF, also known as Version of Record (includes final page, issue and volume numbers)

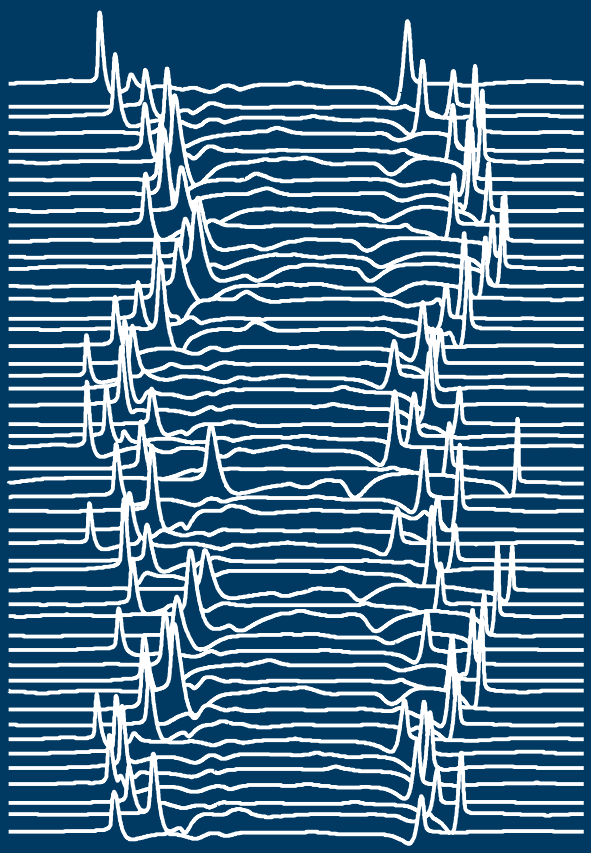

On-line Signal Analysis of Partial Discharges in Medium-Voltage Power Cables

Jeroen Veen

On-line Signal Analysis of Partial Discharges in Medium-Voltage Power Cables

PROEFSCHRIFT

ter verkrijging van de graad van doctor aan de
Technische Universiteit Eindhoven, op gezag van de
Rector Magnificus, voor een commissie
aangewezen door het College voor
Promoties in het openbaar te verdedigen
op donderdag 7 april 2005 om 16.00 uur.

door

Jeroen Veen

geboren te Dordrecht

Dit proefschrift is goedgekeurd door de promotoren:

prof.dr.ir. J.W.M. Bergmans
en
prof.dr.ir. E.F. Steennis

Copromotor:
dr. P.A.A.F. Wouters

Printed by Eindhoven University Press.
Kindly supported by Technology Foundation STW, KEMA Nederland B.V., N.V. Continuon Netbeheer, ENECO Netbeheer B.V.

CIP-DATA LIBRARY TECHNISCHE UNIVERSITEIT EINDHOVEN

Veen, Jeroen

On-line signal analysis of partial discharges in medium-voltage power cables / by Jeroen Veen. - Eindhoven : Technische Universiteit Eindhoven, 2005.
Proefschrift. - ISBN 90-386-1693-7
NUR 959
Trefw.: elektrische kabels ; isolatie / foutendiagnose / elektrische deelontladingen / signaalanalyse.
Subject headings: power cable testing / fault location / partial discharges / signal detection.

Summary

Partial discharges are symptomatic of many degradation phenomena in power cables and may cause further deterioration of the insulation in many cases. Electrical impulses, generated by partial discharges, travel towards the cable ends, and can there be detected using appropriate sensors. Continuous monitoring of the insulation condition can be achieved by on-line detection and location of partial discharge (PD) signals. An important aspect of such a diagnostic is the analysis of on-line measurements. The research reported in this thesis is aimed at analysis of PD signals from on-line measurements and location of discharge sites.

Signal analysis depends on knowledge of both signals and disturbances that are to be expected. To that end, characteristics of PD signals in medium voltage cables are studied in this thesis. The result of this study is a signal model of the propagation path between the discharge site and the sensors. The model accounts for cable sections with different properties, and incorporates the propagation channel load impedances, i.e. the equipment to which a cable is terminated in an on-line situation. The exact propagation properties and load impedances depend on the specific cable connection under test, and are unknown a priori. For this reason, research is conducted on methods that enable experimental characterization of the parameters, by evaluating the response of the cable to applied transients. The presented methods rely on the extraction of pulses that are reflected on impedance transitions within the cable system under test.

On-line field measurements are corrupted by noise and interference, which impede PD signal detection and location. Generally, narrowband interferences resulting from radio broadcasts dominate the measurements, thus prohibiting data-acquisition triggered by PD signals. Broadband background noise is present within the entire PD signal bandwidth, and therefore poses a fundamental limit on PD signal analysis.

Generally, existing extraction techniques for PD signals only partially exploit a priori knowledge of both signals and interference. In this thesis, matched filters are applied that are derived from the signal model, and are optimally adapted to the signals that can be expected. Besides signal extraction, matched filters provide a means to estimate the PD magnitude and the signal arrival time. Likewise, discharge location methods based on the signal model are proposed, resulting in optimal location estimators. Computer simulations illustrate the effectiveness of the proposed algorithms and show that the attainable accuracy can be specified by theoretical bounds.

Accurate PD location relies on estimation of the difference in arrival times of signals originating from the same discharge. In case of on-line detection, the cable is connected to the grid, and signals are not necessarily reflected at the cable ends. Therefore signal detection at both sides is generally required for the purpose of discharge location. Synchronization of the measurement equipment is achieved using

pulses that are injected into the cable connection.

Finite-energy disturbances, such as PD signals that originate outside the cable connection under test, frequently occur in on-line situations. Since measurements are synchronously conducted at both cable ends, pulses originating within and outside the cable can be distinguished by examining the difference in time of arrival. Moreover, in many situations, the signal direction of arrival can be determined by detecting pulses in two different current paths at a cable termination. This method is applied as an additional technique to discriminate PD signals and disturbances.

Based on the results of research, a measurement system is proposed, which enables automated on-line PD detection and location in medium voltage cable connections. The conceptual design is validated by experiments, and the results demonstrate that the practical application is promising.

Samenvatting

Partiële ontladingen zijn symptomatisch voor veel degradatieprocessen in energiekabels en hebben in veel gevallen verdere verslechtering van de isolatie tot gevolg. Ontladingen genereren stroompulsen die naar de kabeluiteinden propageren, waar ze gedetecteerd kunnen worden met behulp van geschikte sensoren. De conditie van de isolatie kan bewaakt worden door continu de signalen die ontstaan ten gevolge van ontladingen, te detecteren, terwijl de kabelverbinding 'on-line' is, d.w.z. in bedrijf blijft. De analyse van metingen die op deze wijze verkregen worden, is een belangrijk aspect van een dergelijke diagnostiek. Dit proefschrift is gewijd aan de studie en ontwikkeling van technieken voor de extractie van ontladingssignalen (PD signalen) en de lokalisatie van ontladingsplaatsen.

Signaalanalyse vereist een gedegen kennis van zowel de signalen als de verstoringen die verwacht kunnen worden. Met dat doel worden in dit proefschrift de kenmerken van ontladingen in middenspanningskabels bestudeerd. Resultaat van deze studie is een signaalmodel van het propagatiepad tussen de ontladingsplaats en de sensoren. Het model houdt rekening met kabelsecties met verschillende eigenschappen en omvat de kanaalbelastingen, d.w.z. de impedanties van de apparatuur waardoor de kabelverbinding wordt afgesloten. De exacte propagatie-eigenschappen en belastingsimpedanties hangen af van de specifieke kabelverbinding, en zijn vooraf niet bekend. Om deze reden is er onderzoek gedaan naar methoden om de parameters van het model experimenteel te bepalen door de responsie van de kabel op toegevoerde transiënten te beschouwen. De gepresenteerde methoden maken gebruik van pulsen die gereflecteerd worden op impedantiesprongen in het te diagnostiseren kabelsysteem.

On-line veldmetingen worden gehinderd door ruis en verstoringen, waardoor signaaldetectie en de lokalisatie van ontladingen bemoeilijkt wordt. Over het algemeen worden de metingen gedomineerd door smalbandige continue verstoringen, afkomstig van radio-uitzendingen. Daarbij is er, over de gehele bandbreedte van PD signalen, achtergrondruis aanwezig, waardoor een fundamentele limiet voor PD signaalanalyse gevormd wordt.

Bestaande extractietechnieken voor PD signalen benutten beschikbare voorkennis doorgaans slechts gedeeltelijk. In dit proefschrift worden extractietechnieken toegepast die afgeleid worden uit het signaalmodel en daarmee optimaal zijn aangepast aan de signalen die verwacht kunnen worden. Ook de methodes om de ontladingsplaatsen te bepalen berusten op het signaalmodel en resulteren in optimale lokatieschatters. Computersimulaties illustreren de effectiviteit van de ontworpen algoritmes en laten zien dat de haalbare lokalisatienauwkeurigheid door middel van theoretische grenzen aangegeven kan worden.

Met behulp van het verschil in aankomsttijd van twee PD signalen die van dezelfde ontlading afkomstig zijn, kunnen ontladingsplaatsen nauwkeurig gelokaliseerd worden.

Wanneer de kabel aan het distributienet gekoppeld blijft, worden signalen niet noodzakerlijkerwijs gereflecteerd aan de kabeluiteinden. Om deze reden is signaaldetectie aan beide zijden van de kabelverbinding nodig om ontladingsplaatsen te kunnen lokaliseren. Om een tijdreferentie voor de meetapparatuur aan beide kabeluiteinden te verkrijgen worden synchronizatiepulsen geïnjecteerd.

In on-line meetsituaties komen stoorpulsen met eindige energie-inhoud veelvuldig voor, bijvoorbeeld PD signalen die buiten de te testen kabelverbinding ontstaan. Omdat tegelijkertijd aan beide zijden van een kabelverbinding gemeten wordt, kunnen signalen die binnen en buiten de kabel ontstaan onderscheiden worden door middel van looptijdverschillen. Bovendien kan in veel situaties de richting van aankomst van gedetecteerde pulsen aan een kabeluiteinde bepaald worden door de stromen in twee verschillende paden te beschouwen. Deze aanvullende methode kan ook worden toegepast om stoorpulsen te herkennen.

Gebaseerd op de onderzoeksresultaten wordt een meetsysteem voorgesteld dat in staat is ontladingen in een middenspanningskabel te detecteren en te lokaliseren terwijl deze aan het distributienetwerk gekoppeld blijft. Door middel van experimenten worden de principes gevalideerd. De experimentele resultaten laten zien dat de praktische toepassing van het conceptuele ontwerp veelbelovend is.

Contents

Chapter 1

Introduction

1.1 Partial Discharge Detection for Power Cable Diagnostics

World-wide, electric power distribution relies on a vast network of underground medium-voltage (MV) cables for short distance power transport. The distribution grid has a finite life span, and at some stage a network operator has to decide when to replace its components or is confronted with unforeseen outages. In the past, corrective maintenance was normally applied, i.e. components were replaced after a failure. At present, de-regularization of the energy market has enforced grid owners to increase the reliability of an aging network, while to cut costs and postpone investments. Moreover, as a result of the ever-increasing demand for energy, existing connections are being loaded more extensively. Consequently, operators are interested in determining the condition of the network components, and ultimately their remaining lifetime, before initiating maintenance or replacement. The application of condition-based maintenance strategies can prevent outages due to cable failures, and results in substantial savings for network operators as well as increased power supply reliability [Sch99a].

Frequently, a single power cable is not long enough to bridge the distance as desired by the grid design and multiple cable sections are cascaded. In practice, the different sections are interconnected by joints, which are assembled manually in the field. An important cause of cable system failures is a breakdown of the electrical insulation between the conductors, which may occur particularly within cable accessories, such as joints. In the Netherlands, for instance, several types of cable joints suffer from deterioration and breakdown, causing about 50 % of the outages as experienced by customers [Wol04]. This deterioration is the result of a combination of ageing, stress, manufacturing and installation errors, etc (see e.g. [Sch00, Sch03]). As a part of condition assessment, several diagnostic methods are practiced to identify and locate weak components within the distribution network. Among the available diagnostic methods, partial discharge (PD) detection provides a non-intrusive and mostly non-destructive test to identify weak components at an early stage of deterioration [Kre64, Tan83, Bar00, Bog00].

Local electrical discharges that do not completely bridge the insulation between two conductors are called partial discharges [Kre64, IEC00]. These discharges occur at defects, such as air-filled cavities, within the insulation material, when the local field strength exceeds some threshold level. Discharges further degrade the material; therefore partial discharge is both a cause and an indicator of dielectric deterioration.

It should be noted, however, that not all degradation phenomena may produce discharges, and in addition, the relation between PD activity and insulation condition itself is non-trivial. For this reason, the interpretation of partial discharge diagnostic tests is not straightforward [Kre64, Tan83, Bog00]. Although mentioned here, further discussion on this topic is beyond the scope of this thesis, and research is focused exclusively on PD measurements.

The charge displacement that results from a partial insulation breakdown generates an electrical transient within the system conductors. The duration of a discharge is short and travelling waves are formed that propagate towards the cable ends. By detecting these PD signals at the cable terminations and estimating the arrival times, the discharge site and thus possible weak spots can be located along the cable length [Kre64, IEC00]. Cable connections generally do not degrade uniformly; therefore accurate mapping of weak components within the system is of crucial importance. Consequently, partial discharge based diagnostics contribute to the condition assessment of individual components within power cable systems.

1.2 On-line Partial Discharge Detection and Location

Up to now, field application of PD measurement methods is almost exclusively performed off-line. In this section, the extension to PD detection within a cable system that operates in service, is motivated. A short overview of available on-line PD measurement systems shows that practical techniques for on-line detection of discharges in underground MV cable connections with the capability to locate discharging defects, currently do not exist. The extension of off-line methods to on-line cable systems gives rise to a number of challenges. This thesis contributes to the development of on-line PD measurement methods, which can be applied in the underground distribution grid. In order to provide a framework for this research, the implications of on-line PD detection and location are identified in this section.

1.2.1 Motivation

For decades, extensive research has been conducted on PD diagnostic methods for cables in the field, producing several commercial apparatus [Ste91, Mas92, Lem95, Gul98, Mas00]. All conventional methods have in common that they are off-line in the sense that the cable under test is disconnected from the grid during measurements. This way, coupling devices can easily be installed without safety hazard, and moreover, the measurement equipment itself introduces no additional risk to the reliability of power delivery. In order to characterize the discharge phenomena active in an operating situation, the cable connection is energized using a separate mobile generator. Both the repetition rate at which partial discharges are excited and the discharge magnitude can be correlated, to a certain degree, with the stage of the degradation process [Ste04]. The effect of partial discharge on the cable system insulation may depend on other time-varying factors, such as thermal and mechanical stress. For these reasons, repetitive measurements or (semi-)continuous monitoring of PD activity is required to provide a solid basis for insulation condition assessment. Clearly, off-line systems can only obtain snapshots and only under the specific testing conditions. In order to capture trends in PD activity, an on-line diagnostic method, which can remain installed in a live cable system, is essential. All operations needed

to perform a conventional off-line PD test, such as switching, energizing, and testing itself, have to be done by specialized personnel. In addition, the cable must be taken out of service for some time. Ideally, on-line PD detection and location methods do not require these costly actions, thus potentially providing an economical advantage over off-line tests.

At present, several diagnostic methods are available that enable on-line PD detection within cable accessories, such as joints and cable terminations. The primary detection techniques make use of sensors that are either permanently installed within accessories during manufacturing [Hen96] or non-contact probes that can be placed afterwards without interrupting cable service [Fuk91, Pul95, Ahm98b]. Since accessories are physically small, condition assessment of the accessory as a whole is generally sufficient and PD location is not required in this case. In the literature, Ahmed and Srinivas report an extension of this method that is capable of on-line PD location within a cable section of very short length [Ahm01]. However, in order to diagnose a complete cable system, multiple sensors have to be applied closely spaced along the cable length. In addition to electromagnetic waves, some of the discharge energy is emitted as pressure waves, which can be detected using acoustic sensors [Lun92, Lun98]. However, acoustic waves are quickly attenuated; therefore, within power cable systems, discharges can only be detected using acoustic sensors installed close by a defect. In the underground distribution grid none of the above methods is widely applied, since the majority of cable accessories cannot be easily accessed. Also, application of many sensors in a cable connection is very expensive and is therefore only suitable for main energy transmission cables [Pla99].

Another class of tests that has recently been developed, aims at on-line detection of discharging defects within a distribution cable system but without the ability to locate discharging defects. Such tests serve as tools for the pre-selection of possibly weak cables, after which conventional off-line diagnostics are applied to quantify and locate discharging defects [Mac98, Ham01, Wal01, Mic03]. Although this approach is an important step forward and provides a valuable supplement to conventional off-line methods, it does not offer the desired functionality of an ideal on-line diagnostic test. At present, measurement methods capable of on-line PD detection and location, using sensors only at the cable ends do not exist, which motivates the research presented in this thesis.

1.2.2 Implications of On-line Partial Discharge Detection and Location

An on-line PD detection and location diagnostic method places some major restrictions on the coupling devices that can be applied. The sensors should preferably be installed on-line; therefore installation should be possible without safety hazard and at easily accessible points, i.e. at the cable system terminations. In order to prevent additional power supply failure risk, there should be no galvanic coupling of the cable under test with the measurement apparatus. Since partial discharge pulses are wideband but small as compared to the power grid operating voltage, the applied sensors should be sensitive in a wide frequency range excluding the grid operating frequency, namely 50 or 60 Hz.

Practical PD measurements are generally impeded by noise and interference. Especially in case of on-line detection, the signal to noise ratio (SNR) of the PD pulses is much lower as compared to an off-line situation [Ahm98a, Shi00, LP03]. Electromagnetic interference as well as partial discharges may be generated by adjacent

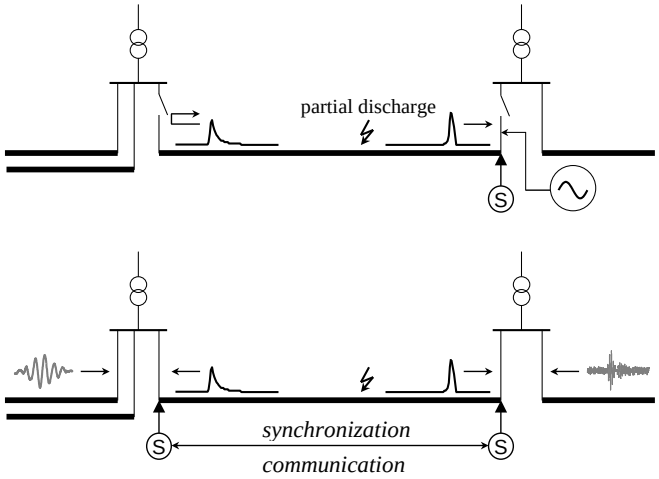

Figure 1.1 *In an off-line situation (top plot), the cable under test is disconnected from the grid and energized by a separate generator. PD signals, travelling in both directions, can be detected at one side, because of full signal reflection at the far end. In an on-line situation (bottom plot), signals are not necessarily reflected at the cable ends, and detection at both ends is required for the purpose of discharge location. In addition, disturbances that originate elsewhere, propagate through the cable under test.*

high-voltage equipment and are conducted or radiated to the sensors or accessories of the cable under test. In addition, operational switching can create large transients that permeate widely throughout the power system [Wal95]. Radio broadcasts and communications can be picked up by badly shielded grid components or by the sensors themselves [Ahm98a, Shi00, Wal01]. In order to deal with this noisy environment, appropriate sensors and their location within the system must be carefully selected. Moreover, signal processing is required to extract PD signals from corrupted measurements. In order to achieve monitoring of PD activity, huge amounts of data have to be analyzed. Clearly, monitoring is practically feasible only if data processing is fully automated. In addition, depending on the number and types of defects present, the discharge rate can be high. Consequently, processing efficiency is an important issue for fully automated PD detection and location.

In case of conventional off-line PD detection, the measurement and energizing equipment is generally connected to a single cable-end, while the other end is left open (see Fig.1.1). Since the pulse arriving at the open end will be fully reflected, the time difference of the signals arriving at the sensor provides a basis for PD location [Kre64, IEC87, Gul03]. In case of on-line detection, the cable is connected to the grid and PD pulses are not necessarily reflected. For this reason, signal detection at both cable ends is preferred in order to locate discharging defects. As a consequence, the measurement equipment must be synchronized and information must be communicated. Moreover, the components connected to the cable-ends transform the PD pulses, and must be taken into account for proper signal analysis.

In contrast to off-line methods where a voltage is applied to only a single phase, on-line PD measurements are performed while the cable under test is energized by a three-phase symmetric voltage. For single-phase shielded cables, the energizing

method has no effect on the electric field distribution within the dielectric. However, in case of three-phase belted power cables with a common earth screen, which are used extensively in e.g. the Netherlands, the off-line and on-line situations are substantially different. Discharge magnitude as well as discharge inception related to the field within a defect are important parameters of the degradation process [Kre64, IEC00]. When a single phase is energized, the field distribution within such a belted cable differs from the distribution in a normal operating situation. Consequently, discharging defects may behave differently in an on-line and an off-line measurement situation and test interpretations cannot be simply interchanged [Wie05]. Although this implication may have major consequences for condition assessment, research on this topic is beyond the scope of this thesis. Multi-conductor cables allow multiple measurement configurations to detect PD pulses, and the position of the sensors within the system under test is non-trivial. Depending on the measurement configuration, the characteristics of the measured signals vary and must be carefully analyzed in order to detect discharges and correctly quantify PD magnitude.

1.3 On-line Signal Analysis of Partial Discharges

The variety of challenges associated with on-line PD detection and location requires an approach based on multiple engineering disciplines. To that end, the research and development of an on-line PD measurement system is subdivided into different topics, partly addressed in this thesis and partly in [Wie05]. The main objective of this thesis is the research on signal analysis techniques for the purpose of automated on-line PD detection, location, and monitoring. In this section, the research topics, addressed in this thesis, are defined and related to [Wie05]. Then, as a starting point, a brief overview of existing PD signal analysis techniques is presented, which are mainly intended for off-line detection, and their applicability to on-line measurements is discussed. The work presented in this thesis is validated by measurements on an experimental grid. A description of the experimental grid is also given in this section.

1.3.1 Research Goals

This thesis is aimed at automated extraction of PD signals from on-line measurements and location of PD sources. This objective requires an approach based on digital processing of measurement data. To that end, the research is focused on signal-analysis algorithms for on-line PD detection and location. This research is relatively new, and various approaches are discussed in this thesis.

In order to deal with the harsh environment in which PD signals must be detected, the choice and location of the sensors is the first step towards a successful on-line method. The work presented in [Wie05] includes partial discharge signal measurement and deals with important topics such as sensor selection, design, and location. Although research on sensors for PD detection is not a part of this thesis, the choice of sensors influences the signals to be analyzed and must be taken into account.

The ability to separate a signal from disturbances improves with a priori knowledge about the signal and its source. To that end, characteristics of partial discharge signals in power cables are studied both in this thesis and in [Wie05]. The interpretation of measured signals benefits greatly from this study; therefore signal modelling is an important topic of this research. In order to effectively reject interference, knowledge

of the various classes of disturbance and their properties is essential. For this reason, part of the research involves characterization of noise and interference. In this thesis, the approach towards PD signal extraction is based on both the PD signal model as well as practical disturbance characteristics. In Section 1.3.2, the chosen method is related to existing algorithms for partial discharge signal extraction and interference rejection, which are primarily used for off-line detection.

Subsequent to extraction of PD signals from measurement data, the defects generating PD must be located. Accurate location relies on estimation of the difference in time of arrival (DTOA) of PD signals resulting from the same discharge. If both the cable length and the propagation velocity are known, PD generating defects can then be located along the cable system length. Besides imprecise knowledge of the cable length, other factors impede accurate location, such as attenuation and dispersion introduced by the cable, interference, and synchronization inaccuracies. An important research topic of this thesis is PD signal analysis for the purpose accurate defect location, where these factors are taken into account. Again the chosen approach is based on the signal model, which is related to off-line location algorithms as will be discussed in Section 1.3.3.

The ultimate goal of the research reported in this thesis is the development of an automated on-line PD measurement system that can locate discharging defects using sensors only at the cable ends. Part of [Wie05] concerns the design of a complete measurement system, with topics such as synchronization and communication, whereas in this thesis mainly integration of signal analysis techniques is discussed. Evidently, both studies are largely related and in many cases the research areas overlap; therefore part of the work was done in close cooperation.

1.3.2 Partial Discharge Signal Extraction and Interference Rejection

The large majority of existing signal extraction and disturbance rejection techniques is realized by digital processing algorithms [Bog00, Shi00]. In addition, analogue filters are commonly used to suppress interference prior to digitization [Shi00]. In practice, disturbance properties may vary with time and among measurement situations [LP03]; therefore analogue pre-filters should adapt to the situation at hand. Since the measurement bandwidth is generally large, the feasibility of analogue adaptive filters is very limited, and they are not discussed in this thesis.

Most digital processing algorithms are intended for off-line PD signal analysis; nevertheless, some are applicable to the on-line case as well. A number of generic methods has been proposed for the purpose of extracting PD signals and increasing SNR, such as averaging [Su94, Wlo94] and wavelet-based denoising [Shi01, Sat03]. Other methods explicitly aim at rejecting specific classes of interference. For instance, algorithms have been proposed for elimination of periodic short-time interferences [Nag94, Köp95]. By clustering similar signals based on their waveshape and time occurrence, repetitive interferences can be identified. Other methods aim at reduction of stationary stochastic disturbance by linear prediction [Bor92, Sch94a, Köp95]. Based on the correlation that exists between noise samples, (adaptive) filters are applied to predict noise sample values from previous samples. The estimates are then subtracted from the actually measured data in order to reduce stochastic interference. Also cancellers are applied that use a PD-free signal as a reference [Har96, Shi00]. In this case, the reference signal is obtained from an antenna placed nearby the PD sensor. Other techniques mitigate narrow-band interference from radio broadcasts

using notch filters with various implementations [Nag93, Du94a, Sch94b]. In this thesis, some of the above interference rejection methods are applied as a part of the PD signal extraction algorithms.

The foregoing processing methods make little or no use of knowledge of PD signals or process characteristics. In off-line PD diagnostics, the local field strength at a defect is directly proportional to the alternating voltage that energizes the cable. As mentioned, discharge excitation is related to the field strength within a defect, and thus to the phase angle of the applied voltage. This relation can be parameterized and regarded as a stochastic variable, of which the statistical properties can be characterized empirically to some extent [Kre64, Kre93a]. Based on the occurrence of pulses with respect to the phase angle, PD signals can be discriminated from pulse-shaped disturbance [Kre64, Bor95, Tan95]. Moreover, such phase distribution analysis is widely applied to classify defects types [Kre64, Kre93a, IEC00]. In the on-line case, the field strength at a defect is not necessarily related to an externally observable quantity, and these methods may not be applicable.

Another class of methods exists that uses a generic waveshape template to extract PD signals by means of correlation techniques [Kna90, Ste92, Su94, Hes99] or frequency domain matching [Buc96, Ahm01]. In practice, both signal and noise characteristics vary among measurement situations. In this thesis, an extraction technique is proposed that accounts specifically for these properties and adapts to the situation at hand. Since the method is based on waveshape matching, it can be regarded as an extension of the work presented in [Ste92]. The extraction method makes use of the signal model, which is specifically tailored to the cable system under test by measuring both signal model parameters and noise characteristics in the field. Unlike previous work, the proposed method applies to cable systems composed of sections with different properties. Moreover, the study presented in this thesis applies to both off-line and on-line PD measurements, whereas existing methods are merely intended for the off-line case. Theoretical performance bounds are derived, which enable accurate evaluation of the proposed method. In addition, algorithms for efficient automated signal extraction are developed.

1.3.3 Partial Discharge Location

As mentioned, the DTOA of PD signals from the same discharge forms the basis for defect location. Again, the majority of existing methods for PD location is primarily intended for off-line diagnostics. Here, usually a single sensor is employed, which detects both direct and reflected signals; therefore time synchronization is not an issue. In some cases, two-sided detection is applied, where time-base alignment is achieved using global positioning system (GPS) satellites [Ste01]. In the on-line case, signal detection at both cable ends is preferred and accurate synchronization is essential. In this thesis, signal processing concepts for time-base alignment are discussed.

Various algorithms have been proposed to enable DTOA estimation of PD signals corrupted by noise and interference, for instance by crosscorrelation of received PD pulses [Ste92]. Other methods aim at time of arrival (TOA) estimation of individual PD signals by matched filtering using generic waveform templates [Kna90, Ste92, Hes99]. Some methods employ a signal model adjusted to the specific cable under test [Mas92, Du94b]. Here, the model responses for various parameters are compared to received PD pulses and estimated by optimization of some criterion. In this thesis, location methods are proposed, which can be regarded as major extensions of the

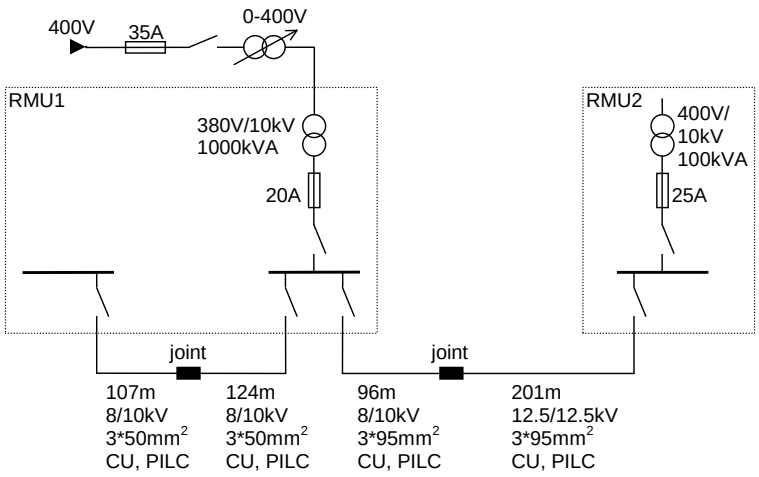

Figure 1.2 *Experimental grid consisting of an MV cable that connects two full-scale RMUs. Each RMU contains a MV distribution transformer and appropriate switch-gear. At RMU2, also an additional cable can be connected.*

work presented in [Mas92]. Unlike previous research, the methods apply to both off-line and on-line PD detection, as well as both one-sided and two-sided measurements. Moreover, novel implementations are developed and their theoretical performance bounds are derived and evaluated.

1.3.4 Experimental Validation

Signal measurement and analysis concepts, presented in this thesis, are validated by means of experiments. For testing purposes, a full-scale experimental set-up has been constructed at KEMA, the Netherlands. MV power cables are usually applied for power distribution from a substation to ring main units (RMUs), where the voltage is transformed to a low voltage for the customers. Fig. 1.2 shows a schematic drawing of the experimental grid, consisting of a MV cable connection between two RMUs. The connection was composed of a 10 kV 3×95 mm^2 Cu paper insulated lead covered (PILC) cable of 96 m length and a 12.5 kV 3×95 mm^2 Cu PILC cable of 201 m length. The two cables were wound up on cable drums and interconnected by a silicon-filled joint. At one end, the cable was terminated to an RMU with a 1000 kVA MV distribution transformer. Besides the cable under test, another PILC cable was terminated to this RMU. At the other end, the cable connection was terminated to a compact RMU, which contained a 100 kVA medium-voltage distribution transformer and no out-going cables. The exact configuration of the experimental grid could be altered utilizing the switch-gear present in the RMUs. Since the cables were wound up on drums, the two RMUs were actually located close to each other, allowing easy installation of measurement equipment.

The experimental grid can be energized by applying a 50 Hz symmetric three-phase voltage to the secondary windings of the 1000 kVA transformer, i.e the low-voltage side. A variable transformer was used to control the voltage applied to the distribution transformer, and thus the cable energizing voltage.

1.4 Thesis Outline

This thesis is focused on PD signal analysis, which is subdivided into signal modelling, signal extraction and discharge location. To that end, characteristics of partial discharge signals in power cables are studied extensively and a signal model is derived. The model forms the basis for further studies and discussions on signal analysis techniques, and for the theoretical evaluation of proposed methods. In Chapter 2, the signal model and its empirical evaluation is described. The propagation of a PD signal from its generation to the sensors is studied, where the properties of the sensors and the sensor positions at the cable ends are taken into account as well.

Besides the properties of PD signals, the design of analysis algorithms depends on the noise and interferences that can be expected. A number of tentative field measurements was conducted and the results of this survey are reported in Chapter 3. Disturbance classes are identified and first directions towards interference rejection are given. Based on the measurements, PD signal quality measures are defined and quantified roughly. The noise and interference characteristics observed in the tentative on-line measurements, are used in computer simulations for theoretical evaluation of signal analysis algorithms.

In field measurements, the PD signal characteristics depend and the specific cable connection under test. For the purpose of signal extraction and discharge location, the parameters of the signal propagation model must be measured prior to PD detection. Chapter 4 is devoted to the estimation of signal model parameters in practical off-line and on-line situations. It is shown that the parameters of interest can be measured by evaluating the response of the cable system to an applied transient. Various methods are presented and their feasibility and quality are evaluated by theoretical simulations and practical experiments.

Based on the signal model and interference classification, a PD detection and extraction method is proposed in Chapter 5 that can be adapted to practical measurement situations. Interference rejection techniques are studied and applied. The chosen methods allow full automation of PD signal detection. As a first step towards semi-continuous monitoring of PD activity, efficient processing implementations are presented. The proposed method is validated by simulation experiments, and its quality and limitations are discussed.

Chapter 6 deals with location of partial discharges in power cables. The performance of location methods based on both one-sided and two-sided PD detection is studied and evaluated by theory. Concepts for time-base alignment in case of a two-sided measurement topology are presented. A model-based location method is proposed and the quality of location estimation is discussed and evaluated by simulation experiments.

The ultimate goal of the research is the development of an automated PD measurement system that can detect and locate partial discharges within an on-line cable connection. In Chapter 7, the research presented in the previous chapters converges to a conceptual design of an on-line measurement system. The system proposal is validated by experiments and evaluated by comparing results to conventional off-line results.

In conclusion, Chapter 8 summarizes the main contributions of this work and gives directions for future research.

Chapter 2

Partial Discharge Signal Characteristics

2.1 Introduction

Signal analysis methods depend on knowledge of the signals that are to be expected. The occurrence and nature of partial discharge signals in power cables are determined by the cable system properties. In this chapter, characteristics of partial discharges occurring in distribution cable connections are studied, and a theoretical signal model is proposed for PD detection.

Power distribution networks are generally operated at medium voltage, i.e. up to about 30 kV. For this voltage class, mainly two types of power cable are applied, namely paper insulated lead covered (PILC) cable and cross-linked polyethylene (XLPE) cable. In the Netherlands, most power distribution cables are belted PILC cables; therefore the characteristics of this cable type are primarily considered. Fig. 2.1 shows an example of a belted PILC cable. Three sector shaped conductors are separately insulated by windings of paper tape which are impregnated with compounds of oil, wax and epoxy resin, in various proportions. The phase conductors can be aluminium or copper, and stranded or solid. In electrical considerations, stranded phase conductors can be regarded as solid, since currents are homogeneously distributed over the surface of the phase conductor. The exact dimensions depend on the cable load conditions, and a single conductor surface can range from 25 to over 200 mm^2. A common insulation or belt is wrapped around the cores and a lead shield or earth screen serves as a reference conductor. The core and belt insulation thicknesses depend on the maximum and normal operating voltages. Bitumenized paper and jute separate the shield from a steel armor, which is again covered by bitumenized jute. An underground cable system consists of a cascade of several three-phase belted cable sections interconnected by joints. At each end, the cable connection is terminated at a substation or ring main unit (RMU). In an RMU, the phase and neutral conductors are connected to other high-voltage (HV) equipment, such as switch gear, distribution transformers, as well as adjacent cable systems. Underground cables can only be non-intrusively accessed at the terminals. Therefore easy installation of sensors on a medium voltage grid is only possible within RMUs. Preferably, there should be no galvanic coupling of the sensors with HV equipment, in order to prevent safety hazards or power failure risk. Inductive probes that are connected to the earth strap

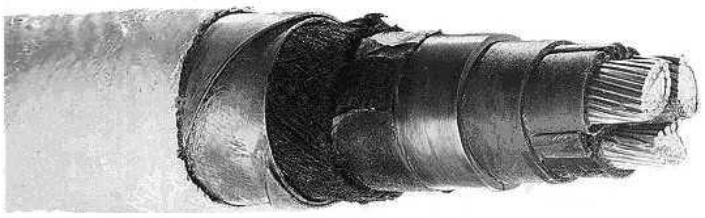

Figure 2.1 *Typical layout of a belted PILC cable (courtesy of TKF, the Netherlands).*

at a termination meet these requirements (see e.g. [Mac98, Mor99, Ham01]). For this reason, the study of PD signals detected in the earth screen is emphasized.

The following section gives a short summary of partial discharge signal excitation in three-phase belted cables based on a simplified model [Wie03a]. Probability distributions of PD parameters are used extensively for off-line PD signal analysis, see e.g. [Kre64, Kre93a, Bor95, Tan95]. In Section 2.2 it is shown that a priori probability distributions cannot be assumed for analysis of PD signals detected in on-line three-phase belted cables. A power cable can be considered as a waveguide for PD signals [Sto82, Bog96]. In Section 2.3 the propagation of partial discharges in cascaded three-phase belted cables is studied. Physical propagation parameters are identified and quantified by experiments and theoretical considerations. The RMU and its components as well as the applied sensors have a major influence on PD signal characteristics. Sensors and their positions within RMUs are discussed in Section 2.4. In Section 2.5 a complete model for partial discharge signal waveforms in cable systems is proposed and validated by experimental results. Conclusions and recommendations are given in Section 2.6.

2.2 Partial Discharge Excitation

Within the insulation of belted cable systems, inclusions of relatively low dielectric strength are present, such as air-filled cavities and alien particles. Especially cable joints commonly have such insulation defects, since joints are constructed manually in the field. When a voltage is applied to the cable conductors, the electrical field may cause breakdown of the defective material if some threshold is exceeded. The electrical field drop caused by breakdown, results in a current induced in the conductors. At the RMU, the current impulse is the only measurable effect related to partial insulation breakdown. In this section probability distributions associated with partial discharge signal excitation in three-phase belted paper cables are discussed. The section is a short summary of the work presented in [Wie03a], and should be regarded as a starting point for partial discharge signal characterization.

2.2.1 Partial Discharge Magnitude Distribution

Besides the electrical field strength, discharge magnitude is related to the defect shape, size, and material, as well as the defect location within the cable system cross-section [Kre64, Cri89]. As a consequence the discharge magnitude is an important measure of

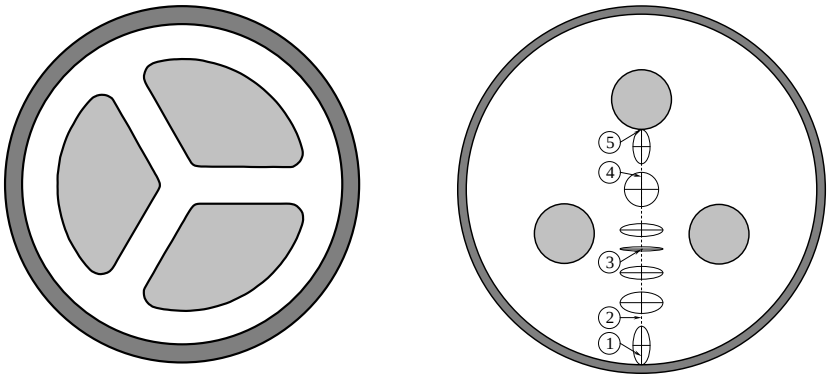

Figure 2.2 *Schematized cross-sections of a three-phase belted cable (left) and a three-phase cable joint (right). In the right-hand plot, the path followed by a rotating electrical field vector is visualized by an ellipse for various transversal positions within the insulation. The numbers* $1-5$ *indicate reference points for Fig. 2.3.*

the nature and state of a degradation process. Besides the deterministic defect properties, the PD magnitude depends on varying quantities such as the remaining charge after breakdown as well as chemical reactions caused by discharge. Therefore discharge magnitude is commonly regarded as a stochastic variable [Kre93a, Cac95, Tan95]. The magnitude probability density function parameters can provide information on defect properties, and thus on degradation phenomena.

For spherical voids, charge displacement is directed along the electrical field lines between two conductors, and a charge is induced accordingly [Cri89]. In case of single-phase shielded cables, the field is radially directed within the cable cross-section. The ratio of induced and actual discharge magnitude does not depend on the operating voltage angle or the transversal position of the defect. In contrast, within the cross-section of a three-phase belted cable, as depicted in Fig. 2.2, the electrical field direction is not radial, but depends upon the location of a defect. Moreover, since the three conductors are energized simultaneously but with a mutual phase-shift of 120 degrees, the electric field direction is a function of the operating voltage phase angle as well. Especially in cable joints, the field is determined by more than two conductors for almost any point within the configuration. Therefore the electric field rotates with the operating voltage angle, as depicted in Fig. 2.2. This observation implies that induced charge magnitude may not be only related to the field drop caused by breakdown of the defect material [Wie03a]. For instance, consider cylindrical voids at transversal positions $1-5$ depicted in the right-hand plot in Fig. 2.2. Note that the plots are not drawn on the same scale, since, in reality, the conductor surfaces are equal for a cable and a joint. Assume that after partial discharge the field within the void is neutralized. Any stochastic parameter influencing PD magnitude is ignored. Consequently, the electric field strength, and therefore the operating voltage angle, determines the discharge magnitude. In Fig. 2.3, the ratio of apparent charge induced in the cable earth screen and the actual defect discharge magnitude is plotted as a function of the phase angle. At positions 1 and 5 the electrical field is (almost) linear, i.e there exists only one field direction, and the absolute ratio is independent of the phase angle. At positions where the field is rotating, e.g. position 2 (circular field)

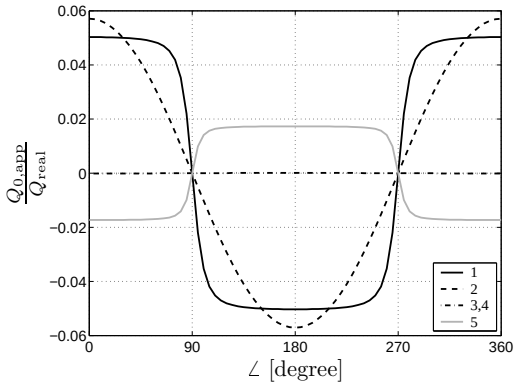

Figure 2.3 *Ratio of apparent charge induced in the cable earth screen ($Q_{0,\mathrm{app}}$) and the real discharge magnitude (Q_{real}) of idealized voids at locations $1-5$ depicted in Fig. 2.2. Details of the simulation can be found in [Wie03a].*

in Fig. 2.2, the induced charge is a function of the phase angle. Moreover, at some positions a discharge may not produce a detectable current within the screen at all, as is the case for positions 3 and 4. It can be concluded that the magnitude probability distribution of induced charges is not necessarily similar to the defect discharge distribution. As a consequence, for three-phase belted cables the induced charge magnitude probability distribution can be rather arbitrary in contrast to systems with a linear electric field [Wie03a].

2.2.2 Phase Angle Distribution

Both the electrical field within a defect and the defect breakdown strength depend on the defect properties. In case of a linear electrical field configuration, the local field strength is directly proportional to the applied sinusoidal voltage. The occurrence of discharge as a function of the energizing voltage phase angle is an important parameter of a defect. Therefore phase patterns that are obtained by plotting partial discharge activity against the phase angle, are utilized to characterize degradation phenomena [Kre64, Kre93a, Tan95]. In case of three-phase belted cables, the field within a defect may be rotating and cannot be simply linked to the phase angle. A rotating field can be parameterized by the field eccentricity η, defined as the ratio of the minimum and maximum field strength of the elliptical field vector. The field eccentricity increases from zero for a linear field to unity for a circular field. Defect discharge in a rotating field is a function of the local field strength and eccentricity, the phase angle, and the discharge inception field strength. In Fig. 2.4, the simulated number of discharges in an idealized void per cycle of the operating voltage is plotted as a function of the phase angle and the field eccentricity. Clearly, the PD phase distribution is a function of the field eccentricity. For a linear field, patterns arise that have a strong phase angle dependency, which corresponds to e.g. [Kre93a, Tan95]. In case of a circular field, PD occurrence may not be related to the phase angle at all. Thus apart from the defect properties, PD distribution depends on the defect location in the component cross-section [Wie03a].

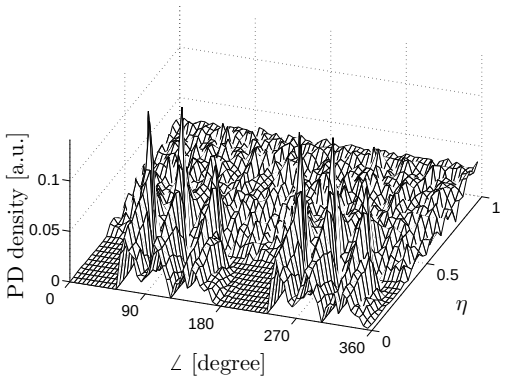

Figure 2.4 *Example of the distribution of partial discharges in idealized void as a function of the local field-eccentricity (η) and operating voltage phase-angle.*

It can be concluded that for three-phase belted cables the transversal location of a defect has a pronounced effect on discharge occurrence and induced charge magnitude. As a consequence, neither magnitude probability nor phase angle distributions can be assumed as a priori knowledge for the purpose of PD signal extraction.

2.3 Partial Discharge Signal Propagation

When an insulation defect discharges, the signal generated within the conductors travels away from the discharge origin. Besides its excitation, PD signal characteristics are determined by the propagation path. Although PILC cables have compound insulation, it is assumed that the dielectric is approximately homogeneous. Wavelengths much larger than the distance between conductors are considered; therefore the transverse electromagnetic mode of propagation applies. This section starts with a description of signal propagation in single-phase cables, which is then extended to three-phase belted cables. Physical parameters are investigated and a simplified model is proposed.

2.3.1 Single-Phase Shielded Cables

A single-phase power cable can be regarded as a two-conductor transmission line consisting of a core and a concentric neutral conductor. For a cable of uniform cross-section along its length, propagation can be described by a set of differential equations. In the frequency domain, the phase voltages $V(z,\omega)$ and currents $I(z,\omega)$ at an infinitesimal distance ∂z apart are related as

$$\frac{\partial}{\partial z}\begin{pmatrix} V(z,\omega) \\ I(z,\omega) \end{pmatrix} = -\begin{pmatrix} 0 & Z(\omega) \\ Y(\omega) & 0 \end{pmatrix}\begin{pmatrix} V(z,\omega) \\ I(z,\omega) \end{pmatrix} \tag{2.1}$$

where $Z(\omega)$ and $Y(\omega)$ represent the per-unit-length line impedance and admittance, respectively. By decoupling the differential equations, the plane wave solutions in

terms of forward and backward travelling waves are obtained

$$\begin{aligned} V(z,\omega) &= V^{+}e^{-\gamma(\omega)z} + V^{-}e^{+\gamma(\omega)z} \\ I(z,\omega) &= I^{+}e^{-\gamma(\omega)z} - I^{-}e^{+\gamma(\omega)z} \,. \end{aligned} \tag{2.2}$$

The effect of attenuation and dispersion introduced by the cable is described by the product of the propagation factor $\gamma(\omega) = \sqrt{Y(\omega)Z(\omega)}$ and the travelled distance z. The ratio of voltage and current waves defining the characteristic wave impedance is given by $Z_{\mathrm{c}}(\omega) = \sqrt{Z(\omega)/Y(\omega)}$.

2.3.2 Three-Phase Shielded Cables

Signal propagation in multi-conductor transmission lines can be described by a generalization of the two-conductor equations. For three-phase belted cables, the system of equations is given by

$$\frac{\partial}{\partial z}\begin{pmatrix} \underline{V}(z,\omega) \\ \underline{I}(z,\omega) \end{pmatrix} = -\begin{pmatrix} \mathbf{0} & \mathbf{Z}(\omega) \\ \mathbf{Y}(\omega) & \mathbf{0} \end{pmatrix}\begin{pmatrix} \underline{V}(z,\omega) \\ \underline{I}(z,\omega) \end{pmatrix} \tag{2.3}$$

where the phase voltage and current vectors equal $\underline{V}(z,\omega) = (V_1, V_2, V_3)^t(z,\omega)$ and $\underline{I}(z,\omega) = (I_1, I_2, I_3)^t(z,\omega)$. The 3×3 matrices $\mathbf{Z}(\omega)$ and $\mathbf{Y}(\omega)$ represent the per-unit-length impedance and admittance, respectively. The solution to the system is obtained by changing variables and represents three propagation channels, each of which can be interpreted as a two-conductor transmission line, see e.g. [DZ93, Pau94]. In three-phase belted cables, only two distinct propagation channels exist because of the rotation-symmetric and reflection-symmetric cable structure (see Appendix A). Sensors, measuring the current in the cable earth screen, exclusively detect signals in the shield-to-phase (SP) channel, which propagates the sum of voltages or currents on all three phases. For instance, the forward travelling wave (indicated by the superscript $^{+}$) of some initial SP voltage and current vector is expressed as

$$\begin{pmatrix} V_1^{+} + V_2^{+} + V_3^{+} \\ I_1^{+} + I_2^{+} + I_3^{+} \end{pmatrix}(z,\omega) = e^{-\gamma_{\mathrm{SP}}(\omega)z}\begin{pmatrix} V_1^{+} + V_2^{+} + V_3^{+} \\ I_1^{+} + I_2^{+} + I_3^{+} \end{pmatrix}(0,\omega) \,. \tag{2.4}$$

Propagation of the difference between two phase voltages or currents corresponds to the phase-to-phase (PP) channel, e.g.

$$\begin{pmatrix} V_1^{+} - V_2^{+} \\ I_1^{+} - I_2^{+} \end{pmatrix}(z,\omega) = e^{-\gamma_{\mathrm{PP}}(\omega)z}\begin{pmatrix} V_1^{+} - V_2^{+} \\ I_1^{+} - I_2^{+} \end{pmatrix}(0,\omega) \,. \tag{2.5}$$

The existence of multiple propagation channels is illustrated by an experiment on a three-phase XLPE cable, with a common earth screen enclosing the three conductors. Generally, XLPE cables do not have a solid shield. Instead, the concric neutral consists of spaced helical copper wires. As a consequence the propagation path for signals travelling through the SP channel is effectively longer than for signals travelling through the PP channel. When, at a cable end, a pulse is applied to a single phase conductor with respect to the earth screen, the signal is distributed among the propagation channels. As depicted in Fig. 2.5, two pulses appear in the response measured at the same conductor at the other cable end, because of the different channel delays. Theoretically, each PP channel is orthogonal to the SP channel. However, in practice a cable is not perfectly uniform along its length. As a consequence, some cross-talk

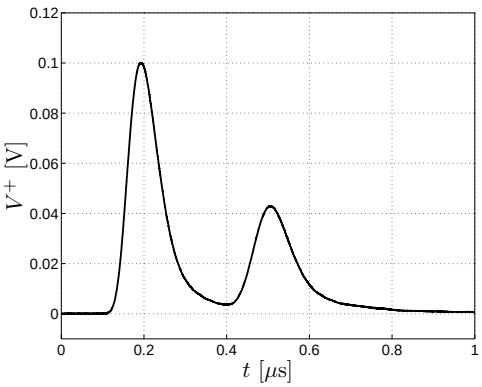

Figure 2.5 *Response of a 192 m long 3×95 mm^2 Al XLPE cable to a pulse injected between one phase conductor and the screen.*

may exist between the channels. In an experiment the cross-talk was examined for a typical belted PILC cable of 200 m length, see [Wie03a]. A pulse was injected in the SP channel at one cable end, and the responses of the various channels at the other end were measured. The results indicate that cross-talk between the SP and PP channels is very small, and does not exceed -35 dB. It should be noted that cross-talk can also be due to coupling at the injection site.

2.3.3 Propagation Parameters

The propagation parameters are determined by the cable parallel admittance and series impedance matrices, which again depend on the dimensions and material properties. In this section, physical parameters are investigated and a simplified model of the SP channel parameters is proposed.

Impedance

The impedance per unit length consists of the conductor resistance and inductance in a cross-section of the propagation path. Imperfect conductors give rise to losses that increase with temperature. As a result of self-inductance, alternating currents tend to flow near the surface of a conductor. Due to this skin-effect, the effective conductor resistance increases with frequency. Since the cable cores and shield are closely spaced, the external magnetic flux links the currents in the conductors, and the return currents are drawn towards the leaving currents. The direct solution for the resistance and internal inductance of conductors can be obtained using a variety of methods for solving the diffusion equation in the transverse plane. For instance, the SP channel can be approximated by a single-core coaxial model, where the three segment-shaped phase-conductors are substituted by a single solid conductor having the same radius. For skin-depths that are small with respect to the conductor radii, an approximated direct solution of the diffusion equation can be obtained (see e.g. [Kad59, Pau94]). For these frequencies, the resistance $R_{\mathrm{SP}}(\omega)$ and self-inductance

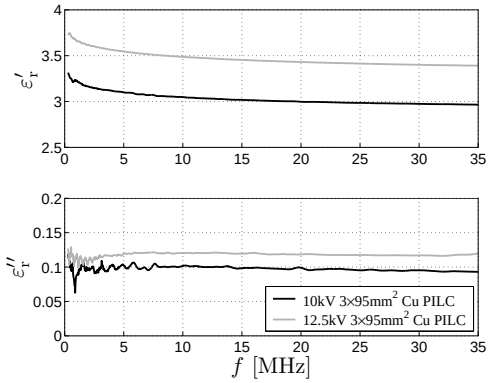

Figure 2.6 *Measured complex dielectric constants of two typical PILC cables.*

$L_{\mathrm{SP,i}}(\omega)$ are approximated by

$$R_{\mathrm{SP}}(\omega) \approx \frac{1}{2\pi r_{\mathrm{c}}\delta_{\mathrm{c}}\sigma_{\mathrm{c}}} + \frac{1}{2\pi r_{\mathrm{s}}\delta_{\mathrm{s}}\sigma_{s}} , \tag{2.6}$$

$$L_{\mathrm{SP,i}}(\omega) \approx \frac{\mu_0\delta_{\mathrm{c}}}{4\pi r_{\mathrm{c}}} + \frac{\mu_0\delta_{\mathrm{s}}}{4\pi r_{\mathrm{s}}} \tag{2.7}$$

where r_{c} and r_{s} are the core radius and screen inner radius, and σ_{c} and σ_{s} are the specific conductivities. The skin depths in the core and screen are represented by δ_{c} and δ_{s}, respectively, and are defined as

$$\delta_{\mathrm{s,c}} = \sqrt{\frac{2}{\omega\mu_0\sigma_{\mathrm{s,c}}}} . \tag{2.8}$$

The magnetic flux outside the conductors determines the external inductance

$$L_{\mathrm{SP,e}} = \frac{\mu_0}{2\pi} \ln \frac{r_{\mathrm{s}}}{r_{\mathrm{c}}} . \tag{2.9}$$

The total per-unit-length impedance of the SP channel equals

$$Z_{\mathrm{SP}}(\omega) = R_{\mathrm{SP}}(\omega) + j\omega(L_{\mathrm{SP,i}}(\omega) + L_{\mathrm{SP,e}}) . \tag{2.10}$$

Admittance

The admittance per-unit-length consists of the conductance and capacitance in a cross-section of the propagation path. The capacitance is determined by considering the displacement current flowing in a transverse plane between the conductors as a result of an applied voltage. Due to the restricted movement of charges within a dielectric, an alternating electric field gives rise to various polarization mechanisms [Sil73]. Electromagnetic wave propagation in PILC cables therefore results in the excitation and polarization of dipoles at molecular scale. Energy is absorbed and dissipated as heat when the dipoles are aligned with the electric field component, which manifests itself as dielectric loss. Moreover, dipole orientation takes time, and the ability of dipoles to align decreases with the frequency of the electric field, which

contributes to dispersion of travelling waves. When the frequency is sufficiently high, the molecular forces impeding dipole orientation dominate, and the dipoles become unable to follow the changing field. At these frequencies the orientation of dipoles no longer contributes to the dielectric constant [Zae03]. The electric displacement and the applied field are related by the complex dielectric constant, given by

$$\varepsilon(\omega) = \varepsilon_0 \varepsilon_\mathrm{r}(\omega) = \varepsilon_0(\varepsilon'_\mathrm{r}(\omega) - j\varepsilon''_\mathrm{r}(\omega)) \tag{2.11}$$

where $\varepsilon'_\mathrm{r}(\omega)$ represents the relative permittivity and $\varepsilon''_\mathrm{r}(\omega)$ is the dielectric loss factor. Again by considering a single-core coaxial approximation, the capacitance of the SP channel is expressed as

$$C_\mathrm{SP}(\omega) = \frac{2\pi\varepsilon_0\varepsilon_\mathrm{r}(\omega)}{\ln\frac{r_\mathrm{s}}{r_\mathrm{c}}} \ , \tag{2.12}$$

since $L_\mathrm{e}\, C = \mu\varepsilon$ for homogeneous dielectrics [Pau94]. In addition to the effect of polarization, free charges are transported between the conductors, which results in conduction,

$$G_\mathrm{SP} = \frac{2\pi\sigma_\mathrm{d}}{\ln\frac{r_\mathrm{s}}{r_\mathrm{c}}} \tag{2.13}$$

where σ_d is the specific conductivity of the dielectric. The total per-unit-length admittance of the SP channel equals

$$Y_\mathrm{SP}(\omega) = G_\mathrm{SP} + j\omega C_\mathrm{SP}(\omega) \ . \tag{2.14}$$

In certain XLPE cables, semi-conducting layers are applied between the conductors and the insulation material. The influence of the semi-conducting layer can be modelled as an additional contribution to the per-unit-length admittance [Wou91]. Although mentioned here, further study of XLPE cables is not discussed in this thesis.

Quantitatively, the permittivity and loss factor of paper insulation depend on the impregnating mass, the paper type, mechanical pressure and other properties that vary from cable to cable. When in service, the dielectric constant changes with parameters such as electrical and mechanical stress, age, chemical deterioration, temperature, and moisture ingress [Cla62, Con65]. As a consequence, no generic theoretical or experimental dielectric constant can be assumed. For instance in Fig. 2.6, the dielectric constants of two PILC cables are plotted. Results were obtained by comparing the SP propagation factors to the single-core coaxial approximation and leaving $\varepsilon(\omega)$ as the only unknown, as described in Appendix B.

Attenuation and Dispersion

The complex propagation factor can be split into a real and an imaginary part,

$$\gamma(\omega) = \sqrt{Y(\omega)Z(\omega)} = \alpha(\omega) + j\beta(\omega) \tag{2.15}$$

where $\alpha(\omega)$ is the attenuation per unit length and $\beta(\omega)$ is the phase shift per unit length. Clearly, both quantities depend on the cable dimensions and material properties, and therefore vary from cable to cable. Since the dielectric constant is unknown, cable propagation properties can only be modelled up to this material parameter. In order to verify the coaxial model for the SP channel, boundary element simulation results were compared to model results. In the comparison the permittivity was set

to constant and the loss factor was neglected. In Fig. 2.7, the simulated and modelled attenuation of PILC cables with different dimensions are plotted. Clearly, the model gives good approximations of the simulation results. Because dielectric losses are neglected, a $\sqrt{\omega}$ behavior due to skin losses predominates.

The measured SP attenuation is plotted in Fig. 2.8 for two typical cable types. Attenuation measurements were obtained by cable pulse response analysis as described in Appendix B. Attenuation simulations result from the coaxial model, where the measured dielectric constants, presented in Fig. 2.6, were used. The figures show that the measurements and models match for a broad frequency range. As the dependency is close to linear with frequency, it is concluded that dielectric losses dominate over the skin-effect losses for the considered frequency range. In addition, PP channel properties were obtained as described in Appendix B. Fig. 2.9 illustrates that SP and PP attenuation may differ for certain cable types.

Dispersion introduced by the propagation path can be examined by expressing the phase velocity for each frequency component in terms of the phase shift

$$v_{\mathrm{p}}(\omega) = \frac{\omega}{\beta} \,. \tag{2.16}$$

As shown in Fig. 2.10, low frequency components travel at a lower speed than components of higher frequency. Moreover, Fig. 2.10 illustrates that the propagation velocity can vary depending on the cable type. For frequencies such that $R \ll \omega L$ and $G \ll \omega C$, the phase shift is approximated by

$$\beta(\omega) \approx \omega\sqrt{LC} \,. \tag{2.17}$$

Since the external inductance dominates the total inductance, the phase velocity is approximated by

$$v_{\mathrm{p}}(\omega) \approx \frac{c}{\sqrt{\varepsilon'_{\mathrm{r}}(\omega)}} \,. \tag{2.18}$$

where $c = 1/\sqrt{\mu_0\varepsilon_0}$ is the velocity of light in vacuum. Consequently, the propagation speeds in the SP and PP channel are approximately equal, as shown in Fig. 2.10.

As a result of frequency dependent attenuation, the frequency content of PD signals is determined by the propagation distance. Typical distances, where $\alpha(\omega)z = 1$ Np, vary from z=100 m for f=10 MHz to close to z=10 km for f=0.1 MHz. Due to dispersion, frequency components spread as they travel through the cable. Although propagation properties can be approximated by simplified models that comprise the cable dimensions, the dielectric constant determines the exact attenuation and dispersion to a large extent.

Characteristic Impedance

The ratio of travelling voltage and current waves is defined as the characteristic impedance $Z_{\mathrm{c}}(\omega) = \sqrt{Z(\omega)/Y(\omega)}$. In Fig. 2.11, an example of the characteristic impedances of the SP and PP channel is depicted, as obtained by pulse response measurements. Clearly, the measured characteristic impedances are approximately real and can be considered as approximately frequency independent. Since the capacitance of the SP channel is generally larger than the PP channel, the SP characteristic impedance is smaller than the PP impedance.

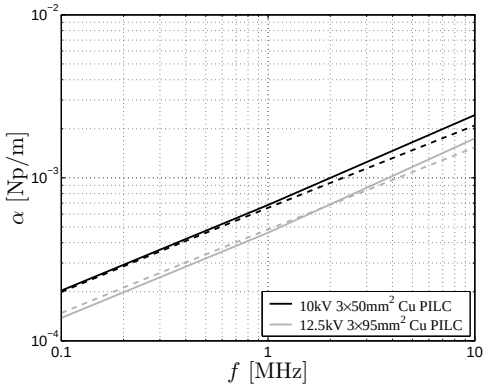

Figure 2.7 *SP channel attenuation of two typical PILC cables obtained by boundary element simulations (solid) and coaxial model simulations (dashed), where dielectric losses were ignored.*

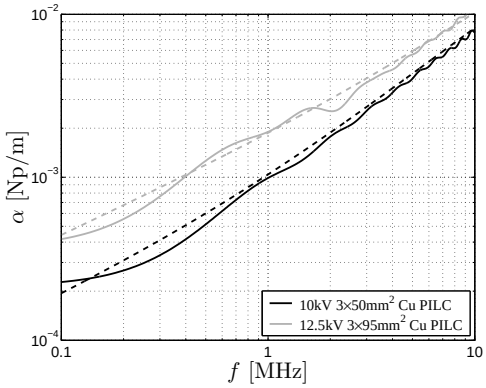

Figure 2.8 *SP channel attenuation measurements of two typical PILC cables obtained by pulse response analysis (solid). Dashed lines represent coaxial model simulations, where the measured dielectric constants, presented in Fig. 2.6, were used.*

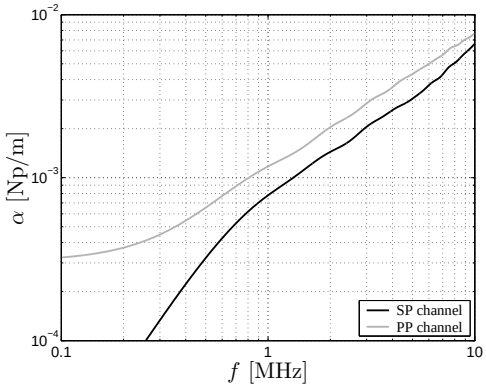

Figure 2.9 *SP and PP channel attenuation of a 10 kV 3×95 mm^2 PILC cable obtained by pulse response analysis.*

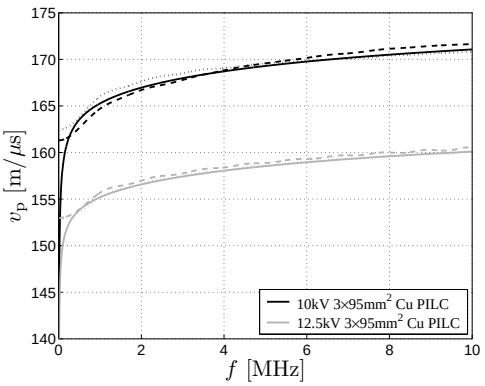

Figure 2.10 *Propagation velocity of typical PILC cables. Dashed and dotted lines represent SP and PP channel velocities, respectively, as obtained by pulse response analysis. Solid lines represent coaxial model simulations of the SP channels.*

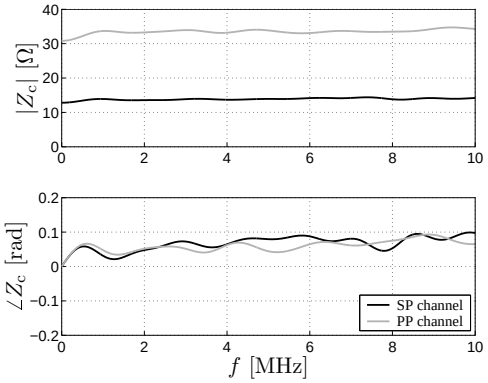

Figure 2.11 *Measured SP and PP channel characteristic impedance of a 12.5 kV 3×95 mm^2 Cu PILC obtained by pulse response analysis.*

2.3.4 Composite Cable Systems

An underground cable system consists of a cascade of multiple three-phase cable sections interconnected by joints. In a cable system different cable types may be present. For this reason, separate propagation properties have to be taken into account. A uniform cable section can be characterized as a generic two-port. For a section of length l, the following relation holds for the input and output of a single propagation channel (see e.g. [Pau94])

$$\begin{pmatrix} V_{\mathrm{in}}(\omega) \\ I_{\mathrm{in}}(\omega) \end{pmatrix} = \mathbf{\Theta}(\omega) \begin{pmatrix} V_{\mathrm{out}}(\omega) \\ I_{\mathrm{out}}(\omega) \end{pmatrix} \tag{2.19}$$

where the chain parameter matrix $\mathbf{\Theta}(\omega)$ equals

$$\mathbf{\Theta}(\omega) = \begin{pmatrix} \cosh(\gamma(\omega)l) & Z_{\mathrm{c}}(\omega)\sinh(\gamma(\omega)l) \\ \sinh(\gamma(\omega)l)/Z_{\mathrm{c}}(\omega) & \cosh(\gamma(\omega)l) \end{pmatrix} . \tag{2.20}$$

Within a composite cable system, each section is characterized by a chain matrix, with parameters Z_{c}, l and $\gamma(\omega)$ (see Fig. 2.12). The overall chain parameter matrix

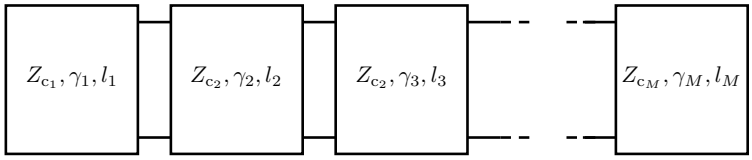

Figure 2.12 *A composite cable connection can be modelled as a cascade of two-ports, each of which characterizes a cable section.*

of a cascade of M sections is now expressed as

$$\mathbf{\Theta}(\omega) = \mathbf{\Theta}_1(\omega)\mathbf{\Theta}_2(\omega) \ldots \mathbf{\Theta}_M(\omega) \tag{2.21}$$

where $\mathbf{\Theta}_m(\omega)$ equals the chain parameter matrix of the m-th cable section.

Cable joints that interface two sections, can be regarded as lumped impedances, since the dimensions are small with respect to the minimal wavelength considered. Many different joint types are employed, depending on mechanical, electrical, and economical requirements. Generally, a three-phase cable joint for medium voltage consists of an iron shell and a plastic inner housing. Barring some exceptions, the metal cable screens are attached to the iron shell. Within the plastic inner housing, the separate phase conductors of the cables are bonded and enclosed by insulating caps. The inner housing can be filled with insulation materials such as oil, rubber, epoxy resin, bitumen, etc. Although ideally the joint geometry has rotation and reflection symmetry in many cases, in practice this symmetry can be upset. For instance, in some cable joint types the phase conductors are not symmetrically arranged with respect to the center, so there is no rotation symmetry. Moreover, in some cases the phase conductors may be crossed during assembly, which completely upsets any symmetry. Due to the possible upset of symmetry, signals propagating through orthogonal channels can be mixed, thus influencing PD signal characteristics. Because of the large variety of joints and their construction, no generic characterization can be obtained. However, in general it can be stated that attenuation, dispersion, and mixing introduced by cable joints is negligible, since their length is small and the cross-section geometry is approximately isomorphic to the cable.

2.4 Partial Discharge Signal Measurement

On-line PD detection in power cables places some major restrictions on the measurement techniques that can be applied. Since sensors should preferably be installed non-intrusively, installation is only possible at the cable terminations. Consequently, besides the cable propagation properties, PD signal characteristics are determined by the RMU and its components. In this section, the propagation channel load impedances are studied. Although research on sensors for PD detection is not a part of this thesis, the sensors influence the signals to be analyzed and must be taken into account. To that end, in this section the characteristics of the applied sensors are briefly discussed. The position of sensors in an RMU determines which propagation channel is measured. In this section, practically applicable sensor positions and the effect on measured PD signals are studied. More details on sensors and sensor positions within RMUs can be found in [Wie05].

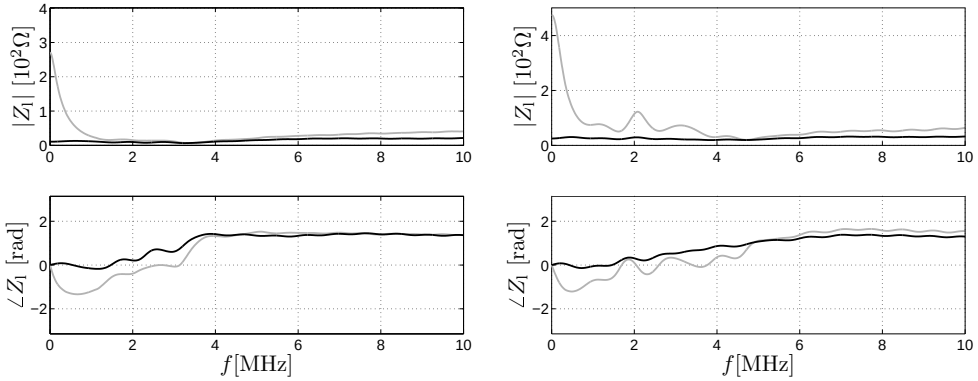

Figure 2.13 *Measured SP channel (left) and PP channel (right) impedances of a typical compact RMU with a distribution transformer and either a single cable termination (grey) or two terminations (black).*

2.4.1 Propagation Channel Load Impedance

In an RMU, the cable phase conductors and screen can be connected to a distribution transformer as well as to adjacent power cables. For example, in a ring structure, typically two cables with their terminations and a transformer for the distribution of power to the low-voltage grid are present. Although RMU components may introduce mixing of signals in the distinct propagations channels, tentative measurements indicate that symmetry can be assumed. In an experiment, the cross-talk between the channels was examined for a typical compact RMU that is frequently employed in practice, see [Wie04a]. A pulse was injected in the SP channel at the RMU, and the responses of the various PP channels were measured. The measurement results show that the cross-talk between the SP and PP channels is very small, and does not exceed -20 dB.

If wavelengths much larger than the RMU dimensions are considered, the individual components can be modelled as lumped impedances. In [Wou03a] it is indicated that for both the SP and PP channel, the impedance of distribution transformers is predominantly capacitive in the frequency range of interest. In addition, the inductances of transformer windings may give rise to resonances. The rail system interconnecting the various RMU components, is generally unshielded and introduces inductances in the signal path. Since particularly the distance between the phase conductors and the neutral is relatively large, the rail system self-inductances may influence signals propagating in the SP channel to a considerable extent. Moreover, due to the skin-effect, conductor losses have to be taken into account, as well as radiation losses. Distribution transformers are usually connected to the rail system by three separate single-phase shielded cables. Since a transformer connection cable is short (usually up to 4 m) with respect to the signal wavelengths considered, the cable can be considered as an additional lumped capacitance.

Evidently, the exact values of the load impedances depend on the specific RMU configuration. In particular, the connection rail self-inductances may vary to a large extent due to differing dimensions and routes of rail systems among RMUs. As an example, in Fig. 2.13 the SP and PP channel load impedances for two typical RMU configurations are depicted. Results were obtained by the same pulse response anal-

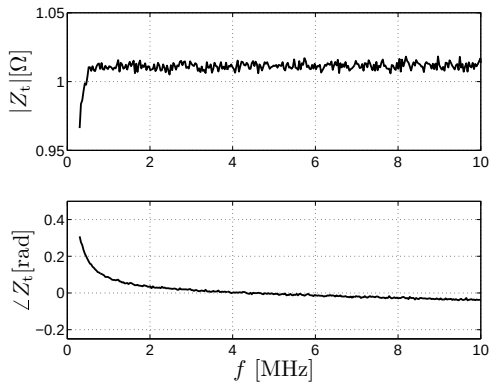

Figure 2.14 *Transfer impedance of a Fischer F75 current transformer.*

ysis as applied to measure cable characteristic impedances described in Appendix B and B. The RMU contained a 100 kVA medium voltage distribution transformer, and only the cable under test was terminated to the RMU in the first configuration (grey). As a result of the various inductances and capacitances present in an RMU, the load impedances of the propagation channels clearly exhibit resonances in the frequency range of interest. For relatively high frequencies, inductive components dominate the load impedance, whereas for low frequencies capacitive influence can be distinguished. In the second configuration (black), another cable with its termination was present, which can be regarded as an additional parallel impedance. The characteristic impedances of cable propagation channels are small with respect to the configuration reactance. Therefore, especially in the lower frequency range, the cable impedance dominates the load impedance.

2.4.2 Sensor Types

For the purpose of on-line PD detection, two sensor types can be applied, namely a capacitive sensor or an inductive sensor, measuring voltage or current, respectively. In conventional off-line PD detection, an HV capacitor in series with a resistive measurement impedance is commonly employed [Kre64]. The component values are chosen such that the high-pass filter effectively suppresses the grid operating frequency. Although applicable to on-line detection as well, this method is not preferred, since HV capacitors may not be reliable in the long term and therefore introduce an additional risk to power distribution. Inductive sensors, or current transformers (CTs), can be clamped on the return conductor of the circuit to be measured. Since there is no galvanic coupling to high-voltage conductors, the sensor itself cannot become a cause of failure and, in principle, installation is possible without power supply disruption [Mac98, Mor99, Ham01]. As a consequence, preferably inductive sensors are employed in on-line PD detection. Inductive sensors can only be applied when the PD propagation channel is terminated to a load impedance, i.e. when the circuit is closed. In the Netherlands, RMUs typically connect a single or multiple power cables to a distribution transformer; therefore some load impedance is nearly always present.

PD pulses are wide-band but small as compared to the grid operating voltage. For this reason, the applied sensors should be sensitive in a wide frequency range,

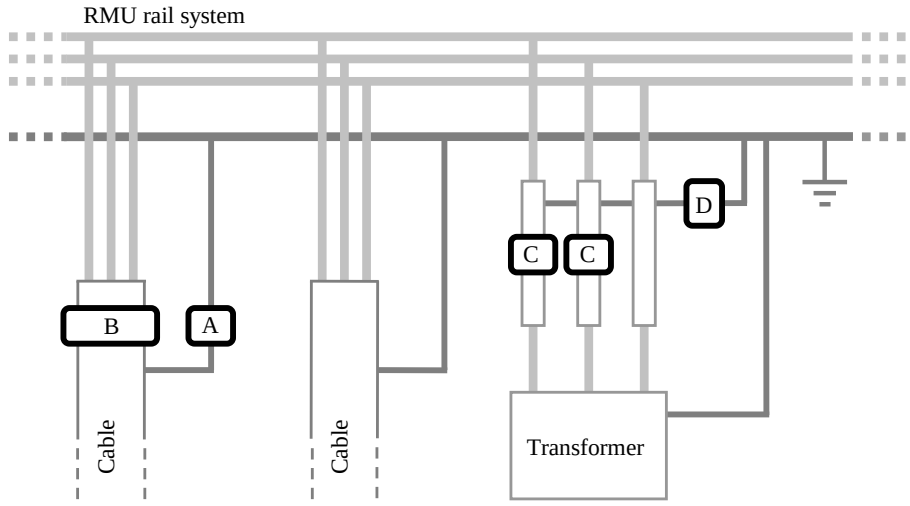

Figure 2.15 *Schematized visualization of practical sensor positions, indicated with A...D, within an RMU.*

excluding the grid operating frequency. Commercially available Rogowski coils with cores of some ferromagnetic material meet these requirements. Various methods are employed to optimize sensors for the purpose of PD detection in live power systems. The application of ferromagnetic core materials with high permeability increases the mutual inductance. To avoid saturation, an air slit is introduced in the core, which also allows the sensor to be split such that it can be clamped around a conductor. Shielding is applied to screen electromagnetic interference radiating to the sensor. Details on sensors for the purpose of on-line PD detection can be found in [Wie05].

As an example, in Fig. 2.14 the transfer impedance Z_t of a shielded Fischer F75 CT is plotted, relating the sensor output voltage across a 50 Ω measurement impedance to the enclosed primary current [Wie05]. All on-line measurements in this thesis are conducted using either this specific CT or a Fischer F70 CT, which have similar characteristics in the frequency range of interest.

2.4.3 Sensor Positions

Split-core CTs are already successfully employed to detect PD signals at a cable terminal in the earth strap connecting the cable screen to the RMU neutral rail [Mac98, Ham01]. In Fig. 2.15, a typical RMU configuration is schematically visualized, where this sensor position is indicated by A. In the Netherlands, often some distance exists between the cable earth connection and the actual ending of the cable screen. A current probe installed around the cable screen past the earth connection can be safely applied, as depicted in Fig. 2.15, location B. A sensor at this location and a sensor at the earth connection measure the same PD signals. However, the amount of disturbance measured by the sensors differs among these positions and will be discussed in Chapter 3.

In principle, sensors on the cable earth strap or past the earth connection exclusively measure PD signals propagating in the SP channel. In certain measurement situations, detection in the PP channel can be of interest. Obviously, sensors cannot

be applied safely to the energized phase conductors at a cable terminal. Moreover, in many situations the phase conductors can not even be accessed. In the Netherlands, a distribution transformer is generally present, which is connected to the RMU rail system by three separate single-phase shielded cables. In most cases, the transformer cable shields are connected together to the system earth rail at a single side, thus allowing safe installation of CTs around the individual phase conductors, as depicted in Fig. 2.15, location C. By subtracting the currents measured in two phase conductors, signals propagating through the PP channel are observed.

The single-sided earth connection of the transformer cables allows an additional sensor position for SP channel PD detection, as depicted in Fig. 2.15, location D. Since a transformer connection cable can be considered as a capacitance, the current flowing through the common earth strap of the transformer cables is capacitively coupled to the superimposed voltages on the phase conductors. Consequently, these RMU configurations allow measurement of signals propagating in the SP channel. Since transformer cables have a capacitance in the order of 1 nF, the measurement method provides sufficient sensitivity in the frequency range of interest. Moreover, by simultaneously measuring at the transformer cable earth connection and at the PILC cable termination, the direction of travel can be determined. In Chapter 3, this property is exploited in order to distinguish signals travelling through the cable under test from other signals.

Evidently, PD signal characteristics can differ depending on the sensor position within an RMU. As a consequence the transfer between the cable terminals and the sensor location has to be taken into account, when PD signals are detected at positions other than directly at the termination.

2.5 Signal Model

A PD signal originates with duration of at most a few nanoseconds [Bog00]; therefore the waveform that is measured at the RMU, approximates the impulse response of the signal propagation path. In this section, the studies from the previous sections are combined resulting in an overall signal waveform model.

2.5.1 Sensor Signal Model

When an insulation defect discharges, the released energy travels towards both cable ends. As depicted in Fig. 2.16, the signal propagation path to one of the load impedances can be modelled as a generic two-port, characterized by a chain parameter matrix (Eq. 2.20). Depending on the specific cable system, a chain matrix can be composed of several other matrices. The input impedance $Z_{\mathrm{in}}(\omega)$ of each two-port can be obtained from the chain matrix $\boldsymbol{\Theta}(\omega)$ and the channel load impedance $Z_{\mathrm{l}}(\omega)$,

$$Z_{\mathrm{in}}(\omega) = \frac{\Theta_{11}(\omega)Z_{\mathrm{l}}(\omega) + \Theta_{12}(\omega)}{\Theta_{21}(\omega)Z_{\mathrm{l}}(\omega) + \Theta_{22}(\omega)} \tag{2.22}$$

where $\Theta_{ij}(\omega)$ represents the matrix element on the i-th row and j-th column. At the instant of discharge, a current $I_{\mathrm{ind}}(\omega)$ is induced, resulting in forward and backward propagating pulses. The current distribution at the discharge site is determined by the input impedances of the two-ports. For instance, the current flowing into the two-port that describes the propagation path between the discharge site and the near-end

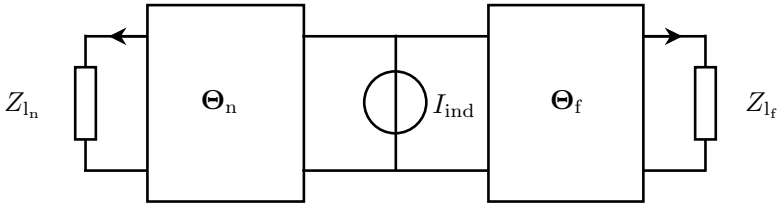

Figure 2.16 *Signal propagation model. A current I_{ind}, induced at the discharge site excites travelling waves that propagate to both ends of the cable system, characterized by chain parameter matrices $\boldsymbol{\Theta}_n$ and $\boldsymbol{\Theta}_f$, and load impedances Z_{l_n} and Z_{l_f}.*

load impedance $Z_{l_n}(\omega)$, is expressed as

$$I_n(\omega) = \frac{Z_{in,f}(\omega) I_{ind}(\omega)}{Z_{in,f}(\omega) + Z_{in,n}(\omega)} \tag{2.23}$$

where $Z_{in,n}(\omega)$ and $Z_{in,f}(\omega)$ can be obtained from $\boldsymbol{\Theta}_n(\omega)$ and $\boldsymbol{\Theta}_f(\omega)$, respectively. The signal transfer between the discharge site and one of the load impedances follows directly from the definition of the chain parameter matrix. Now, the current, flowing through the channel load impedance $Z_l(\omega)$, is expressed as

$$I_l(\omega) = \frac{1}{\Theta_{21}(\omega) Z_l(\omega) + \Theta_{22}(\omega)} I(\omega) \tag{2.24}$$

where the subscript n or f has been omitted for notational convenience.

Eq. 2.24 models the complete response of the cable system, including reflections on impedance transitions. If only the first pulse arriving at a sensor is to be modelled, a much simpler model can be applied. In case of a cable system with M different sections between the discharge site and a sensor, the single-pulse model equals

$$I_l(\omega) = \frac{1}{2} I_{ind}(\omega) \prod_{m=1}^{M} T_{m,m+1}(\omega)\, e^{-\gamma_m(\omega) l_m} \tag{2.25}$$

where l_m is the length of cable section m and $\gamma_m(\omega)$ is the section propagation factor. Note that only if the characteristic impedances to the left and right of the discharge site are equal, the pulse arriving at a single sensor is scaled by a factor two, otherwise this factor will be different.

The current transmission coefficient $T_{m,m+1}(\omega)$ at the section interface is defined as

$$T_{m,m+1}(\omega) = \frac{2 Z_{c,m}}{Z_{c,m+1} + Z_{c,m}} \ . \tag{2.26}$$

Note that $T_{M,M+1}(\omega)$ equals the transmission coefficient at the load impedance. Regardless of the applied model, the sensor output signals at the near and far end are now expressed as

$$\begin{aligned} S_n(\omega) &= Z_t(\omega) H_{s_n}(\omega) I_{l_n}(\omega) \ , \\ S_f(\omega) &= Z_t(\omega) H_{s_f}(\omega) I_{l_f}(\omega) \end{aligned} \tag{2.27}$$

where $Z_t(\omega)$ is the sensor transfer impedance and $H_s(\omega)$ is the transfer function of the system between the cable terminals and the actual sensor position.

2.5.2 Apparent Charge Transport

At the discharge site, the magnitude of currents induced in the conductors depends on the PD direction and the position of the discharging defect within the dielectrics. Consequently, the distribution of charge among the propagation channels is a function of PD direction and position. Nevertheless, the apparent charge or magnitude of a PD signal is a useful insulation defect parameter, and is frequently used for cable diagnostics. The PD magnitude at the discharge site equals

$$Q_{\mathrm{app}} = \int i_{\mathrm{ind}}(t)\, dt \; . \tag{2.28}$$

When PD signals propagate through the cable, energy is dissipated due to attenuation. Moreover impedance changes at cable section interfaces result in energy losses. As a consequence, the magnitude of a detected PD pulse is related to the apparent charge at the discharge location by the transfer functions in the signal path. The apparent charge of a detected PD signal equals

$$Q_{\mathrm{app},d} = \frac{1}{2\pi} \int \int \frac{Z_{\mathrm{t}}(\omega)}{Z_0} H_{\mathrm{s}}(\omega) I_{\mathrm{l}}(\omega)\; e^{+j\omega t}\, d\omega\, dt \tag{2.29}$$

where Z_0 is the measurement system impedance. As a result of the various transfer functions present in the propagation path, the estimated charge of a detected signal differs from the PD magnitude at the discharge location. Using the signal model, the magnitude at the discharge site can be estimated from the detected PD signal.

2.5.3 Discrete Time Signal Model

For computer simulations of PD signals, the analogue signal model is sampled and quantized. It is assumed that amplitude quantization results in accurate approximations of measured signals; therefore only sampling is discussed here. Moreover, in order to prevent aliasing, continuous signals are assumed to be properly bandlimited prior to sampling. On the fundamental interval the i-th discrete Fourier transform (DFT) coefficient of the sampled sensor signal equals

$$S(i\Delta f) = W(\omega = 2\pi i \Delta f) S_{\mathrm{c}}(\omega = 2\pi i \Delta f) \tag{2.30}$$

where $S_{\mathrm{c}}(\omega)$ is the continuous sensor signal and $W(\omega)$ is a rectangular window, which equals unity for frequencies below half the sampling rate and zero elsewhere. The frequency domain resolution of the sampled signal is defined by $\Delta f = 1/BT_{\mathrm{s}}$, where B equals the DFT length and T_{s} is the sampling period. In the time-domain the sampled sensor signal is obtained by the inverse discrete Fourier transformation (IDFT)

$$s(kT_{\mathrm{s}}) = \Delta f \sum_{i=0}^{B-1} S(i\Delta f) e^{+j2\pi ik/B} \tag{2.31}$$

By computing the DFT coefficients of the sensor signals and inverse Fourier transformation, the digitized sensor signals can be simulated. Clearly, the observation interval BT_{s} must be chosen long enough such that no time-domain aliasing occurs. The continuous signal $s_{\mathrm{c}}(t)$ is obtained by interpolation of the discrete signal, e.g.

$$s_{\mathrm{c}}(t) = T_{\mathrm{s}} \sum_{k} s(kT_{\mathrm{s}}) \operatorname{sinc}\left(\pi \frac{t - kT_{\mathrm{s}}}{T_{\mathrm{s}}}\right) \tag{2.32}$$

where $\operatorname{sinc}(x) = \sin(x)/x$.

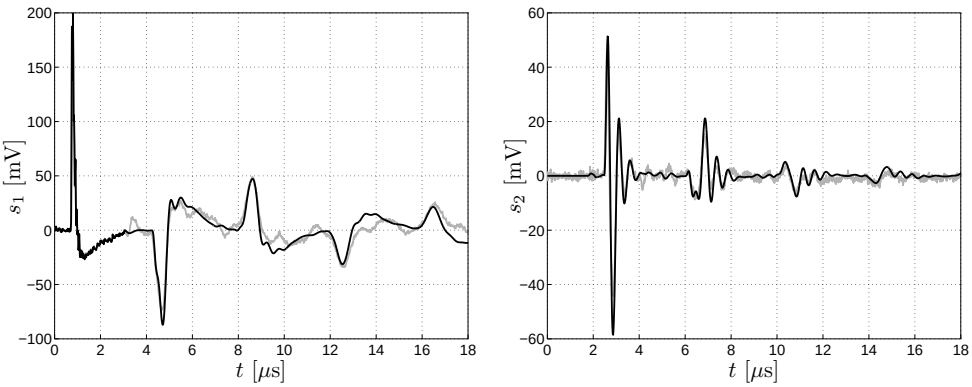

Figure 2.17 *Simulated (black) and measured (grey) sensor signals for the experimental set-up. The left plot shows the sensor signals at the injection end, the right-hand plot shows signals at the far-end terminal.*

2.5.4 Experimental Validation

In order to validate the signal waveform model, pulse propagation measurements were conducted on the experimental grid that was described in Section 1.3.4. The cable connection consisted of a 10 kV 3×95 mm^2 PILC cable of 96 m length and a 12.5 kV 3×95 mm^2 PILC cable of 201 m length. At one end, the cable was terminated to RMU2, which contained a 100 kVA medium voltage distribution transformer. At RMU1, the cable terminals were disconnected from the rail system and pulses were injected at the cable termination. Current transformers were clipped onto the cable earth connection at each end of the cable system, in order to measure the signals propagating through the SP channel. Since the two RMUs were actually located close to each other, the signals were recorded using a multi-channel 14 bit 62.5 MSPS digitizer.

Prior to the assembly of the cable system, the propagation parameters of the individual cable sections and the channel load impedance were obtained by pulse response analysis. Using the measured parameters a signal model was constructed according to Eq. 2.27. The sensor signals were simulated by convolving the injected signal and the channel impulse responses derived from the signal model. In Fig. 2.17 the simulated signals (black) and measurements (grey) are plotted for the injection end (left) and the other cable end (right). The model, gives good waveform approximations of the first arriving pulses and first reflections. Since modelling errors accumulate, the simulated signals deviate more from the measured signals for further reflections. Small discrepancies arise among others as a result of the fact that the splice was not modelled. In fact, the first small reflection at t=3.5 μs in the near end sensor signal (left) occurs according to the location of the joint within the cable system.

2.6 Conclusions

In this chapter, PD signal characteristics in on-line MV three-phase belted cables were studied for the purpose of signal analysis. Three main stages were distinguished, namely partial discharge signal excitation, propagation, and measurement.

Charge induced in the cable conductors as a result of a partial discharge depends upon the local electrical field strength as well as the field direction. In case of three-phase belted cables the defect location has a pronounced effect on PD occurrence and induced charge magnitude. As a consequence no a priori probability distributions related to PD magnitude or operating voltage phase angle can be assumed. This observation is important for signal analysis, since methods that exploit a priori information on signal generation, can be excluded immediately.

Propagation in three-phase belted cables can be modelled two distinct propagation channels as was shown by theory and experiments. The shield-to-phase and phase-to-phase propagation channels are orthogonal and can exhibit differing attenuation properties. On-line PD detection is often done using a current transformer clipped on the earth strap at a cable termination. Therefore studies were mainly focussed on the SP propagation channel and a simple coaxial model was applied to obtain the propagation parameters. The proposed model shows good agreement with boundary element simulations. The exact attenuation and dispersion introduced by the propagation channel depend on the permittivity and loss factor of the insulation material, as well as on electrical and mechanical stress, temperature, and age. As a consequence, no generic theoretical or experimental dielectric constant can be assumed. Cable systems generally consist of multiple cables in cascade. Each individual section can be characterized by a chain matrix incorporating the propagation parameters, and the cascade can be represented by matrix multiplication.

At each end, a cable system is terminated to an RMU, which interconnects multiple cables and other high-voltage equipment. If wavelengths much larger than the RMU components are considered, the complete configuration can be considered as a single channel load impedance. Situations where this assumption does not hold are not considered in this thesis. The load impedance is determined by the inductances of the cable termination and the RMU rail system as well as the impedances of other HV components within the RMU. Consequently, the exact channel load impedance depends on the specific RMU configuration. Although RMU components may introduce mixing of signals in the propagations channels, tentative measurements indicate that the cross-talk does not exceed -20 dB and orthogonality can be assumed.

Split-core current transformers can be clipped on the return conductor of the circuit to be measured. Since there is no galvanic coupling to the high-voltage conductors, this sensor type introduces no additional power failure risk. In many situations in the Netherlands, a distribution transformer is connected to the RMU rail system by three separate shielded cables. Frequently, the transformer cable shields are connected to the RMU neutral rail only at one side. Besides the conventional location at the cable earth strap, a CT can also be installed at the one-sided earth connection of the transformer cables. Moreover, CTs can be clamped on the transformer connection cables in order to detect signals in the phase-to-phase channel.

A complete signal model was proposed based on the channel propagation characteristics, the load impedances, and the applied measurement method. The model was validated by measurements on the experimental grid.

Chapter 3

Noise and Interference Characteristics

3.1 Introduction

Practical partial discharge measurements are generally corrupted by noise and interference, impeding partial discharge (PD) signal detection and location. In general, three main disturbance classes can be distinguished, namely broadband background noise, finite-energy interference, and continuous periodic interference. Broadband background noise is stochastic in nature, with statistical properties that vary both with frequency and time. This type of disturbance results from the summation of numerous natural and artificial sources, such as noise radiated by electrical equipment, cars, lightning, thermal noise, etc. High-voltage equipment can generate electromagnetic interference of short duration, which is radiated or conducted to the sensors or to unshielded ring main unit (RMU) components. In addition, operational switching can create large transients that permeate widely through the power system [Wal95]. This type of disturbance is referred to as finite-energy interference. Continuous periodic interference is generally narrow-band and has time-varying properties. Common examples are radio communications and broadcasts, which are picked up by badly shielded RMU components or by the sensors themselves [Ahm98a, Shi00, Wal01].

The aim of this chapter is to characterize disturbances encountered in on-line PD measurements in the Netherlands and provide insight into practical values of PD signal to disturbance ratios. In addition, first directions towards disturbance rejection are given. Disturbance properties can vary widely among measurement situations. For this reason, as a tentative study, a number of on-line noise and interference measurements were performed on RMUs at various sites in the Netherlands. In the field measurements a shielded split-core Fischer F75 current transformer (CT) was applied at various positions within the RMUs. Conventionally, PD signals are analyzed by using a digital storage oscilloscope, which triggers on signals that exceed a preset amplitude level for a specific time duration [Bog00]. Clearly, this approach applies only to those measurement situations where signal amplitudes exceed the noise and interference levels. In on-line measurements, however, the disturbance amplitudes can be much higher than PD signal amplitudes, and particularly radio broadcasts may completely swamp PD signals. Since triggered data acquisition is generally not applicable, measurement data is obtained by digitizing blocks of signals at random.

The position of sensors in a substation determines which propagation channel is measured. Moreover, the amount of disturbance radiated or conducted to the sensors depends on the measurement locations within an RMU. In Section 3.2, the effect of sensor positions on measured disturbances is studied. PD detection in the cable earth screen is most widely applicable; therefore the study of disturbances measured in the earth screen is emphasized. For each class of disturbance a different approach towards characterization as well as rejection is required. Since generally narrow-band periodic interference dominates the measurements, first the properties of this class are discussed in Section 3.3. After application of narrow-band rejection techniques, the remaining disturbances can be characterized. In Section 3.4, broadband background noise properties are discussed. Finite-energy interferences frequently encountered in on-line PD measurements are studied in Section 3.5. In order to quantify noise and interference present in practical measurements, quality measures of detected PD signals, such as signal to noise ratio (SNR), are essential. In addition, these measures can be used to evaluate the performance of signal processing techniques under various conditions. In this Chapter, quality measures are defined and practical values obtained from the tentative measurements are given. For the purpose of defect location, sensors at both cable-ends can be applied in order to determine the difference in time of arrival between PD signals originating from the same discharge. Correlation between the noise and continuous interference measured at both cable ends is an important parameter for the choice of PD signal analysis methods; therefore this effect is studied in Section 3.6. Conclusions are drawn in Section 3.7.

3.2 Effect of Sensor Positions

The amount of disturbance radiated or conducted to the sensors depends on the sensor positions within an RMU. In this section, this effect is studied. In addition, a directional sensing method is proposed that can be applied to distinguish between signals originating from the cable under test and signals originating elsewhere.

3.2.1 Shield to Phase Measurement

Current transformers clipped on the cable earth strap are already employed to measure signals present in the cable screen [Mac98, Ham01]. In this configuration, PD signals and disturbances in the shield-to-phase (SP) channel are measured. Cable screens are insulated from the surrounding ground, and common mode (CM) currents flow through the screen with the actual ground as a return path. Thus besides the differential mode (DM) currents flowing through the phase conductors, CM currents superimposed on the signals of interest are also measured. In Fig. 3.1, a cable termination is schematically visualized, where a sensor placed at the earth strap is indicated by A. For simplicity only a single-phase conductor is depicted, and the RMU components are represented by a load impedance Z_1. Belted cable systems are well shielded; therefore CM currents merely consist of interference radiated to the cable screen and contain no PD signals. However, in the majority of measurement situations in the Netherlands, the cable screen is continued over a short length past the earth connection. A current probe installed around the cable screen at this position only measures DM currents without CM interference [Wie03c, Wou03a], visualized as position B in Fig. 3.1.

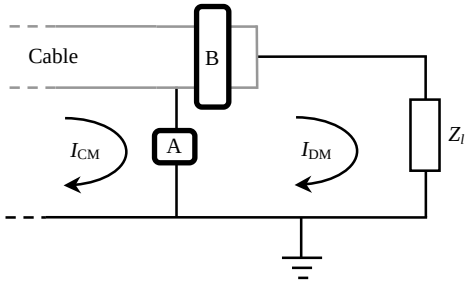

Figure 3.1 *Sensor positions at a cable termination, where A is a sensor clipped on the earth strap, and B is a sensor placed around the short continuation of the screen.*

Particulary radio broadcasts are picked up by the cable screen. In a tentative measurement, the maximum amplitudes of interferences observed using a CT clipped on the earth strap were 20 times higher compared to interferences measured with a CT placed past the earth connection, whereas PD signal amplitudes were approximately equal. Consequently, a sensor installed around the cable screen past the cable earth connection is preferred in order to detect PD signals in the SP channel [Wie03b, Wie03c].

3.2.2 Phase to Phase Measurement

The most widely applicable method of PD detection utilizes an inductive probe installed around the cable screen past the cable earth connection or clipped on the cable earth strap. Earth paths within RMUs can have arbitrary shapes and lengths; therefore the SP channel has large antennae picking up disturbance radiated to the RMU. As described in Chapter 2, CTs can be installed around the transformer cables in many situations in the Netherlands. By subtracting the currents measured in two phase conductors, signals propagating through the PP channel are observed. Within an RMU, the phase conductors usually run parallel to each other and have approximately equal geometries and dimensions. Consequently, a differential measurement method is implicitly applied when PD signals are detected in the PP channel.

In case of PP channel detection, noise and interference which is coupled equally to the phase conductors at the RMU or elsewhere in the grid is cancelled or suppressed. In the tentative measurements, the amplitude ratios of radio broadcasts present in the SP channel and PP channel were examined. It was found that continuous periodic interference in the SP channel can exceed the interference present in the PP channel up to a factor 10. In addition, the noise power in the SP channel can be up to 5 dB larger than in the PP channel. However, signals propagating in the PP channel can only safely be detected in the transformer cables; therefore the PP channel load impedance is dominated by the transformer impedance. Generally, the SP channel load impedance is small compared to the PP channel load impedance, particularly when more than one cable is terminated to the RMU. Therefore the signal levels measured in the SP channel are higher compared to the PP channel. For this reason it is concluded that, although disturbance levels in the PP channel are lower compared to the SP channel, PP channel PD detection does not necessarily result in higher signal quality. Moreover, at a discharge origin the magnitudes of PD signals induced

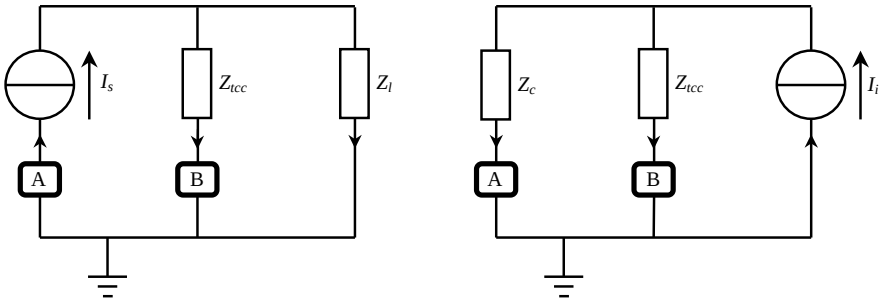

Figure 3.2 *Directional sensing method using sensors A and B installed at the cable termination (Z_c) and at the transformer cable earth connection (Z_{tcc}), respectively. Z_l represents the parallel impedances of all other MV equipment.*

in each propagation channel depend upon the location of the defect within the cable cross-section and the local field direction. Consequently, apparent PD magnitudes and thus the signal quality can vary among the propagation channels.

3.2.3 Directional Sensing

Generally, cable systems are well shielded and finite-energy disturbances merely originate outside the cable under test. A well-known technique to discriminate between signals originating from a system and signals propagating to the system, is by determining the direction of travel. If PDs are detected at both cable ends and if the measurements are properly synchronized, pulses originating within and outside the cable can be distinguished by examining the difference time of arrival [Ste01]. In addition, directional sensing can in principle be achieved by separately measuring the electric and magnetic fields associated with travelling waves. However, galvanic coupling to the phase conductors is not allowed; therefore this method cannot be applied. As mentioned in Chapter 2, directional sensing can be achieved by simultaneously measuring at the transformer cable earth connection and at the cable termination. Likewise, a CT can be installed around the three transformer-connection cables together in order to detect signals propagating to the distribution transformer.

In Fig. 3.2, the proposed method is schematically visualized, where the SP channel is represented by a two-conductor model. The sensor installed at the cable termination is indicated by A, and B is the sensor at the transformer cable earth connection. The impedance Z_c models the SP channel impedance of the cable under test as well as the cable termination inductance. Likewise, Z_l is the combined impedance of (multiple) other cables and terminations as well as the distribution transformer. The transformer connection cables are represented by Z_tcc. For simplicity rail inductances are omitted. A PD signal, originating from the cable under test and arriving at the RMU, is modelled by a current source I_s as visualized in the left plot in Fig. 3.2. In this case, the currents enclosed by both sensors flow in opposite directions. However, a signal I_i originating from another cable results in currents flowing in the same direction, as visualized in the right-hand plot. Thus, finite-energy disturbances can be distinguished from PD signals by examining the direction of currents.

In an experiment, finite-energy disturbances were simulated by injecting pulses into the RMUs that terminate the cable under test at each end. In Fig. 3.3, the

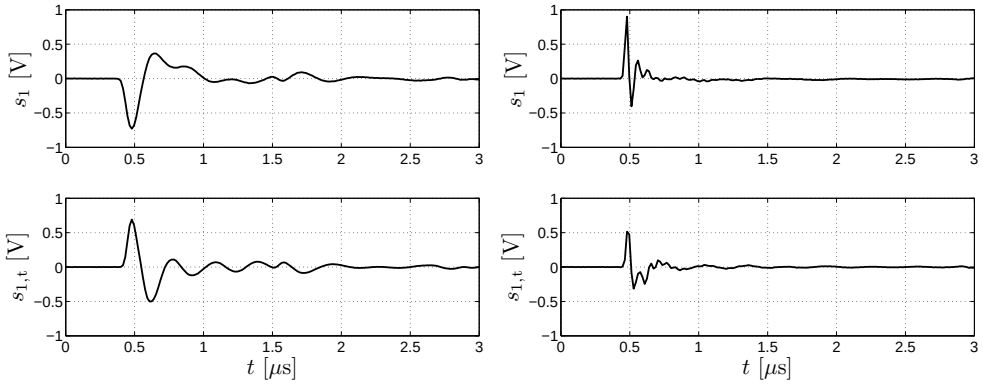

Figure 3.3 *Signals measured at the cable termination ($s_1(t)$) and at the transformer cable earth connection ($s_{1,t}(t)$), in case of a pulse arriving from the cable (left) and an external pulse (right).*

sensor signals measured at the cable termination past the earth connection in the near-end RMU (top plots) and at the transformer cable earth connection (bottom plots) are depicted. On the left, the sensor signals are plotted for a pulse injected at the far-end RMU, thus mimicking a signal from the cable under test at the near-end RMU. In the right-hand plot, the measured signals are shown when a pulse is injected in a different cable termination at the near-end RMU, i.e. simulating finite-energy interference. The experimental results show that the direction of the current, measured by the CT at the cable termination, changes with the pulse direction of arrival. In principle the transfer function between the sensor positions should be taken into account for proper signal analysis. However, the experiment shows that when a finite-energy signal is detected at the cable terminals, the sign of the signal measured at the transformer cables can be used as a reference for directional sensing. It can be concluded that direction of arrival (DOA)-based discrimination provides a powerful tool to distinguish finite-energy signals originating within and outside the cable under test.

3.3 Continuous Periodic Interference

Typically, periodic interference encountered during PD field tests results from double sideband radio communications with large carriers, i.e. amplitude modulation (AM). Radio stations are required to maintain 85% to 95% modulation to allow envelope or square-law detection, which results in large carrier signals. The permissible carrier power of commercial AM broadcasts can be high; therefore this type of interference dominates the spectrum in many cases. The carrier frequencies for commercial AM radio broadcasting in Europe are allocated in the kilohertz and lower megahertz range with small transmission bandwidths and spacing. In addition, short-wave radio broadcasts may dominate the spectrum as well, especially at night [LP03]. As an example, in Fig. 3.4 the averaged noise and interference power spectrum obtained from SP channel measurements is depicted. Pronounced narrow-band peaks in the spectrum indicate the presence of continuous periodic interference. Note that the interference is actually quasi-periodic, since the carrier waves are modulated. Within the frequency

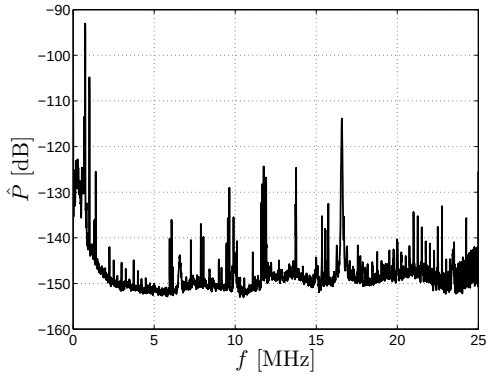

Figure 3.4 *Averaged noise and continuous interference power spectrum obtained from SP channel measurements the length of one grid operating voltage cycle.*

range of interest, the spacing between carrier frequencies for radio broadcasting can be as close as 10 kHz depending on the application. Therefore the frequency resolution Δf of the averaged power spectrum is chosen accordingly. In order to allow application of fast Fourier transform (FFT) algorithms, the transform length must equal a power of 2. The example in Fig. 3.4 was obtained with a 50 MSPS data acquisition system, thus the sampling period equals $T_\mathrm{s} = 20$ ns. The FFT length was chosen as $B = 8192$, which results in a frequency domain resolution of $\Delta f = 1/BT_\mathrm{s} \approx 6.2$ kHz. Moreover, a Hamming window was applied in order to reduce spectral leakage, which is inherent to the FFT (see e.g. [Kay88]). The averaged power spectrum was obtained by averaging over 122 spectra, measured during on e cycle of the grid operating voltage.

Although the presence of radio broadcasts is time-variant, a closer observation reveals that the interference can be considered stationary on a short time-scale, e.g. during a cycle of the grid operating voltage. In Fig. 3.5, frequency components with power exceeding a predefined threshold of -110 dB are plotted for one operating voltage cycle. Note that in this context 0 dB is defined as 1 V^2/Hz. The power spectra were obtained using the same method as described above. Clearly, the time-domain resolution obtained in this manner is quite low, since power spectra are computed approximately every 160 μs. Nevertheless, the experiment is only intended to illustrate the time-variation of periodic interference, and to this end the measurement provides sufficient accuracy. The measurement results show that a number of dominant broadcast carrier frequencies are continuously present during the entire cycle. In addition, some large components repetitively appear with relatively short durations, appearing as small blobs in Fig. 3.5. These are ascribed to finite-energy disturbances and are discussed in more detail in Section 3.5. Monitoring the power of continuous periodic interferences using band-pass filters shows that the carrier amplitudes are indeed modulated, as illustrated in Fig. 3.5.

In principle, a power ratio can be defined as a quality measure for PD signals corrupted by continuous periodic interference. However, since disturbances belonging to this class are generally narrow-band with respect to detected PD signals, a power measure is of little interest. Continuous periodic interference can have much larger amplitude than PD signals. As a consequence, PD signals cannot be digitized by means of triggered data acquisition. In addition, the digitizer dynamic range needs

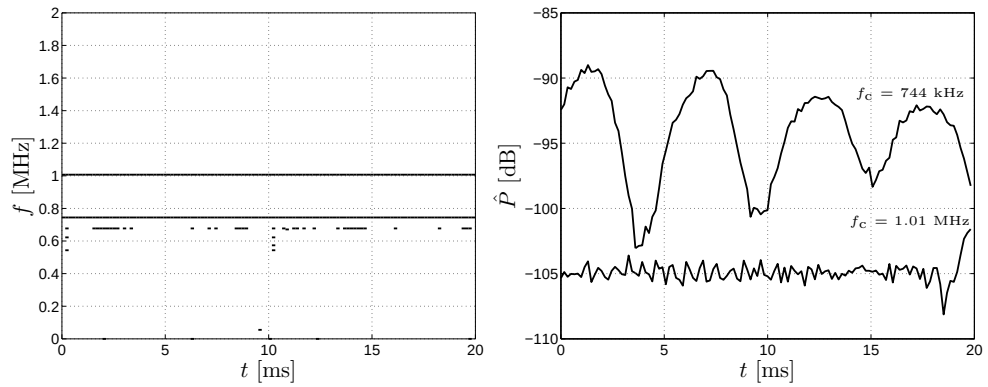

Figure 3.5 *Evolution of large frequency components (left) and continuous periodic interference power (right) measured during a cycle of the grid operating voltage.*

to be large in order to quantize small PD signals with reasonable resolution. For the purpose of digitizer dynamic range selection, it is of interest to define the signal to periodic interference amplitude ratio (SPIAR) as a quality measure, expressed as

$$\text{SPIAR} = \frac{V_\text{p}}{V_\text{a}} \tag{3.1}$$

where V_p is the PD signal peak value and V_a is the peak amplitude of interfering broadcasts within the observation interval. Note that a limited number of narrowband interference poses no fundamental limit on PD signal analysis, and the SPIAR is only of interest from a practical point of view.

In the tentative studies, PD signal and interference amplitude estimates were obtained by visual inspection of measurement data. Clearly, only PD signals with relatively large SPIAR are observed in this manner. In worst-case scenarios, signal to interference amplitude ratios around 0.5 are reached only for large PD signals, with magnitudes in the order of several thousand picocoulombs. However, since discharge magnitude is linearly related to signal amplitude for PD signals originating from the same location, small PDs will have much lower SPIARs as compared to the signals observed in the tentative measurements. On the other hand in best-case scenarios, the SPIARs can be much larger, in the order of 10. It is impossible to give a generic characterization of practical SPIARs, since a wide variety of measurement situations and signals are encountered in practice. Consequently, the results presented here should be regarded as indications rather than exact values.

3.4 Noise

Broadband background noise in PD measurements results from the summation of numerous natural and artificial sources. As a consequence, background noise can be considered as a stationary or slowly time-varying stochastic process. Noise encountered in PD measurements generally depends on frequency and can be characterized by its discrete power spectral density function (PSDF). Within the detection bandwidth the PSDF of a properly bandlimited noise process is defined as

$$P_N(i\Delta f) = \Delta f E\{|N(i\Delta f)|^2\} \tag{3.2}$$

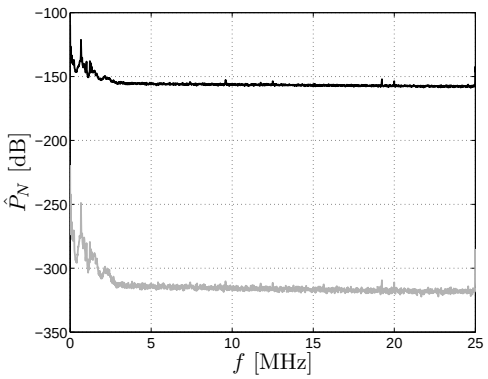

Figure 3.6 *Mean (black) and variance (grey) of averaged periodograms obtained from measurements during 20 cycles of the operating voltage.*

where $E\{\cdot\}$ denotes expectation and the i-th discrete Fourier transform (DFT) coefficient of the noise observation equals

$$N(i\Delta f) = T_\mathrm{s} \sum_{k=0}^{B-1} n(kT_\mathrm{s}) e^{-j2\pi i \Delta f k T_\mathrm{s}} \; . \tag{3.3}$$

Assuming that the process is ergodic, the statistical averages can be obtained from time averages. For a stationary and ergodic process, the usual non-parametric PSDF estimator is the periodogram [Kay88], which equals the power per frequency bin. In order to improve the estimator, the periodograms of several observations are averaged, thus the overall estimation variance is decreased. The averaged periodogram is obtained directly from the definition of the PSDF and is expressed as

$$\hat{P}_\mathrm{N}(i\Delta f) = \frac{\Delta f}{R} \sum_{j=1}^{R} |N_j(i\Delta f)|^2 \tag{3.4}$$

where $N_j(i\Delta f)$ is the i-th DFT coefficient of the j-th noise observation and R equals the total number of observations. In Fig. 3.6, the mean and variance of averaged periodograms obtained during 20 cycles of the grid operating voltage are depicted in a single plot. Again, the measurements were obtained with a 50 MSPS data acquisition system. The FFT length was chosen as $B = 8192$, which results in a frequency domain resolution of $\Delta f \approx 6.2$ kHz. In this particular case, only few finite-energy interferences and PD signals occurred during a cycle of the grid operating voltage. The PSDF estimate is obtained by averaging approximately 2500 periodograms; therefore the contribution of finite-energy signals to the estimate is negligible. Moreover, in this case only disturbing radio broadcasts were present below 2 MHz, as can be seen in Fig. 3.6. The measurements illustrate that the background noise is stationary during the observation time. Nevertheless, it should be noted that observations in the order of days to months show that background noise properties are slowly time-varying [LP03].

In order to quantify noise encountered in on-line measurements, the spectral energy distribution of a PD signal with respect to the noise PSDF is defined as a quality measure. Assuming that a detected PD signal is properly bandlimited to avoid aliasing

and sampled with sampling period T_s, the i-th DFT coefficient equals

$$S(i\Delta f) = T_\mathrm{s} \sum_{k=0}^{B-1} s(kT_\mathrm{s}) e^{-j2\pi i \Delta f k T_\mathrm{s}} \; . \tag{3.5}$$

If the signal is observed entirely on some interval $0 \leq t < BT_\mathrm{s}$, an estimate of the signal energy can be obtained from its sample values,

$$E_\mathrm{s} = T_\mathrm{s} \sum_{k=0}^{B-1} |s(kT_\mathrm{s})|^2 = \Delta f \sum_{i=0}^{B-1} |S(i\Delta f)|^2 \tag{3.6}$$

A PD signal has finite-energy; therefore a proper dimensionless signal to noise ratio must be defined using the signal power dissipated during some observation interval T_o. Generally, a detected PD signal does not have a duration exceeding 1 μs. Therefore for all measurements and simulations the observation interval is defined as T_o=1 μs. Now, the SNR per frequency bin equals

$$\mathrm{SNR}(i\Delta f) = \frac{|S(i\Delta f)|^2}{T_\mathrm{o} P_N(i\Delta f)} \; . \tag{3.7}$$

The average single-bin SNR equals

$$\overline{\mathrm{SNR}} = \frac{1}{B} \sum_{i=0}^{B-1} \mathrm{SNR}(i\Delta f) \; . \tag{3.8}$$

Noise is present within the entire PD signal bandwidth, and poses a fundamental limit on PD signal analysis techniques. For this reason, the SNR is the most important signal quality measure.

In a practical measurement situation, one is often interested in a quick estimate of the PD signal quality from visual inspection of a signal on e.g. an oscilloscope. The average SNR can only be obtained if the signal and noise spectra are known, and is therefore inappropriate as a visually observable measure. However, assuming additive white noise, the averaged single-bin SNR equals the total average SNR, i.e.

$$\overline{\mathrm{SNR}} = \frac{E_\mathrm{s}}{T_0 \, \sigma_n^2} \tag{3.9}$$

where $\sigma_n^2 = E\{|n(kT_\mathrm{s})|^2\}$ equals the noise variance. Neglecting the influence of the channel load impedance, a rough estimate of the PD energy is obtained from the peak value V_p and the full width half maximum time t_FWHM,

$$E_\mathrm{s} \approx V_\mathrm{p}^2 \, t_\mathrm{FWHM} \; . \tag{3.10}$$

Consequently, the total average SNR can be estimated directly by visual examination of measured signals. As an example a simulated PD signal in white noise, with average SNR of 14 dB, is depicted in Fig. 3.7. Visually, the SNR is estimated at 15 dB. Note that in practice, the white noise assumption can result in quite pessimistic average SNR estimates if noise is dominantly present outside of the signal band.

The broadband background noise observed in the tentative measurements was indeed colored, and most dominantly present in the low frequency range. In order to

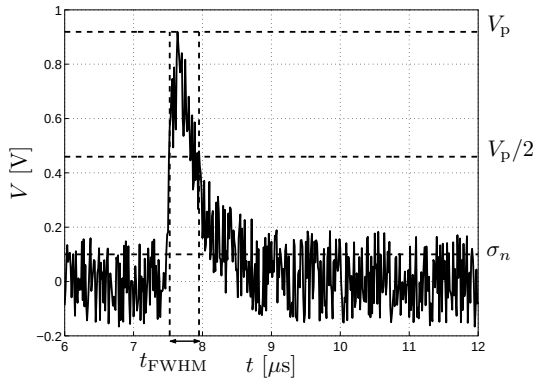

Figure 3.7 *Simulated PD pulse in white noise with 14 dB average SNR.*

determine average SNR values for colored noise, a whitening filter is applied, which flattens the noise spectrum by amplifying frequency bins depending on the noise power within each bin. After whitening of the measurements, the average noise power and PD signal energies can be estimated by visual inspection. This approach results in accurate estimates only if the noise power distribution does not vary too much within the signal band, thus allowing reliable signal energy estimation by visual inspection. In Chapter 5, the whitening filter will be discussed in more detail. Since continuous periodic interference amplitudes can be much larger than PD signals as well as other disturbances, dominating narrow-band broadcasts need to be suppressed before the SNR can be measured. To that end, notch filters were applied to measurement data and, after whitening of the measurements, the average noise power and PD signal energies were estimated by visual inspection. In the tentative measurements, total average SNRs were observed ranging from -6 dB to 16 dB for PD magnitudes ranging from one thousand to fifteen thousand picocoloumb.

3.5 Finite-Energy Interference

Disturbances of relatively short duration and finite-energy frequently occur in on-line PD measurements. Examples of finite-energy disturbances are thyristor pulses, switching transients, PDs from adjacent HV systems, etc. Belted cable systems are well shielded and external interference is merely picked up by unscreened RMU components such as terminations and rail systems. An additional antenna can be used to receive and classify external interference radiating to the terminations where sensors are placed [Su01]. In this case, large transients are blocked by disabling data-acquisition for a period of time. However, this method cannot be applied straightforwardly, since in many situations disturbances are picked up elsewhere in the grid and propagate to the sensors. In the majority of the tentative measurements, bandlimited finite-energy disturbances were observed. In Fig. 3.8, an example of such an interfering signal is plotted obtained in an on-line field measurement. Typically, the center frequency of the disturbance band is in the order of several hundreds of kilohertz and -3 dB bandwidths lie between 50 kHz and 200 kHz. Also bandlimited finite-energy disturbances were encountered with center frequencies up to 2 MHz. In the tentative

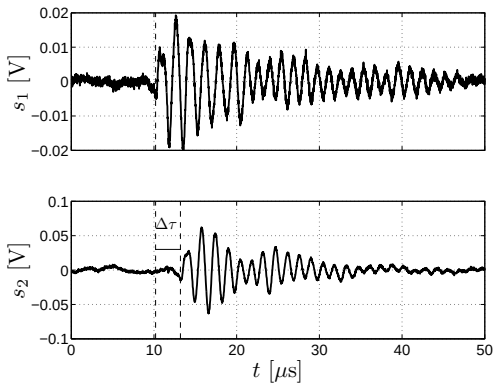

Figure 3.8 *Typical bandlimited finite-energy interference observed by two synchronized sensors at the terminations of a 410 m long PILC cable.*

measurements, bandlimited finite-energy disturbances were observed with maximum amplitudes twice as large as maximum PD signal amplitudes.

Frequently, finite-energy disturbances originate far away from the sensors and propagate through the power grid to the system under test. Moreover, in many cases discharges occur at insulation defects in adjacent cable systems as well as in distribution transformers, cable terminations, or other components within the RMUs. These PD signals are considered as interference, since they do not contribute to the diagnosis of the cable system under test. Clearly, such interferences have waveforms that are comparable to PD signals from the cable, as they propagate through similar paths. Although in off-line measurements PD signals can be discriminated from broadband disturbances based on their occurrence with respect to the energizing voltage phase angle [Kre64, Bor95, Tan95], this method does not necessarily apply to on-line measurements as clarified in Chapter 2. However, as discussed in Section 3.2.3, directional sensing can be applied to discriminate between signals originating from the cable and signals propagating to the system. This method only allows identification of finite-energy disturbances at the first RMU where the interferences arrive. Since a disturbance propagates through the cable under test as well, the resulting current distribution in the second RMU will be similar to the distribution for an arriving PD signal. Belted cable systems are well shielded and in general interferences are not picked up by accessories of the cable under test. Therefore discrimination is possible if sensors are applied at both cable ends. The two finite-energy interference signals depicted in Fig. 3.8 are obtained by two sensors at each end of a 410 m long paper insulated lead covered (PILC) cable. The difference in arrival times of the interference at each sensor corresponds to the cable propagation delay, viz. $\Delta\tau \approx 2.50\ \mu s$. In the measurements, time-base alignment of the sensor signals was achieved using global positioning system (GPS) satellites [Ste01].

Commonly, a number of similar finite-energy interferences are observed in on-line PD measurements. In Fig. 3.9, the short-time power spectra during a cycle of the operating voltage are depicted, clearly showing repetitive bandlimited disturbances. It has been suggested in the literature that repetition rates of distinctive disturbances can be used to distinguish finite-energy interference from PD signals [Nag94, Köp95]. Although disturbances can recur with some regularity, repetition periods of individual

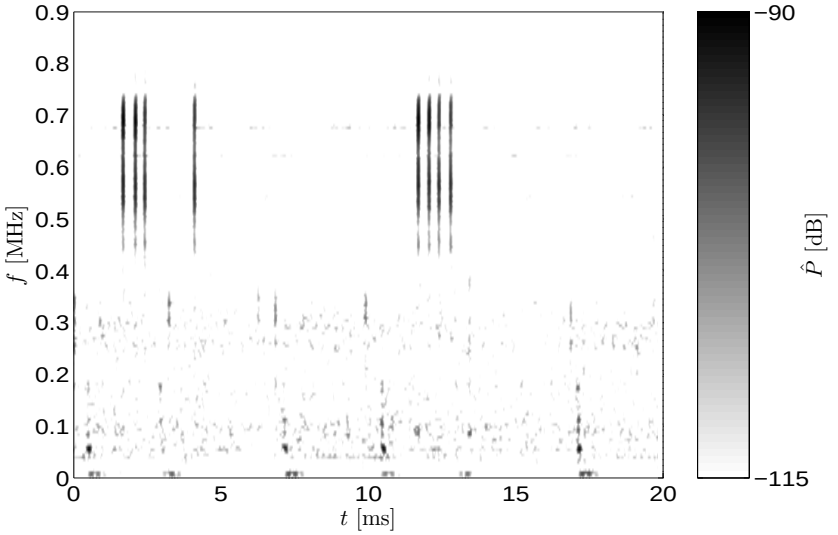

Figure 3.9 *Short-time power spectra measured during a cycle of the operating voltage.*

disturbances as well as patterns of disturbances deviate in the order of tens to hundreds of microseconds among measured data records. Since the recurrence of these disturbances is only quasi-periodic, and since PD signals can occur with some repetition as well, finite-energy disturbances cannot be eliminated based on this property alone. Moreover, the method would apply only to a limited class of disturbances. As a consequence, finite-energy rejection based on repetition rates alone is hardly feasible, and is therefore not discussed in this thesis.

Based on the tentative measurements it can be concluded that a range of methods can be applied to distinguish PD signals from finite-energy interferences. Bandlimited finite-energy disturbances can be rejected based on their waveshapes, as will be discussed in Section 5.4. Direction of arrival discrimination combined with a double-sided measurement topology, provides a powerful tool to distinguish PD signals originating within and outside the cable under test. Discrimination based on the arrival times of signals measured at both cable ends is most widely applicable. For this reason, the latter method is emphasized in this thesis, and will be illustrated in Section 5.5.4. The performance of disturbance rejection based on difference in time of arrival (DTOA) is bounded by the ability to accurately estimate signal arrival times. Evidently, the time of arrival (TOA) estimation quality is determined by the SNR of a finite-energy disturbance. Therefore the SNR of finite-energy disturbances is an adequate measure for quantifications. In worst-case scenarios encountered in the tentative measurements, the maximum average SNR of bandlimited disturbances exceeded the maximum average SNR of PD signals up to 16 dB. Again, since only PD magnitudes in the order of several thousand of picocoulombs are observed visually, this difference can be much larger for small discharges. On the other hand, the maximum average SNR of PD signals originating outside the cable under test is in the same order of PD signals originating within the cable under test.

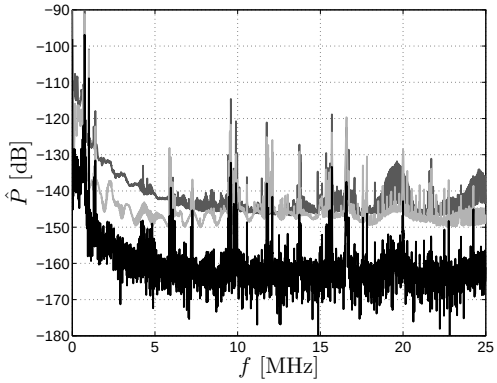

Figure 3.10 *Averaged power spectra of signals obtained by sensors at the terminations of a 410 m long PILC cable (light and dark grey) and the averaged cross power spectrum (black).*

3.6 Noise and Interference Cross-Correlation in Two-Sided Measurements

For the purpose of defect location, sensors at both cable-ends can be applied in order to determine the difference in time of arrival between PD signals originating from the same discharge. In this case, sensor signals are synchronized and some correlation can exist between the disturbances measured at each end. In a tentative on-line measurement, sensors were installed at the cable terminations at each end of a 410 m long paper insulated lead covered (PILC) cable. Time-base alignment of the sensor signals was achieved using GPS satellites. In order to determine the correlation, the averaged cross-power spectrum of the sensor signals was examined. In Fig. 3.10, the averaged cross-power spectrum obtained during a cycle of the grid operating voltage is depicted (black). As a reference, the averaged power spectra of both sensor signals are plotted as well (light and dark grey). Again, the measurements were obtained with a 50 MSPS data acquisition system. The FFT length was chosen as $B = 8192$, which results in a frequency domain resolution of $\Delta f \approx 6.2$ kHz. A Hamming window was applied to reduce spectral leakage. Notch filters were not applied in this case, and the peaks in the power spectra indicate that radio broadcasts are picked up by the sensors at both cable ends.

The measurements show that for dominant radio broadcasts in the low megahertz range, the cross-power of the sensor signals is almost equal to the power of the individual sensor signals. These observations imply that continuous periodic interference observed by both sensors can be strongly correlated. However, in the entire frequency range the cross-power of the broadband background noise is 15 dB to 20 dB lower compared to the noise power observed in each of the sensor signals individually. Consequently, the noise observed by both sensor signals is only very weakly correlated. These observations are important for PD signal analysis, and are taken into account.

3.7 Conclusions

In this chapter noise and interference characteristics present in on-line partial discharge measurements in power cables were studied. The results of tentative on-line measurements, performed at various sites in the Netherlands, indicate that three main disturbance classes can be distinguished, namely continuous periodic interference, broadband background noise, and finite-energy interference. In order to quantify the impact of noise and interference on PD signals, signal quality measures were introduced for these disturbance classes.

The amount of measured noise and interference is partly determined by the sensor locations within a ring main unit. On-line PD detection can be performed using a current transformer clipped on the cable earth strap at a termination in order to measure signals travelling in the SP channel. In many situations in the Netherlands, a CT can also be installed around the cable screen past the earth connection. The tentative measurements show that the latter sensor position results in better PD signal quality, and is therefore preferred. PD signals propagating in the PP channel can be detected by CTs installed on two transformer connection cables, if the cable screens are connected to the RMU neutral rail only at a single side. Since the two sensor signals are subtracted a differential measurement method is applied, and disturbances coupled equally to the phase conductors are cancelled. Tentative measurements indicate that continuous periodic interference and noise levels are significantly smaller for PP channel detection compared to SP channel detection. However, it must be stressed that signal qualities are not necessarily improved, since the PP channel load impedance is generally higher than the SP load impedance. In addition, the magnitudes of PD signals present in the propagation channels depend on the amount of charge induced in the conductors at the defect location. Moreover, the possible existence of crosstalk between propagation channels can result in attenuation of signals. Whether SP channel or PP channel detection is preferred depends on the specific measurement situation and a general statement cannot be made. In addition, a directional sensing method can be applied by SP channel measurement, simultaneously at the cable termination and at the transformer connection cables. The proposed method can be used to determine if a signal arriving at an RMU has propagated through the cable or originated from elsewhere.

Generally, narrow-band interference resulting from commercial radio broadcasts dominates the measurements. In worst-case scenarios encountered in the tentative measurement, quasi-periodic interference amplitudes comparable to PD signal amplitudes in the order of several thousands of picocoloumbs were observed. Evidently, for smaller PD magnitudes the signal to periodic interference amplitude ratios will be much lower. Although radio broadcasts are time-varying, the interference can be considered quasi-periodic on a short time scale, e.g. during a cycle of the grid operating voltage. Tentative measurements indicate that radio broadcasts, picked up by sensors installed at both cable ends, can be strongly correlated. However, since radio broadcasts are narrow-band, they can be suppressed using notch filters or interference cancellers.

Broadband background noise in PD measurements can be considered stationary or slowly time-varying. Rough signal quality estimates can be obtained as the ratio of average signal power within a predefined time-interval and the average noise power. However, the noise power distribution is frequency dependent, and components in the

range up to 3 MHz dominate. Since the noise observed in the tentative measurements was colored, more realistic SNRs were obtained by applying a whitening filter and measuring the average signal and noise power at the output. In the tentative measurements, PD signals with magnitudes ranging from one thousand to fifteen thousand picocoloumb were observed, and average SNRs were estimated ranging from -6 dB to 16 dB. In addition, the tentative measurements show that in case of synchronized measurement at both cable ends, the noise observed by both sensors is only weakly correlated. This observation is important for signal analysis, since the correlation can be neglected.

Finite-energy disturbances frequently occur in on-line PD measurements at arbitrary time-instants or with some quasi-periodic repetition. Examples of finite-energy disturbances are PDs from adjacent HV systems, thyristor pulses, switching transients, etc. In the tentative measurements bandlimited finite-energy disturbances were observed, mostly with center frequencies of several hundred kilohertz and bandwidths ranging from tens to hundreds of kilohertz. In worst-case scenarios this type of disturbance was present with amplitudes exceeding amplitudes of large PD signals by up to a factor 2. In principle, bandlimited finite-energy disturbances can be rejected based on their waveshapes. Although some disturbances can occur with some regularity, repetition rates deviate in the order of tens to hundreds of microseconds. As a consequence, rejection based on repetition rates alone is hardly feasible, and is therefore not discussed in this thesis.

In addition to bandlimited disturbances, PD signals from other high-voltage equipment than the cable system under test are considered as interference. This type of interference cannot be distinguished from PD signals based on signal waveforms or repetition rates. In this case, DOA-based discrimination can be applied to distinguish PD signals originating within and outside the cable under test. However, this method only allows identification of finite-energy disturbances at the first RMU where the interferences arrive, since disturbances propagate through the cable under test as well. Generally, cable systems are well shielded and finite-energy disturbances merely originate outside the cable under test. If sensor signals are obtained synchronously at each cable end, discrimination is possible by estimating the difference of arrival times of finite-energy signals at each sensor , but cancellation is not possible in general. Discrimination based on the arrival times of signals measured at both cable ends applies to all finite-energy disturbances; therefore this is the most powerful tool for finite-energy disturbance rejection. The performance of DTOA-based disturbance rejection is bounded by the ability to accurately estimate signal arrival times and thus by the SNR. In worst-case scenarios encountered in the tentative measurements, the maximum average SNR of bandlimited disturbances exceeded the maximum average SNR of PD signals up to 16 dB. Again, since only PD magnitudes in the order of several thousand of picocoulombs are observed visually, this difference can be much larger for small PDs. On the other hand, the maximum average SNR of PD signals originating outside the cable under test is often in the same order of PD signals originating within the cable under test.

Chapter 4

Measurement of Signal Model Parameters

4.1 Introduction

For the purpose of signal analysis, discharge location, as well as apparent charge estimation, the parameters of the partial discharge signal model must be measured prior to PD detection. In this chapter, methods are presented that enable model parameter estimation, which apply to both off-line and on-line PD detection.

The parameters of the signal model can be measured by evaluating the response of the cable system to an applied transient. Parameter estimation from mixtures is generally not feasible; therefore the injected signals and the response must be separable. In Section 4.2, the basics of this measurement method are introduced Sensors are installed at the terminations of each end; therefore the transmission coefficients at the propagation channel load impedances are important signal model parameters. The exact transmission coefficients depend on the various components present within a ring main unit (RMU), and can differ among measurement situations. In Section 4.3, methods for estimation of transmission coefficients are proposed. By evaluating the transfer of the injected signal from one cable end to the other, the channel propagation properties can be estimated. However, prior knowledge of the cable system under test is of essential importance, since propagation properties per length unit can only be obtained if the travelled distance is known. If the sensor signals obtained at the cable ends are not synchronized, the propagation velocity can only be determined using signals that are reflected at the opposite cable end. In Section 4.4, estimation of propagation properties using synchronized and non-synchronized measurements is discussed. In a composite cable system, various cable sections with differing attenuation and velocity may be present. If a section interface gives rise to an impedance transition, the injected signal is partly reflected. The reflected signals can be used to estimate the propagation properties of individual cable sections.

In Sections 4.3 to 4.4, the proposed analysis methods are evaluated theoretically using computer simulations, based on the signal model presented in Chapter 2. In Section 4.5, the methods are validated using measurements obtained from the experimental grid that was described in Section 1.3.4. It is shown that parameters can be estimated if reflections on impedance transitions can be extracted. Conclusions are given in Section 4.6.

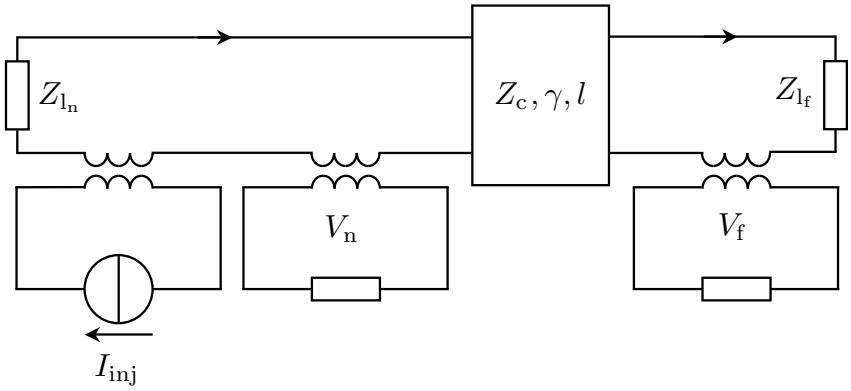

Figure 4.1 *Signal injection and measurement in a uniform cable system, characterized by propagation factor γ, wave impedance Z_c, and length l; with load impedances Z_{l_n} and Z_{l_f}. At the near end a signal is injected (I_{inj}) and measured at the near end (V_n) and far end (V_f), by means of CTs.*

4.2 Measurement Method

Excitation of the cable system with a known signal forms the basis for model parameter measurements described in this thesis. Similarly to the sensor selection considerations, signal injection into a live cable system is preferably realized by inductive coupling [Ste02a, Wou, Wou03a, Wou03b]. In Fig. 4.1, a measurement set-up is schematically visualized, where signals are injected into a uniform propagation channel at one end of the on-line cable system, and measured at both ends simultaneously. Besides its application to system identification, the scheme is used for synchronization of PD measurements obtained at both cable system terminations. Without loss of generality, only shield-to-phase (SP) channel measurements are considered here. The injection CT and the sensor are assumed to be spaced sufficiently far, such that direct mutual coupling is negligible. However, if some coupling does exist, the transfer between the CTs can be measured prior to installation and compensated for during measurements.

In principle, the sensor used for measurements can also be utilized for signal injection. However, for the purpose of parameter measurements as well as synchronization, injected signals must have sufficient energy , such that they can be detected at both cable ends. Depending on the measurement situation, large currents may have to be injected. Commercially available CTs are generally not intended for transferring such signals and the core material saturates if high currents are applied, resulting in strongly non-linear behavior. Instead, a custom-made Rogowski air coil is used for pulse injection in the experiments presented in this thesis. In Fig. 4.2, the measured transfer impedance of the injection CT is depicted [Wie05].

Commercially available signal generators and amplifiers are generally not suitable for generating high broadband currents into an inductive load. The experimental results reported in this thesis are therefore obtained using a custom-made transient generator, implemented by the Eindhoven University of Technology (TU/e). The generator is realized by discharging a capacitor over the self-induction of the injection coil using an electronic switch, which results in a pulse with its energy concentrated

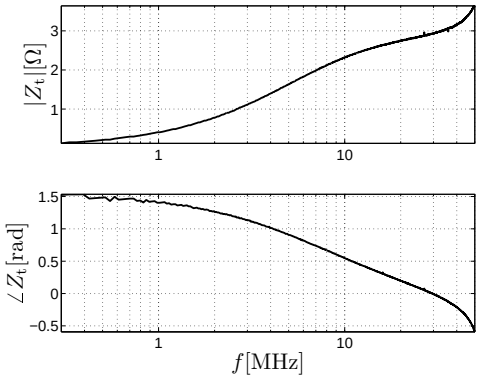

Figure 4.2 *Measured transfer impedance of a custom-made Rogowski air coil used for signal injection.*

in the low MHz range [Wou, Wou03a, Wou03b, Tal04]. The voltage excited in the secondary circuit is a band-pass transient, since the injection CT transfer impedance has a high-pass character.

A CT placed around a conductor introduces only a weak coupling between the primary and secondary circuit, which implies that the circuits can be described independently. In the frequency domain, the current through the near-end load impedance $Z_{\mathrm{l_n}}(\omega)$ as a result of an injected current $I_{\mathrm{inj}}(\omega)$ equals

$$I_{\mathrm{l_n}}(\omega) = \frac{Z_{\mathrm{t_i}}(\omega)}{Z_{\mathrm{l_n}}(\omega) + Z_{\mathrm{c}}} I_{\mathrm{inj}}(\omega) \tag{4.1}$$

where Z_{c} is the characteristic impedance of the propagation channel and $Z_{\mathrm{t_i}}(\omega)$ is the transfer impedance of the injection CT. The sensor signal at the cable system input equals

$$V_{\mathrm{n}}(\omega) = Z_{\mathrm{t_m}}(\omega) Z_{\mathrm{t_i}}(\omega) Y_{\mathrm{n}}(\omega) I_{\mathrm{inj}}(\omega) \tag{4.2}$$

where $Y_{\mathrm{n}}(\omega) = 1/(Z_{\mathrm{l_n}}(\omega) + Z_{\mathrm{c}})$ is the near-end admittance and $Z_{\mathrm{t_m}}(\omega)$ is the transfer impedance of the measurement CT. In case of a uniform cable system and equal sensors at both sides, the sensor signal at the opposite cable end is expressed as

$$V_{\mathrm{f}}(\omega) = e^{-\gamma(\omega) l} T_{\mathrm{l_f}}(\omega) V_{\mathrm{n}}(\omega) = H_{\mathrm{n,f}}(\omega) V_{\mathrm{n}}(\omega) \tag{4.3}$$

where $T_{\mathrm{l_f}}(\omega) = 2Z_{\mathrm{c}}/(Z_{\mathrm{c}} + Z_{\mathrm{l_f}}(\omega))$ is the current transmission coefficient at the far-end load impedance, $\gamma(\omega)$ is the propagation factor, and l is the cable length.

Eq. 4.2 and Eq. 4.3 alone do not provide sufficient information to measure the unknown signal model parameters. Consequently, injection at the far cable end is

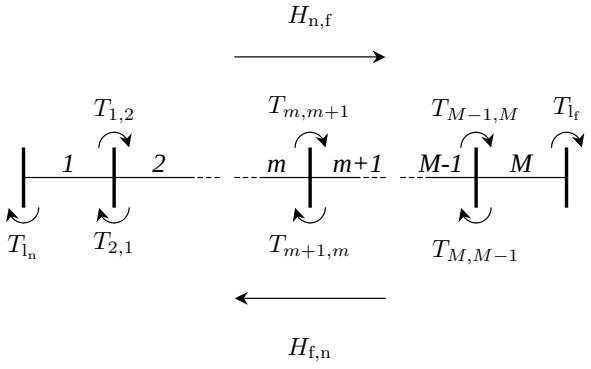

Figure 4.3 *Schematic visualization of transmission coefficients encountered by a signal propagating in a cable with M sections. The cable transfer function equals $H_{\mathrm{n,f}}$ in case of near-end injection and $H_{\mathrm{f,n}}$ in case of far-end injection.*

required to obtain more information, viz.

$$\begin{aligned} Y_{\mathrm{n}}(\omega) &= \frac{1}{Z_{\mathrm{l_n}}(\omega) + Z_{\mathrm{c_1}}} \\ H_{\mathrm{n,f}}(\omega) &= T_{\mathrm{l_f}}(\omega)\, e^{-\gamma_M(\omega) l_M} \prod_{m=1}^{M-1} T_{m,m+1}\, e^{-\gamma_m(\omega) l_m} \\ Y_{\mathrm{f}}(\omega) &= \frac{1}{Z_{\mathrm{l_f}}(\omega) + Z_{\mathrm{c}_M}} \\ H_{\mathrm{f,n}}(\omega) &= T_{\mathrm{l_n}}(\omega)\, e^{-\gamma_M(\omega) l_M} \prod_{m=1}^{M-1} T_{m+1,m}\, e^{-\gamma_m(\omega) l_m} \end{aligned} \tag{4.4}$$

where the measurement method is generalized to a composite cable system with M sections. The first two and last two expressions result from near-end and far-end injection, respectively. The m-th cable section is parameterized by the propagation factor $\gamma_m(\omega)$, characteristic impedance Z_{c_m} and length l_m. The current transmission coefficients at the load impedances are defined as $T_{\mathrm{l_n}}(\omega) = 2Z_{\mathrm{c_1}}/(Z_{\mathrm{c_1}} + Z_{\mathrm{l_n}}(\omega))$ and $T_{\mathrm{l_f}}(\omega) = 2Z_{\mathrm{c}_M}/(Z_{\mathrm{c}_M} + Z_{\mathrm{l_f}}(\omega))$, for the near and far end, respectively. Likewise, the transmission coefficient at a section interface equals $T_{a,b} = 2Z_{\mathrm{c}_a}/(Z_{\mathrm{c}_a} + Z_{\mathrm{c}_b})$ for an impedance transition from Z_{c_a} to Z_{c_b}. In Fig. 4.3 the structures of the transfer from one cable end to the other is visualized.

In the foregoing analysis it was assumed that the cable system input and output signals are obtained simultaneously. In practice, the cable ends are located far apart and synchronization is required in order to measure the channel propagation delay. In this chapter, two methods are discussed that enable time-base alignment. The first method employs time-labels obtained from the global positioning system to synchronize pulse-injection with measurements at both terminations [Ste01]. If sufficient measurements are conducted, the estimation errors introduced by deviation of the time-labels can be minimized by averaging of results. The second method relies on the feasibility to extract signals that are reflected on the impedance transition at the opposite cable end. Moreover, as a second condition the injected transients must greatly exceed the noise and interference levels at both terminations, such that signals

can be detected by triggered data-acquisition. In this case, an additional unknown time-shift between the sensor signals exists.

The set of equations (4.4) does not provide sufficient information to estimate the transmission coefficients and the propagation properties of the individual sections. For this reason, signals reflected on impedance transitions must be evaluated as well, as will be discussed in the next sections. Generally, an RMU interfaces multiple cable systems (typically two in a ring distribution network). When a transient is injected at the termination of the cable system under test, part of the signal travels through adjacent cable(s). As a consequence, besides reflections on impedance transitions within the cable under test or the far-end load impedance, other reflections are detected. In order to discriminate reflections from the cable under test and from adjacent cables, a directional sensing method such as described in Section 3.2 can be applied. Moreover, a priori knowledge of the section lengths and approximate knowledge of propagation delays of both the cable under test and the adjacent cable(s) can be used to distinguish the origins of reflected signals. It must be stressed that the reflection-based identification methods presented in this chapter require that reflections can be separated, since parameter estimation from mixtures is generally not possible.

On-line measurements are corrupted by continuous periodic interference, finite energy disturbances and broadband background noise. Generally, the repetition period of finite energy disturbances is large with respect to the cable propagation delay. Therefore it is assumed that the measurements are free of such disturbances, which can be accomplished by taking multiple measurements into account, and eliminating waveshapes that significantly differ from the mean. Prior to the interpretation of the measurements, dominant narrow-band radio broadcasts can be suppressed by application of notch filters. Consequently, in model parameter measurements only broadband background noise has to be considered.

4.3 Transmission Coefficients at the Channel Loads

As a result of the various characteristics of RMU components, the propagation channel load impedances give rise to resonances in the frequency range of interest. Consequently, the transmission coefficients at the near and far end have a major influence on the waveshapes of detected PD signals. Since the exact values depend on the specific RMU as well as the channel characteristic impedance, field measurement of the transmission coefficients is of crucial importance. In this section, methods are proposed that allow measurement of the transmission coefficients at the channel load impedances.

4.3.1 Uniform Cable Systems

Eq. 4.4 shows that the transmission coefficient at a load impedance is directly related to the admittance of the secondary circuit in which a transient is excited, i.e.

$$T_{\mathrm{l}}(\omega) = 2Z_{\mathrm{c}}Y(\omega)\ . \tag{4.5}$$

Note that the excitation voltage has a band-pass character; therefore the transmission coefficient can only be obtained in the frequency range where sufficient energy is supplied. The characteristic impedance is approximately real and frequency independent; therefore the transmission coefficient is determined up to a constant. In principle, a

scaled version of the transmission coefficient is sufficient to model waveshapes of detected PD signals. However, for the purpose of apparent charge estimation, the characteristic impedance must be obtained as well.

At the injection side, the reflection on the opposite cable end can be expressed as a function of the sensor signal. For instance at the near end, the transfer function of the measured injected signal and the reflection can be expressed as

$$H_{\mathrm{n,r}}(\omega) = \frac{V_{\mathrm{in,r}}(\omega)}{V_{\mathrm{n}}(\omega)} = T_{\mathrm{l_n}}(\omega)\, R_{\mathrm{l_f}}(\omega)\, e^{-\gamma(\omega)2l} \tag{4.6}$$

where $R_{\mathrm{l_f}}(\omega) = T_{\mathrm{l_f}}(\omega) - 1$ is the current reflection coefficient at the far end. Assuming that the reflected signals can be separated in the time-domain, the characteristic impedance can be estimated by evaluating the ratio of the reflection transfer functions obtained at both the near and far end, given by

$$\frac{H_{\mathrm{n,r}}(\omega)}{H_{f,r}(\omega)} = \frac{T_{\mathrm{l_n}}(\omega)\,(T_{\mathrm{l_f}}(\omega) - 1)}{T_{\mathrm{l_f}}(\omega)\,(T_{\mathrm{l_n}}(\omega) - 1)}\ . \tag{4.7}$$

Subsequently, with Eq. 4.5, the characteristic impedance can be estimated (estimates are indicated by $\hat{}$)

$$\hat{Z}_{\mathrm{c}}(\omega) = \frac{H_{\mathrm{n,r}}(\omega)Y_{\mathrm{f}}(\omega) - H_{\mathrm{f,r}}(\omega)Y_{\mathrm{n}}(\omega)}{2Y_{\mathrm{n}}(\omega)Y_{\mathrm{f}}(\omega)(H_{\mathrm{n,r}}(\omega) - H_{\mathrm{f,r}}(\omega))}\ . \tag{4.8}$$

As a result of the frequency dependent attenuation introduced by the cable and the load impedances, the reflection transfer functions are only reliable in a limited frequency range. However, the characteristic impedance is approximately constant, and an estimate can be obtained by averaging $\hat{Z}_{\mathrm{c}}(\omega)$ in the frequency range where the SNR of the reflected signals is sufficient, or by computing a weighted average. Since the injected pulses are uncorrelated with additive disturbances, in principle, the estimation variance can be decreased arbitrarily by averaging multiple measurements. Note that the estimation method relies on the ability to extract reflections from sensor signals and does not require synchronized measurements. In practical situations, however, reflections cannot always be extracted. In such cases the transmission coefficients are only determined up to a scaling factor.

As an example, a computer simulation experiment was conducted for a typical 1 km long 12.5 kV 3×95 mm^2 paper insulated lead covered (PILC) cable with a theoretical wave impedance of $Z_{\mathrm{c}} = 11.4\ \Omega$. At one end, the cable was terminated to a real load impedance equal to half the characteristic impedance of the cable. At the other end, the load impedance was chosen equal to twice the cable impedance. Using the model as described in Section 2.5, the system responses to injected signals at each cable end were simulated in additive white noise. The injection was a band-pass signal with a center frequency of 1.25 MHz and −3 dB bandwidth of 1.5 MHz, i.e. the low and high cut-off frequencies equal 0.5 MHz and 2 MHz, respectively. In Fig. 4.4, the cable characteristic impedance (black) and the estimated impedance as obtained from Eq. 4.8 (grey) are depicted. The estimate is shown for the frequency range where the single-bin SNR of the sampled reflected signals, $\mathrm{SNR}(i\Delta f) = |V_{\mathrm{in,r}}(i\Delta f)|^2 / T_0 P_{\mathrm{N}}(i\Delta f)$, exceeded 10 dB. In this case, the observation interval for SNR computation was defined as $T_0 = 10\ \mu s$, since the reflected signals could be observed entirely on this interval. It can be concluded that good estimates of the characteristic impedance can be obtained by averaging in the frequency range where the SNR of the reflected signals is large.

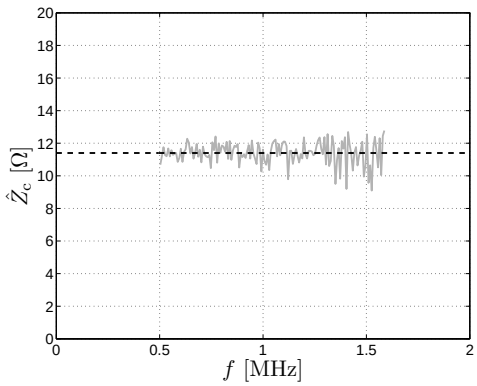

Figure 4.4 *Characteristic impedance estimate (grey) and true value (black dashed) of a uniform cable system based on computer simulations.*

4.3.2 Composite Cable systems

In case of a composite cable system, Eq. 4.7 may not provide a unique solution, since the characteristic impedances of the first and last cable sections can differ. In this section, estimation of load transmission coefficients for composite cable systems is discussed, in case of synchronized and non-synchronized measurements.

Synchronized Measurements

In case of a composite cable system with M sections, the M-th direct reflection arriving at one cable end results from the characteristic impedance transition at the opposite end. for instance at the near end, the transfer function of the excitation and the far-end reflection can be expressed as

$$H_{\mathrm{n,r}_M}(\omega) = T_{\mathrm{l_n}}(\omega)\, R_{\mathrm{l_f}}(\omega)\, e^{-\gamma_M(\omega)2l_M} \prod_{m=1}^{M-1} (1 - R_{m,m+1}^2)\, e^{-\gamma_m(\omega)2l_m} \,. \tag{4.9}$$

The signal passes a section interface from both directions, and the transmission coefficients are combined accordingly, i.e. $T_{m,m+1}\, T_{m+1,m} = 1 - R_{m,m+1}^2$, where $R_{m,m+1}$ equals the reflection coefficient at an impedance transition from Z_{c_m} to $Z_{\mathrm{c}_{m+1}}$. By combining the transfer functions of the signals measured at both cable terminations for injection at both the near and far end, the following expression can be obtained

$$H_{\mathrm{n,f}}(\omega) H_{\mathrm{f,n}}(\omega) = T_{\mathrm{l_n}}(\omega)\, T_{\mathrm{l_f}}(\omega)\, e^{-\gamma_M(\omega)2l_M} \prod_{m=1}^{M-1} (1 - R_{m,m+1}^2)\, e^{-\gamma_m(\omega)2l_m} \,. \tag{4.10}$$

Now the ratio of Eq. 4.10 and Eq. 4.9,

$$\frac{H_{\mathrm{n,f}}(\omega) H_{\mathrm{f,n}}(\omega)}{H_{\mathrm{n,r}_M}(\omega)} = \frac{T_{\mathrm{l_f}}(\omega)}{T_{\mathrm{l_f}}(\omega) - 1} \,, \tag{4.11}$$

provides sufficient information to estimate the far-end transmission coefficient regardless of the properties of the cable system as well as the number of sections, i.e.

$$\hat{T}_{\mathrm{l_f}}(\omega) = \frac{H_{\mathrm{n,f}}(\omega) H_{\mathrm{f,n}}(\omega)}{H_{\mathrm{n,f}}(\omega) H_{\mathrm{f,n}}(\omega) - H_{\mathrm{n,r}_M}(\omega)} \,. \tag{4.12}$$

Intuitively, Eq. 4.11 can be verified by recognizing that both the numerator and denominator represent the transfer function of a signal propagating back and forth through the propagation channel. A similar expression can be obtained by considering the ratio of $H_{\mathrm{n,f}}(\omega)H_{\mathrm{f,n}}(\omega)$ and $H_{\mathrm{f,r}_M}(\omega)$ from which the near-end transmission coefficient can be estimated. The ratios can be evaluated only within the frequency range where the reflected signals have sufficient SNR. Evidently, this frequency range can be small, due to the frequency-dependent attenuation of the propagation path.

Instead of determining the transmission coefficients directly from the ratios, first the characteristic impedances can be estimated. E.g. by substitution of $T_{\mathrm{l_f}}(\omega)$ with $2Z_{\mathrm{c},M}(\omega)Y_{\mathrm{f}}(\omega)$ in Eq. 4.12, the characteristic impedance of the last cable section can be estimated. Since the characteristic impedance is approximately constant, an estimate can be obtained by averaging in the appropriate frequency range, or by computing a weighted average based on the SNRs of the various transfer functions involved. By combining the estimate with Eq. 4.5, the transmission coefficients can be obtained in the frequency range where the excitation has sufficient SNR, which is obviously much broader compared to the range where Eq. 4.12 gives reliable results.

Non-Synchronized Measurements

The foregoing analysis applies only if synchronized measurements can be obtained. Without synchronization, unknown time-shifts between the various transfer functions exist, and Eq. 4.11 becomes

$$\frac{H_{\mathrm{n,f}}(\omega)H_{\mathrm{f,n}}(\omega)}{H_{\mathrm{n,r}_M}(\omega)}\, e^{j\omega\tau} = \frac{T_{\mathrm{l_f}}(\omega)}{T_{\mathrm{l_f}}(\omega) - 1} \tag{4.13}$$

where τ equals the addition of the time-shifts. Taking additive disturbance into account, the expression can be rewritten as

$$N(\omega) = T_{\mathrm{l_f}}(\omega)\left(H_{\mathrm{n,f}}(\omega)H_{\mathrm{f,n}}(\omega) - H_{\mathrm{n,r}_M}(\omega)\, e^{-j\omega\tau}\right) - H_{\mathrm{n,f}}(\omega)H_{\mathrm{f,n}}(\omega) \tag{4.14}$$

where $N(\omega)$ consists of the broadband background noise in the various transfer function measurements. Theoretically, the noise picked up by both sensors is mutually correlated, since the noise propagates from one end to the other through the cable itself or via some other path. However, besides interfering radio broadcasts, no strong cross-correlation between continuous interference measured at the cable terminations was observed in practice. Radio broadcasts are suppressed by application of notch filters, consequently the remaining weak cross-correlation between the noise processes at the cable terminations can be neglected.

As a result of the time-shift τ, the transmission coefficient cannot be obtained directly from Eq. 4.14. In order to measure the unknown parameters, an estimation procedure is proposed based on application of maximum-likelihood estimation theory (see e.g. [Tre68]). In the following derivations, the estimation problem is evaluated in a discrete-time representation, which, in this case, allows a more simple notation compared to a continuous-time representation. Assuming that the signals and transfer functions are properly bandlimited and sampled, the a posteriori scaled likelihood of

Eq. 4.14 can be constructed

$$L(Z_{\mathrm{c},M},\tau) = \\ \Delta f \sum_{i=0}^{B-1} -\frac{|2Z_{\mathrm{c},M}Y_{\mathrm{f}}(i\Delta f)\left(H_{\mathrm{c}}(i\Delta f) - H_{\mathrm{n,r}_M}(i\Delta f)\,e^{-j2\pi i\Delta f\tau}\right) - H_{\mathrm{c}}(i\Delta f)|^2}{2|2Z_{\mathrm{c},M}Y_{\mathrm{f}}(i\Delta f)|^2 P_N(i\Delta f)} \tag{4.15}$$

where $H_{\mathrm{c}}(i\Delta f) = H_{\mathrm{n,f}}(i\Delta f)H_{\mathrm{f,n}}(i\Delta f)$. Eq. 4.15 expresses the likelihood of parameter values given the discrete Fourier transforms (DFTs) of the measured transfer functions and the noise PSDF. Assuming that the background noise is zero-mean and Gaussian, and that at each cable-end the noise has the same order of magnitude, the PSDF of $N(i\Delta f)$ can be approximated by $P_N(i\Delta f) \approx |T_{\mathrm{l_f}}(i\Delta f)|^2 P_{N_{\mathrm{n}}}(i\Delta f)$, where $P_{N_{\mathrm{n}}}(i\Delta f)$ is the PSDF of the near-end measurement noise. The approximation can be verified intuitively by recognizing that, within the frequency range where the SNR of the reflection transfer function is sufficiently large, this SNR is still significantly lower than the SNRs of the remaining transfer functions. For this reason, the term $N(i\Delta f)$ is dominated by the noise in the reflection transfer function.

Since the likelihood function is not linear-quadratic, analytical expressions for the optimal parameter estimates cannot be obtained. Moreover, there exist multiple local maxima in the parameter space and iterative optimization procedures cannot be applied straightforwardly.

In tentative measurements of cable propagation properties, as described in Section 2.3, it was found that the SP channel characteristic impedances generally range from 10 Ω to 20 Ω. Consequently, an initial estimate $\hat{Z}_{\mathrm{c},M}$ is already available or, alternatively, can be obtained using Eq. 4.8. From the initial value of $Z_{\mathrm{c},M}$, the transmission coefficient can be estimated. Subsequently, by substitution of the initial transmission coefficient estimate $\hat{T}_{\mathrm{l_f}}(i\Delta f)$ in Eq. 4.14, an initial estimate of τ can be obtained by evaluating the time-domain cross-correlation,

$$\varphi(\tau) = T_{\mathrm{s}} \sum_{k=0}^{B-1} s_1(kT_{\mathrm{s}} - \tau)\, s_2(kT_{\mathrm{s}}) \tag{4.16}$$

where

$$s_1(kT_{\mathrm{s}}) = \Delta f \sum_{i=0}^{B-1} (\hat{T}_{\mathrm{l_f}}(i\Delta f) - 1)H_{\mathrm{n,f}}(i\Delta f)H_{\mathrm{f,n}}(i\Delta f)\, e^{+j2\pi ik/B} \tag{4.17}$$

$$s_2(kT_{\mathrm{s}}) = \Delta f \sum_{i=0}^{B-1} \hat{T}_{\mathrm{l_f}}(i\Delta f)H_{\mathrm{n,r}_M}(i\Delta f)\, e^{+j2\pi ik/B}\,. \tag{4.18}$$

Now the delay τ that maximizes the cross-correlation equals an initial estimate of the time-shift between the various transfer functions. The initial estimates are close to the global maximum, and an iterative optimization procedure can be applied to search for the maximum-likelihood parameter estimates. The likelihood function can be effectively compressed by evaluating only the frequency range where the reflection transfer function has sufficient SNR.

By removing the negation in Eq. 4.15, a minimization problem is obtained, which can be solved iteratively, for example using Newton's method, see e.g. [Pre92, Moo99]. The noise PSDF in Eq. 4.15 depends on the characteristic impedance, which generally complicates the derivation of iterative algorithms. However, $Z_{\mathrm{c},M}$ is frequency

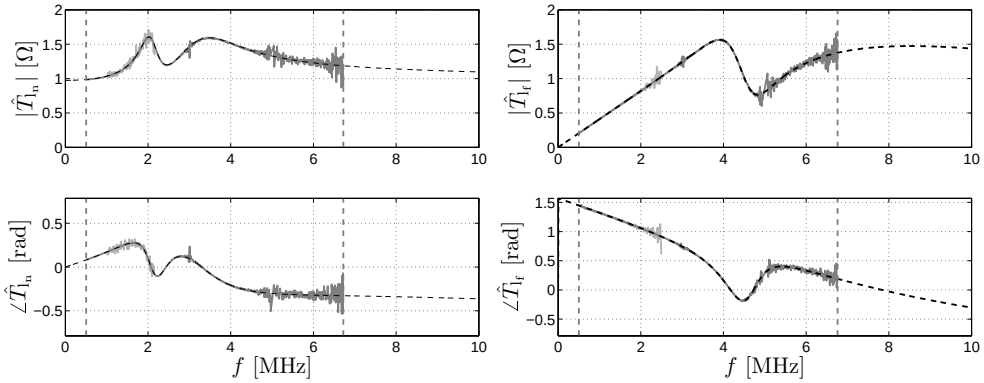

Figure 4.5 *Simulation of load transmission coefficients (black dashed) and estimates for synchronized measurements (light grey) and non-synchronized measurements (dark grey) based on computer simulations.*

independent, and has no influence on the location of the global minimum. Consequently, by neglecting this term in the denominator, analytic expressions for the gradients of Eq. 4.15 can be obtained. The parameter estimates are correlated, since $Z_{\mathrm{c},M}$ determines the phase-shift of the estimated far-end reflection coefficient $R_{\mathrm{l,n}}(i\Delta f) = T_{\mathrm{l_n}}(i\Delta f) - 1$, which influences the time-shift estimate, and vice versa. This correlation must be taken into account by considering the second derivatives of the function with respect to the parameters in all possible directions.

Clearly, the convergence and performance of the proposed method depend on various parameters, but most significantly on the SNR of the far-end reflection. Fundamental bounds on the estimation variance can be derived from Eq. 4.15. However, the variance is largely governed by the injected energy, and theoretical bounds are of little interest and are omitted, since they can simply be moved by altering the injected signal. If Eq. 4.8 is used as a starting point, the initial estimates are extremely close to the optimal estimates and convergence to the global optimum is guaranteed.

As an example, a simulation experiment was conducted for a composite cable system consisting of a 500 m long 12.5 kV 3×95 mm^2 PILC cable and a 500 m long 10 kV 3×95 mm^2 PILC cable. At the near end, the cable system was terminated to an RMU consisting of a distribution transformer and two cable terminations. Thus besides the cable under test, another cable was terminated to this RMU. At the far end, the cable system was terminated to an RMU consisting of a distribution transformer and a single termination. The load impedances used in this simulation were taken from [Wag03]. The impedances of the various RMU configurations were obtained by field measurements. Using the model as described in Section 2.5, the system responses to injected signals at each cable end were simulated in additive white noise. The injection was a band-pass signal with a center frequency of 1.25 MHz and -3 dB bandwidth of 1.5 MHz. In Fig. 4.5, the transmission coefficient at the near-end and far-end RMU are depicted (dashed black), as well as the estimated transmission coefficients as obtained from synchronized measurements using Eq. 4.12 (light grey). The estimate is shown for the frequency range where the SNR of the far-end reflected signal exceeded 10 dB. Subsequently, the simulated sensor signals were shifted with arbitrary delays, and an initial estimate of the combined characteristic impedances was obtained using

Eq. 4.8. Initial estimates of the transmission coefficients and the combined time-shift between the transfer functions were obtained using the procedure described above. Then, appropriate minimization criteria were constructed and Newton's method was applied to estimate the characteristic impedances of both cable sections separately. Using Eq. 4.5, the transmission coefficients were estimated for the frequency range where the SNR of the excitation exceeded 10 dB, as depicted in Fig. 4.5 (dark grey). For clarity, the frequency range is explicitly indicated by vertical dashed lines. It can be concluded that good transmission coefficient estimates can be obtained in the frequency range where the SNR of the evaluated signals is large.

Evidently, the transmission coefficients can only be estimated in the frequency range where the injected signal has sufficient energy. In practice, the transmission coefficients cannot be measured for the entire detection bandwidth, due to limitations of the available equipment. For relatively low frequencies, the measurement results can be extrapolated, under the assumption that dominant resonances appear outside this frequency range. A priori knowledge of the RMU configuration can be used as a basis for extrapolation. For low frequencies, the load impedance is dominantly capacitive if no outgoing cables are present. If multiple cables are terminated to the RMU, the load impedance can be considered as capacitive and resistive for low frequencies. For relatively high frequencies, extrapolation is not preferred, since resonances can be present.

4.4 Propagation Parameters

In order to be able to model PD signals originating from any location within the cable system under test, the channel propagation properties must be obtained. In this section, methods are proposed for propagation parameter estimation, which apply to both synchronized and non-synchronized measurements.

4.4.1 Uniform Cable Systems

For a uniform cable system, the attenuation per unit length can be estimated directly from the transfer between the signals measured at both cable terminations, e.g.

$$\hat{\alpha}(\omega) = -\frac{1}{l} \ln \left(\frac{|H_{\mathrm{n,f}}(\omega)|}{|\hat{T}_{\mathrm{l_f}}(\omega)|} \right) . \tag{4.19}$$

Evidently, attenuation estimation does not require synchronization of sensor signals.

If synchronized measurements are available, the phase-shift per unit length can be estimated by

$$\hat{\beta}(\omega) = -\frac{1}{l} \left(\angle\, H_{\mathrm{n,f}}(\omega) - \angle\, \hat{T}_{\mathrm{l_f}}(\omega) \right) . \tag{4.20}$$

The propagation channel is dispersive; therefore $\beta(\omega)$ is a non-linear function of frequency, and Eq. 4.20 must be evaluated separately for each frequency component. Clearly, $H_{\mathrm{n,f}}(\omega)$ describes a non-minimum phase system, since the transfer function comprises the channel propagation delay. In practice, estimates of the propagation parameters are obtained by evaluating the discrete Fourier transforms (DFTs) of sampled signals. When the phase of the discrete transfer function is computed, e.g. by $\angle\, H_{\mathrm{n,f}}(i\Delta f) = \mathrm{Im}\{\ln(H_{\mathrm{n,f}}(i\Delta f))\}$, the result is mapped onto the unit circle in the

complex plane, and information on the propagation delay is lost, i.e.

$$\angle H_{\mathrm{n,f}}(i\Delta f) = \angle T_{\mathrm{l_f}}(i\Delta f) - \beta(i\Delta f)l + 2\pi k(i\Delta f) \tag{4.21}$$

where $k(i\Delta f)$ equals some integer, such that $-\pi < \angle H_{\mathrm{n,f}}(i\Delta f) < +\pi$. Generally, this problem can be solved by unwrapping the phase, i.e. if the relative phase-shift between two successive DFT coefficients exceeds some threshold value, the absolute phase jump is changed to its 2π complement. The procedure requires a starting point with a known phase-shift, which is usually the zeroth DFT coefficient. However, the excitation voltage is a band-pass signal; therefore the transfer function is unknown for low frequencies. An alternative starting point can be obtained by estimating the channel delay in the time-domain, by cross-correlating filtered versions of the sampled sensor signals,

$$\varphi(\tau) = T_{\mathrm{s}} \sum_{k=0}^{B-1} s_1(kT_{\mathrm{s}} - \tau)\, s_2(kT_{\mathrm{s}}) \tag{4.22}$$

where $s_1(kT_{\mathrm{s}})$ and $s_2(kT_{\mathrm{s}})$ are the filtered sensor signals

$$\begin{aligned} s_1(kT_{\mathrm{s}}) &= \Delta f \sum_{i=0}^{B-1} W(i\Delta f)\hat{T}_{\mathrm{l_f}}(i\Delta f)\, e^{-\hat{\alpha}(i\Delta f)l}\, V_{\mathrm{n}}(i\Delta f)\, e^{+j2\pi kT_{\mathrm{s}}i\Delta f} \\ s_2(kT_{\mathrm{s}}) &= \Delta f \sum_{i=0}^{B-1} W(i\Delta f)V_{\mathrm{f}}(i\Delta f)\, e^{+j2\pi kT_{\mathrm{s}}i\Delta f} \end{aligned} \tag{4.23}$$

and $W(i\Delta f)$ is a rectangular window which equals unity below a cut-off frequency $f_c = i_c\Delta f$ and zero elsewhere. Note that the near-end sensor signal is filtered such that it resembles the far-end sensor signal as closely as possible, by using the parameters of the signal model that are already known. Now the delay $\tau_{\max}$ that maximizes the cross-correlation function $\varphi(\tau)$, approximates the channel delay estimate $\hat{\tau}_{\mathrm{c}}(i_c\Delta f)$ for the chosen cut-off frequency. With $\beta(i\Delta f)l = 2\pi i\Delta f\tau_{\mathrm{c}}(i\Delta f)$ the integer $k(i_c\Delta f)$ in Eq. 4.21 is chosen such that

$$\min_{k(i_c\Delta f)} \left|2\pi k(i_c\Delta f) - 2\pi i_c\Delta f\tau_{\max} - \angle H_{\mathrm{n,f}}(i_c\Delta f) + \angle \hat{T}_{\mathrm{l_f}}(i_c\Delta f)\right| . \tag{4.24}$$

When $k(i_c\Delta f)$ is known, an estimate $\hat{\tau}_{\mathrm{c}}(i_c\Delta f)$ can be obtained that serves as the starting point from which the phase-shift of the channel transfer function can be unwrapped.

The accuracy of the delay estimate $\tau_{\max}$ depends on the SNR of the filtered sensor signals within the pass-band of $W(i\Delta f)$. The variance decreases if more and higher frequency components with sufficient SNR are considered. In this respect, it is preferred to choose the cut-off frequency of the filter high. However, from Eq. 4.24 it can be observed that the probability of false identification of $k(i_c\Delta f)$ due to delay estimation errors, increases linearly with frequency. From this point of view, f_c should be chosen as low as possible. In principle, some optimality criterion can be formulated that compromises between these two contradictory constraints. However, such a criterion inevitably depends on $\beta(i\Delta f)$, and can therefore not be computed a priori. Generally, reliable estimates can be obtained by selecting f_c equal to the frequency component of the output sensor signal with maximum SNR, which lies between 1 MHz and 2 MHz depending on the total cable attenuation and the injected transient.

The proposed method can also be applied to non-synchronized measurements. However, in this case the starting point must be obtained from cross-correlation of the filtered excitation voltage and the reflection on the opposite cable end, i.e.

$$\begin{aligned} s_1(kT_\mathrm{s}) &= \Delta f \sum_{i=0}^{B-1} W(i\Delta f)\hat{T}_{\mathrm{l_n}}(i\Delta f)(\hat{T}_{\mathrm{l_f}}(i\Delta f)-1)\, e^{-\hat{\alpha}(i\Delta f)2l}\, V_\mathrm{n}(i\Delta f)\, e^{+j2\pi ik/B} \\ s_2(kT_\mathrm{s}) &= \Delta f \sum_{i=0}^{B-1} W(i\Delta f) V_{\mathrm{in,r}}(i\Delta f)\, e^{+j2\pi ik/B}\ . \end{aligned} \tag{4.25}$$

Now the delay τ_max that maximizes the cross-correlation function, approximates twice the channel delay estimate $\hat{\tau}_\mathrm{c}(i_c\Delta f)$ at the cut-off frequency.

As an example, a simulation experiment was conducted for a 1 km long 12.5 kV 3×95 mm^2 PILC cable. At the near end, the cable system was terminated to an RMU consisting of a distribution transformer and two cable terminations. At the far end, the cable system was terminated to an RMU consisting of a distribution transformer and a single termination. Using the model as described in Section 2.5, the system responses to injected signals at each cable end were simulated in additive white noise. The injection was a band-pass signal with a center frequency of 1.25 MHz and −3 dB bandwidth of 1.5 MHz. The transmission coefficients at the load impedances were estimated using the method described in the previous section. Subsequently, the attenuation of the propagation channel was estimated using Eq. 4.19. In the left plot in Fig. 4.6, the attenuation is depicted (dashed black) and the estimate (dark grey) is shown for the frequency range where the SNR of the evaluated signals exceeded 10 dB. The frequency range is explicitly indicated by vertical dashed lines. The starting point for phase-shift estimation was obtained by estimating the propagation delay of the far-end reflection, resulting from injection at the near end. Using the cross-correlation procedure described above, the initial channel delay estimate at $f_c = 1$ MHz equals $\tau = 12.16$ μs. In the right-hand plot in Fig. 4.6 the corresponding phase-velocity of $v_\mathrm{p}(f_c) = 164.5$ m/μs is marked by a grey cross. Subsequently, the integer $k(i_c\Delta f)$ was determined, and the channel phase-shift was estimated for the frequency range where the SNR of the reflected signal exceeded 10 dB. In Fig. 4.6, the resulting propagation velocity is depicted (dark grey), and the selected frequency range is indicated by vertical dashed lines.

The propagation parameters can only be estimated in the frequency range where the injected signal has sufficient energy. Outside this frequency range, the estimates have to be extrapolated in order to determine the parameters for the entire detection bandwidth. Generally, an approximation of the attenuation can be parameterized by $\alpha(\omega) \approx a\sqrt{\omega} + b\omega$ where the first term describes the skin-effect and the second term approximates conductor and dielectric losses, see Section 2.3. By estimating the polynomial coefficients in the observable frequency range, the attenuation can be extrapolated. As an example, the extrapolated attenuation is depicted (light grey) in Fig. 4.6 for the simulation experiment. The parameterized attenuation shows good agreement with the true attenuation. The propagation velocity $v_\mathrm{p}(\omega) \approx c_0/\sqrt{\varepsilon'_\mathrm{r}(\omega)}$ depends on the dielectric permittivity. As discussed in Section 2.3, various mechanisms determine the permittivity, which cannot be easily parameterized on a theoretical basis. However, the measurements presented in Section 2.3 could be approximated by a polynomial $\varepsilon'_\mathrm{r}(\omega) \approx a - b\sqrt{\omega}$. This empirical parametrization can be used to extrapolate the propagation velocity. As an example, the extrapolated velocity is

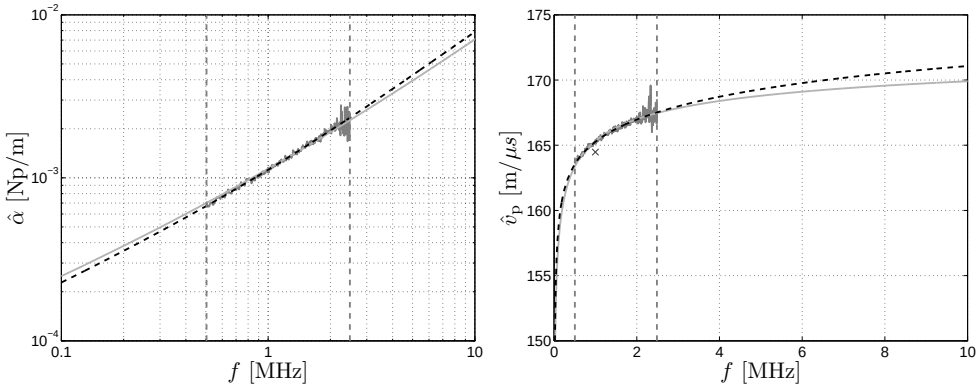

Figure 4.6 *Simulation of attenuation (left) and velocity (right) for a uniform cable. True values are depicted as black dashed lines, dark grey lines show parameters estimates, and grey lines show polynomial approximations of the estimates.*

depicted (light grey) in Fig. 4.6 for the simulation experiment. It can be observed that the extrapolation approximates the true velocity quite closely.

4.4.2 Composite Cable systems

In a composite cable system, various cable types can be present and their propagation properties may differ. If a cable section interface gives rise to an impedance transition, the injected signal is partly reflected at that point. At the near end, the transfer function of the excitation voltage and the reflection on the j-th section interface can be expressed as

$$H_{\mathrm{n,r}_j}(\omega) = T_{\mathrm{l_n}}(\omega)\, R_{j,j+1}\, e^{-\gamma_j(\omega)2l_j} \prod_{m=1}^{j-1} (1 - R^2_{m,m+1})\, e^{-\gamma_m(\omega)2l_m} \tag{4.26}$$

for $j = 1 \ldots M-1$. Likewise, at the far end, the reflection transfer function equals

$$H_{\mathrm{f,r}_j}(\omega) = T_{\mathrm{l_f}}(\omega)\, R_{j+1,j}\, e^{-\gamma_{j+1}(\omega)2l_{j+1}} \prod_{m=j+1}^{M-1} (1 - R^2_{m,m+1})\, e^{-\gamma_{m+1}(\omega)2l_{m+1}} \tag{4.27}$$

where j is counted from the near end. In Fig. 4.7 a schematic visualization of the impedance transitions encountered by excitation signal and the reflection on the j-th section interface is depicted. Combination of the reflected signals measured at both cable-ends provides information on the impedance transition. The ratio of these expressions and Eq. 4.10 equals

$$\frac{|H_{\mathrm{n,r}_j}(\omega)||H_{\mathrm{f,r}_j}(\omega)|}{|H_{\mathrm{n,f}}(\omega)||H_{\mathrm{f,n}}(\omega)|} = \frac{|R_{j+1,j}||-R_{j+1,j}|}{|1-R^2_{j+1,j}|} = \frac{R^2_{j+1,j}}{1-R^2_{j+1,j}}, \tag{4.28}$$

since $-1 \leq R^2_{j+1,j} \leq 1$ and $R^2_{j+1,j}$ is real. Now, without synchronization, the reflection coefficient at a section interface can be estimated,

$$\hat{R}^2_{j+1,j} = \frac{|H_{\mathrm{n,r}_j}(\omega)||H_{\mathrm{f,r}_j}(\omega)|}{|H_{\mathrm{n,r}_j}(\omega)||H_{\mathrm{f,r}_j}(\omega)| + |H_{\mathrm{n,f}}(\omega)||H_{\mathrm{f,n}}(\omega)|} \tag{4.29}$$

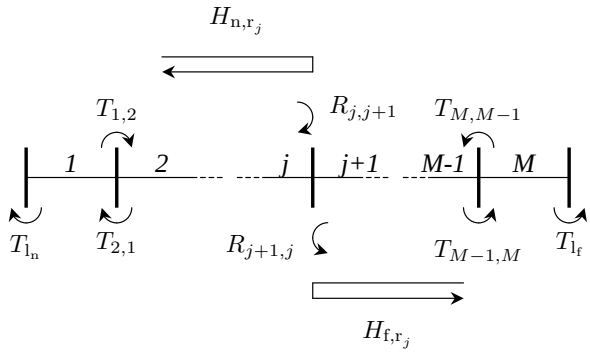

Figure 4.7 *Schematic visualization of impedance transitions encountered by a signal reflected in the j-th section interface in a cable with M sections. The reflection transfer function equals $H_{\mathrm{n,r}_j}$ in case of near-end injection and $H_{\mathrm{f,r}_j}$ in case of far-end injection.*

where the sign of the reflection coefficient equals the sign of $H_{\mathrm{n,r}_j}(\omega)/\hat{T}_{\mathrm{l_n}}(\omega)$.

Starting from the reflection on the first section interface, the attenuation $\alpha_1(\omega)$ of the first section can be obtained from the reflection transfer function, i.e.

$$\hat{\alpha}_1(\omega) = -\frac{1}{2l_1} \ln\left(\frac{|H_{\mathrm{n,r}_1}(\omega)|}{|\hat{T}_{\mathrm{l_n}}(\omega)||\hat{R}_{1,2}|}\right) . \tag{4.30}$$

Likewise, the phase shift per unit length can be estimated by

$$\hat{\beta}_1(\omega) = -\frac{1}{2l_1}\left(\angle H_{\mathrm{n,r}_1}(\omega) - \angle \hat{T}_{\mathrm{l_n}}(\omega)\right) . \tag{4.31}$$

If the sign of the reflection coefficient is negative, a phase shift of $\pi/2l_1$ is added to the expression. The maximum phase part of $\beta_1(\omega)$ should be estimated as discussed earlier.

When the propagation properties of the first cable section have been obtained, the procedure is repeated for the next section, and so on, until all parameter estimates are obtained. Clearly, the procedure can only be applied if reflections can be extracted. In practice, reflection coefficients at section interfaces can be small, and may not be detectable. In this case, only average propagation parameters can be measured by considering the system as (partly) uniform. Nevertheless, the study shows that in principle all signal model parameters of a composite cable system can obtained by evaluating the response of the system to a known excitation.

4.5 Experimental Validation

In order to validate the proposed methods, measurements were conducted on the experimental grid that was described in Section 1.3.4. Summarizing, the experimental set-up consisted of a 10 kV 3×95 mm^2 PILC cable of 96 m length and a 12.5 kV 3×95 mm^2 PILC cable of 201 m length. At one end the cable was terminated to a compact RMU, which contained a 100 kVA medium voltage distribution transformer.

At the other end the cable was terminated to an RMU with a 1000 kVA transformer. When the experiments were conducted, the extra cable was not yet made available; therefore no outgoing cables were connected to the RMUs. Although the cable system was not energized, for the purpose of model parameter measurements the experimental set-up effectively simulates an on-line situation.

The model parameter estimation methods described in the previous sections require that reflections can be separated in the time-domain. However, the cable length in the experimental set-up is relatively short; therefore oscillations in the excitation voltage are not completely damped when reflections on impedance transitions appear in the sensor signal. Note that in a more practical situation, outgoing cables are connected to at least one of the RMUs. In this case, oscillations will be damped much quicker, as a result of the additional real impedance introduced by an outgoing cable. In order to still test the proposed methods using the available experimental grid, two different experiments were conducted. In the first experiment, the cable terminals were disconnected from the RMU phase rails at each cable end, and connected to the ground rail. This situation is referred to as the off-line case. Now, the load impedances are mainly inductive, and the current is quickly damped after excitation, thus enabling the separation of pulses in the time-domain. In the low megahertz range, the load impedances are small with respect to the cable impedance. As a consequence, the reflected signals have relatively high SNR as compared to the on-line case, which is a benefit for reflection-based identification methods. Moreover, the disturbance levels in off-line measurements are significantly lower as compared to on-line measurements. The measurements obtained in the first experiment were used to estimate the propagation properties of the cable system, i.e. attenuation, velocity, and characteristic impedance of each of the two sections. In the second experiment, the cable terminals were connected to the RMU rails at each cable end. Now, the reflections on the cable section joint are mixed with the excitation signal. Moreover, the far-end reflections could not be clearly distinguished from the excitation. Consequently, in the on-line case, the transmission coefficient estimates are perturbed, as will be shown later on. In addition, the propagation properties obtained in this case equal a weighted average of the properties of the individual sections.

At each termination, a measurement and injection CT were clamped around the cable screen, past the last earth connection. Signals were injected using the custom-made transient generator and injection CT [Wie05]. Since the cable ends were located close to each other, signals could be recorded using a single 4-channel 14 bit 62.5 MSPS data acquisition card, and no synchronization was required. All estimation results presented in this section are obtained by averaging the results of approximately 200 measurements. Prior to the assembly of the cable system, the propagation parameters of the individual cable sections were obtained by pulse response analysis, as described in Section 2.3. Likewise, the propagation channel load impedances were obtained in a similar manner.

Off-line Measurements

Using the synchronized measurements obtained in the first experiment, Eq. 4.12 is evaluated, which enables estimation of the transmission coefficients at each cable end. In Fig. 4.8, solid grey lines show the estimated transmission coefficients in the frequency range where the reflected signals have sufficient energy. In order to validate the estimation procedure proposed for non-synchronized measurements, the sensor

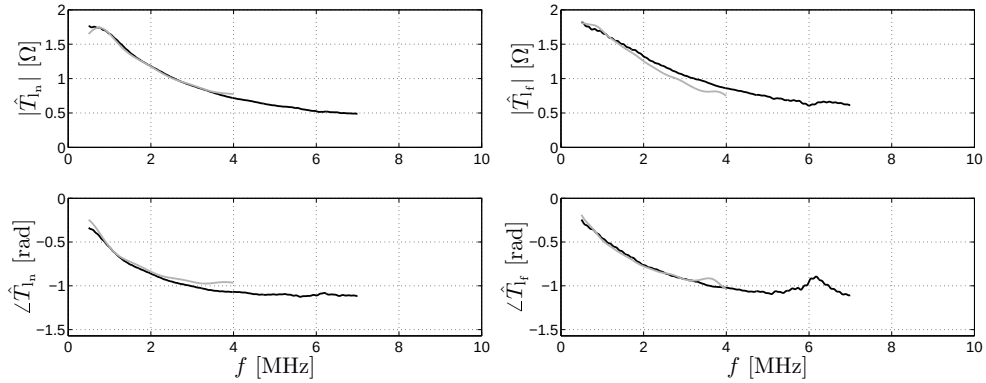

Figure 4.8 *Transmission coefficient estimates obtained from analysis of off-line measurements. The left and right-hand plot show the transmission coefficients at the cable terminations in RMU1 and RMU2, respectively. Grey lines show results from synchronized measurements and black lines show non-synchronized measurements.*

signals were deliberately shifted by arbitrary time periods. An iterative method was applied to estimate the characteristic impedances of the two sections. The transmission coefficients were obtained directly from the measured admittances using Eq. 4.5 and the characteristic impedance estimates. In Fig. 4.8, black lines show the transmission coefficient estimates obtained using the iterative method. The estimates closely approximate the results obtained from synchronized measurements.

After the transmission coefficients at the cable ends have been obtained, the reflection coefficient of the impedance transition at the cable section interface was obtained using Eq. 4.29. Subsequently, the propagation properties of the two cable sections were estimated by evaluating the reflected signals on the impedance transition. In the left-hand plot in Fig. 4.9, the estimated attenuation of each of the two cable sections is depicted (dashed lines) in the frequency range where the reflected signals have sufficient energy. The attenuation, obtained prior to the assembly of the cable system, is shown as a reference measurement (solid lines). In this particular case, the attenuation of the two sections was approximately equal. In the right-hand plot in Fig. 4.9, the estimated velocity of each of the two cable sections is depicted (dashed lines) in the frequency range where the reflected signals have sufficient energy. Solid lines represent reference measurements. The off-line experiment shows that the proposed methods result in good parameter estimates if reflections with sufficient energy are present that can be extracted from the sensor signals.

On-line Measurements

In the second experiment, the cable terminals were connected to the RMU rails at each cable end. Using the methods as described previously, the load transmission coefficients were estimated. In Fig. 4.10, the results are shown (dashed lines), as well as the reference measurements (solid lines). The reflected signals were mixed with the injected signal, which manifests itself as apparent oscillations in the transmission coefficient estimates. In addition, part of the discrepancy between the reference measurements and the on-line estimates can be ascribed to the difference in measurement methods. The reference measurements were obtained by directly connecting the mea-

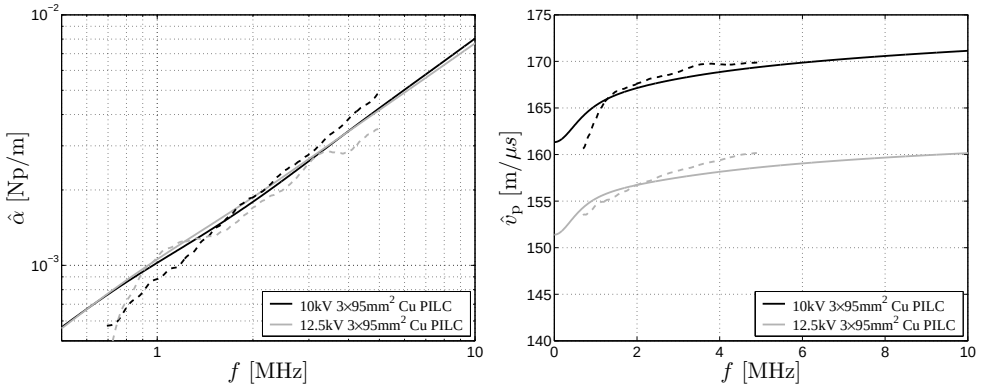

Figure 4.9 *Attenuation (left) and velocity (right) of the two sections of the test cable system obtained by the analysis of off-line measurements (dashed) and by reference measurements (solid).*

surement equipment to the RMU rails. Much care was taken to keep the connections as small as possible, and closely resemble the on-line situation. Despite of these efforts, the connection inevitably differs from the real cable termination in the on-line situation.

Since signals, reflected on the impedance transition at the section interface, could not be separated from the injection, the propagation properties of the individual cable sections could not be determined in the on-line case. Instead, the system was considered as a uniform cable, and the propagation properties were estimated by evaluating the transfer between the two cable ends using synchronized measurements. In Fig 4.11, the estimated attenuation and velocity are represented by dashed lines. The velocity estimate equals an average of the velocities of the individual sections, weighted according to the section lengths. In the right-hand plot in Fig 4.11, the reference velocities of the individual sections are depicted (grey) as well as the weighted average (solid black). In the left-hand plot, only the average attenuation is shown. Again, the reflected signals were mixed with the injected signal, which result in a perturbed measurement of the injected signal. The oscillations in the measured propagation properties are ascribed to this effect. Moreover, since the cable under test was short, the far-end reflection could not be properly separated from the injected signals, which also contributes to estimation errors. Nevertheless, it can be concluded that crude signal model parameter estimates can be obtained in this particular case.

4.6 Conclusions and Discussion

In this chapter, methods were presented that enable parameter estimation of the signal model of a cable connection. These parameters are important for the purpose of PD signal analysis, discharge location, as well as apparent charge estimation. The transmission coefficients at an RMU and the propagation properties of the cable system determine the waveshapes of PD signals that are to be expected. Moreover, the propagation velocity is required to locate PD sources.

By excitation of the cable system with a known signal and evaluating the response using sensors installed at each cable end, information on the propagation properties

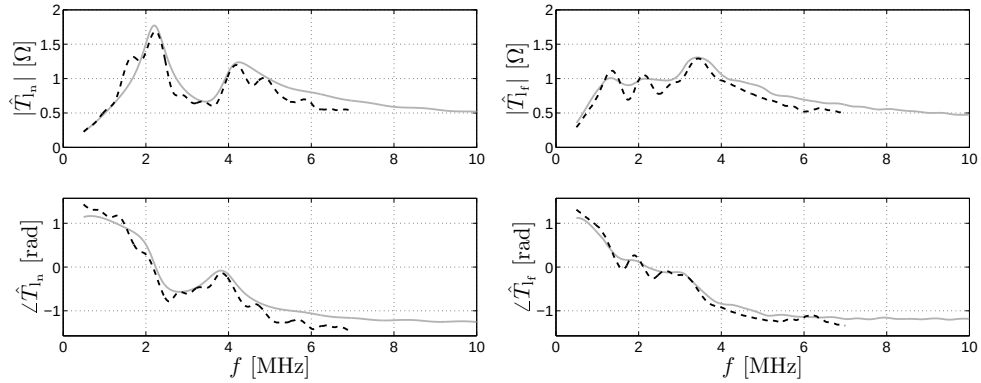

Figure 4.10 *Transmission coefficient estimates obtained from the analysis of on-line measurements. Dashed black lines show on-line estimates and grey lines show off-line reference measurements. The left and right-hand plot show the transmission coefficients at the cable terminations in RMU1 and RMU2, respectively.*

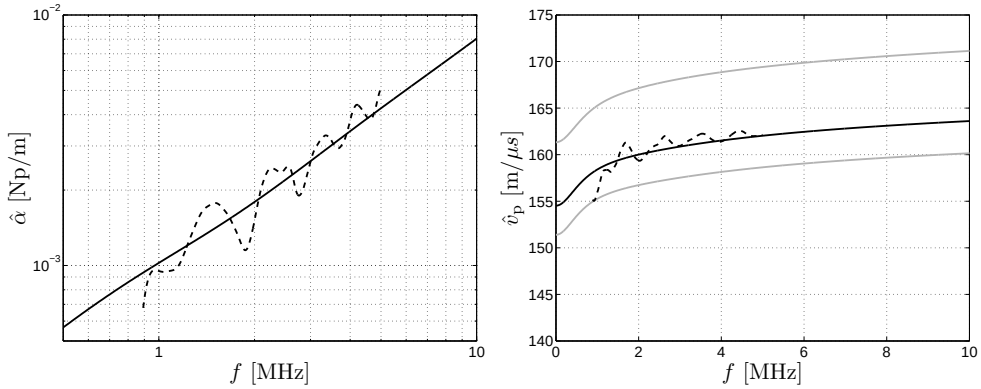

Figure 4.11 *Average attenuation (left) and average velocity (right) of the test cable system. Dashed lines show estimates obtained from the analysis of on-line measurements and solid lines represent reference measurements. In the right-hand plot the velocities of the individual sections are shown (grey) as obtained from reference measurements.*

can be obtained. The proposed methods rely on the extraction of signals that are reflected on impedance transitions within the cable system under test. Consequently, the injected and reflected signals must be separable, since exact parameter estimation from mixtures is generally not feasible. The study shows that, under this condition, all relevant signal model parameters of a composite cable system can be obtained by evaluating the response of the system to a known excitation.

When a signal is injected at a termination of the cable under test, the induced current is proportional to the transmission coefficient. Thus the transmission coefficient can be directly estimated up to a scaling factor, namely the characteristic wave impedance of the propagation channel. In this chapter, methods were presented to estimate the transmission coefficient or the characteristic impedance for various configurations. By evaluating the transfer from one cable end to the other, the channel propagation properties can be estimated. In a composite cable system, various cable

sections with differing attenuation and velocity may be present. It was shown that in principle the properties of the individual sections can be measured using signals reflected on the section interfaces.

Although accurate measurement principles were elaborated in this chapter, the procedures may not always be applicable in practice. If reflections on section interfaces within a composite cable system cannot be extracted, the propagation parameters of the individual sections cannot be estimated. However, generally average propagation parameters can be obtained by considering the system as uniform, as was shown by experiments. In practice, the estimates obtained from this simplification are still very valuable, since in many cases cable connections are composed of similar cable sections. From this respect, the experimental set-up can be regarded as a particular difficult case. If the injected signal and reflections on section interfaces are mixed, the estimated transmission coefficients are somewhat perturbed. However, the reflected signals have much lower energy than the injected signals. For this reason, the perturbations are relatively small and have minor impact on waveshape models.

Accurate knowledge of the channel delay and propagation velocity is essential for the purpose of partial discharge location. In an on-line situation, these parameters can only be estimated if either a reflection on the far cable end can be extracted or if the measurements are synchronized based on a reference, e.g. the global positioning system (GPS). From both a practical and an economical point of view, application of GPS is not preferred. However, as was shown by experiments, far-end reflections may not always be detectable. This problem can only be overcome by temporarily disconnecting the cable and performing propagation measurements on the off-line system.

It can be concluded that the methods proposed in this chapter, provide a range of possible procedures for signal model parameter estimation. Consequently, a different strategy for parameter estimation can be chosen depending on the specific measurement situation and the available equipment.

Chapter 5

Partial Discharge Signal Extraction

5.1 Introduction

Extraction of partial discharge (PD) signals from perturbed measurements has been extensively studied for many years (see e.g. [Shi00] and the references therein). Conventionally, PD signal extraction is performed by comparing a measured signal to some threshold. If the measured signal exceeds this threshold for a certain time interval, then a PD signal is presumed to be present. Since disturbance levels can greatly exceed PD signal amplitudes, this approach can generally not be applied to on-line PD detection. A number of general methods has been proposed for the purpose of extracting PD signals and increasing signal to noise ratios, such as wavelet-based denoising [Shi01, Sat03]. Another class of methods uses a generic waveshape template to extract PD signals by means of correlation techniques [Kna90, Ste92, Hes99] or frequency domain matching [Buc96, Ahm01]. In this chapter, a similar technique is discussed, which specifically utilizes the signal model of the cable under test. Since the shape of a PD signal is determined solely by the propagation channel, its load impedance, and the response of the detection circuit, filters can be constructed that match to the PD signals that are to be expected.

In this chapter, PD signal extraction by matched filtering is discussed, which is applicable to both on-line and off-line PD detection. Besides signal extraction, matched filters can also be applied to estimate PD apparent charge and signal arrival time. These parameters are crucial for the purpose of defect location and classification. In Section 5.2 partial discharge matched filtering and parameter estimation is studied and theoretical performance bounds are derived. In order to pursue semi-continuous monitoring of PD activity, efficient processing methods are presented in Section 5.3. Besides continuous periodic interference and noise, PD power cable diagnostics are also troubled by finite energy interferences. In Section 5.4, rejection techniques are proposed that effectively separate PD signals from finite energy interference. In order to verify the proposed methods, the algorithms are tested using computer simulated PD measurement data, and the results are presented in Section 5.5. Conclusions are given in Section 5.6.

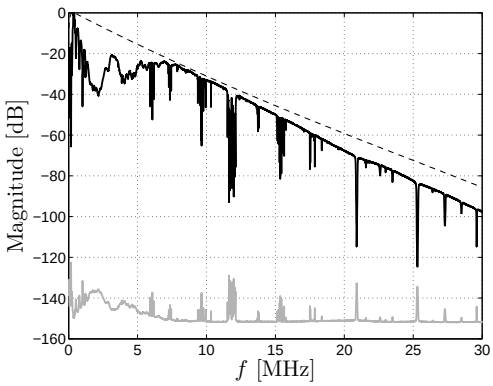

Figure 5.1 *Example of the transfer function magnitude of a matched filter (solid). The dashed line shows the amplitude spectrum of the PD signal model ($|S(f)|$). The grey line show the combined noise and interference power spectrum. The actual spectra were scaled in order to produce this plot.*

5.2 Partial Discharge Matched Filtering

A PD pulse originates with duration of at most a few nanoseconds; therefore the waveform that is measured at the cable end, approximates the impulse response of the channel through which the pulse propagates. Since the channel characteristics are constant during measurements, a PD signal can be regarded as being deterministic in shape. Matched filtering is a standard technique for detection of deterministic pulses in the presence of noise and the basic theory can be found in many textbooks (see e.g. [Tre68, Wai62]). The matched filter is optimal in the sense that the average signal to noise ratio (SNR) at the output of the filter is maximized, provided that the signal waveform and the noise spectral power distribution are known or can be estimated. In this section the application of matched filters to PD signal extraction and PD parameter estimation is discussed.

5.2.1 Definition

The PD matched filter transfer function for colored noise is given by definition as

$$H_{\mathrm{m}}(i\Delta f) = \frac{1}{\sqrt{P_N(i\Delta f)}} \frac{S^*(i\Delta f)}{\sqrt{P_N(i\Delta f)}} \tag{5.1}$$

where $S(i\Delta f)$ equals the discrete Fourier transform (DFT) of the measured PD signal and $P_N(i\Delta f)$ is the noise power spectral density function (PSDF). According to the model described in Section 2.5, a PD signal that has propagated through M different cable sections between the discharge site and the sensor, is expressed as

$$S(i\Delta f) = Z_{\mathrm{t}}(i\Delta f) H_{\mathrm{s}}(i\Delta f) \prod_{m=1}^{M} e^{-\gamma_m(i\Delta f) l_m} T_{m,m+1}(i\Delta f) \tag{5.2}$$

where l_m is the length of cable section m, $\gamma_m(i\Delta f)$ is the section propagation factor, and $Z_{\mathrm{t}}(i\Delta f)$ is the sensor transfer impedance. If the sensor is placed directly at the cable termination, the sensor transfer function $H_{\mathrm{s}}(i\Delta f)$ can be omitted. The

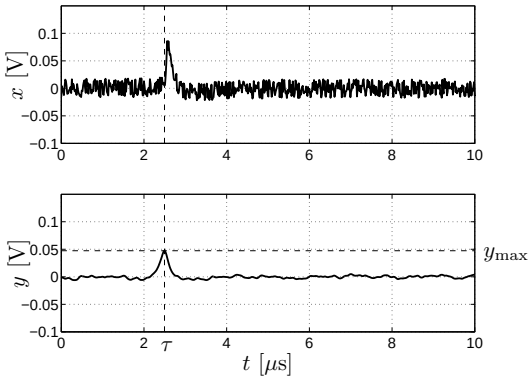

Figure 5.2 *Example of a PD signal corrupted by white noise ($x(t)$) with $\overline{\mathrm{SNR}}$ = 8 dB, which is applied to a matched filter. The maximum in the filter output signal ($y(t)$) occurs at the PD signal arrival time (τ). The maximum filter response ($y_{\max}$) is proportional to the PD magnitude.*

current transmission coefficients $T_{m,m+1}(i\Delta f)$ at section interfaces reduce to real scaling factors, since the channel characteristic impedances are real and constant. The transmission coefficient at the load impedance, denoted here as $T_{m,m+1}(i\Delta f)$, depends on the specific ring main unit (RMU) configuration. Without loss of generality, in this section only examples are given for real load impedances. The influence of the channel load impedance on PD signal extraction is studied in Section 5.5.

Eq. 5.1 can be interpreted as a cascade of a whitening filter and a whitened matched filter. The whitening filter flattens the noise spectrum and the whitened matched filter is matched to the signal as filtered by the whitening filter. The overall magnitude of the transfer function is directly proportional to the amplitude spectrum of the PD signal; therefore the optimal detector bandwidth is automatically selected. Furthermore, the transfer function is inversely proportional to the noise PSDF. Consequently, each frequency bin of the input signal is weighted corresponding to the single bin SNR, as depicted in Fig. 5.1. Frequency components with relatively high SNR contribute to the output signal to a large amount, while bins with low SNR do not. Thus the average SNR of the output signal is optimized regardless of the noise probability density function. Without loss of generality, in the remainder of this section only examples are given for additive white noise, thus the whitening filter reduces to a scaling factor. In Section 5.3, the whitening filter is discussed in more detail. PD signal extraction performance in the presence of disturbances with practical properties is studied in Section 5.5.

5.2.2 Partial Discharge Parameter Estimation

In addition to its noise suppressing capabilities, a matched filter provides a means to determine accurately some important PD parameters, as illustrated in Fig. 5.2. In this section, the quality of PD magnitude and PD arrival time estimation are discussed. Since time of arrival (TOA) estimation based on matched filters is bounded by the sampling grid, an interpolation scheme is applied to reduce estimation bias. In this section, parameter estimation quality is studied as a function of the channel transfer function as well as the sampling rate.

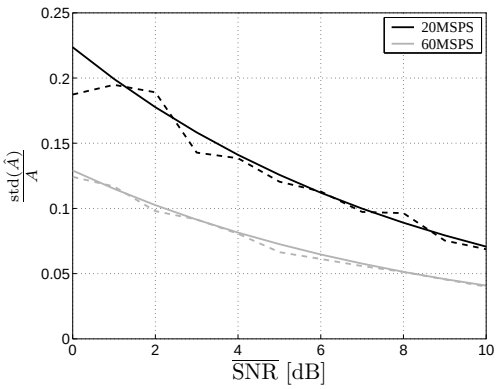

Figure 5.3 *Theoretical evaluation of PD scaling estimation standard deviation. Solid lines represent matched filter bounds and dashed lines represent simulation results.*

Partial Discharge Magnitude Estimation

At the discharge site, a PD signal can be considered as a Dirac pulse on the sampling grid, and the apparent charge can be modelled as

$$Q_{\text{app}} = 2AT_{\text{s}} \,, \tag{5.3}$$

where A is a scaling factor. A discharge results in a forward and backward propagating pulse; therefore the perturbed sensor equals

$$x(kT_{\text{s}}) = As(kT_{\text{s}}) + n(kT_{\text{s}}) \,. \tag{5.4}$$

Since the charge of a PD pulse is unknown, the filter (5.1) is matched to a scaled version of the actually measured pulse. The expected value of the maximum filter response $y(kT_{\text{s}})$ to the measured signal $x(kT_{\text{s}})$ equals

$$E\left\{y_{\max}\right\} = A\Delta f \sum_{i=0}^{B-1} \frac{|S(i\Delta f|^2}{P_N(i\Delta f)} \,. \tag{5.5}$$

Since the value of the summation is known a priori, i.e. the average noise power after filtering, the filter output provides an estimate $\hat{A}$ of the scaling factor. Using the signal model (Eq. 5.2), the apparent charge at the discharge site can now be determined from the scaling factor and the filter template. If the noise PSDF is known exactly, the estimate is unbiased. Moreover, if the noise probability density function is assumed to be Gaussian, the maximum-likelihood (ML) estimate is obtained from Eq. 5.5. The normalized estimation variance is expressed as (see Appendix C)

$$\frac{\text{var}\left(\hat{A}\right)}{A^2} = \frac{T_{\text{s}}}{T_0}\left(\frac{1}{B}\sum_{i=0}^{B-1}\frac{|AS(i\Delta f)|^2}{T_0 P_N(i\Delta f)}\right)^{-1} = \frac{T_{\text{s}}}{T_0}\frac{1}{\overline{\text{SNR}}} \,, \tag{5.6}$$

which equals the scaled inverse of the average single bin SNR.

As an example, PD pulses originating 1 km from the sensor within a typical 12.5 kV 3×95 mm^2 paper insulated lead covered (PILC) cable were simulated in additive white noise. In Fig. 5.3 the standard deviation of the normalized scaling

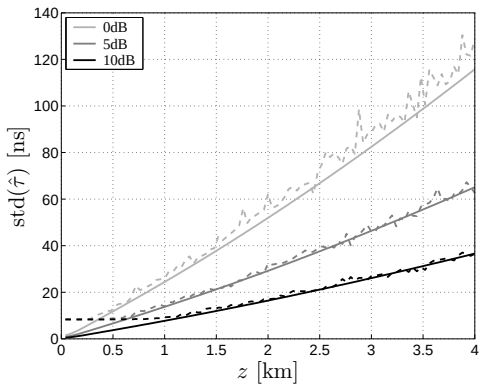

Figure 5.4 *Theoretical evaluation of TOA estimation standard deviation for a sampling rate of 60 MSPS. Solid lines represent Cramer-Rao lower bounds and dashed lines represent simulation results.*

factor estimates over 500 trial runs is plotted as a function of the average SNR, and for two typical sampling rates. It can be concluded that good estimates of the scaling factor are obtained using matched filters. Moreover the estimation variance can be theoretically predicted by Eq. 5.6.

Partial Discharge Time of Arrival Estimation

When a PD signal is applied to a matched filter, the time-instant at which the maximum output occurs provides an estimate of the PD signal arrival time. Since the filter output is computed at the sampling moments, a biased estimate of the time of arrival is obtained. If the additive noise is assumed to be Gaussian and zero-mean, the TOA estimation variance is bounded by the Cramer-Rao lower bound (see e.g. [Tre68]). For a measured PD signal $x(kT_\mathrm{s}) = As(kT_\mathrm{s} - \tau) + n(kT_\mathrm{s})$ the Cramer-Rao lower bound (CRLB) equals (see Appendix C)

$$\mathrm{var}\,(\hat{\tau}) \geq \frac{T_\mathrm{s}}{T_0}\left(\frac{1}{B}\sum_{i=0}^{B-1}(2\pi i\Delta f)^2\frac{|AS(i\Delta f)|^2}{T_0 P_N(i\Delta f)}\right)^{-1}, \tag{5.7}$$

which equals a weighted average of the single bin SNRs. Thus signal components of relatively high frequency and SNR contribute more to estimation variance reduction than low frequency signal components. Likewise, the maximum filter output provides a biased estimate of the PD magnitude, and thus Eq. 5.6 equals the CRLB on the estimation variance, as shown in Appendix C.

As an example PD pulses originating along the length of a 4 km long 12.5 kV 3×95 mm^2 PILC cable and sampled with 60 MSPS were simulated in white noise for different average SNR. The standard deviation of the TOA estimates from 500 trials are plotted in Fig. 5.4. Clearly, the statistical averages of the TOA estimations correspond to the theoretical bound. The figure shows that for long propagation paths the estimation variance can increase to a large extent, particularly for low average SNR.

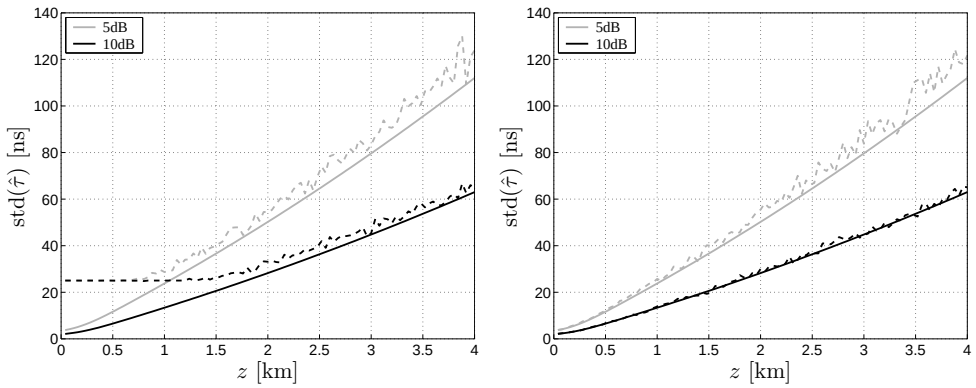

Figure 5.5 *Theoretical evaluation of matched filter TOA estimation variance (left) and estimation standard deviation in case of matched filter output interpolation (right) with a sampling rate of 10 MSPS. Solid lines represent Cramer-Rao lower bounds and dashed lines represent simulation results.*

Matched Filter Output Interpolation

In Fig. 5.5, simulation results are plotted in case the sampling rate equals 10 MSPS. In the simulations, the value of τ was chosen equal to half the sampling period, namely 50 ns. Consequently, the matched filter approach results in biased TOA estimates. The estimation mean error equals zero, since the distribution is uniform among the closest sampling moments. However, the estimation standard deviation is lower bounded by a quarter of the sampling period, as depicted in the left-hand plot. The estimation variance can be reduced by local interpolation of filter output samples close to the maximum output. For instance, a TOA estimate can be determined as a fraction of the sampling period by upsampling the matched filter output. For reasonable sampling rates it can be stated that the filter output is convex near the maximum. Therefore in principle, the estimation bias can be reduced arbitrarily by searching for the ML TOA estimate using iterative maximization algorithms. For example, an interval method can be applied which decreases the time-interval in which the filter maximum is known to occur. First the sampling period between the two highest matched filter output values is defined as the initial interval. Then the output value in the middle of the interval is computed by inverse Fourier transformation

$$y(t) = \Delta f \sum_{i=0}^{B-1} X(i\Delta f) H_{\mathrm{m}}^{*}(i\Delta f) e^{+j2\pi i \Delta f t} \; . \tag{5.8}$$

Subsequently, the new interval is chosen between the time instants at which the two highest values appear on the previous interval. The process is iterated until a desired accuracy is obtained. The right-hand plot in Fig. 5.5 shows the results of the application of this interpolation method. In addition to ideal interpolation, the matched filter output can be interpolated by fitting a parabola on the maximum filter response. The apex of the parabola provides an approximate estimate of the PD signal arrival time.

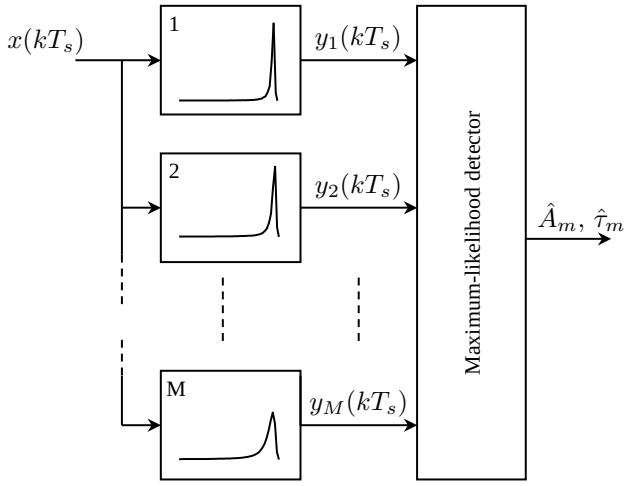

Figure 5.6 *Schematic visualization of a bank of M filters, matched to PD signals with various distances propagated. The matched filter bank is followed by a maximum likelihood detector, which determines the most likely filter and selects the signal parameters accordingly.*

5.2.3 Matched Filter Bank and Maximum-Likelihood Detection

Partial discharges originate from various locations within the cable under test, resulting in an equal variety of signal waveforms at the sensor(s). For this reason, the measurement system must employ multiple matched filters, as illustrated in Fig. 5.6. Theoretically, the diversity of waveforms is infinite since there exists an infinite number of possible PD locations. As mentioned, pulse shapes do not differ appreciably for PD signals originating close together, especially when the propagation distance is long. As a consequence, a finite set of signal templates is sufficient to match every possible PD waveshape from the cable system.

Applying a measured signal to a bank of matched filters results in multiple output signals. In order to select the best matching filter, a proper test statistic is required. Under the assumption that the additive noise has a Gaussian probability density distribution with zero mean, maximum-likelihood theory can be applied to obtain a test statistic (see e.g. [Moo99, Tre68]). The a posteriori likelihood of the m-th matched filter is expressed as

$$L(S_m) = \Delta f \sum_{i=0}^{B-1} -\frac{|X(i\Delta f) - \hat{A}_m S_m(i\Delta f) e^{+j2\pi i \Delta f \hat{\tau}_m}|^2}{2P_N(i\Delta f)} \tag{5.9}$$

where $\hat{A}_m$ and $\hat{\tau}_m$ equal the scaling factor estimate and time of arrival estimate obtained from the matched filter output. The equation expresses the likelihood that the matched filter, based on signal template $s_m(kT_\mathrm{s})$, was observed in the measurement $x(kT_\mathrm{s}) = As(kT_\mathrm{s} - \tau) + n(kT_\mathrm{s})$. Since the same signal $x(kT_\mathrm{s})$ is applied to all matched filters, the likelihood can be simplified as

$$L(S_m) = \hat{A}_m y_{m,\max} - \tfrac{1}{2}\hat{A}_m^2 \Delta f \sum_{i=0}^{B-1} \frac{|S_m(i\Delta f)|^2}{P_N(i\Delta f)} \tag{5.10}$$

where $y_{m,\max}$ equals the maximum response of the m-th matched filter, viz.

$$y_{m,\max} = \Delta f \sum_{i=0}^{B-1} \frac{\mathrm{Re}\{X(i\Delta f) S_m^*(i\Delta f) e^{+j2\pi i \Delta f \hat{\tau}_m}\}}{P_N(i\Delta f)} \; . \tag{5.11}$$

Thus the modified likelihood equals the scaled maximum filter output biased by a term related to the average SNR. Considering the test statistics of M matched filters in the bank, a maximum-likelihood detector must decide which filter has maximum probability, i.e.

$$m = \arg\max_m \; L(S_m) \tag{5.12}$$

for $m = 1 \ldots M$. Note that the maximum response of one filter does not necessarily occurs synchronously to the maximum response of another filter. For this reason, the filter outputs must be evaluated on a certain time interval. When the best matching filter has been selected using the decision criterion (5.12), the corresponding scaling factor and time of arrival estimates equal the best possible PD signal parameter estimates and are used for further computations.

In practice, multiple PD signals can be present in the sensor signal; therefore the detector must employ a threshold device to correctly extract PD signals. For each matched filter, the threshold can be selected by evaluating the average noise power in the filter output signal, given by

$$\sigma^2_{N_{ym}} = \Delta f \sum_{i=0}^{B-1} P_N(i\Delta f) |H_{\mathrm{m},m}(i\Delta f)|^2 \tag{5.13}$$

where $H_{\mathrm{m},m}(i\Delta f)$ equals the transfer function of the m-th matched filter, based on signal template $s_m(kT_\mathrm{s})$. Assuming that the noise is Gaussian, 98% of the filtered noise absolute sample values do not exceed $3\,\sigma_{N_y}$, which can be applied as a threshold. Note that for each filter a different threshold applies.

5.2.4 Signal Template Selection

Due to additive noise, the variance of the a posteriori likelihood can result in errors as the maximum-likelihood detector selects the wrong filter. If the probability of error is large, PD waveforms corresponding to subsequent matched filters cannot be distinguished with sufficient reliability. As a consequence, the resulting PD signal parameter estimates could have been obtained with equal accuracy using a smaller set of filters. Given the partial discharge signal model (5.2), appropriate signal templates can be selected such that the error probability does not exceed some acceptable value.

The probability that a filter adjacent to the correct filter has maximum response largely determines the overall error probability, and can be regarded as a lower bound. For example, consider two normalized signal templates $S_1(i\Delta f)$ and $S_2(i\Delta f)$, corresponding to PD location z and $z + \delta z$, respectively. Assuming additive white noise, the maximum-likelihood decision criterion (5.12) reduces to a test statistic based only on the maximum matched filter outputs, i.e.

$$\Phi = y_{1,\max} - y_{2,\max} \; . \tag{5.14}$$

When a signal originating from location z is applied to the filters $\Phi > 0$, and $\Phi < 0$ for a signal from $z + \delta z$. Under the additive white Gaussian noise assumption, Neyman-Pearson theory for binary hypothesis testing can be applied (see e.g. [Moo99, Tre68]).

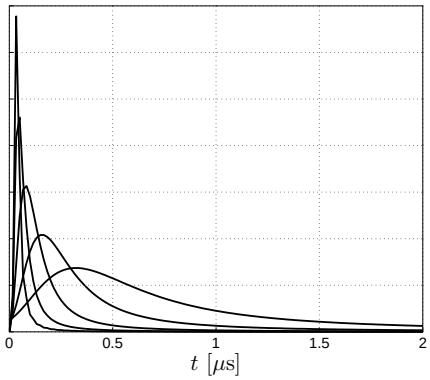

Figure 5.7 *Matched filter bank templates for a 4 km long 12.5 kV 3×95 mm² PILC cable, corresponding to propagation path lengths of 70 m, 170 m, 380 m, 860 m, and 1900 m.*

The error probability is expressed as

$$p_{\mathrm{E}} = Q\left(\sqrt{\frac{1}{2}\frac{T_0}{T_{\mathrm{s}}}\overline{\mathrm{SNR}}\,(1-\varphi_{\max})}\right) \tag{5.15}$$

where the Q-function is defined as $Q(x) = \int_x^\infty \frac{1}{\sqrt{2\pi}} e^{-y^2/2}\,dy$. The maximum cross-correlation coefficient of the two normalized signal templates equals

$$\varphi_{\max} = \Delta f \sum_{i=0}^{B-1} \mathrm{Re}\Big\{S_1(i\Delta f)S_2^*(i\Delta f)e^{+j2\pi i\Delta f(\tau_2-\tau_1)}\Big\} = T_{\mathrm{s}} \sum_{k=0}^{B-1} s_1(kT_{\mathrm{s}})s_2(kT_{\mathrm{s}}-\tau_2+\tau_1)\ .$$

As an example, in Fig. 5.7 matched filter bank (MFB) templates are plotted for a typical 12.5 kV 3×95 mm² PILC cable of 4 km length and real load impedances. The filters were chosen such that the error probability for two successive filters equals 10^{-3} for PD pulses contaminated in white noise with 5 dB average SNR and sampled with 60 MSPS. Note that the length steps between the signal templates are approximately exponentially distributed, since the spectrum of a PD signal (Eq. 5.2) is an exponential function of the propagated distance.

5.3 Efficient Matched Filter Bank Implementation

In order to achieve semi-continuous monitoring of PD activity, an efficient implementation of the PD MFB is of interest. As follows from the matched filter definition (Eq. 5.1) and signal template model (Eq. 5.2), a matched filter bank can be implemented as a cascade of filters applicable to all templates and a parallel filter bank corresponding to individual PD pulse shapes. The first common filter is the whitening filter, followed by the conjugated sensor transfer impedance, load impedance transmission coefficient, and sensor position transfer function. Instead of a direct implementation of the whitening filter based on an estimate of the noise PSDF, in this section a more efficient implementation is pursued. Signals from subsequent discharge locations partly propagate through the same path. This property can be exploited by implementing the parallel filter bank as a cascade.

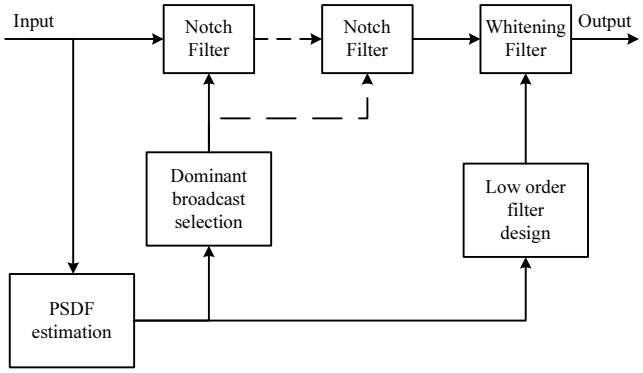

Figure 5.8 *Efficient implementation of the whitening filter as a cascade of recursive notch filters and a low order FIR whitening filter.*

5.3.1 Whitening Filter

As illustrated by the tentative disturbance measurements, noise as well as radio broadcasts can be considered stationary with respect to multiple cycles of the grid operating voltage. Consequently, estimates of the noise and periodic interference PSDF are simultaneously obtained by the averaged periodogram [Kay88]

$$\hat{P}_N(i\Delta f) = \frac{\Delta f}{M} \sum_{m=1}^{M} |N_m(i\Delta f)|^2 \tag{5.16}$$

where $N_m(i\Delta f)$ is the i-th DFT coefficient of the m-th noise observation and M equals the total number of observations. In practical measurements, the noise and periodic interference cannot be observed without PD signals and finite energy disturbance. However, if a number of instantaneous power spectrum estimates is averaged, the contribution of finite energy signals to the PSDF estimate is negligible.

Evidently, a whitening filter can be realized directly by designing a finite impulse response (FIR) filter with transfer function corresponding to the inverse of the averaged periodogram. Thus effectively, the broadband background noise is whitened, whereas dominating radio broadcasts are suppressed. Since PD signals can have large bandwidths, the whitening filter should be wide-band, while having narrow stop bands at the disturbing radio broadcast carrier frequencies. However, wide-band transversal filters with narrow notches cannot be designed with reasonable filter lengths. For instance, if the Parks-McClellan filter design algorithm is applied [Par72], which is available in many mathematical software packages, these stringent conditions can lead to filter lengths in the order of several thousands of sampling intervals, depending on the tolerated transfer function approximation errors. Evidently, such filters have high computational loads and are not preferred. More practical FIR filters can be designed by relaxing the transfer function constraints; e.g. by widening the notches or decreasing attenuation in the stop band. However, this approach will inevitably lead to unnecessary PD signal energy loss or insufficient interference rejection.

In the literature, several methods are presented aiming at reduction of noise as well as narrow-band interference suppression by forward linear prediction [Bor92, Sch94a, Köp95]. Exploiting the correlation that exists between continuous distur-

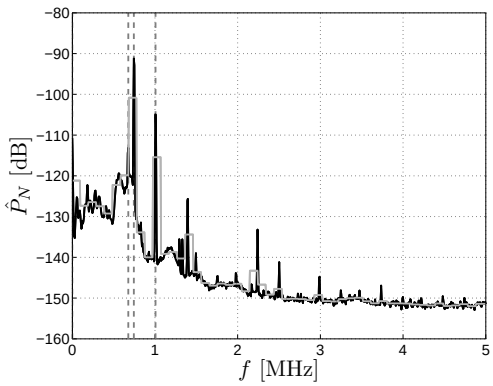

Figure 5.9 *Dominant carrier frequencies (dashed lines) are identified by comparing the averaged periodogram (black) to its smoothed version (grey).*

bance samples, adaptive low order FIR filters are applied to estimate sample values from previous samples. The estimates are then subtracted from the actually measured data in order to minimize continuous interference, thus effectively whitening the measurement [Wid85]. Ultimately, adaptive filters should converge to a solution that is optimal, no matter what steering algorithm is applied. In the context of periodic interference rejection for PD detection, optimality implies a wide-band all-pass filter with very narrow notches at the disturbing broadcast frequencies. Consequently, an adaptive FIR filter of low order cannot converge to an optimal solution. In addition, adaptation of the filter coefficients is influenced by the presence of PD signals and finite interferences in the measurement data. In order to overcome this problem, it has been suggested to use a PD signal free measurement as a training set to obtain the prediction filter coefficients [Köp95]. Then a time-varying prediction filter is applied to the measurement data. This approach is highly impractical if automated PD extraction is pursued.

In principle, a high order transversal implementation is required in order to obtain the desired whitening filter transfer function. A more efficient implementation can be achieved by realizing the whitening filter as a cascade of multiple recursive filters or adaptive cancellers for radio broadcast rejection, followed by a low order FIR filter for whitening of broadband background noise. In Fig. 5.8 this concept is schematically visualized. Dominating narrow-band interference can be distinguished from background noise by comparing a high resolution periodogram to a low resolution periodogram, which acts as a basis for thresholding. For example, in Fig. 5.9 an averaged periodogram and its smoothed version are depicted. For clarity, only a small frequency range is depicted, but the method is applicable to the entire detection bandwidth. The frequency domain resolution Δf of the original periodogram was chosen such that radio broadcasts with small transmission bandwidths are clearly resolvable. Dominant carrier frequencies were selected that sufficiently exceed the smoothed periodogram. Since the interference characteristics are slowly time-varying, the selected notch frequencies and bandwidths, and the background noise whitening filter do not have to be updated frequently. For example, change detection of the average disturbance power can be used as a decision criterion for filter coefficient update.

Recursive filters are already employed to reject dominating radio broadcasts in PD

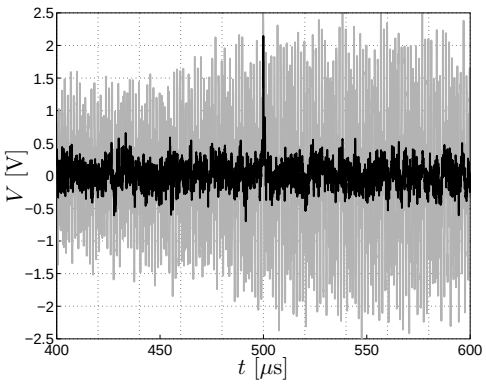

Figure 5.10 *Simulated matched filter output signals with a low order transversal whitening filter (grey) and with a cascade of recursive notch filters and a low order transversal whitening filter (black).*

measurements (see e.g. [Nag93, Du94a]). Infinite impulse response (IIR) filters offer a distinctive advantage over FIR filters, since interference rejection can be achieved at substantially lower filter orders. The design of IIR notch filters has been extensively studied in the literature, and many realizations exist (see e.g. [Mit98]). Unlike linear phase FIR filters, recursive filters introduce phase distortion. However, since the phase non-linearity merely occurs in the notch frequency range, the distortion hardly affects PD signals and can be disregarded. Alternatively, cancellation of radio broadcasts can be achieved by substraction of synthesized interferences from the measured signal. In this approach, a reference signal is obtained by local generation of the broadcast carrier signals. The instantaneous amplitude and phase of the interfering broadcasts are estimated using an adaptive algorithm which compares the reference signal to the measured signal. Effectively, cancellation is equivalent to IIR notch filtering if a stochastic gradient adaptation is applied [Wid85].

Clearly, the performance of the whitening filter depends on the disturbances present in the measurements, and general statements cannot be made. As an illustrative example in Fig. 5.10 simulation results are depicted as a comparison of the efficient whitening filter implementation to a straightforward transversal implementation. In the simulation, a PD signal contaminated by colored noise was simulated. Large radio broadcasts with carrier frequencies within the PD signal bandwidth were added with signal to periodic interference amplitude ratio (SPIAR) equal to one half in order to resemble practical measurements. The simulated sensor signal was applied to an efficient whitening filter followed by a matched filter to produce the black output signal. The efficient whitening filter consisted of a cascade of appropriate second order IIR notch filters and an FIR whitening filter of 128 filter taps. In addition, the signal was applied to a cascade of a straightforward 128 taps FIR whitening filter and the matched filter to produce the grey signal. Clearly, the straightforward FIR whitening filter does not result in the same interference suppression as compared to the cascade of IIR notch filters and an FIR whitening filter. In fact, equal disturbance rejection could only be achieved with an FIR filter with four times as many coefficients. It can be concluded that the proposed whitening filter implementation is more efficient as compared to a straightforward FIR implementation, when narrow-band interfer-

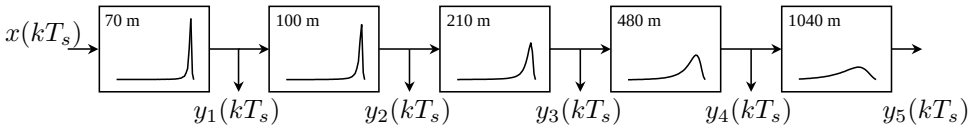

Figure 5.11 *Schematic visualization of a cascade MFB implementation, with templates corresponding to total propagation path lengths of 70 m, 170 m, 380 m, 860 m, and 1900 m.*

ence is present. Note that in practice, FIR whitening filters of much lower order can be designed, and the filter length of 128 chosen here only serves as an illustrative example.

5.3.2 Cascade Matched Filter Bank

A matched filter bank can be implemented as a cascade of filters applicable to all templates and a parallel filter bank with individual PD pulse shapes. Filter templates corresponding to subsequent discharge locations are related, since PD signals from different locations partly propagate through the same path. This property can be exploited by implementing the parallel MFB as a cascade. The distance between two locations is shorter than the distance of the furthest location to the sensor, as visualized in Fig. 5.11. Time-domain pulse spread is proportional to the amount of dispersion and attenuation introduced by the channel, and thus to the propagation path length. As a consequence a cascade matched filter bank requires fewer filter coefficients than a parallel implementation.

In order to quantify the computational complexity of both filter bank realizations, a definition of pulse start and duration is required, such that the filter template length is properly defined. Since a propagation channel can be considered as a low-pass filter, the channel impulse response is spread in time accordingly. Moreover, signal components with high frequencies travel at a higher speed through the cable as compared to low frequency components. Therefore the appropriate channel delay is obtained using the propagation velocity at some maximum frequency component. The channel transfer function bandwidth is defined by evaluating the energy in each frequency bin compared to the maximum energy, i.e. at DC. If the low-pass filter is approximated by a rectangular transfer function, the time-domain spread equals the main lobe width of the corresponding sinc-function. Now, the resulting channel delay is expressed as

$$t_\mathrm{s} = \frac{z}{v_\mathrm{p}(f_\mathrm{max})} - \frac{1}{2f_\mathrm{max}} \tag{5.17}$$

where f_max equals the highest frequency component with sufficient energy. Since the delay is not necessarily an integer multiple of the sampling period, a signal template starting at t=0 is obtained by shifting the channel transfer function in the frequency domain

$$S_\mathrm{t}(i\Delta f) = e^{j2\pi i\Delta f t_\mathrm{s}} e^{-\gamma(i\Delta f)z} \tag{5.18}$$

where for simplicity a single cable section is considered here. The signal duration is defined by selecting part of the impulse response that exceeds a threshold related to the time-domain maximum.

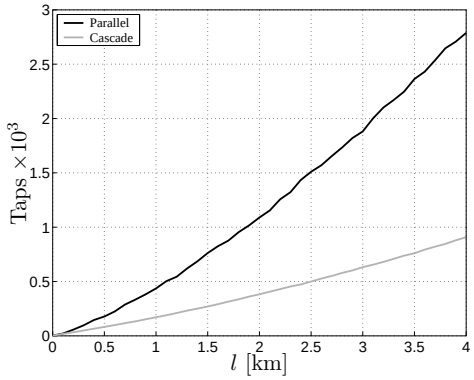

Figure 5.12 *Total number of filter taps required by a parallel (black) and a cascade (grey) MFB implementation as a function of the cable length.*

As an example, in Fig. 5.12 the total number of filter taps required by a parallel and a cascade MFB implementation are depicted as a function of the cable length for a typical 12.5 kV 3×95 mm^2 PILC cable. The templates were chosen such that the error probability for two successive filters equals 10^{-3} for PD pulses sampled with 60 MSPS and contaminated in white noise, with average SNR of 5 dB. The template length is defined by considering only sample values that exceed 1% of the template maximum. Each filter bank realization can have a different number of filters; therefore the y-axis of the figure represents the summation of the total number of filter taps of all filters in the bank. Clearly, the cascaded MFB implementation is more efficient than the straightforward parallel realization, particularly for long cables.

5.4 Finite Energy Interference Rejection

Generally, finite energy disturbances are coupled into the cable system under test at unshielded high voltage (HV) equipment within an RMU. In addition, disturbances may be picked up or generated elsewhere in the grid and propagate to the cable under test. The tentative disturbance measurements indicate that basically two types of finite energy interferences can be distinguished based on their spectral energy distribution. Firstly, bandlimited disturbances from e.g. power electronic devices are frequently encountered. Secondly, broadband interferences such as PD signals from other high voltage equipment than the cable system under test are commonly present.

In the literature, algorithms are proposed for elimination of repetitive finite energy interferences based on their periodicity [Köp95]. In the tentative on-line measurements performed in the Netherlands, clear periodicity of finite energy interference was not observed and repetition rates tend to deviate in the order of tens to hundreds of microseconds, as discussed in Chapter 3. For this reason, repetition rates can generally not be used to discriminate interference from PD signals in on-line PD measurements. In the off-line case, the local field strength at a defect is directly proportional to the alternating voltage that energizes the cable. Therefore partial discharge excitation is related to the operating voltage phase angle. Based on the occurrence of PD signals with respect to the phase angle, discrimination from finite energy disturbance disturbance can be achieved to a certain extent [Bor95, Kre64, Tan95]. As discussed in

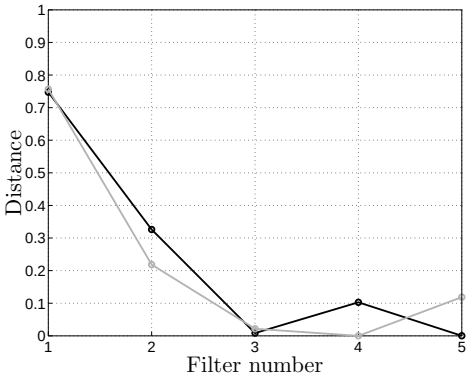

Figure 5.13 *Normalized Euclidean distances for MFB responses to narrowband finite energy disturbances with center frequencies of 700 kHz (black) and 2 MHz (grey). Filter numbers refer to templates in Fig. 5.7.*

Chapter 2, in the on-line case, the field strength at a defect is not necessarily related to an externally observable quantity, and these methods can generally not be applied. Nevertheless, bandlimited finite energy interference can be distinguished from PD signals based on the difference in waveshapes.

In principle, optimal rejection of bandlimited interferences is achieved by adding filter templates to the signal MFB that match the disturbance waveforms. In practice, such templates cannot be obtained beforehand, since disturbance characteristics can vary with time as well as among measurement situations. However, a matched filter bank can be considered as a signal decomposition tool, and the bank will respond differently to narrowband finite energy interference compared to PD signals. This a priori knowledge can be exploited by adding expertise to the correlation detector. When a maximum is detected within the MFB output signals, the expected response of the other filters can be predicted based upon the signal model. By comparing a measured response pattern to the predicted pattern, a decision criterion can be implemented in order to distinguish wideband and narrowband finite energy signals. For example, the normalized Euclidean distance can be used as a PD probability measure, which is given by

$$d_m = \frac{|y_m(kT_\mathrm{s}) - y_{m,\mathrm{exp}}(kT_\mathrm{s})|}{|y_{m,\mathrm{exp}}(kT_\mathrm{s})|} \tag{5.19}$$

where $y_m(kT_\mathrm{s})$ is the output value of the m-th filter and $y_{m,\mathrm{exp}}(kT_\mathrm{s})$ is the expected value, based on the overall maximum of all filter outputs. As an example in Fig. 5.13, the distances between MFB responses and the expected values are plotted per filter output for typical finite energy interferences. The filters are chosen equivalent to the templates in Fig. 5.7 and ordered with ascending propagation path length. The black circles show the computed distances in case of a disturbing signal with a center frequency of 700 kHz and 100 kHz bandwidth. Since the spectral energy distribution is concentrated in the low frequency range, the last filter gives the maximum response. The expected maximum responses of the matched filters to a PD signal from this part of the cable result in the distances presented in the plot. Likewise, the grey circles show the distances in case of a disturbing signal with a center frequency of 2 MHz and 300 kHz bandwidth.

By evaluating the distances between the filter responses and the expected responses, the maximum-correlation detector can assign a confidence measure to the results or reject extracted signals. It should be noted that instead of simply observing the matched filter outputs at a single time-instant, the outputs can also be evaluated on a certain time-interval in order to increase decision reliability. Once a bandlimited finite energy disturbance has been identified, an additional filter bank template can be created based on the measured waveform in order to reject recurrences of similar interferences.

PD signals originating from the cable under test and broadband interferences, such as PD signals from other cable systems or HV equipment have similar signal characteristics. As a consequence, broadband finite energy disturbances cannot be distinguished from PD signals based on signal waveforms. If synchronized sensor signals are obtained at each cable end discrimination is possible by estimating the arrival times of finite energy signals at each sensor. In addition, a directional sensing method as described in Section 3.2.3 can be applied by shield-to-phase channel measurement simultaneously at the cable termination and the transformer cables.

5.5 Simulation Results

In this section, typical on-line measurement situations are simulated based on the signal and disturbance characteristics observed in the tentative measurements. Subsequently, the ability of the proposed methods to extract PD signals and signal parameters from artificial sensor signals is tested. In addition, finite energy interference rejection by difference in time of arrival discrimination is evaluated. Evidently, the performance of the proposed methods depends to a large extent on the specific characteristics of the cable system under test, the disturbance present in the measurements, as well as the quality of the signal model. Therefore it should be noted that the simulation experiments only serve as illustrative examples.

5.5.1 Simulation Description

The PD signal extraction and parameter estimation performance of the proposed methods was tested using simulated sensor signals as if obtained in typical on-line field measurement situations. The signal model as described in Chapter 2 was implemented in Matlab, thus enabling simulation of PD signal waveforms originating from any location within a test cable system. The model parameters were obtained by measurements as described in Chapter 2. A 4 km long cable system was modelled consisting of 20 sections of 200 m long PILC cable, which was terminated to an RMU at both ends. The odd sections were 12.5 kV 3×95 mm^2 PILC cables and the even sections were 10 kV 3×95 mm^2 PILC cables. Typical noise and disturbances were simulated with characteristics based on the tentative measurements as presented in Chapter 3. Radio broadcasts were simulated by amplitude modulation of stochastic processes with transmission bandwidths and carrier frequencies similar to the broadcasts observed in the tentative measurements.

In the simulations, both the RMU configurations and the noise characteristics were varied. In experiment 1 and 2, both RMUs contained a distribution transformer and two cable terminations. Thus besides the cable under test, another cable was terminated to an RMU. This configuration is typical for MV distribution networks

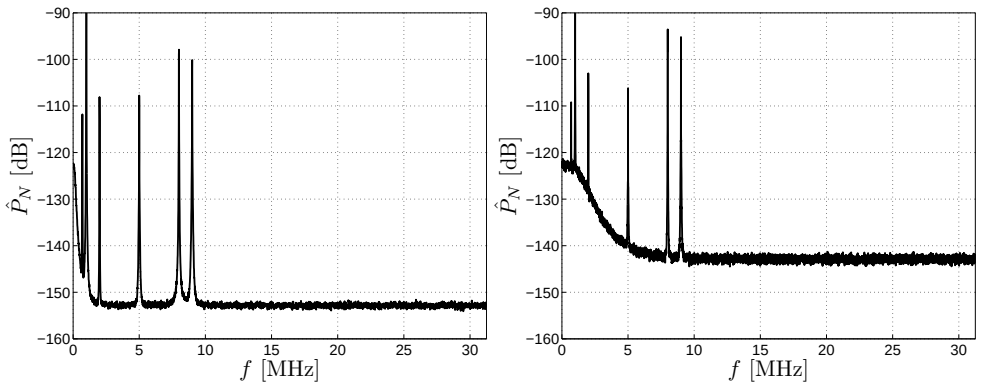

Figure 5.14 *Estimated power spectral density functions of simulation experiment 1 and 3 (left), and experiment 2 and 4 (right).*

with a ring topology, as frequently employed in the Netherlands. At one RMU within a ring distribution network, the ring is interrupted and the two cables are not interconnected. In experiment 3 and 4, this situation is simulated using the same configuration as described above, except for one RMU, where only a distribution transformer is present. The load impedances used in the simulations, were taken from [Wag03]. In experiment 1 and 3, noise and disturbances were simulated with equal characteristics. In experiment 2 and 4, again equal noise characteristics were simulated, but different from experiment 1 and 3. In Fig. 5.14, the estimated PSDF of the noise and continuous periodic interferences are depicted for both situations.

In each case, partial discharges with various magnitudes were simulated, originating from locations equidistantly distributed along the cable system length. For each defect location and PD magnitude, 150 PD signals were simulated. The simulated signals were spread among 20 ms records of measurement data and disturbances were added. The resulting digitized sensor signals were simulated as obtained by current transformers (CTs) clipped onto the cable screens at the terminations past the last earth connection and sampled with 65 MSPS.

The whitening filter and the matched filter bank as described in the previous section were implemented in Labview. The MFB templates were chosen such that the error probability for two successive filters does not exceed 10^{-3} for an average SNR of 15 dB. Clearly, this SNR is chosen more or less arbitrarily, since PD signals with various SNRs are present within the measurement data. In order to ensure that the algorithms do not give false results, the detection threshold was set to 5 times the expected average noise power at a matched filter output. When local maxima within matched filter outputs were detected, the signals were interpolated using parabolic interpolation in order to reduce the TOA estimation variance.

5.5.2 Partial Discharge Signal Extraction Performance

PD signal extraction performance can be quantified as the ratio of the number of extracted PD signals to the number of PD signals that were actually present. Since the detection threshold was set quite high, the false alarm rate is insignificant, and can therefore be neglected. In the first experiment, defects inducing apparent charges of 1 nC, 5 nC, 10 nC, and 20 nC at the discharge locations were simulated. The

			Exp. 1	Exp. 2
Q_{app} [nC]	$Q_{\text{app},d}$ [nC]	SPIAR	$\overline{\text{SNR}}$ [dB]	$\overline{\text{SNR}}$ [dB]
1	0.40 ... 0.45	$4.1{\cdot}10^{-3}$ ... $7.0{\cdot}10^{-2}$	-34 ... 0	
5	1.99 ... 2.24	$1.9{\cdot}10^{-2}$ ... 0.33	-20 ... 14	-20 ... 1
10	3.99 ... 4.47	$3.7{\cdot}10^{-2}$ ... 0.65	-14 ... 20	-14 ... 7
20	7.98 ... 8.94	$7.0{\cdot}10^{-2}$ ... 1.3	-8 ... 26	-8 ... 13
50	19.9 ... 22.4	0.19 ... 3.25		0 ... 21
			Exp. 3	Exp. 4
Q_{app} [nC]	$Q_{\text{app},d}$ [nC]	SPIAR	$\overline{\text{SNR}}$ [dB]	$\overline{\text{SNR}}$ [dB]
10	0.20 ... 2.62	$4.1{\cdot}10^{-3}$ ... 0.36	-25 ... 19	-37 ... 6
20	0.40 ... 5.23	$8.2{\cdot}10^{-3}$ ... 0.72	-19 ... 25	-32 ... 12
50	1.00 ... 13.1	$2.0{\cdot}10^{-2}$ ... 1.8	-11 ... 33	-23 ... 20
100	2.00 ... 26.2	$4.1{\cdot}10^{-2}$ ... 3.6	-5 ... 39	-17 ... 26

Table 5.1 *Signal quality of the simulated PD signals for the different experiments.*

average SNRs of 1 nC PD signals were between 0 dB for a defect at 500 m from the sensor, and -35 dB for a defect at 4 km. The average SNRs of 5 nC, 10 nC, and 20 nC PDs ranges from 14 dB to -20 dB, 20 dB to -14 dB, and 26 dB to -8 dB, respectively. In the second simulation experiment, apparent charges of 5 nC, 10 nC, 20 nC, and 50 nC were simulated. For both experiments, similar AM radio broadcasts were simulated. In simulation experiment 3 and 4, PD signals were extracted from sensor signals obtained at the RMU with a single cable termination. Apparent charges of 10 nC, 20 nC, 50 nC, and 100 nC were simulated. In Table 5.1, the average SNRs and SPIARs are listed for all simulations.
PD signals were simulated such that the apparent charge at the discharge origin equals the value Q_{app} in Table 5.1. However, some PD measurement methods simply define the apparent charge as the integral of the detected current pulse (see e.g. [Sch99b]),

$$Q_{\text{app},d} = \int s(t)\, dt \; . \tag{5.20}$$

For convenience, the values of the detected charge according to this definition are shown in the table as well. Since the attenuation of PD signals is a function of the propagated distance, $Q_{\text{app},d}$ differs depending on the discharge location.

In Fig. 5.15, the extraction performance of the implemented algorithms for the simulation experiments is presented. Evidently, PD extraction performance depends to a large extent on the specific characteristics of the noise and interference present in the measurements. If the measurement conditions are relatively good, as is the case in experiment 1, small PD signals from defects situated at considerable distances from the sensor can be extracted. It should be noted that on-line power cable diagnostics require only a small percentage of defect discharges to be detected, since in the long term enough PD signals are extracted to be able to characterize a defect. In case of higher noise and interference levels, extraction of small PD signals generated far from a sensor is virtually impossible. However, since defects commonly generate discharges of various magnitudes, in long term measurements sufficient information may be gathered for the purpose of cable diagnostics. The simulation experiments show that the extraction performance depends on the propagation channel load impedance. As de-

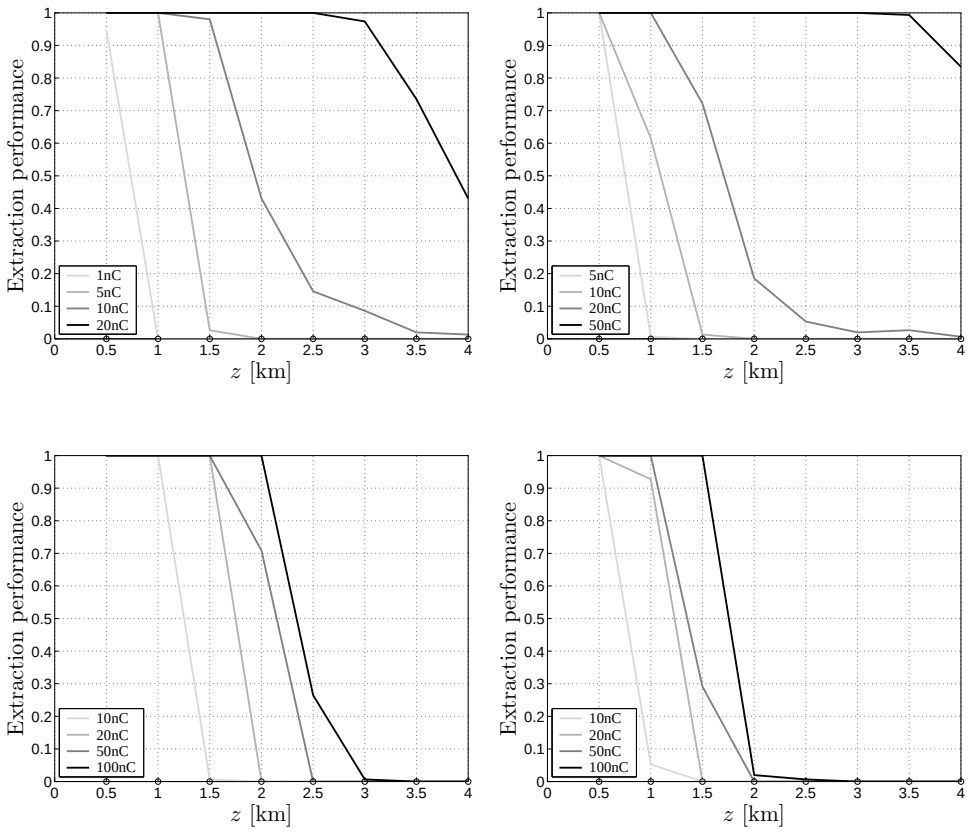

Figure 5.15 *PD signal extraction performance for simulation experiment 1 (top left), experiment 2 (top right), experiment 3 (bottom left), and experiment 4 (bottom right). Circles on the horizontal axes indicate the simulated defect locations.*

picted in Fig. 2.13, an RMU with only a single cable termination has a substantially higher impedance in the low frequency range as compared to an RMU with multiple cable terminations. As a consequence, PD signals which are detected using CTs, can have much lower average SNRs and SPIARs. Especially the quality of PD signals originating far from the sensor decreases to a large extent, since the signal energy is concentrated in the low frequency range. It should be noted that experiment 4 represents a worst-case scenario, since high noise and interference levels are combined with a large load impedance.

As mentioned, in the experiments the detection thresholds were set quite high above the expected noise levels in order to prevent false alarms. Clearly, the extraction performance can be increased by lowering the thresholds, which inevitably leads to falsely extracted signals as well. In Fig. 5.16, for two simulated defects, the relative numbers of missed PD signals are plotted as a function of the ratio of the number of falsely extracted signals to the total number of extracted signals. The simulated defects were chosen such that a low extraction performance was obtained (see Fig. 5.16). The sensor signals were simulated under the same conditions as in ex-

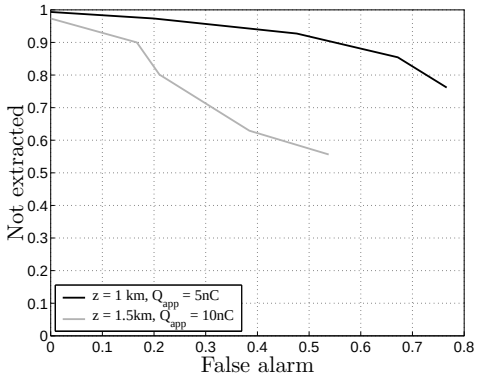

Figure 5.16 *Relative number of missed PD signals versus the relative number of falsely extracted signals simulated under the same conditions as in experiment 2.*

periment 2. The number of missed PD signals is decreased somewhat by lowering the thresholds, however, the number of false alarms increases dramatically. The falsely extracted signals are distributed arbitrarily among a measured data record, since a false alarm results from threshold crossing of noise samples. In principle, the false alarm rate can be decreased by considering extraction results from sensor signals at both cable ends. Nevertheless, it can be stated that high false alarm rates are generally not preferred since the minor improvement of extraction performance results in excessive computational and communication channel loads.

5.5.3 Partial Discharge Signal Parameter Estimation Quality

Besides the extraction performance of the PD signal analysis methods, the signal parameter estimation quality was tested. In Fig. 5.17, the means and standard deviations of the TOA estimation errors are presented in the top plots for experiment 2 (left-hand) and 3 (right-hand). So a situation with low SNR and a situation with an unfavorable RMU configuration were tested. In the bottom plots, the magnitude estimation errors are depicted, normalized to the apparent charge at the defect location. Estimation results are only depicted for PD signals that could actually be extracted from the measurements. For each defect location and apparent charge, the means and standard deviations of the estimation errors are plotted as squares and diamonds, respectively. In addition, dotted lines equal the theoretical standard deviation lower bounds, obtained from the CRLBs. The simulation show that for high average SNRs, viz. above 0 dB for experiment 2 and 6 dB for experiment 3, the parameter estimation results are approximately unbiased. Moreover, the estimation deviations are well predicted by the theoretical lower bounds. For low average SNRs, the extraction performance deteriorates and consequently the estimation variance increases and the estimations become biased. It should be noted that when the extraction performance decreases, the statistical averages of the estimation errors become less accurate, since averages of a small number of results are computed. The energy distribution of a PD signal that originates far from the sensor, is concentrated in the low frequency range, which makes accurate time of arrival estimation difficult. Consequently, the TOA estimation standard deviation can be as high as 160 ns, for measurements with high noise and interference levels, as is the case in experiment 2. When sensor signals

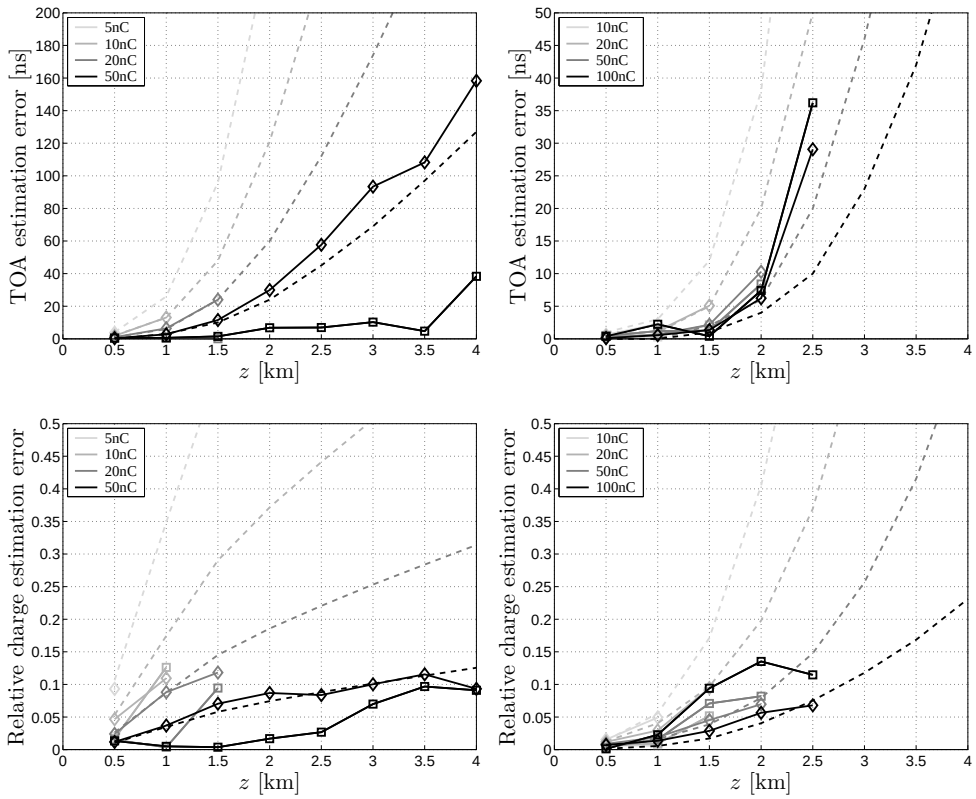

Figure 5.17 *PD signal TOA estimation quality (top plots) and magnitude estimation quality (bottom plots) for simulation experiments 2 (left plots) and 3 (right plots). Squares and diamonds show the estimation error means and standard deviations, respectively. Dashed lines equal the theoretical lower bounds on error standard deviations.*

are obtained at an RMU with a single cable termination, the propagation channel load impedance introduces signal attenuation and additional phase distortions, thus impeding parameter estimation. The results of experiment 3 show that for defects situated more than 1500 m from the sensor, the estimation quality deteriorates with respect to the theoretical performance bounds. Although the proposed methods do not attain the theoretical lower bounds in all cases, the experiments show the effectiveness of the proposed methods. The parameter estimators provide sufficient accuracy for defect location as will become clear in Chapter 6.

5.5.4 Finite Interference Rejection Performance

Finite energy interference originating outside the cable system can be distinguished from PD signals by DTOA discrimination. In a simulation experiment, PD signals generated in a distribution transformer were simulated, which are considered as interferences. For this experiment, the cable system under test and the measurement conditions were equivalent to experiment 2. Sensor signals were simulated for both cable ends, with perfect synchronization. Discharges in the distribution transformer

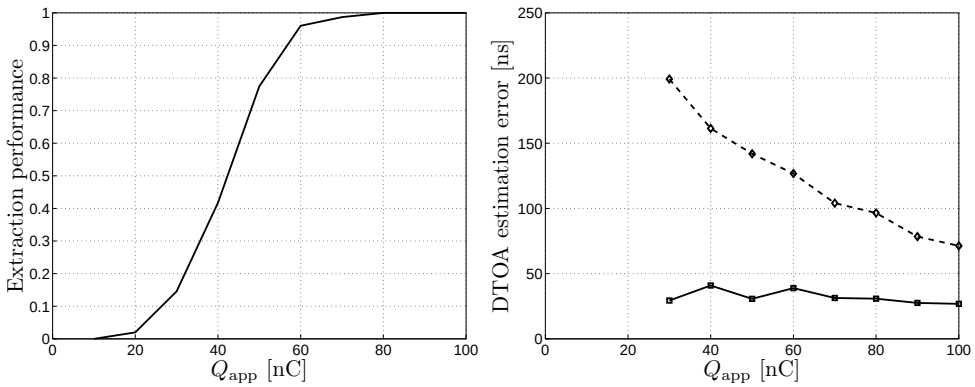

Figure 5.18 *Finite interference extraction performance (left plot) and DTOA estimation quality (right plot). Solid and dashed lines represent means and standard deviations of the DTOAs estimation errors.*

with apparent charges ranging from 10 nC to 100 nC were simulated. The average SNRs of the signals measured by the near-end sensor, where the discharging transformer was situated, range from 32 dB for 10 nC PDs to 52 dB for 100 nC PDs. At the far-end sensor, the average SNRs range from -14 dB to 6 dB. Clearly, signals with low average SNRs cannot be extracted from the measurement data obtained at the far end. In the left-hand plot in Fig. 5.18 the extraction performance is depicted as a function of the apparent charge. When signals could be extracted at both cable ends, the difference in time of arrival between signals detected at the near and far end was computed and compared to the cable system propagation delay as obtained from the model. In the right-hand plot in Fig. 5.18, the means and standard deviations of the DTOA estimation errors are plotted as squares and diamonds, respectively. Evidently, the estimation variance can be large for disturbances with relatively low average SNRs. As a consequence, PD signals that originate near the cable terminals, cannot be distinguished from finite energy interferences based on the difference arrival times alone. Moreover, small interferences with low average SNRs cannot be extracted at both cable ends. For this reason, in such cases, broadband finite interferences can only be rejected using a directional sensing method such as described in Section 3.2.3.

5.6 Conclusions

In this chapter, PD signal extraction by matched filtering was discussed, which can be applied to both on-line and off-line PD detection. A matched filter is optimal in the sense that the average SNR at the filter output is maximized, provided that the signal and noise properties are known or can be estimated. PD signal waveforms are determined solely by the signal propagation paths. Therefore, based on the signal model, matched filters can be designed specifically for the cable system under test.

Besides signal extraction, matched filters provide a means to estimate PD apparent charge and signal arrival time. Based on the signal and noise properties, theoretical lower bounds on the parameter estimation quality were derived. Since time of arrival estimation using matched filters is bounded to the sampling grid, interpolation schemes were applied to increase estimation accuracy.

Discharging defects can be present at any location along the cable length, resulting in a variety of signal waveforms at the sensor. PD pulse shapes do not differ appreciably for defect sites situated close together, especially when the propagation distance is long. As a consequence, a finite set of signal templates is sufficient to match every possible PD waveshape from the cable system. In this chapter, a method to select waveform templates from the signal model was presented. If the waveshapes of discharges originating close together are to be distinguished, the discrimination error probability due to measurement noise, is proposed as a selection criterion. As a first step towards semi-continuous processing, an efficient matched filter bank implementation was presented. An MFB can be realized as a single whitening filter, which flattens the noise and interference spectrum, followed by a bank of signal matched filters. From the tentative measurements it follows that the disturbance spectrum is composed of narrowband radio broadcasts embedded in broadband noise. By dealing separately with these two disturbance classes, an efficient implementation of the whitening filter is realized. Signals originating from subsequent discharge locations partly propagate through the same path. This property can be exploited by implementing the parallel MFB as a cascade, which results in shorter filters and thus to the reduction of computational load.

The proposed methods were evaluated using computer simulated PD measurement data, with characteristics based on the tentative on-line measurements. The simulation results indicate that PD signals originating up to 3 km from the sensor with apparent charges of at least 10 nC at the discharge sites can be extracted under typical measurement conditions. In case of defects situated further away, only PD signals of larger magnitudes can be extracted. However, since defects commonly generate discharges of various magnitudes, in long term measurements sufficient information may be gathered for the purpose of cable diagnostics. The arrival times and magnitudes of PD signals with relatively high average SNRs can be estimated with accuracies that approximate the theoretical performance bounds. By application of interpolation schemes, arrival times of PD signals originating from defects close to the sensor can be estimated within fractions of the sampling period. For low average SNRs, the extraction performance and parameter estimation quality deteriorates. Due to attenuation of high frequency components, the standard deviation of TOA estimations for PD signals originating several kilometers from the sensor can increase up to 160 ns, even for relatively high average SNRs. Although the implemented estimators do not reach the theoretical optima in all cases, the results are promising.

Besides continuous periodic interference and noise, PD measurements are troubled by finite energy interferences. Narrowband disturbances can be distinguished from PD signals based on their waveshapes, either by template matching or by analysis of the MFB responses. Broadband disturbances, such as PD signals from other HV equipment or cables cannot be rejected using this method. Since finite energy disturbances originate outside the cable under test, discrimination can be achieved by estimating the difference in arrival times of signals measured by synchronized sensors installed at both cable ends. However, this method has it limitations, since only disturbances with large average SNRs can be extracted at both cable ends. Moreover, the quality of DTOA estimation depends on the spectral energy distributions of disturbances. For instance, in case of long power cables, PD signals that originate near the cable terminals, cannot be distinguished from finite energy interferences based on the difference arrival times alone, as was illustrated by a simulation experiment.

Evidently, the performance of the proposed methods depends to a large extent on the specific characteristics of the cable system under test, the disturbance present in the measurements, as well as the quality of the signal model. Therefore it should be noted that the simulation experiments only serve as illustrative examples.

Chapter 6

Partial Discharge Source Location

6.1 Introduction

Location of discharging insulation defects is of crucial importance for the mapping of degraded components in power cable systems. Off-line time-domain reflectometry (TDR) with a sensor at one cable end is the most commonly applied method to locate partial discharges [Kre93b]. In case of on-line detection, a partial discharge (PD) signal reflected on a propagation channel load impedance can have low signal quality, depending on the ring main unit (RMU) configuration and the cable system properties. As a consequence, reflections can generally not be extracted from measurement data, and sensors at both cable ends are required to locate discharge sources.

Regardless of the measurement topology, accurate PD location relies on estimation of the difference in time of arrival (DTOA) of signals originating from the same discharge. If both the cable length and the propagation velocity are known, discharging defects can then be located. Apart from imprecise knowledge of the cable length, other factors impede accurate location, such as attenuation and dispersion introduced by the cable, as well as noise and interference [Mas90, Kre93b, Ste91, Gul03]. In Section 6.2 it is shown that location errors due to dispersion can be predicted and corrected using the signal model as described in Section 2.5.

Various algorithms have been proposed to estimate the DTOA of PD signals corrupted by noise and interference, for instance by crosscorrelation of received PD pulses [Ste92]. Other methods employ a propagation model adjusted to the cable under test [Mas92, Du94b]. The model responses for various parameters are compared to received PD pulses and optimized by minimization of an error criterion. In Section 6.3, a similar technique is discussed, which utilizes the likelihood of the signal model as a test statistic. To that end, maximum-likelihood (ML) estimation theory (see e.g. [Tre68]) is applied, which serves as a framework for PD location. Theoretical lower bounds on estimation accuracy are derived and similarities with DTOA-based location are pointed out. In addition, location based on only the waveshape of a detected PD pulse is discussed. All results apply to both off-line and on-line PD location.

A two-sided measurement topology requires synchronized data acquisition. In Section 6.4, time-base alignment of recorded data using synchronization pulses is discussed [Ste02a, Wou03c]. In order to validate the proposed methods, the algorithms are tested using computer-simulated PD measurement data, and the results are presented in Section 6.5. Conclusions are given in Section 6.6.

6.2 Difference in Time of Arrival Based Location

Generally, discharging defects are located by estimating the difference in arrival times of PD signals resulting from the same discharge. If the cable section lengths and the propagation velocities are known, PD generating defects can then be located along the cable system length.

In some on-line measurement situations, e.g. on relatively short cable connections, reflections on the far-end cable termination can be extracted at the near end. In such cases TDR can be applied to locate discharging defects. For off-line PD detection usually a single sensor is employed and TDR is widely applied to locate PD sources (see e.g. [Mas90, Ste91, Ste92, Bor92]). Considering a cable system that can be parameterized by a single propagation factor and cable length l, the PD location estimate $\hat{z}$ is computed by

$$\hat{z} = l - \frac{1}{2} v_\mathrm{c} \Delta\hat{\tau} \tag{6.1}$$

where v_c is a constant propagation velocity and $\Delta\hat{\tau} = \hat{\tau}_\mathrm{r} - \hat{\tau}_\mathrm{d}$ is the estimated DTOA between the first pulse arriving at τ_d, and the reflection on the opposite cable end at τ_r. Usually, the cable propagation velocity is obtained prior to PD detection by injecting a known pulse and measuring the propagation channel delay.

In the majority of on-line measurement situations, a far-end reflection can generally not be extracted and sensors are installed at each cable termination. Likewise, in off-line measurements on very long power cables a two-sided measurement topology is required [Ste01]. For a uniform cable system, the PD location with respect to the near end is computed by

$$\hat{z} = \frac{1}{2}(l - v_\mathrm{c} \Delta\hat{\tau}) \tag{6.2}$$

where in this case $\Delta\hat{\tau} = \hat{\tau}_\mathrm{f} - \hat{\tau}_\mathrm{n}$ is the estimated DTOA between the pulses arriving at the near and far end, with arrival times τ_n and τ_f, respectively.

Due to dispersion, the choice of a reference point in a PD wave shape for the purpose of DTOA estimation is non-trivial. As a consequence well-known methods such as level crossing, peak-value detection, and correlation techniques give rise to location errors as described in e.g. [Kna90, Ste92, Kre93b]. Moreover, dispersion inevitably leads to location estimation bias if a single propagation velocity is assigned [Ste92]. The PD signal start is defined as some (more or less arbitrary) point within the signal waveshape, which generally can not be related directly to the location of the PD source. As a consequence, an analytical expression for the location estimation bias cannot be derived. However, the estimation bias can be predicted based on the signal model presented in Section 2.5 and the applied time of arrival (TOA) definition. If the location bias is ignored, a theoretical lower bound on the location estimation variance equals

$$\mathrm{var}(\hat{z}) \geq \frac{1}{4} v_\mathrm{c}^2 (\mathrm{var}(\hat{\tau}_\mathrm{d}) + \mathrm{var}(\hat{\tau}_\mathrm{r})) \tag{6.3}$$

for single-sided measurements, and

$$\mathrm{var}(\hat{z}) \geq \frac{1}{4} v_\mathrm{c}^2 (\mathrm{var}(\hat{\tau}_\mathrm{n}) + \mathrm{var}(\hat{\tau}_\mathrm{f})) \tag{6.4}$$

for two-sided measurements. In Eq. 6.4 synchronization errors that arise in a two-sided measurement topology, are ignored. Two-sided time base synchronization is discussed in Section 6.4.

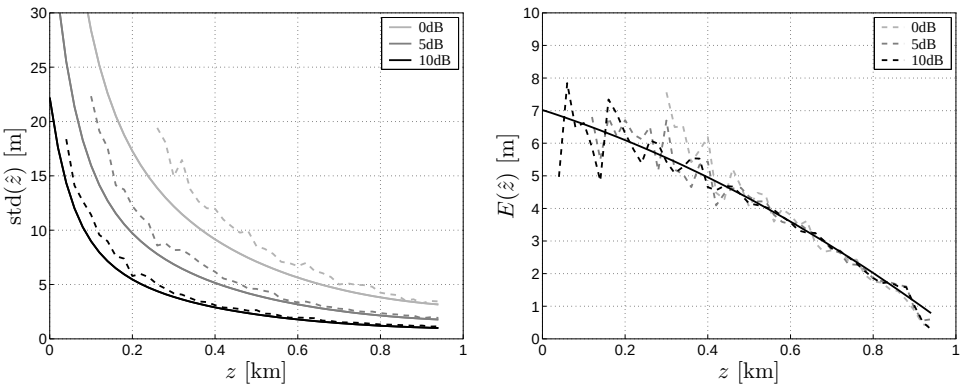

Figure 6.1 *Theoretical simulation of location performance based on time-domain reflectrometry for various average SNRs. In the left-hand plot, dashed lines represent standard deviations of simulation results and solid lines represent approximated lower bounds. In the right-hand plot, dashed lines represent means of simulation results and the solid line represents the predicted biases.*

As an example PD signals originating along the length of a 1 km long 12.5 kV 3×95 mm^2 paper insulated lead covered (PILC) cable and sampled with 65 MSPS were simulated in white noise. For simplicity, the propagation channel was characteristically terminated at the near end and the far end was left open. The arrival times of the PD signals were estimated using appropriate matched filters, where the start of the signal templates were defined according to Eq. 5.17. The cable propagation velocity was obtained by simulating an injected pulse and measuring the propagation channel delay. The standard deviation of the TDR location estimates obtained from 500 trials are shown in the left-hand plot in Fig. 6.1 for different average signal to noise ratios (SNRs) of the first arriving pulses. Although the proposed bound on the estimation is quite loose, the simulation results show that the approximation is reasonable. In the right-hand plot, the means of the simulation results are depicted as well as the estimation bias as computed using the signal model. Since the location estimation bias can be well predicted, a correction method using e.g. a look-up table can be applied to reduce location errors. Note that close to the far-end cable termination, no simulation results and lower bounds are depicted. Here, the first pulse and the reflected signal cannot be separated in the time-domain and TDR is not applicable. In addition, for defects located in regions within the first half of the cable, the number of reflected PD signals that were extracted, was insufficient to obtain reliable estimates of the statistical averages. Very close to the near-end termination, reflected PD signals could not be extracted at all, thus no TDR results could be obtained.

In Fig. 6.2, simulation results of two-sided DTOA-based location in a 4 km 12.5 kV 3×95 mm^2 PILC cable are shown for different average SNRs of the first arriving pulse. Note that for discharges located in the first half of the cable, the first pulse arrives at the near end, likewise in the second half the first pulse arrives at the far end, which explains the symmetries of the plots. In this case the cable was characteristically terminated at both cable ends. It can be concluded that the estimation bias can be well predicted from the signal model. Similar to TDR, the theoretical estimation standard deviation provides a rather loose bound on the actual results. Again, by compensating for the errors due to dispersion, an estimator is obtained that does

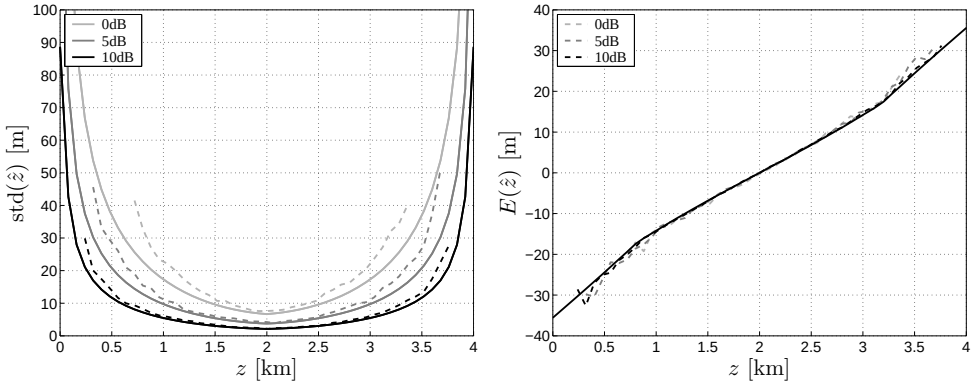

Figure 6.2 *Theoretical simulation of two-sided DTOA-based location performance for various average SNRs. In the left-hand plot, dashed lines represent standard deviations of simulation results and solid lines represent approximated lower bounds. In the right-hand plot, dashed lines represent means of simulation results and the solid line represents the predicted biases.*

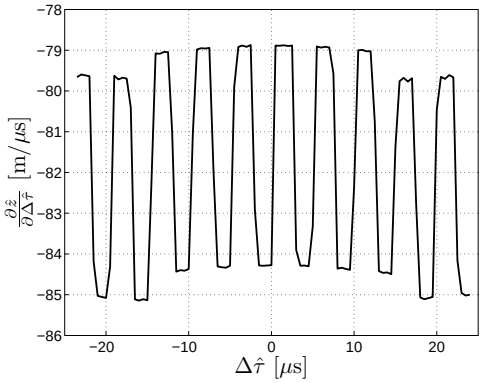

Figure 6.3 *Derivative of the mapping $\hat{z} = f(\Delta\hat{\tau})$ of a DTOA estimate to a location estimate for a composite cable system.*

achieve the lower bound.

An underground cable system consists of a cascade of multiple three-phase cable sections interconnected by joints. Different cable types may be present with different propagation properties, which implies that a PD location cannot be computed from an estimated DTOA by a simple velocity. Based on the signal model of the composite cable system the DTOA can be related to a PD location. The function that maps the DTOA to a location, is slightly non-linear due to section-dependent propagation properties and dispersion. For example, in Fig. 6.3, the derivative of the relation between DTOA and PD location for a 4 km long composite cable system is depicted. The cable system consisted of 20 different sections of 200 m. The odd sections were 12.5 kV 3×95 mm^2 PILC cables and the even sections were 10 kV 3×95 mm^2 PILC cables. Clearly, by a piecewise approximation of the function the mapping of an estimated DTOA to a location estimate can be obtained efficiently.

6.3 Model-Based Location

Discharging defects can be located by comparing measured PD signals to a signal model. By testing the model for various parameter values, the most likely PD source location can be determined. If analysis of two PD pulses forms the basis of defect location, the proposed method implicitly deals with location errors due to dispersion. If only a single detected pulse is used for location, the method exploits dispersion and attenuation of the propagation path. In this section, theoretical performance bounds of both one-sided and two-sided location methods are presented. Without loss of generality, uniform cable systems are considered for the purpose of analytical tractability. The concepts can be directly extended to composite cable systems.

6.3.1 Location Based on a Single-Pulse Signal Model

Although reflections on the far-end termination cannot be extracted in many on-line situations, one-sided PD location can be achieved using the waveshape of a detected PD pulse. As described in Section 2.5, a detected PD signal originating in a uniform cable system is modelled as

$$S(i\Delta f, z) = Z_{\mathrm{t}}(i\Delta f) H_{\mathrm{s}}(i\Delta f) T_{\mathrm{l}}(i\Delta f) e^{-\gamma(i\Delta f)z} \tag{6.5}$$

where z is the discharge site, $Z_{\mathrm{t}}(i\Delta f)$ is the sensor transfer impedance, and $T_{\mathrm{l}}(i\Delta f)$ equals the transmission coefficient at the interface of the cable and the load impedance. If the sensor is located directly at the cable termination, the sensor transfer function $H_{\mathrm{s}}(i\Delta f)$ can be omitted. Measurements are not synchronized with PD signal excitation; therefore an unknown initial delay t_0 is introduced, and a perturbed sensor signal is expressed as $x(kT_{\mathrm{s}}) = As(kT_{\mathrm{s}} - t_0) + n(kT_{\mathrm{s}})$. Some point t_{s} within the waveshape is defined as the signal start (see e.g. Eq. 5.17); therefore the PD signal time of arrival simply equals $\tau = t_0 + t_{\mathrm{s}}$. Now the model essentially comprises three unknown parameters, viz. the scaling factor A, the TOA τ, and the defect location z. By application of maximum-likelihood estimation theory the optimal parameter estimators can be derived (see e.g. [Tre68]). Assuming that the additive noise is zero-mean and Gaussian distributed, the a posteriori log likelihood of the single-pulse model equals

$$L(A, \tau, z) = \Delta f \sum_{i=0}^{B-1} -\frac{|X(i\Delta f) - AS(i\Delta f, z) e^{-j2\pi i \Delta f(\tau - t_{\mathrm{s}})}|^2}{2P_N(i\Delta f)} , \tag{6.6}$$

which expresses the likelihood of the model for the parameter values given a measured signal $x(kT_{\mathrm{s}})$, the signal model, and the noise power spectral density $P_N(i\Delta f)$. From the likelihood function, the Cramer-Rao lower bound (CRLB) on the PD source

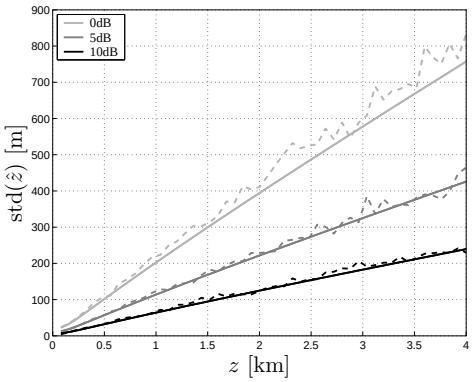

Figure 6.4 *Theoretical evaluation of the standard deviation of discharge location estimates obtained from the waveshapes of single PD signals for various average SNRs. Solid lines represent Cramer-Rao lower bounds and dashed lines represent simulation results.*

location variance based on a single detected PD pulse equals (see Appendix D)

$$\begin{aligned}\mathrm{var}(\hat{z}) \geq \frac{T_\mathrm{s}}{T_0}\Bigg(&\frac{1}{B}\sum_{i=0}^{B-1}|\gamma(i\Delta f)|^2\mathrm{SNR}(i\Delta f)\\ &-\frac{1}{B}\frac{\left(\sum_{i=0}^{B-1}(2\pi i\Delta f)\beta(i\Delta f)\mathrm{SNR}(i\Delta f)\right)^2}{\sum_{i=0}^{B-1}(2\pi i\Delta f)^2\mathrm{SNR}(i\Delta f)}\\ &-\frac{1}{B}\frac{\left(\sum_{i=0}^{B-1}\alpha(i\Delta f)\mathrm{SNR}(i\Delta f)\right)^2}{\sum_{i=0}^{B-1}\mathrm{SNR}(i\Delta f)}\Bigg)^{-1}.\end{aligned} \tag{6.7}$$

The first term inside the brackets expresses the uncertainty of the location parameter estimation alone, which equals the average of the weighted single-bin SNRs. The signal TOA estimate and the estimate of the frequency dependent phase shift introduced by the channel ($\beta(i\Delta f)z$) are dependent variables. As a result of the coherence between these parameters the location estimation variance increases, which is quantified by the second term inside the brackets. Likewise, the signal scaling factor A and the attenuation of the channel ($\alpha(i\Delta f)z$) have a mutual dependency, thus increasing the location estimation variance as expressed by the third term inside the brackets. If the PD signal scaling factor and TOA would be known a priori, the last two terms inside the brackets would vanish.

As an example PD signals originating along the length of a 2 km long 10 kV 3×95 mm^2 PILC cable and sampled with 65 MSPS were simulated in white noise for different average SNRs. For simplicity, the propagation channel was characteristically terminated at each cable end, and the sensor transfer impedance was omitted. The standard deviation of the location estimates from 500 trials are plotted in Fig. 6.4. For most discharge sites, the statistical averages of the location estimates correspond to the theoretical bound. The figure shows that the standard deviation can be very large. This result is not at all unexpected, since waveshapes of PD signals originating close together do not differ appreciably, especially when the propagation distance is long.

Consequently, if accurate localization is desired, estimation based on a single pulse is not applicable. Nevertheless, initial location estimates can be based on a single pulse, providing information that can be useful to check results obtained by a DTOA location method. Note that in practical measurements, the load impedances generally differ from the cable characteristic impedance. Therefore PD signals originating close to the far-end cable termination are composed of a direct pulse and a reflection. Since the reflected signal is not incorporated in the single-pulse model, the location performance will degrade even further.

The test statistic (Eq. 6.6) is a non-linear function of the parameter z, and a closed-form expression for the ML location estimator does not exist. Moreover, the likelihood function comprises multiple local maxima in the parameter space. As a consequence, iterative optimization procedures cannot be applied, since convergence to the global maximum is not guaranteed. Therefore the most likely PD source location can only be determined by a fine grid search, resulting in excessive computational complexity. However, as discussed in Section 5.2.3, a matched filter bank (MFB) can be applied to obtain a single-pulse-based location estimate. Loosely speaking, by observing Eq. 6.6 more closely it can be seen that the likelihood function can be interpreted as the result of matched filtering by an infinite number of filter templates. In case of an MFB, the filters correspond to a finite set of defect locations; therefore single-pulse-based location results in biased estimates. However, if sufficient filters are applied, the MFB results in parameter estimates that approximate the optimal estimates. Close to the global maximum the likelihood function can be considered convex and in principle iterative maximization algorithms could be used to obtain the ML estimates (see e.g. [Pre92]).

6.3.2 Location Based on a Double-Pulse Signal Model

Instead of location estimation using a single-pulse model, discharging defects can be located using a model of multiple arriving pulses. In general only the first two arriving PD signals from the same defect have sufficient signal quality; therefore only these signals are considered here. In case of a one-sided measurement topology, the model comprises the first arriving PD signal and the reflection on the far-end termination. If sensors are applied at both cable ends, the model comprises the first arriving pulses at each side.

One-Sided Measurement Topology

If a uniform cable system is considered, a reflected PD signal can be modelled as

$$S_{\mathrm{r}}(i\Delta f, z) = R_{\mathrm{l,f}}(i\Delta f)e^{-\gamma(i\Delta f)(2l-z)}S_{\mathrm{d}}(i\Delta f, z) \tag{6.8}$$

where $R_{\mathrm{l,f}}(i\Delta f)$ is the reflection coefficient at the far-end termination, l is the cable length, and $S_{\mathrm{d}}(i\Delta f, z)$ equals the model of the first arriving pulse, given by Eq. 6.5. Subsequently, the double-pulse signal model equals

$$S(i\Delta f, z) = S_{\mathrm{d}}(i\Delta f, z) + S_{\mathrm{r}}(i\Delta f, z) \tag{6.9}$$

for $z < l$. Similar to single-pulse-based location, the test statistic Eq. 6.6 is used to evaluate the likelihood of the model parameters A, τ and z for a measured signal. In case of double-pulse location using a single sensor, the CRLB on the PD source

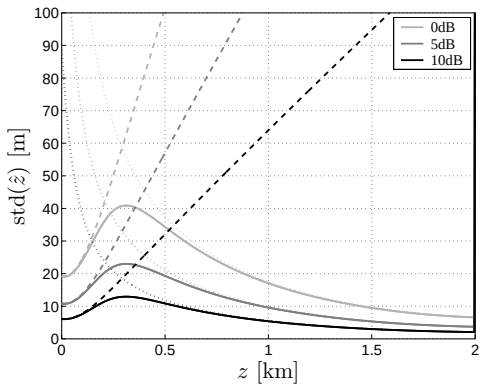

Figure 6.5 *Theoretical lower bounds on location estimation standard deviation in case of double-pulse-based location (solid lines), single-pulse-based location (dashed lines), and TDR (dotted lines) for various average SNRs.*

location variance equals (see Appendix D)

$$\begin{aligned}\mathrm{var}(\hat{z}) \geq \quad & \frac{T_\mathrm{s}}{T_0}\left(\frac{1}{B}\sum_{i=0}^{B-1}|\gamma(i\Delta f)|^2(\mathrm{SNR_d}(i\Delta f)+\mathrm{SNR_r}(i\Delta f))\right. \\ & -\frac{1}{B}\frac{\left(\sum_{i=0}^{B-1}(2\pi i\Delta f)\beta(i\Delta f)(\mathrm{SNR_d}(i\Delta f)-\mathrm{SNR_r}(i\Delta f))\right)^2}{\sum_{i=0}^{B-1}(2\pi i\Delta f)^2\mathrm{SNR}(i\Delta f)} \\ & \left.-\frac{1}{B}\frac{\left(\sum_{i=0}^{B-1}\alpha(i\Delta f)(\mathrm{SNR_d}(i\Delta f)-\mathrm{SNR_r}(i\Delta f))\right)^2}{\sum_{i=0}^{B-1}\mathrm{SNR}(i\Delta f)}\right)^{-1}. \qquad (6.10)\end{aligned}$$

where $\mathrm{SNR}(i\Delta f)$ is the signal to noise ratio of the received signal. $\mathrm{SNR_d}(i\Delta f)$ and $\mathrm{SNR_r}(i\Delta f)$ equal the individual SNRs of the first arriving pulse and the reflection, respectively. As explained in the appendix, Eq. 6.10 holds for discharge locations along the entire cable length, except for a small region near the far-end termination.

As mentioned earlier, the test statistic is a non-linear function of the parameters and has multiple maxima. Consequently, the most likely estimates can only be obtained by a grid search within the parameter space, again resulting in excessive computational load. However, by examining the properties of the location estimator more closely, approximations can be made using the methods presented earlier. As an example, in Fig. 6.5 the theoretical lower bounds on the location estimation standard deviations are depicted for different average SNR values of the first arriving pulses. The simulated system was a uniform 12.5 kV 3×95 mm^2 PILC cable of 2 km length. For simplicity, the propagation channel was characteristically terminated at the near end, and the far end was left open. The solid lines in Fig. 6.5 represent the lower bounds on the standard deviations for double-pulse-based location. Close to the near-end termination, the SNR of the first arriving pulse is substantially higher than the reflection SNR, and double-pulse location essentially reduces to single-pulse-based location. The dashed lines in Fig. 6.5 show the standard deviation lower bounds for

the location method based on a single pulse. Further away from the sensor, the reflection has sufficient energy and location mainly relies on DTOA estimation. However, contrary to conventional TDR, the model-based method implicitly accounts for estimation errors resulting from group delay distortion. In Fig. 6.5, the dotted lines show the deviation lower bounds for TDR. If the direct pulse and the reflection cannot be separated in the time-domain, TDR is not applicable. So for locations close to the far-end terminal, a grid search is still required. Note that if a discharging defect is located exactly at the far-end termination, only a single pulse arrives at the sensor, and the standard deviation lower bounds equal the bounds for single-pulse-based location. It can be concluded that in principle the optimal location estimator for a one-sided measurement topology can be approximated for a large number of locations by a combination of the single-pulse-based method and modified TDR.

Two-Sided Measurement Topology

In a two-sided measurement topology, sensor signals are obtained at both cable ends. For now it is assumed that the signals are perfectly synchronized. If a uniform cable system is considered, the PD signals resulting from a discharge located z meters from the near-end sensor are modelled as

$$\begin{aligned} S_{\mathrm{n}}(i\Delta f, z) &= Z_{\mathrm{t}}(i\Delta f) H_{\mathrm{s,n}}(i\Delta f) T_{\mathrm{l,n}}(i\Delta f) e^{-\gamma(i\Delta f) z} \,, \\ S_{\mathrm{f}}(i\Delta f, z) &= Z_{\mathrm{t}}(i\Delta f) H_{\mathrm{s,f}}(i\Delta f) T_{\mathrm{l,f}}(i\Delta f) e^{-\gamma(i\Delta f)(l-z)} \,. \end{aligned} \tag{6.11}$$

Theoretically, the noise picked up by both sensors is mutually correlated, since the noise propagates from one cable end to the opposite end through the cable itself or via some other transmission path. However, besides interfering radio broadcasts, no strong correlation between the noise processes was observed in practice. Since continuous periodic interference is cancelled or suppressed before PD location, it can be stated that the additive noise in one sensor signal is independent from the noise in the other sensor signal. As a consequence, the combined likelihood function of the two signal models equals

$$\begin{aligned} L(A, t_{0,} z) &= \Delta f \sum_{i=0}^{B-1} -\frac{|X_{\mathrm{n}}(i\Delta f) - A S_{\mathrm{n}}(i\Delta f, z) e^{-j2\pi i \Delta f (\tau_{\mathrm{n}} - t_{\mathrm{s,n}})}|^2}{2 P_{N_1}(i\Delta f)} \\ &\quad - \frac{|X_{\mathrm{f}}(i\Delta f) - A S_{\mathrm{f}}(i\Delta f, z) e^{-j2\pi i \Delta f (\tau_{\mathrm{f}} - t_{\mathrm{s,f}})}|^2}{2 P_{N_2}(i\Delta f)} \,, \end{aligned} \tag{6.12}$$

given the noisy sensor signals $x_{\mathrm{n}}(kT_{\mathrm{s}})$ and $x_{\mathrm{f}}(kT_{\mathrm{s}})$. Note that $\tau_{\mathrm{n}} - t_{\mathrm{s,n}} = \tau_{\mathrm{f}} - t_{\mathrm{s,f}} = t_0$. Similar to Eq. 6.10, the CRLB on PD source location variance equals (see Appendix D)

$$\begin{aligned} \mathrm{var}(\hat{z}) \geq \quad & \frac{T_{\mathrm{s}}}{T_0} \left(\frac{1}{B} \sum_{i=0}^{B-1} |\gamma(i\Delta f)|^2 (\mathrm{SNR}_{\mathrm{n}}(i\Delta f) + \mathrm{SNR}_{\mathrm{f}}(i\Delta f)) \right. \\ & - \frac{1}{B} \frac{\left(\sum_{i=0}^{B-1} (2\pi i \Delta f) \beta(i\Delta f) (\mathrm{SNR}_{\mathrm{n}}(i\Delta f) - \mathrm{SNR}_{\mathrm{f}}(i\Delta f)) \right)^2}{\sum_{i=0}^{B-1} (2\pi i \Delta f)^2 (\mathrm{SNR}_{\mathrm{n}}(i\Delta f) + \mathrm{SNR}_{\mathrm{f}}(i\Delta f))} \\ & \left. - \frac{1}{B} \frac{\left(\sum_{i=0}^{B-1} \alpha(i\Delta f) (\mathrm{SNR}_{\mathrm{n}}(i\Delta f) - \mathrm{SNR}_{\mathrm{f}}(i\Delta f)) \right)^2}{\sum_{i=0}^{B-1} (\mathrm{SNR}_{\mathrm{n}}(i\Delta f) + \mathrm{SNR}_{\mathrm{f}}(i\Delta f))} \right)^{-1} \end{aligned} \tag{6.13}$$

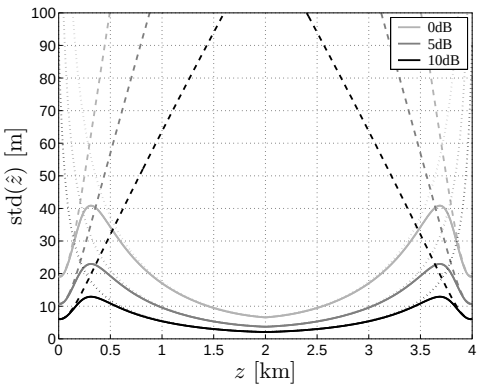

Figure 6.6 *Theoretical lower bounds on location estimation standard deviation in case of two-sided model-based location (solid lines), single-pulse model-based location (dashed lines), and two-sided DTOA-based location (dotted lines) for various average SNRs.*

where $\mathrm{SNR_n}(i\Delta f)$ and $\mathrm{SNR_f}(i\Delta f)$ equal the SNRs of the pulses arriving at the cable near end and far end, respectively.

Analogous to model-based location in a one-sided measurement topology, the ML location estimate can only be obtained by a fine grid search. Besides its computational complexity, now large amounts of data have to be communicated between the two cable ends, which impedes practical realization of the estimator. Again approximations can be made using a combination of DTOA location and single-pulse-based location. As an example in Fig. 6.6 the theoretical location lower bounds are depicted for different average SNRs of the first arriving pulse. Note that for discharges in the first half of the cable, the first pulse arrives at the near end. Likewise in the second half, the first pulse arrives at the far end, which explains the symmetries of the plots. The simulated system was a uniform 12.5 kV 3×95 mm^2 PILC cable of 4 km length, with characteristic termination at each end. The solid lines in Fig. 6.6 represent the lower bounds on the standard deviations for two-sided model-based location. Close to the terminations, the SNR of the first arriving pulse is substantially higher than the SNR of the second pulse, and double-pulse location essentially reduces to single-pulse-based location. The dashed lines in Fig. 6.6 show the standard deviation lower bounds for the location method based on the first arriving pulse. Further away from the terminations, both signals have sufficient energy and location mainly relies on DTOA estimation. However, contrary to conventional DTOA location, the model-based method implicitly accounts for estimation errors resulting from group delay distortion. In Fig. 6.6, the dotted lines show the deviation lower bounds for DTOA location. It can be concluded that in principle the optimal location estimator for a two-sided measurement topology can be approximated for a large number of locations by a combination of the single-pulse-based method and modified DTOA-based location.

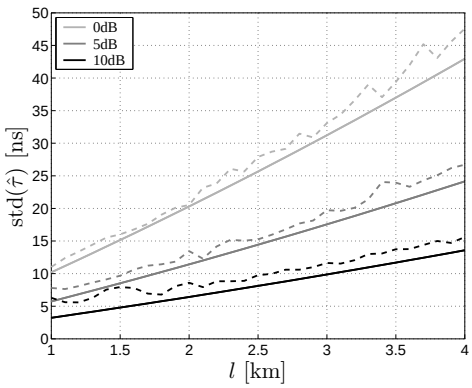

Figure 6.7 *Time of arrival estimation deviation of synchronization pulses arriving at the far cable end. Solid lines represent theoretical lower bounds and dashed lines represent simulation results.*

6.4 Time-Base Alignment

PD location using a two-sided measurement topology requires synchronization of the measurement equipment. A patented solution, already successfully applied in off-line PD measurements, utilizes the global positioning system (GPS) to align the time bases of data records obtained at both cable ends [Aar98, Ste01]. Another option to achieve time-base alignment is by injection of synchronization pulses at one cable end and detection at the other end [Ste02a, Wou03c, Wie03d]. If large data sets are recorded, the digitizer sample clocks may deviate during acquisition. To correct for time-base wander, a method using multiple synchronization pulses is applied [Wie04b].

6.4.1 Synchronization

In addition to determining the location of a receiver, the global positioning system can provide time-labels with a deviation in the order of 100 ns that can be used for the purpose of synchronization [Ste01]. Besides its price, the requirement that satellites have to be continuously visible to the receiver is the main drawback of GPS-based synchronization. The latter condition implies that a GPS antenna has to be placed outside the RMU, which is not desirable from a practical point of view. Moreover, depending on the measurement situation insufficient satellites may be present within the line of sight, thus making time-labelling impossible.

At an RMU, synchronization pulses can be injected into a live cable system using a signal coupling scheme as described in Section 4.2. By estimating the arrival times of the sync pulses at both cable ends and compensating for the channel propagation delay, time-base alignment of measured data records can be achieved [Ste02a, Wou03c]. This synchronization scheme can be realized at considerably lower costs as compared to the GPS-based method. Moreover, no components external to the RMU are employed, which is another distinct advantage of the technique. Evidently, the synchronization error of the method is governed by the estimation variance of the pulse arrival time at the far-end termination. A matched filter of the synchronization pulse can be obtained from the signal model and the spectrum of the injected signal. If the matched filter is used to estimate the pulse arrival time, the estimation variance is

lower bounded by Eq. 5.7. As an example, synchronization pulses were simulated for uniform 12.5 kV 3×95 mm^2 PILC cable of different lengths, with load impedances equal to the cable characteristic impedance. The simulated sync pulses injected at the near-end termination were dirac delta pulses applied to the injection coil characterized by Fig. 4.2. White measurement noise was added to the sensor signals. In Fig. 6.7, the standard deviations of TOA estimation are depicted as a function of the cable length for different average SNRs of the pulses arriving at the far-end termination. If sufficient energy can be injected, synchronization by pulse injection outperforms GPS-based synchronization. More details on time-base alignment using pulse injection can be found in [Wie05].

Using pulse synchronization, the DTOA between PD signals arriving at the near and far-end sensors is computed as

$$\Delta\hat{\tau} = (\hat{\tau}_{\mathrm{f}} - \hat{\tau}_{\mathrm{sync,f}}) - (\hat{\tau}_{\mathrm{n}} - \hat{\tau}_{\mathrm{sync,n}}) + \tau_{\mathrm{c}} \tag{6.14}$$

where τ_{c} is the channel propagation delay and $\hat{\tau}_{\mathrm{sync,n}}$ and $\hat{\tau}_{\mathrm{sync,f}}$ equal the sync pulse arrival time estimates at the near-end and far-end termination, respectively. Since sync-pulse TOA estimation can be considered as being independent from PD signal TOA estimation, for DTOA-based location, the variance lower bound can be expressed as

$$\mathrm{var}(\hat{z}) \geq \frac{1}{4} v_{\mathrm{c}}^2 (\mathrm{var}(\hat{\tau}_{\mathrm{n}}) + \mathrm{var}(\hat{\tau}_{\mathrm{f}}) + \mathrm{var}(\hat{\tau}_{\mathrm{sync,n}}) + \mathrm{var}(\hat{\tau}_{\mathrm{sync,f}})) \; . \tag{6.15}$$

For instance, considering the example in Fig. 6.2, the location standard deviation is raised approximately 3 m for every location along the cable length, if a sync pulse with 0 dB average SNR is received at the far end. Generally, pulses of much higher SNR can be injected, and sync-pulse estimation variance does not contribute significantly to the location errors.

6.4.2 Time-Base Wander Correction

The frequency of the sampling clock used for digitizing measurements varies slightly as a result of aging, thermal instabilities, and other environmental influences. Crystal oscillators employed in digitizers generally have extremely low magnetic field sensitivity, and the influence of the large fields present in the RMU can be neglected. On a short time-scale, e.g. with respect to PD signal duration, the sampling clock frequency deviation is negligible. However, in case of on-line measurements, digitizing equipment cannot be triggered by PD signals due to low signal to interference amplitude ratios. Since the occurrence of PD signals may be rare, large data blocks have to be recorded in order to detect PDs. Moreover, for the purpose of defect characterization, PD measurement data are acquired preferably over at least a cycle of the grid operating voltage. Within large data records, variations in the sampling clock have to be taken into account for the benefit of accurate DTOA estimation.

When recording signals at both cable ends, it can be assumed that the mutual difference between the sampling clock frequencies at both ends, changes linearly with time. As a consequence, the DTOA estimation results have an error bias that increases linearly for PD signals present at the start of the record to PD signals at the end. The slope of the DTOA error can be determined by ensuring that two synchronization pulses are present within a data record [Wie04b]. The time differences between the two sync pulses are equal at both cable ends, and deviations of the sampling clocks manifest as deviations in the DTOA of the sync pulses. Thus by estimating the

sync-pulse arrival time difference, the error in the PD signal DTOA due to time-base wander can be corrected. Assume the time-base at the far-end sensor is to be aligned to the time-base at the near end, the corrected PD signal TOA estimate at the far end $\hat{\tau}_{\mathrm{f,c}}$ is computed as

$$\hat{\tau}_{\mathrm{f,c}} = \frac{\Delta\hat{\tau}_{\mathrm{sync,n}}}{\Delta\hat{\tau}_{\mathrm{sync,f}}}\ \hat{\tau}_{\mathrm{f}} \tag{6.16}$$

where $\Delta\hat{\tau}_{\mathrm{sync,n}}$ and $\Delta\hat{\tau}_{\mathrm{sync,f}}$ equal the differences in arrival times of the sync pulses at the near-end and far-end termination, respectively. Formally, the ratio of $\Delta\hat{\tau}_{\mathrm{sync,n}}$ and $\Delta\hat{\tau}_{\mathrm{sync,f}}$ is Cauchy distributed, since both estimators are independent Gaussian variables. However, since the sync pulses DTOA estimation quality is much better than the PD signal TOA estimation quality, the correction factor can be considered as being deterministic. Consequently, the corrected PD signal TOA estimate is again a Gaussian variable, with variance approximately equal to the original estimate, since the correction factor is close to unity.

6.5 Simulation Results

In this section, PD location is evaluated for typical on-line measurement situations. Similar to Section 5.5, results are presented for simulation experiments, based on the signal and disturbance characteristics, observed in the tentative measurements. Firstly, the ability to extract reflected PD signals is examined. Subsequently, PD source location accuracy using two-sided measurements, is evaluated.

6.5.1 Reflected Partial Discharge Signal Extraction Performance

TDR can only be applied to defect location only if PD signal reflections at one cable termination can be extracted at the other termination. In this section, the reflection extraction performance for typical on-line situations is evaluated in order to test if defects can be located using TDR. Similar to the experiments described in Section 5.5, the reflection extraction performance, i.e. the number of extracted PD signals divided by the total number of PD signals, was evaluated. In order to ensure that the algorithms do not give false results, the detection threshold of the maximum correlation detector was set to 5 times the expected average noise power at a matched filter output. For this reason, false alarms are insignificant, and can be neglected.

Reflected PD signals originating within a uniform 12.5 kV 3×95 mm^2 PILC cable were simulated for various propagation path lengths and discharge magnitudes. In the first experiment, the cable was terminated at each side to identical RMUs consisting of a distribution transformer and two cable terminations. In the second experiment, the far-end RMU contained only a transformer and no outgoing cable. Typical noise and radio broadcasts were simulated, equivalent to the situations described in Section 5.5. In the first experiment, the power spectral density function (PSDF) of the noise and continuous periodic interferences equals the PSDF depicted in the right-hand plot in Fig. 5.14. This simulation experiment corresponds to experiment 2 in Section 5.5. The PSDF of the second simulation experiment is depicted in the left-hand plot in Fig. 5.14. This simulation experiment corresponds to experiment 3 in Section 5.5.

The sensor signals were simulated as if obtained by a current transformer (CT) installed at the near cable end, around the cable earth screen past the last earth connection. For each path length and magnitude, 150 PD signals were simulated and

Experiment 1			
Q_{app} [nC]	$Q_{\text{app},d}$ [nC]	SPIAR	$\overline{\text{SNR}}$ [dB]
10	0.15 ... 2.83	$2.0{\cdot}10^{-3}$ ... 0.2	-42 ... 1
20	0.30 ... 5.65	$4.0{\cdot}10^{-3}$ ... 0.4	-36 ... 7
50	0.75 ... 14.1	$9.0{\cdot}10^{-3}$ ... 1.0	-28 ... 15
100	1.49 ... 28.3	$1.8{\cdot}10^{-2}$ ... 2.0	-22 ... 21
Experiment 2			
Q_{app} [nC]	$Q_{\text{app},d}$ [nC]	SPIAR	$\overline{\text{SNR}}$ [dB]
10	0.22 ... 2.60	$2.1{\cdot}10^{-2}$ ... 1.1	-27 ... 19
20	0.43 ... 5.21	$4.3{\cdot}10^{-2}$ ... 2.2	-21 ... 25
50	1.09 ... 13.0	0.1 ... 5.5	-13 ... 33
100	2.16 ... 26.0	0.2 ... 11	-7 ... 39

Table 6.1 *Signal quality of the simulated PD signals for the different experiments.*

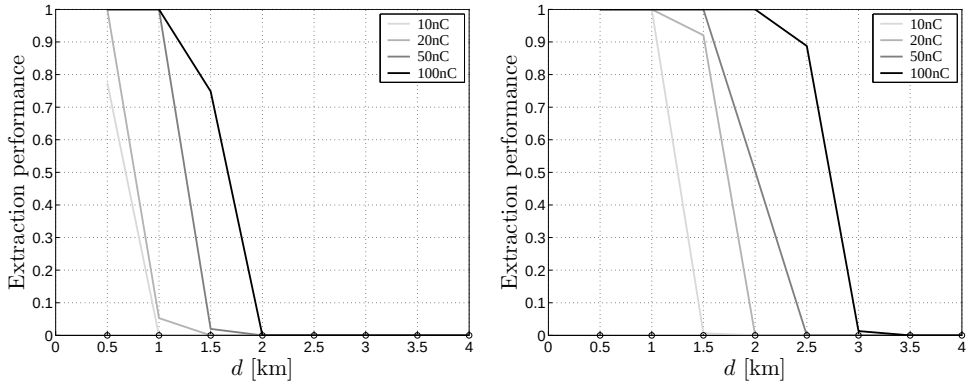

Figure 6.8 *Theoretical evaluation of reflected PD signal extraction performance as a function of the propagated distance for simulation experiment 2 (left) and 3 (right) for various apparent charge magnitudes. Circles on the horizontal axes indicate the simulated defect locations.*

spread among 20 ms records of measurement data. In Table 6.1, the average SNRs and SPIARs of the reflected signals are listed for the simulation experiments. In addition, the values of the detected charge according to Eq. 5.20, but computed from the reflection, are shown in the table as well.

In Fig. 6.8, the reflection extraction performance are depicted for experiment 1 and 2 in the left and right-hand plot, respectively. In the first situation, the propagation channel characteristic impedance and the load impedance were relatively similar in a broad frequency range, since an outgoing cable connection was present. As a consequence, reflections on the far-end termination are small. In addition, the noise and interference levels were relatively high, thus the quality of the reflected signals is generally low. This experiment represents a worst-case scenario for reflection extraction. Fig. 6.8 shows that only PD signals with large magnitudes can be extracted in this case, and only for relatively short propagation distances. An RMU with only a single cable termination has a substantially higher impedance in the low frequency range, and the amount of reflected signal energy is much higher compared to the previous

case. Moreover, the measurement conditions in experiment 2 were relatively good, since the disturbance levels were low. Although reflected signals can be extracted for longer distances propagated, the extraction performance is insufficient for TDR-based location in long cable connections. It can be concluded that on-line PD source location by means of TDR can only be done in a limited number of measurement situations, i.e. on short cables and under low noise and interference levels.

6.5.2 Location Accuracy for Two-Sided Measurements

In the majority of on-line measurement situations, discharging defects can be located by extracting PD signals at both cable ends. In order to evaluate the location accuracy, the results of simulation experiments 2 and 3 as described in Section 5.5 are used. For convenience, the simulation description is briefly repeated here. A 4 km long cable system was modelled, consisting of 20 sections of 200 m length where the odd sections were 12.5 kV 3×95 mm^2 PILC cables and the even sections were 10 kV 3×95 mm^2 PILC cables. In experiment 2, the cable system was terminated at both ends to identical RMUs consisting of a distribution transformer and two cable terminations. In experiment 3, the near-end RMU contained a single cable termination and a distribution transformer. Sensor signals were simulated as if obtained by CTs installed around the cable earth screen past the last earth connection. Typical disturbance were added to the simulated signals, with equal characteristics for the measurements at each cable end. In experiment 2, the noise and disturbance levels were higher than in experiment 3, especially between 1 and 5 MHz. In Fig. 5.14, the PSDFs of the noise and continuous periodic interferences are depicted for both experiments. In addition to the PD signals, synchronization pulses injected at the far-end termination were simulated. Artificial pulses were applied to an air coil with transfer impedance depicted in Fig. 4.2, which was installed around the cable earth screen past the last earth connection. In experiment 2, the average SNRs of the measured sync pulses were 50 dB at the injection site and 10 dB at the opposite cable end. In experiment 3, the average SNRs were 68 dB and 10 dB, respectively. The simulated sensor signals were sampled with a constant acquisition rate of 65 MSPS, so no time-base wander correction is required.

The extraction and parameter estimation results obtained from both sensor signals are used to compute the DTOA between PD signals originating from the same discharge. A DTOA look-up table was generated based on the signal model for defect locations at the start and end of each cable section. Subsequently, a piecewise approximation was applied within each section in order to relate the estimated DTOA to a defect location. In Fig. 6.9, the PD location results of experiment 2 and 3 are depicted as black dots. Only the results for 20 nC and 50 nC discharges are depicted in order to give a clear presentation of the location and apparent charge estimates. In general, the estimation results remain within the 95% confidence intervals (grey squares), which equal two times the theoretical standard deviations. A few results from false extractions are scattered arbitrarily along the cable. Apparent charge estimates are obtained from extracted PD signals with the highest average SNRs. As a consequence the magnitude estimation accuracy is better near the cable termination. The location accuracy is best for PD locations in the middle of the cable and decreases towards the terminations, since the TOA of the last arriving pulse becomes more difficult to estimate.

In the left-hand plot, it can be seen that the number of located 20 nC PDs is con-

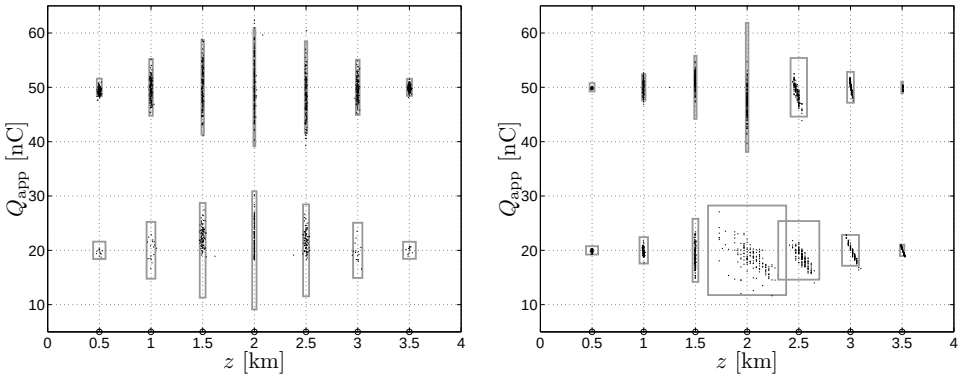

Figure 6.9 *Location results for simulation experiment 2 (left) and 3 (right) for 20 nC and 50 nC discharges. Black dots represent location estimates, grey rectangles show the theoretical 95% confidence intervals, and circles on the horizontal axes indicate the simulated defect locations.*

siderably higher near the middle of the cable system compared to PDs located closer to the cable terminations. This effect can be ascribed to the fact that in the latter case not all PD signals could be extracted at both sensors, as discussed in Section 5.5. Moreover, the magnitude estimates are biased, since measured PD signals of which the additive noise caused the filter outputs to stay below the detector threshold could not be extracted. This behavior can be regarded as a non-linearity in the estimation procedure, which results in a tendency towards slightly higher magnitude estimates. Since the fundamental lower bounds on extraction performance and estimation quality are essentially determined by noise, these limitations are not specific for the methods chosen in this thesis, but hold in general. In the right-hand plot, no 20 nC PD signals could be extracted at the near-end termination (z=0) if the signals originated more than 1.5 km from the sensor. Likewise, 50 nC PD signals could only be extracted at the near-end termination for locations up to 2 km. In both experiments, 20 nC and 50 nC discharges originating in the middle of the cable connection could be located within a 95% confidence interval of 40 m and 10 m, respectively. Likewise, discharge sites situated 500 m from a terminal could be located within a 95% confidence interval of 120 m and 60 m, respectively.

When PD signals could only be extracted at a single cable end, a matched filter based grid search was performed in order to locate the PD source. An efficient implementation was realized by starting the search on a coarse grid, with filters corresponding to only a few locations. Subsequently, the search was refined for the interval in which the defect is most likely to be present. The process was then iterated for a number of steps, until no reliable or significant increase in accuracy was obtained. Evidently, the location estimation results from a single PD signal have significantly larger confidence bounds compared to DTOA-based location. In the simulation experiments, the confidence bound amounts to 800 m for discharge sites situated 2 km from the sensor. Moreover, the method is extremely sensitive to signal modelling errors. As a consequence, it is more useful to map PD signals to a region of defect sites, rather than to a single location, which was already pointed out earlier.

6.6 Conclusions

In this chapter, PD signal location methods was discussed, which can be applied to both on-line and off-line PD signal analysis. Accurate PD location relies on the estimation of the difference in arrival times of signals originating from the same discharge. If PD signals, reflected on one cable termination, can be extracted at the other termination, TDR can be applied to locate insulation defects. However, in on-line PD measurements the cable system remains connected to the grid and relatively small load impedances are nearly always present. The quality of the reflected signals can be low, and TDR can generally not be applied, as was shown by simulation experiments. Consequently, sensors at both cable ends are required to accurately locate discharging defects.

A DTOA estimate can be related to a location by the channel propagation velocity. However, due to dispersion and attenuation introduced by the propagation path, assignment of a single velocity results in a location estimation bias. By simulating PD signals using the signal model, the location error can be predicted and corrected.

Instead of DTOA-based location, discharging defects can be located by comparing measured PD signals to a signal model. By selecting the parameter values that maximize the likelihood of the model, the most likely location estimate is obtained. The relation between the defect location and the resulting PD signal(s) at the sensor(s) is non-linear, and the maximum-likelihood estimate can only be found by evaluating a test statistic. Depending on the measurement topology, either one-sided or two-sided, different likelihood functions apply. If only a single PD signal can be extracted, the ML location estimator explicitly exploits the dispersion and attenuation of the propagation path. If analysis of two PD pulses forms the basis of defect location, errors due to dispersion are implicitly corrected. The variances of the ML estimators can be derived from the likelihood functions and can be regarded as lower bounds on location accuracy. As expected, the accuracy of the DTOA-based method and the theoretical lower bound coincide for the majority of defect locations if two PD pulses can be extracted. Consequently, DTOA-based location with appropriate bias correction results in ML location estimates. If the signal quality of one of the PD pulses is substantially higher compared to the other signal, the two-pulse estimator essentially reduces to the single-pulse location estimator. In this case, the most likely defect location can only be estimated by a search for the global maximum of the test statistic on a fine parameter grid. However, since the waveshapes do not differ appreciably for PD signals originating close to each other, the estimation variance can be large. Consequently, a coarse grid search using matched filters is generally sufficient to approximate the ML location estimate.

PD location using a two-sided measurement topology requires synchronization of the measurement equipment. One patented method, already successfully applied in off-line PD measurements, utilizes the global positioning system to align the time bases of data records obtained at both cable ends. Another option to achieve time-base alignment is by injection of synchronization pulses at one cable end and detection at the other end. This method has been patented as well. If sufficient energy can be injected, synchronization by pulse injection outperforms GPS-based synchronization. If large data sets are recorded, the digitizer sample clocks may deviate during acquisition. To correct for the resulting time-base wander, a method using multiple synchronization pulses can be applied.

The proposed methods were evaluated using computer-simulated PD measurement data, with characteristics based on the tentative on-line measurements. The results show that the accuracy of the location algorithms corresponds well to the theoretical bounds. In the simulation experiments, discharges of at least 20 nC could be located in a 4 km long PILC connection under difficult measurement conditions. Clearly, the location accuracy depends on the signal quality and thus on the discharge site and magnitude. For example, 20 nC and 50 nC discharges originating in the middle of the cable connection could be located within a 95% confidence interval of 40 m and 10 m, respectively. Likewise, discharge sites situated 500 m from a terminal could be located within a 95% confidence interval of 120 m and 60 m, respectively. If PD signals could only be extracted at one sensor, a grid search was performed in order to locate the defect based on the single signal. The inaccuracy of this method can be high and amounts to 800 m for discharge sites situated 2 km from the sensor. Moreover, the method is extremely sensitive to modelling errors and its practical applicability is very limited. As a consequence, it is more useful to map single PD signals to a region of possible discharge sites, rather than to a single location. Nevertheless, it can be stated that, in principle, model-based location using a single-pulse is feasible for PD signals with high SNR.

Evidently, the performance of the proposed methods depends to a large extent on the specific characteristics of the cable system under test, the disturbance present in the measurements, as well as the quality of the signal model. Therefore it should be noted that the simulation experiments only serve as illustrative examples.

Chapter 7

System Design and Experimental Results

7.1 Introduction

In this chapter, a measurement system prototype for on-line partial discharge (PD) signal detection and defect location is proposed, based on the research results presented in this thesis and in [Wie05]. Since signal analysis is the main research topic of this thesis, the discussions are mainly focussed on that aspect of the measurement system. More details on other parts of the system design can be found in [Wie05]. The system proposal is primarily intended as a proof of concept; therefore system requirements related to aspects such as efficiency are not addressed. In order to enable rapid prototyping, measurement control and analysis software is developed for a personal computer (PC) utilizing a high-level programming language, viz. Labview (National Instruments). As discussed in Chapter 6, PD detection at both cable ends is required to accurately locate discharging defects in on-line power cables. To that end, a two-sided measurement system is developed consisting of equipment that is installed in full-scale ring main units (RMUs) at both cable ends. In Section 7.2, the basic principles of the system proposal are presented. An overview of the measurement system is given, as well as a description of the software architecture and integration of signal analysis algorithms.

The performance of the measurement system prototype is evaluated by conducting experiments in a controlled environment. In the first part of Section 7.3, the system is validated using measurements of artificial PD signals introduced in an experimental set-up. The results are compared to results obtained from conventional off-line measurements. Time-base alignment techniques are tested and it is shown that the system prototype enables accurate location of discharges. In the second part of Section 7.3, a discharging defect is created deliberately in the experimental set-up. It is shown that the defect can be identified and located with the on-line measurement system. In addition, some parameters that are useful for the purpose of defect characterization, are quantified. Again the results from both on-line and off-line measurements are discussed. In this context it should be noted that off-line measurements are conducted mainly manually by measurement experts, while the on-line measurements are fully automated. Consequently, the comparison implicitly comprises two areas, namely on-line compared to off-line measurements and manual to automated measurements.

7.2 Measurement System Prototype

This section gives a description of the measurement system proposal. In Section 7.2.1, a conceptual overview of the system prototype is given and the basic concepts are discussed. Section 7.2.2 describes calibration of the measurement equipment. A software model of the proposed system is briefly discussed in Section 7.2.3; more details on the software model can be found in [Wie05]. In Section 7.2.4, integration of signal analysis algorithms within the measurement system prototype is described.

7.2.1 System Overview

As discussed elsewhere in this thesis, a split-core current transformer (CT) is utilized as a sensor for on-line PD detection. The inductive probe is installed around the cable screen past the cable earth connection, so there is no galvanic coupling to high-voltage conductors and the sensor itself cannot become a cause of failure. In Fig. 7.1, a sketch of the measurement system hardware is depicted. An additional sensor can be installed on the transformer cable earth connection in order to determine the direction of arrival (DOA) of detected signals. The sensor signals are digitized using a multi-channel 12 bit data acquisition (DAQ) card with a maximum sampling rate of 62.5 MSPS. Although the DAQ system may be somewhat overdimensioned, it is assured that the performance of the measurement system prototype is not restricted by digitization, which justifies the approach. Depending on the channel attenuation, the channel load impedance and the propagated distance, measured PD signals can be small. Consequently, the sensor may not provide sufficient sensitivity to fully exploit the digitizer dynamic range; therefore the signals are amplified prior to digitization. In order to prohibit damage of the DAQ system by large transients or electrostatic discharges, the measurement apparatus is equipped with surge arresters that clip the sensor signals if the digitizer maximum input range is almost exceeded. Evidently, the system hardware is well-shielded and common-mode currents are effectively conducted to the earth, such that proper electromagnetic compatibility is achieved.

In on-line measurements, interference amplitudes can be much higher than PD signal amplitudes. Consequently, data acquisition triggered by PD signals is generally not applicable and a block-based approach is chosen for the system prototype. Data blocks the size of a single grid operating voltage cycle are analyzed, viz. 20 ms in the Netherlands, which an obvious but not a necessary choice. In principle, only a small percentage of defect discharges have to be detected for the purpose of on-line power cable diagnostics, since in the long term enough PD signals can be extracted to enable defect characterization. Consequently, a relatively large processing delay is accepted for the measurement system prototype.

Generally, PD detection at both cable ends is required to accurately locate discharging defects in on-line power cables. Consequently, a two-sided measurement system is proposed consisting of distributed components both in hardware and in software, which exchange information via some communication link. A transparent communication link between the various measurement system components can be realized using e.g. a local area network, analogue telephone modems, digital subscriber lines, wireless connections, etc. The exact implementations of the network and physical layers are not discussed in this thesis, and it is assumed that some communication network is available (refer to [Wie05] for details). Using the same network (or another), a third PC can be situated at a different location, which enables remote control

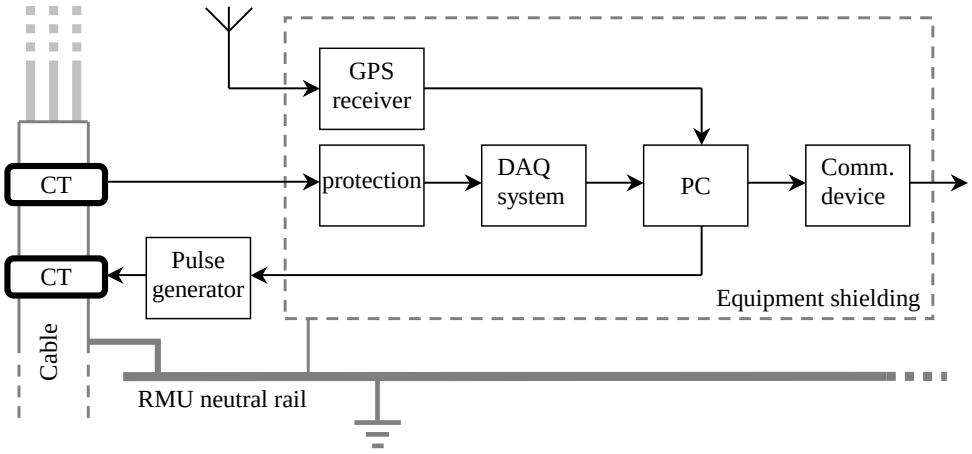

Figure 7.1 *Sketch of the measurement system hardware as installed at a cable termination within an RMU.*

of the measurement system as well as retrieval of analysis results.

A two-sided measurement topology requires synchronized data-acquisition for the purpose of accurate defect location. As discussed throughout this thesis, the global positioning system (GPS) can be used to obtain time-base references. In addition, by injection of synchronization pulses at one cable end and detection at the other, time-base alignment can be achieved. The measurement system prototype employs both synchronization methods. The patented GPS-based method, which was designed and implemented by KEMA [Aar98, Ste01], is already successfully applied in off-line PD measurements and serves as a reference. The pulse-based method is introduced as a new synchronization technique, having both practical and economical advantages over the GPS method. For the purpose of pulse injection, the measurement system prototype is equipped with a custom-made transient generator, designed by the Eindhoven University of Technology (TU/e) [Wou03a, Wou03b, Tal04]. A custom-made Rogowski injection CT is utilized to transfer a transient to the cable system. Like the sensors, the injection CT is installed around the cable earth screen past the last earth connection. In this chapter, only processing of synchronization pulses for the purpose of time-base alignment and system identification is discussed. The implications of pulse synchronization for the measurement system design and the associated practical aspects are studied thoroughly in [Wie05]. The measurement equipment can operate in two synchronization modes. In the GPS synchronization mode, data acquisition is started at predefined time-instants, which are retrieved from the GPS and do not deviate more than 100 ns. In addition, the digitizer clock is referenced to a clock signal obtained from the GPS, which has an accuracy of 10^{-12}. In the pulse synchronization mode, the digitizers at each cable end are programmed to trigger on the injected synchronization pulses. Clearly, in this case the amplitudes of the sync pulses must significantly exceed the noise and interference levels.

Due to environmental influences, the sampling clock of the DAQ system may deviate during acquisition of large data records. As discussed in Section 6.4, time-base wander can be corrected by measuring the difference time of arrival between two

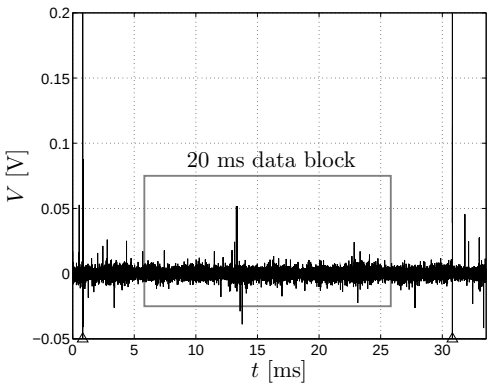

Figure 7.2 *Example of measurement data with synchronization pulses, which are denoted by triangles on the time-axis. A data block of at least 20 ms is selected for analysis.*

successive synchronization pulses. For the measurement system prototype, the time-delay between two sync pulses was chosen equal to 30 ms, such that the response of the cable system to the injected signals is completely attenuated within the 20 ms of data to be analyzed, as depicted in Fig. 7.2. The data block size was chosen slightly larger in order to enable proper acquisition of the sync pulses as well. A general-purpose PC cannot handle the resulting data flow in real-time; therefore the DAQ system is equipped with 2 MS of onboard storage memory in order to enable acquisition of at least 30 ms data blocks at the maximum sampling rate. Sync pulse repetition is implemented in the transient generator hardware [Tal04, Wie05].

Prior to PD detection, measurements of cable system properties are conducted; therefore the system can operate in two measurement modes. In the identification mode, pulses are first injected at one cable end, and measured at both ends. Then pulses are injected at the other cable end. This approach enables measurement of the cable system properties as discussed in Chapter 4. The amplitudes of the injected pulses are set as high as the digitizer input range allows, in order to attain the highest signal to noise ratio (SNR) possible. In the PD detection mode, synchronization pulses are injected at one cable termination. As mentioned, the amplitudes of the injected pulses are set high enough such that the digitizers at both cable ends trigger only on the sync pulses.

7.2.2 Calibration

Evidently, proper calibration is essential for any measurement apparatus. For the measurement system prototype, the current flowing through a conductor enclosed by a CT must be related to the DAQ system output signal. To that end, the CT is installed on a calibration set-up, which is basically a well-defined loop that shorts some impedance. The CT output is connected to the cascade of an amplifier, a surge arrester and the DAQ system. A wide-band transient is injected into the loop, and the output signal of the DAQ system is recorded. Simultaneously, the current in the loop is measured using a calibrated current probe (Tektronix A6302) and amplifier (Tektronix AM503), and its output signal is directly applied to another channel of the DAQ system. Now the transfer function of the two DAQ channels is obtained.

Generally, measurement noise is additive white Gaussian under laboratory conditions; therefore the accuracy of the calibration transfer function is improved by averaging the results of multiple measurements. Since the transfer functions of the amplifier and the surge arrester are almost linear within the DAQ system bandwidth, the calibration transfer function is approximately equal to the transfer impedance of the measurement CT, but scaled by the amplification factor. Clearly, the calibration transfer function must be determined for all sensors that are in use.

Excitation of the cable system with a known signal, forms the basis of model parameter measurements described in this thesis. To that end, a current is injected into the calibration set-up using the transient generator and the injection CT, and the induced current is measured with the calibrated probe. The impedance of the calibration set-up is determined using a calibrated network analyzer (HP8753C). Subsequently, the injection voltage transient is directly obtained from the induced current and the calibration set-up impedance. For the purpose of cable system identification, signals are injected at both cable ends; therefore the injection transients generated by the equipment at both cable ends are measured. If the injection CT and the sensor cannot be spaced sufficiently far, mutual coupling may exist. Prior to installation, the transfer between the CTs can be estimated and compensated for during measurements. For more details on calibration and compensation see [Wie05].

7.2.3 Software Architecture

The two-sided measurement system requires a software architecture consisting of components that are distributed among multiple PCs. The equipment at each cable end is controlled by a software component referred to as a measurement unit (MU). The functionality of the complete measurement system, including the MUs, is controlled by another software component, namely the measurement manager (MM). For the purpose of discharge monitoring and cable diagnostics, the ability to retrieve analysis results at a remote location is desirable and is realized by a remote user interface (RUI). Moreover, an advanced user interface (AUI) allows access to all software components for development and maintenance purposes. A data bank (DB) is employed, which enables storage and retrieval of various kinds of data, such as measurement results, configuration settings, etc. In Fig. 7.3, a component collaboration diagram is depicted. The distributed software architecture allows easy integration of additional software components, such as a monitoring or a notification system that acts as an end-user and can interpret measurement results. High-level communication between the software components is message-switched, which enables a very flexible implementation of the physical network. However, Labview only supports dataflow-driven communication between programs; therefore message handlers were designed that realize an event-driven structure. Transport-level communication is based on the TCP/IP, which was chosen because of its flexibility and popularity. Consequently, the actual locations of the measurement manager and user interface are arbitrary, as long as TCP/IP connections between the components exist. Apart from maintenance tasks, data retrieval and equipment initialization, the behavior of the measurement system comprises mainly two functionalities, viz. cable system identification and PD detection. Both are elaborated in the next section. The overall behavior of the measurement system is controlled in a simple top-down manner; e.g. at the RUI, a system operator initiates PD detection by sending a message to the MM, which again translates the command and routes appropriate message sequences to the MUs. As

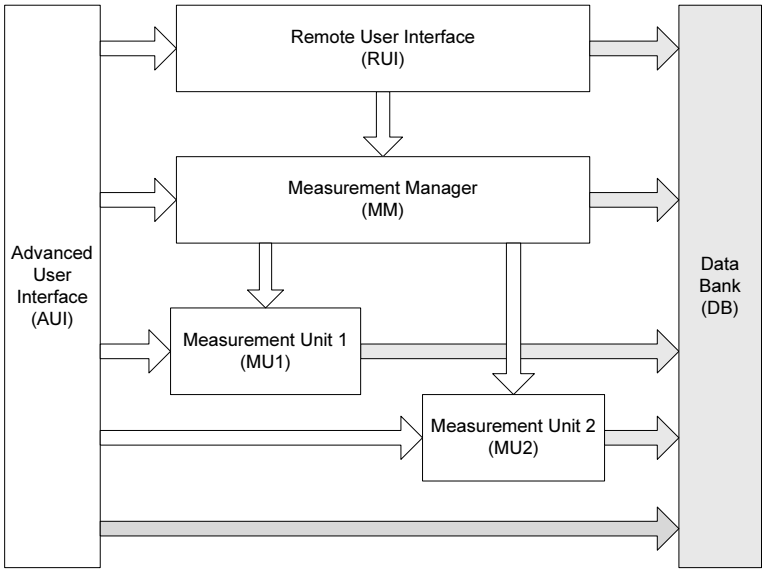

Figure 7.3 *Software component collaboration diagram. Arrows indicate the initiative for functional messages (white) or data transfer (grey).*

an example, in the next section a sequence diagram is depicted in Fig. 7.5, which visualizes the message flow between the various software components in case of cable system identification.

Once PD detection is started, the MM repeats measurements, such that semi-continuous monitoring of PD activity is achieved. Clearly, this behavior results in huge amounts of data that have to be processed. However, the measurement data is only stored locally at the PC where the data is analyzed for PD signal extraction. In order to reduce the communication channel load, extracted PD signals are parameterized by an MU and primarily extraction results are transferred to other software components. In addition, expert-rules, based on a priori knowledge of finite-energy disturbances, attempt to reject false extractions and then prohibit transfer. This is discussed in the next section.

The MM gathers extraction results from both MUs and, by proper combination, detection results are produced. For each detected PD, the data bank maintains references to extraction results and original measurement data, for the purpose of debugging and backtracking of the system behavior. In addition, detection results are associated with system information, including parameters related to configuration of the software component and measurement equipment. A part of the data structure is visualized in Fig. 7.4. Moreover, status, warning, and error messages produced by various sub-programs are stored for all software components. As a consequence, the databank is distributed among the PCs where the software components are installed. In principle, the databank is completely transparent, and the AUI can retrieve and organize all data from the bank at a remote location. Clearly, at some moment no more data can be stored on a computer hard disk drive; therefore the data is managed dynamically, i.e. after a certain time the measurement data are removed and associations are deleted.

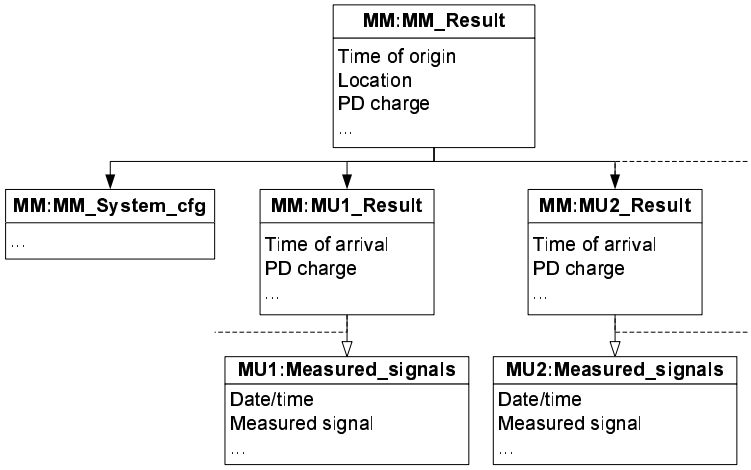

Figure 7.4 *Part of the measurement system data structure. Each PD detection result (MM_result) references to a set of extraction results (MU1_result, MU2_result), which again refer to the measured signals stored. Local and remote references are denoted by closed and open arrows, respectively.*

7.2.4 Description of Signal Analysis Algorithms

Based on the research presented in this thesis, PD signal analysis algorithms were developed. This section provides an overview of the algorithms and discusses integration within the measurement system prototype.

Cable System Identification

System identification measurements are conducted for the purpose of cable model parameter estimation. In the identification mode, the MM first commissions one of the MUs to inject pulses. The transient generator has a digitally adjustable gain, which can be programmed using the parallel bus of a PC. As mentioned, the amplitudes of the injected pulses are set as high as the digitizer input range allows, in order to attain the highest SNR possible. Moreover, the MM commands both MUs to perform data acquisition triggered by the injected pulses; therefore the transients must greatly exceed the noise and interference levels. The cable system response to an injected pulse is recorded at both cable ends. In addition, an estimate of the noise and periodic interference power spectral density function (PSDF) is obtained by computing the averaged periodogram (Eq. 5.16) of a number of data records without pulse injection. As discussed in Chapter 4, model parameter estimation relies on the extraction of signals that are reflected on impedance transitions within the cable under test and on the far-end load impedance. Besides reflections from the cable system under test, reflections from adjacent cables may be detected as well. Therefore the signals measured by the CTs installed on the transformer cable earth connections are also recorded in order to determine the reflection DOA. Subsequently, the MM initiates pulse injection at the MU at the other cable end, and the procedure is repeated. As an example of the message flow between the software components, the sequence diagram for cable system identification is depicted in Fig. 7.5.

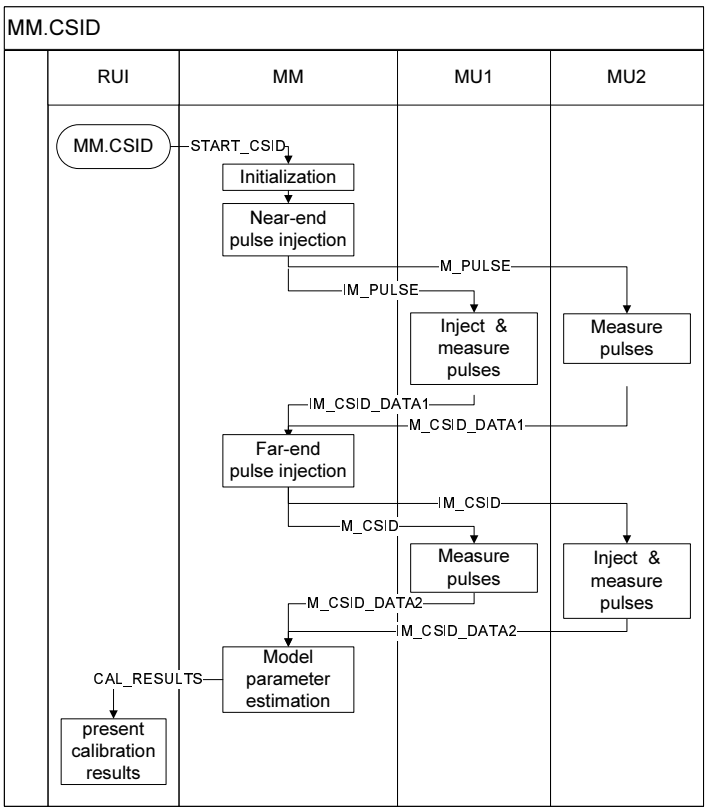

Figure 7.5 *Sequence diagram of the message flow between the various software components in case of cable system identification. Arrows indicate messages and boxes represent processes as initiated on a software component.*

When the identification measurements have been performed, the MM collects the measurement data from both MUs. Based on prior knowledge of the cable system provided by the utility, the cable section lengths and the locations of impedance transitions are known approximately. Although velocities can differ among cable types, they have the same order of magnitude, and intervals can be defined in which reflections will occur. When the reflection intervals have been determined, the injected and reflected signals are selected from the cable response. Subsequently, the DOA of the signal within a reflection interval is determined by evaluating the directions of the currents measured by both CTs, as described in Section 3.2. Only signals that are identified as reflections from the cable under test, are used for further processing. Accurate knowledge of the channel delay and propagation velocity is essential for the purpose of partial discharge location. In the pulse-based synchronization mode, these parameters can only be estimated if a reflection on the far end can be extracted. If this is not the case, the cable system must be temporarily disconnected from the grid in order to determine the propagation parameters. In the GPS-based synchronization mode, the time-bases of the DAQ systems at both cable ends are aligned, and a far-end reflection is not required to estimate the cable propagation delay and velocity.

At each cable end, the injected signal obtained from the cable response is directly

proportional to the near-end admittance (Eq. 4.2). The admittance is estimated by considering the injection voltage transient obtained by calibration, and the induced current. Subsequently, the transfer function between the injected signal and the far-end reflection is computed for both identification measurements. Then the characteristic impedances are estimated using the iterative minimization method described in Section 4.3. Using the load admittances and the cable characteristic impedances, the transmission coefficients at each cable end are computed (Eq. 4.5). Subsequently, the propagation parameters of the cable system are obtained by evaluating the reflection transfer functions as described in Section 4.4. The transmission coefficients and the propagation parameters are stored in a look-up table, which is referred to as the cable model. After interpretation of the identification measurements, the MM transmits the cable model to both MUs where it is used for adaption of the extraction algorithms.

In the PD detection mode, one of the MUs injects pulses for the purpose of synchronization. Time-base alignment is then achieved using arrival-time estimates of the sync pulses. The averaged signals obtained in the identification measurements are used as templates for sync-pulse time of arrival estimation by matched filtering and are therefore stored in the databank.

Partial Discharge Signal Extraction

In the PD detection mode with pulse synchronization, the MM initiates a measurement and commissions one of the MUs to inject two sync pulses. Pulses are injected at the RMU with the lowest impedance, which is known from the identification measurements. The MM commands both MUs to perform data acquisition triggered by the injected pulses. When a digitizer triggers on the first sync pulse, 2 MS of data are acquired by the DAQ system. Prior to PD signal extraction, a matched filter is applied to estimate the sync pulse arrival times using the pulse templates obtained from the system identification measurements. In a practical situation, the DAQ system might be triggered by very large finite-energy disturbances as well. However, since two sync pulses of equal energy are injected with a predefined repetition period, this a priori knowledge is used to detect false triggering, thus enabling robust synchronization.

When the sync pulses have been correctly detected, a data block in between the two sync pulses is selected for further processing. Noise as well as radio broadcasts can be considered stationary during a cycle of the grid operating voltage. Consequently, an estimate of the noise and periodic interference PSDF is obtained by computing the averaged periodogram of the data record (Eq. 5.16). Based on the periodogram, a bank of notch filters is designed for radio broadcast suppression as well as a broadband filter for background noise whitening, as discussed in Section 5.3. Subsequently, the data record is fed through the total whitening filter, consisting of the cascade of notch filters and the broadband filter. The resulting signal is applied to a matched filter bank (MFB), as described in Section 5.3. The matched filter templates are computed based on the cable model obtained from the system identification measurements and the calibration transfer function. In principle, the optimal templates should be selected based on the noise power spectral distribution as well. However, in the tentative measurements it was observed that the noise PSDF does not vary much among subsequent data records. As a consequence, the templates are only recomputed when large noise power variations are detected.

Each MFB output signal is compared to a threshold based on the expected average noise power in the filter output (Eq. 5.13). When the threshold is exceeded, the

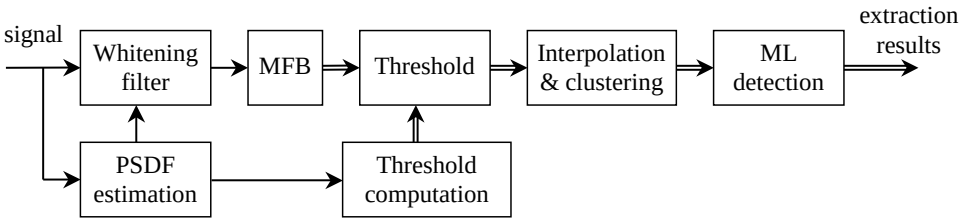

Figure 7.6 *Schematized visualization of partial discharge signal extraction.*

local absolute maximum within the filter output is determined and the optimum is obtained by local parabolic interpolation. Subsequently, the matched filter scaling factor is estimated from the local optimum (Eq. 5.5), and the a posteriori likelihood of the matched filter is computed (Eq. 5.9). For each threshold excess in a filter output signal, the intermediate result is parameterized by saving the likelihood, the scaling factor and the occurrence time, i.e. the PD signal time of arrival (TOA) estimate. Since only these intermediate results are of interest for further processing, the filter output signals themselves do not have to be stored. Therefore all filtering algorithms described above are implemented according to a block-based approach, thus saving working memory. The maximum filter outputs do not necessarily occur synchronously; therefore a clustering algorithm combines intermediate results that occur within some period of threshold excess. Based on the cable model, the spread of the maximum filter responses can be computed a priori to produce the clustering interval.

The clustered intermediate results are applied to the maximum-likelihood (ML) detector, which selects the most likely filter and passes the corresponding extraction results. In Fig. 7.6, a schematic representation of the extraction algorithm is depicted. As described in Section 6.4, the arrival times of both sync pulses are used to construct a time base, independent of the DAQ system, in order to correct for linear time-base wander (Eq. 6.16). Subsequently, the PD signal TOA estimates in the extraction results are related to the first sync pulse TOA, and mapped onto the corrected time-base. Parallel to the ML detector, the clustered filter responses are compared to an expected pattern computed from the cable model. As discussed in Section 5.4, the difference between the measured and expected patterns is used as a criterion to reject finite-energy disturbances of which the waveshapes deviate significantly from PD signals. To that end, an expert-rule is implemented, which removes false extractions.

An additional sensor, installed on the transform cable earth connection, is utilized in order to reject finite-energy disturbances by DOA discrimination. Analog to signal detection using the sensor on the cable termination, pulses are extracted by application of the algorithm as described above. In this case, the transfer function between the sensor positions is embedded in the MFB in order to match PD signals detected in the transformer cable earth connection. Subsequently, signals that have not propagated through the cable connection under test, are identified as finite-energy disturbances and are rejected.

Partial Discharge Source Location

The MM gathers the extraction results from both MUs when a number of measurements have been conducted. The extraction results from one MU are shifted by the cable propagation delay, such that the local time-bases at both MUs are properly aligned (Eq. 6.14). Subsequently, the MM combines results that originate from the same discharge. Basically, the combination algorithm creates pairs of extraction results of which the absolute difference in time of arrival (DTOA) is smaller than the cable propagation delay. Evidently, the combination algorithm implicitly rejects finite-energy disturbances, since extraction results of which the DTOA equals the cable propagation delay do not form valid pairs. Moreover, PD signals detected at both cable ends have the same polarity if originated within the cable, while PD signals from other equipment and propagating to the cable are oppositely directed. Both expert rules enable effective rejection of disturbances that have not yet been identified at an MU. Note that in practice, the DTOA combination criterion is defined slightly smaller than the cable propagation delay (e.g. 100 ns), in order to account for signal DTOA estimation variance. Consequently, robust rejection of finite-energy disturbances is achieved; however, PD signals originating very close to the cable terminals (e.g. up to 1 % of the cable length) are rejected as well. Since such signals can be distinguished from disturbances by DOA or waveshape discrimination, they can simply be mapped on the cable terminations, without accurate location.

If two PD signals, originating from different locations arrive at a sensor with a small difference in time, the combination algorithm can result in ambiguous solutions, since more than two pairs of extraction results meet the combination criterion. However, it is highly unlikely that the two PD signals have the same magnitude and polarity; therefore this prior knowledge is used by an expert-rule in order to remove false combinations. Moreover, if still false combinations are made, the location results will be mapped arbitrarily on the cable length and will not result in concentrations on very well-defined positions.

The extraction results are related to the discharge location using the cable model. As discussed in Section 6.2, the function that maps a DTOA estimate to a location, can be non-linear, if the cable system under test consists of sections with different propagation velocities. Based on the cable model, a look-up table is constructed that assigns a range of DTOAs to each section. For each section, a function is composed that relates a DTOA to a location (Eq. 6.2), and compensates for estimation bias due to dispersion. For each combination result, the section where the pair of PD signals originates is determined by comparing the measured DTOA to the look-up table. Subsequently, the location is estimated using the mapping function for the specific section.

After application of the combination algorithm, extraction results may remain that cannot be combined, but are not identified as finite-energy interferences by means of waveshape, DOA or DTOA discrimination either. In such cases, PD signals could only be extracted at one cable end. As discussed in Section 6.3, the discharge location can still be crudely determined based on the signal waveshape. However, these location results have a much lower accuracy as compared to DTOA location, and may not have much practical value. Nevertheless, signals originating nearby the cable terminations can be located with reasonable precision.

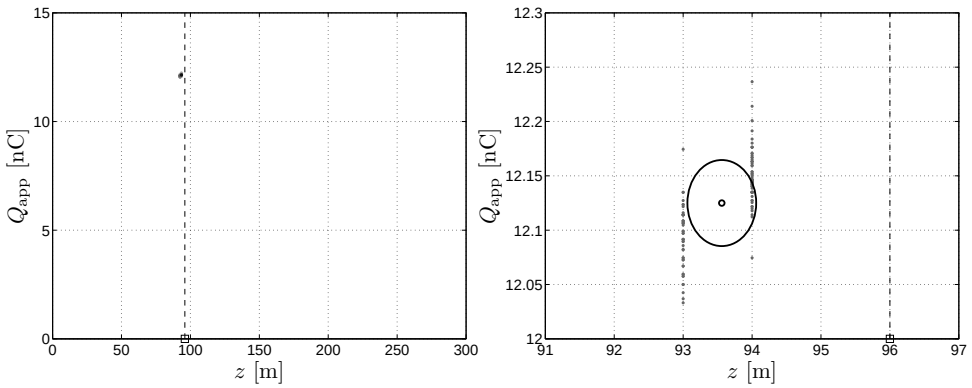

Figure 7.7 *Discharge mapping on the cable length obtained from off-line reference measurements of artificial PD signals injected in the cable joint. The right-hand plot shows an enlargement of the left-hand plot, at the joint location.*

7.3 Experimental Results

In order to validate the proposed measurement system, measurements were conducted on the full-scale experimental grid that was described in Section 1.3.4. Summarizing, the set-up consisted of a 10 kV 3×95 mm^2 paper insulated lead covered (PILC) cable of approximately 96 m length and a 12.5 kV 3×95 mm^2 PILC cable of approximately 201 m length, which were connected by a silicon-filled joint. In the first experiments, no out-going cables were connected to the RMUs. The cable connection could be energized by applying a 50 Hz three-phase voltage to the low-voltage side of the transformer in one of the RMUs.

7.3.1 Measurement System Validation

In a first set of experiments, the joint connecting the two cable sections under test was opened and a galvanic connection was made to one of the phase conductors. Subsequently, pulses were applied to the phase conductor using a transient generator. Measurements were conducted on this configuration, as if the injected pulses resulted from actual discharges; therefore the injected pulses are simply referred to as partial discharge signals. In this section, the results from off-line and on-line measurements are compared in order to validate the proposed measurement system. Evidently, the set-up was not energized in this case. Nevertheless, the results are referred to as obtained from off-line or on-line measurements in order to distinguish the applied methods.

Off-line Reference Measurements

As a reference, measurements were conducted by KEMA using conventional off-line 0.1 Hz testing equipment [Ste91]. In this case, the cable was disconnected from the RMUs and signals were measured with a capacitive sensor connected to the terminals at one cable end. The other termination was left open; therefore the discharge location could be estimated by time-domain reflectometry (TDR). Unlike normal 0.1 Hz measurements, the phase conductors were interconnected at the measurement end,

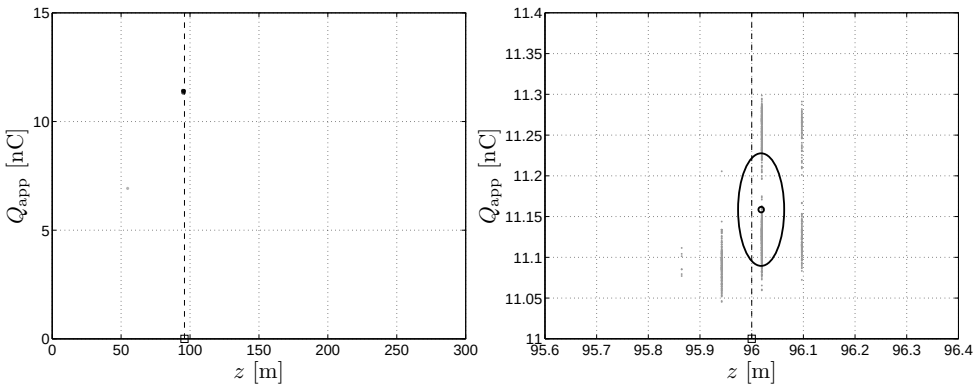

Figure 7.8 *Discharge mapping of on-line measurement results with a multi-channel DAQ system. The right-hand plot shows an enlargement of the left-hand plot, at the joint location.*

such that only signals propagating in the shield-to-phase (SP) channel, are measured, as is the case for the on-line measurement system. Prior to PD detection, the cable propagation delay was measured using a pulse generator, and an average propagation velocity was assigned for the purpose of discharge location. Furthermore, a calibration measurement was conducted in order to enable apparent charge estimation from detected PD signals [IEC00]. Data were acquired using a 100 MSPS digital storage oscilloscope, which triggers on signals that exceed a preset amplitude level. Approximately 100 signals were recorded and analyzed mainly manually but with the help of semi-automated detection software. The results from off-line measurements are depicted in Fig. 7.7, where the left-hand plot shows the results mapped onto the length of the cable connection and the right-hand plot shows an enlargement at the joint location. The joint location is indicated by a square on the horizontal axis and a vertical dashed line. The mean of the distribution is marked by a small circle, and the standard deviation is depicted as a large ellipse. It can be observed that the discharge locations are estimated 2 to 3 m away from the joint location, which is due to the fact that a single propagation velocity was used to compute location estimates. Note that in the off-line analysis method, the location estimates are mapped onto a grid with 1 m resolution.

Validation of On-line Location and Extraction

For the second experiment, the on-line measurement equipment was installed in the experimental set-up and measurements were conducted on the same configuration described previously. For the purpose of system identification, the cable under test was temporarily disconnected from the RMUs before PD detection, and, at each end, the cable terminals were shorted and connected to the RMU neutral rail, after which the cable propagation properties were measured. Subsequently, the cable was connected to the RMUs at both ends and the load impedances were estimated. Then, the pulse generator was switched on and PD signals were detected using the measurement system prototype.

The cables were wound on drums and the two RMUs were located close to each other; therefore signals could be measured at both cable ends using the multi-channel

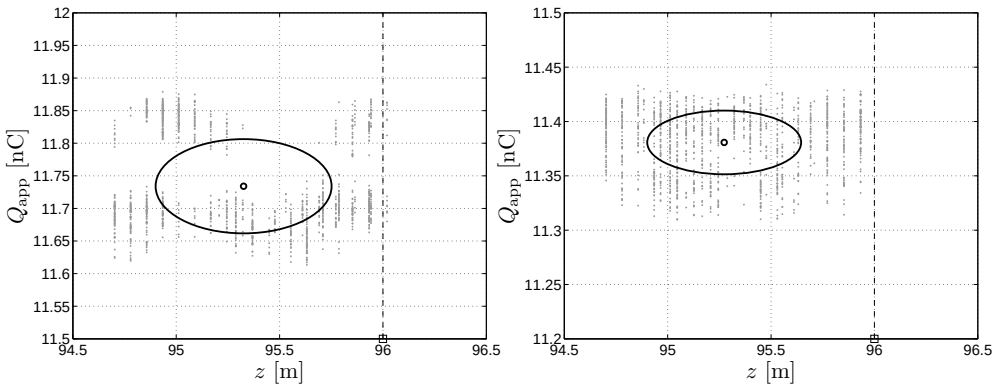

Figure 7.9 *Discharge mapping of on-line measurement results obtained with pulse synchronization. The right-hand plot shows results when the sampling rate of one of the DAQ systems was deliberately altered.*

DAQ system of one PC. In this case, synchronization was not required and data could be acquired by recording of arbitrary 20 ms blocks. In the experiment, 30 data blocks were recorded, with intervals of 1 minute in order to enable storage and processing. The data contained a total number of approximately 1200 PD signals with average SNRs of 40 dB. Fig. 7.8 shows the analysis results of on-line measurements without synchronization. In the left-hand plot, the results are mapped onto the length of the cable connection and the right-hand plot shows an enlargement at the joint location. All PD signals within the data records were correctly extracted, and only a single false extraction occurred. Again, the mean of the distribution is marked by a small circle, and the standard deviation is depicted as a large ellipse, where the false extraction was ignored. It can be observed that the discharge locations are estimated close to the joint location. Note that the locations are mapped onto a grid, which corresponds to the resolution by which DTOA estimates are stored (i.e. 1 ns). Since the on-line location algorithms account for the different propagation velocities of the cable sections, the location estimates are closer to the actual joint location as compared to the off-line results. Clearly, the mean of the distribution lies as close to the actual cable joint location as possible, given the 1 ns DTOA resolution. By comparing the off-line and on-line results it can be observed that the mean of the estimated apparent charges differ. On the one hand, this discrepancy is ascribed to errors in the signal model parameter estimates, as discussed in Section 4.5. Moreover, the extraction algorithms utilize the noise PSDF as a part of the magnitude estimation method, as described in Section 5.2. In practice, errors in the PSDF estimate occur due to the presence of e.g. finite-energy interference, which again manifest themselves as magnitude estimation bias. On the other hand, the calibration of the off-line equipment is a bit rigid [IEC00]; therefore the off-line results are not a perfect reference. Nevertheless, it can be concluded that the on-line and off-line results show good resemblance.

Validation of On-line Location with Time-Base Alignment

In the third experiment the location accuracy of the proposed measurement system using pulse synchronization was examined. Measurements were conducted on the configuration described previously, and the measurement system operated in pulse

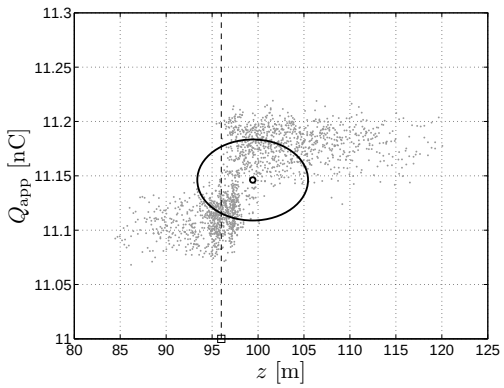

Figure 7.10 *Discharge mapping of on-line measurement results obtained with GPS-based synchronization.*

synchronization mode, as described in Section 7.2. Subsequently, at one of the MUs data was acquired with a sampling rate of 62 MSPS instead of 62.5 MSPS, while the data was analyzed as if sampled at 62.5 MSPS in order to increase time-base wander. Fig. 7.9 shows an enlargement of the analysis results at the joint location. The results without the sampling rate mismatch are depicted in the left-hand plot and the results with different sampling rates are shown in the right-hand plot. For each configuration, the results are shown from analysis of 30 data blocks obtained at 1 minute intervals, which contained a total number of approximately 1200 PD signals. Again, the mean and standard deviation of the distributions are marked by ellipses. It can be seen that location estimates are close to the joint location in both cases. Furthermore, the distributions of location estimates for both experiments show no significant difference. As a result of bias in the time-base alignment, the means of the distributions are located slightly away from the joint. In addition, time-base wander correction gives rise to more deviation in the location estimate distribution. Note that the distribution of charge estimates from both experiments slightly differ, also compared to previous results. This discrepancy is ascribed to small variations in the amplitude of the injected pulses, which occurred since the total measurement time was quite long. Moreover, bias in PSDF estimates results in small discharge magnitude estimation errors as well.

In the fourth experiment the location accuracy of the measurement system using GPS-based synchronization was examined. In this mode, data acquisition is started at predefined time-instants, which are retrieved from the GPS. Again, 30 data blocks of 20 ms were recorded, with intervals of 1 minute. Fig. 7.10 shows an enlargement of the analysis results at the joint location. Evidently, the location estimates show a wide spread due to the fact that the GPS receiver (HP59551A) provides time-labels with a deviation of 100 ns. Moreover, location estimates are biased, probably resulting from limited visibility of GPS satellites during experiments.

From the experimental results, it can be concluded that time-base alignment using sync pulses, results in accurate location estimates and outperforms GPS-based synchronization. However, it should be noted that the accuracy of GPS-based synchronization is independent of the cable length. In case of pulse synchronization, the location accuracy does depend on the cable length, since the longer the cable,

the lower the average SNR of the sync pulses received at the other cable end, thus increasing the deviation of sync pulse TOA estimates.

7.3.2 Experimental Results for an Artificial Defect

In a second set of experiments, a defect in the cable joint was deliberately created by connecting a short wire to the phase conductor. The wire ended close to the metal joint case, such that corona discharges occurred if a sufficiently high voltage was applied. In this section, the results from off-line and on-line measurements on this configuration are compared.

Off-line Measurements

In the first experiment, measurements were conducted by KEMA using the testing equipment as described previously. The cable under test was disconnected from the RMUs and energized with a 0.1 Hz high-voltage generator. The equipment was adjusted such that a 6 kV phase-to-ground voltage was generated, which was sufficient to result in partial discharges at the artificial defect. Again, signals were measured with a capacitive sensor connected to all three terminals at one cable end.

Conventionally, off-line measurements are performed by triggering on signals that exceed a sequence of predefined thresholds. In the experiments, however, a single threshold was set that was low enough to trigger on discharges of at least 100 pC, in order to produce results that can be compared to block-based measurements as obtained with the on-line equipment. Discharges were located by means of TDR, and charge magnitudes were estimated using the calibration done previously. Approximately 2000 signals were detected and analyzed with the help of semi-automated algorithms.

The results of the off-line measurements are mapped on the cable length, as depicted in Fig. 7.11. In order to emphasize the distribution of detected PDs, a grey tone is assigned to a group of results that occur in close proximity, i.e the darker the marker, the more results are clustered. The discharge mapping shows that discharges occur not only at the artificial defect, but also in many regions within the cable itself, which is inherent to mass-impregnated paper as an insulation material of 10 kV cables [Ste04]. At the joint location, merely small partial discharges occurred as a result of the artificial defect. However, the dark marker indicates that the number of discharges from this location is relatively large. From this plot it is difficult to observe the recurrence of small discharges from a specific location; therefore Fig. 7.12 (left plot) shows the number of discharges per unit length Δz normalized by the measurement time T_m, i.e. $n = \sum_j \mathrm{PD}(j\Delta z)/T_\mathrm{m}\Delta z$. When mapped onto the cable length this measure clearly indicates that discharge activity at the cable joint dominated. The plot was produced by clustering results on a grid with $\Delta z = 3$ m resolution, which was the maximal reliable location accuracy in this case. In addition, the right-hand plot shows the normalized cumulative charge $Q'_\mathrm{app} = \sum_j Q_\mathrm{app}(j\Delta z)/T_\mathrm{m}\Delta z$, which is a useful measure for the purpose of defect characterization as well [Ste04].

On-line Measurements

For the second experiment, the on-line measurement equipment was installed in the experimental set-up and measurements were conducted on the same configuration described previously. The cable was connected to the RMUs at both ends, and the

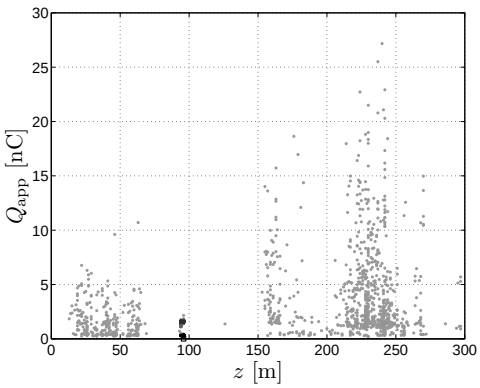

Figure 7.11 *Discharge mapping on the cable length for results obtained from 0.1 Hz off-line measurements on the cable under test.*

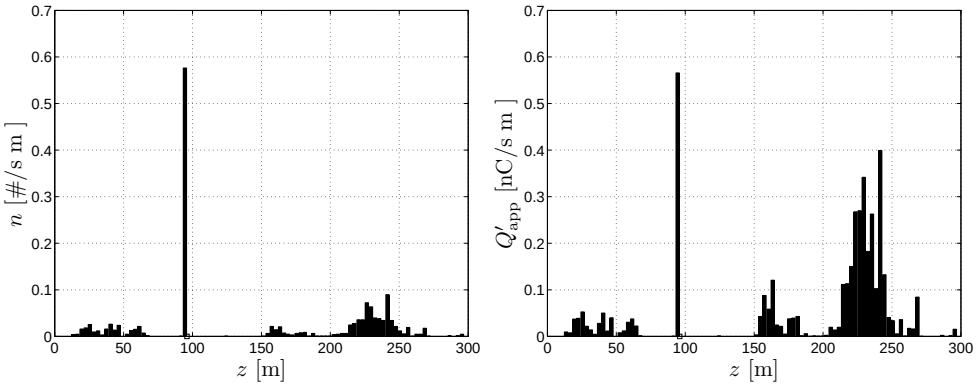

Figure 7.12 *Normalized number of discharges (left) and the normalized cumulative charge (right) as obtained from 0.1 Hz off-line measurements on the cable under test.*

connection was energized by applying a 50 Hz voltage to the secondary windings of the 1000 kVA transformer, such that the phase-to-ground voltages were 6 kV. The cable connection was not loaded, i.e. there was no load impedance connected to the distribution transformers. The measurement system operated in pulse synchronization mode. Approximately 40 data blocks of 20 ms were obtained at 1 minute intervals, from which a total number of approximately 9000 PD signals was extracted.

The results obtained from on-line measurements are depicted in Fig. 7.13. Again, grey tones are assigned in order to emphasize the distribution of detected PDs. The right-hand plot shows the mapping when zoomed in on the joint location. The mean and standard deviation of the results within the enlargement are indicated by ellipses. The average SNRs of extracted PD signals from the joint location were estimated between 0 dB and 17 dB, for discharge magnitudes ranging from 100 pC to 6.5 nC as measured with the sensor located at $z = 0$. At the other sensor, average SNRs ranged from -4 dB to 13 dB. The discharge mapping shows that, besides at the cable joint, discharges occurred in different regions within the cable connection under test, comparable to the off-line results. However, the discharge magnitudes were sub-

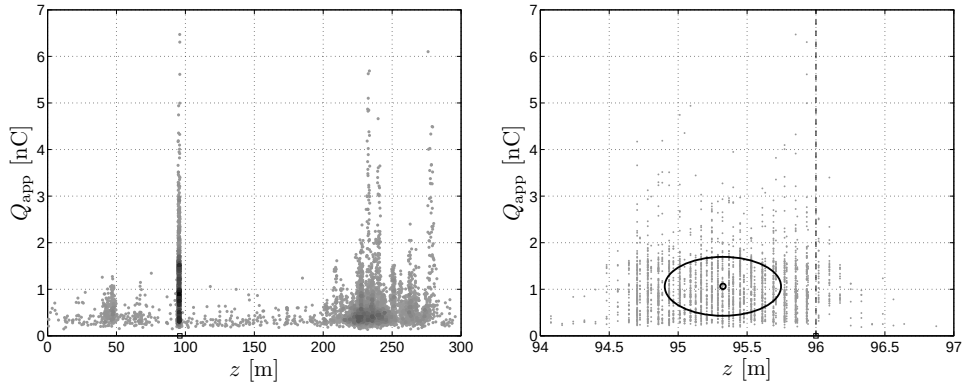

Figure 7.13 *Discharge mapping on the cable length for results obtained from on-line measurements on the cable under test.*

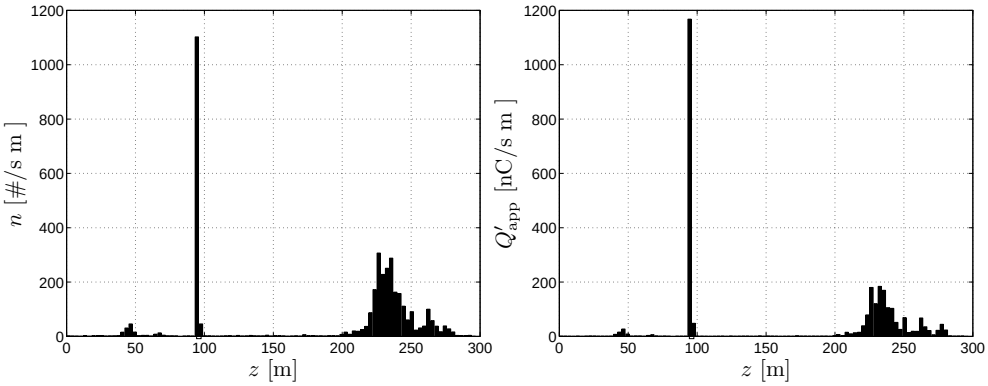

Figure 7.14 *Normalized number of discharges (left) and the normalized cumulative charge (right) as obtained from on-line measurements on the cable under test.*

stantially lower in the on-line measurement results compared to the off-line results. Apparently, the energizing voltage and the consecutive electric field distribution had a pronounced effect on discharge occurrence and magnitude. This interesting observation is not elaborated further in this thesis and is left for further research. In addition, the normalized number of discharges and the normalized cumulative charge, as depicted in Fig. 7.14, show significant differences with the off-line results. Again, the plots were produced by clustering results on a grid with 3 m resolution, in order to make an equal comparison to Fig. 7.12. Partly, the dissimilarities can be ascribed to the different measurement methods. Although the measurement time span was substantially shorter, the extraction results from the on-line measurements (∼9000) outnumbered the detected PD signals in the off-line measurements (∼2000). The frequency of the energizing voltage was extremely low in the off-line case (0.1 Hz), which can explain the relatively small number of detected discharges with respect to the measurement time. Moreover, in the off-line measurements signals were recorded by means of triggered data acquisition. After each trigger, the DAQ system cannot restart recording immediately, since data need to be stored. This deadtime can result

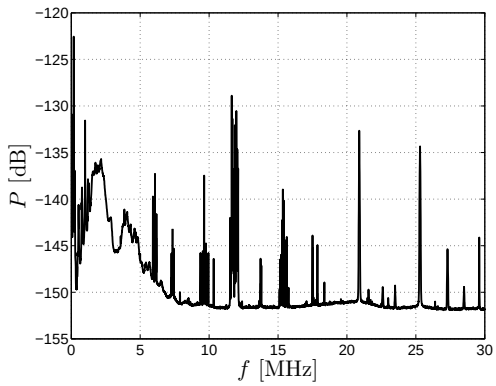

Figure 7.15 *Averaged noise and continuous interference power spectrum obtained during a cycle of the operating voltage.*

in a considerable number of missed detections. In addition, partial discharge activity is a time-varying process as will be shown below. Consequently, measurement results depend on the state of the discharge generating processes during the measurement time span.

In the experiments, no dominant radio broadcasts were present, as is usually the case for field measurements. Nevertheless, Fig. 7.15 shows that the power spectral distribution and magnitude of broadband background noise is comparable to results obtained in the tentative measurements (see Fig. 3.4). It can be concluded that the experiments are representative for actual field measurements on relatively short cables. This statement is justified by the fact that the presence of a limited number of narrowband radio broadcasts poses no fundamental limit on PD signal extraction, while broadband background noise does.

Finite-Energy Interference Rejection

As discussed in Section 7.2, the measurement system employs a number of techniques for the purpose of finite-energy interference rejection. In the third experiment, measurements were conducted that specifically demonstrate disturbance rejection. To that end, besides the cable under test, a 300 m long cable 10 kV 3×50 mm^2 PILC cable was terminated to one of the RMUs, as described in in Section 1.3.4. At the other termination of the extra cable, a defect was created, such that discharges were excited. The signals generated by discharge of this defect propagated towards the cable system under test and were detected by the measurement equipment. However, since discharging occurred outside the cable under test, the signals are considered as interference and must be rejected.

As an example, in Fig. 7.16 (left-hand plot) the sensor signals are depicted in case of a very high discharge at the termination of the extra cable. The top graph shows the signal from the first sensor where the disturbance arrived ($s_1(t)$), which was installed on the termination in one of the RMUs. The middle plot shows the signal $s_{1,\mathrm{t}}(t)$ as obtained using a CT clipped on the single-ended transformer cable earth connection at this RMU. The signal measured on the cable termination in the RMU at the opposite end of the cable under test is depicted in the bottom plot ($s_2(t)$). Three expert-rules implemented in the measurement system have rejected the extraction

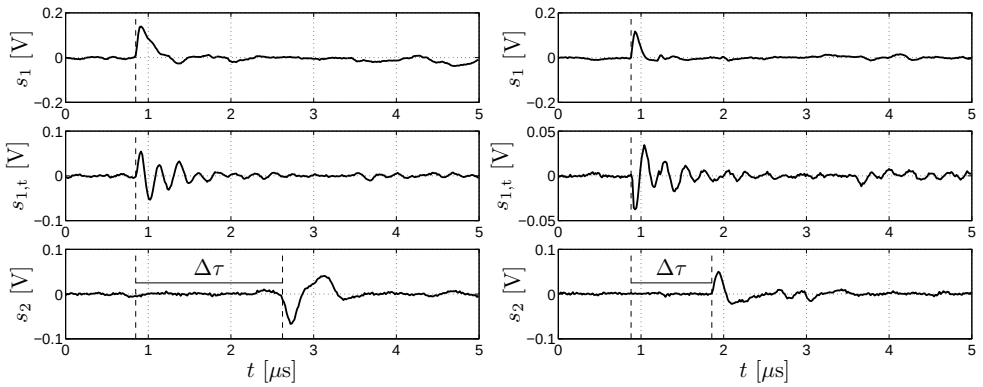

Figure 7.16 *Sensor signals resulting from a discharge in the far cable termination of the extra cable (left) and the signals in case of a discharge within the cable connection under test (right).*

results. The currents measured at the cable termination and the transformer cables have the same direction; therefore the signal was rejected based on its DOA. The difference in arrival times between the signals arriving at both cable ends equals the cable propagation delay ($\Delta\tau$); therefore the signals were rejected based on the DTOA. In addition, the signals have opposite polarity; therefore the third expert-rule rejects the extraction results as well.

For comparison, the sensor signals resulting from a very high discharge at the cable joint are depicted in the right-hand plot in Fig. 7.16. In this case, the DOA shows that the signal originated within the cable under test, since the sensor signals have opposite direction. In addition, the signals from both cable ends have the same polarity and the DTOA does not exceed the cable propagation delay.

On-line Partial Discharge Monitoring

On-line semi-continuous PD detection offers the ability to monitor the evolution of discharge activity. In a fourth experiment, the measurement system was installed in the experimental set-up for approximately 7 hours and data blocks were obtained at 1 minute intervals. Again no current-load was present. In Fig. 7.17 the cumulative charge normalized on the measurement block length (20 ms) and per unit length is depicted as a function of the location and the measurement time-instant. It should be noted that the proposed measurement method provides a sampled representation of discharge processes, since results are obtained with 1 minute intervals. The plot was produced by clustering results on a grid with 3 m resolution. Fig. 7.17 clearly shows that the occurrence of partial discharges slowly varies with time. It can be seen that, during the experiment, the artificial defect almost ceased generating discharges at a certain moment, while later on discharge activity slowly restarted. Partial discharge based cable diagnostics can benefit from the ability to monitor time-variations of discharge activity at specific locations along the cable length. The interpretation of the measurement results for the purpose of defect characterization is not straightforward and is an important topic for further research.

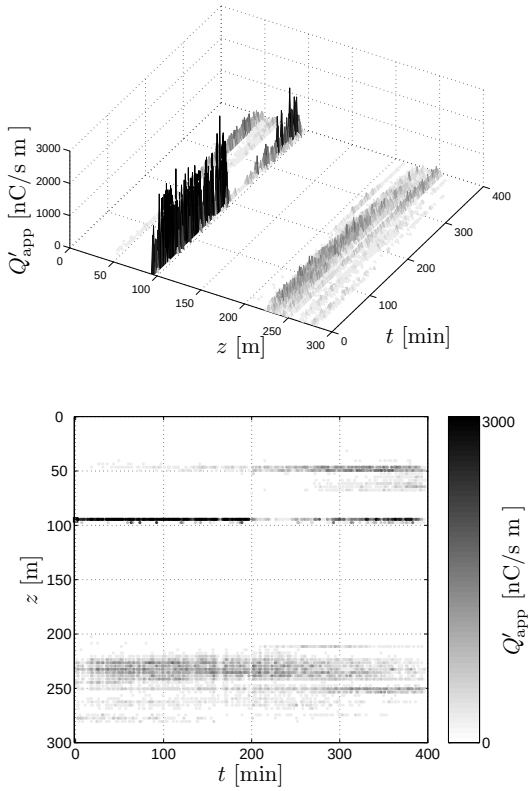

Figure 7.17 *Cumulative charge per time-unit and per unit length as a function of the location and the measurement time-instant. The bottom plot shows a topview.*

7.4 Conclusions

In this chapter, a measurement system prototype for on-line partial discharge (PD) signal detection and defect location was proposed, based on the research results presented in this thesis and in [Wie05]. The system proposal is primarily intended as a proof of concept. For this reason, system requirements related to aspects such as efficiency were not addressed. In order to enable rapid prototyping, measurement control and analysis software was developed for a personal computer (PC) utilizing a high-level programming language.

PD detection at both cable ends is required in order to accurately locate discharging defects in on-line power cables. To that end, a two-sided measurement system was developed consisting of equipment that is installed in the RMUs at both cable ends. The software architecture of the two-sided measurement system is designed for distribution among multiple PCs. A flexible architecture was proposed, which, in addition, enables remote data retrieval and easy integration of monitoring and notification functionalities. In order to reduce the communication channel load, extracted PD signals are parameterized before transfer. Nevertheless, references to original data are stored such that results and decisions can be checked.

For the purpose of accurate defect location, the measurements at both cable ends

must be synchronized. To that end, the system prototype employs two methods. One utilizes GPS for time-base alignment, the other is based on injection of synchronization pulses. Both methods have been patented. In the pulse sync mode, data acquisition at each cable end is triggered by the injected pulses. Clearly, this approach requires that the amplitudes of the sync pulses must significantly exceed the noise and interference levels.

Prior to PD detection, measurements of cable system properties are conducted. For this reason, the system can operate in two measurement modes. In the system identification mode, pulses are sequentially injected at the cable ends, and the cable responses are measured, from which cable model parameters are estimated. In the PD detection mode, synchronized measurements are conducted at each cable end, and PD signals are extracted using a matched filter bank based on the cable model. The extraction results are combined to pairs of which the DTOA is smaller than the cable propagation delay and the discharge location is estimated using the cable model. In order to reject finite-energy disturbances, expert-rules are applied to the extraction and combination results, which are based on signal waveshapes, DOA, DTOA, and polarity.

The system was validated by means of measurements on an experimental set-up, consisting of two cable sections with a total length of approximately 300 m. The cable connection was terminated to RMUs, representing a full-scale field situation. In a first set of experiments, transients were injected into the cable joint that interconnects the two sections. It was shown that the proposed measurement system enables precise location of the origin of the detected signals. The location estimates are more accurate compared to off-line results obtained by manual analysis, since the proposed system accounts for frequency dependent propagation velocity. Moreover, the results show that for the experimental set-up, pulse synchronization outperforms GPS-based synchronization.

In a second set of experiments, a defect in the cable joint was created, such that discharges occurred when the cable was energized. It was shown that the proposed system can identify the defect in an on-line measurement situation. As expected, discharges were detected and located in large regions within the paper-insulated cable as well. Off-line reference measurements were conducted with conventional 0.1 Hz equipment. Comparison between the on-line and off-line results showed a number of dissimilarities, which were mainly attributed to the different measurement methods and time-varying discharge activity.

In a third experiment, an additional cable was terminated to one of the RMUs. PD signals originating from this cable propagate to the cable under test and are considered as interference. The effectiveness of the proposed disturbance rejection techniques was demonstrated by the experiments.

On-line semi-continuous PD detection offers the ability to monitor the evolution of discharge activity. The results of a 7 hours long experiment show that the occurrence of partial discharges varies slowly with time. The interpretation of the measurement results for the purpose of defect characterization, as well as comparison of on-line and off-line results, is not straightforward and is an important topic for further research.

Chapter 8

Conclusions

8.1 Summary and Conclusions

The work reported in this thesis is focused on detection, location, and monitoring of partial discharges in medium-voltage (MV) power cables, which operate in service. A number of challenges arise from the attempt to extend conventional off-line measurement methods to on-line cable connections, including sensor selection and application, analysis of measured signals, and synchronization of measurement equipment. The research results presented in this thesis are primarily concerned with signal analysis.

Signal analysis depends on knowledge of the signals that are to be expected. In order to develop appropriate signal models, characteristics of partial discharge (PD) signals in power cables were studied in Chapter 2. In the Netherlands, the medium-voltage grid mainly consists of three-phase belted cables; therefore the properties of this cable type are emphasized in this thesis, although the results are applicable to all power cables.

Usually, underground cables are applied for MV power distribution and electrical impulses generated by partial discharges can only be detected easily at the cable ends. Signal propagation in three-phase belted cables can be modelled by two distinct propagation channels as was shown by theory and experiments. At each end, a cable system is terminated to a ring main unit (RMU), which interconnects multiple cables and other equipment. Experiments show that, in an RMU, crosstalk between the propagation channels is negligible, and orthogonality can be assumed. Wavelengths much larger than the RMU components were considered. For this reason, the complete configuration was modelled as a channel load impedance.

The most widely applicable method for on-line PD detection utilizes a current transformer (CT) installed around the cable screen past the cable earth connection or clipped on the earth strap. This way, PD signals propagating in a single channel are measured. This channel is referred to as the shield-to-phase (SP) channel. The SP channel properties can be approximated by a simple single-core coaxial model. Cable systems generally consist of multiple cables in cascade; therefore the signal model accounts for the propagation properties of the individual sections. The signal waveshape model was validated by means of measurements on an experimental set-up and the results show good agreement.

On-line field measurements are corrupted by noise and interference, impeding PD signal detection and location. In order to characterize frequently occurring distur-

bances and their implications for signal analysis, a number of tentative measurements was conducted, of which the results were presented in Chapter 3.

Generally, narrow-band quasi-periodic interferences resulting from radio broadcasts or communication dominate the measurements. In off-line measurements, PD signals can be detected utilizing a digital storage oscilloscope, which triggers on signals that exceed a pre-set threshold. Due to dominant radio broadcasts, this approach does not apply to on-line measurements and data must be obtained by recording relatively large sets. This conclusion has only practical implications, since PD signals have a broadband nature, and narrow-band interferences can be suppressed using notch filters or interference cancellers after digitization.

Broadband background noise in on-line PD measurements can be considered stationary during observations in the order of several cycles of the operating voltage. The noise power distribution is frequency dependent, and components in the low megahertz range dominate. Noise is present within the entire PD signal bandwidth, and therefore poses a fundamental limit on PD signal analysis.

Finite-energy disturbances, such as thyristor pulses and PD pulses from equipment other than the cable under test, occur frequently in on-line PD measurements. In the tentative measurements, bandlimited finite-energy disturbances were observed, with bandwidths ranging from tens to hundreds of kilohertz. In principle, such disturbances can be rejected based on their waveshapes. Although some disturbances occurred with some regularity, repetition periods varied in the order of tens to hundreds of microseconds. As a consequence, rejection based on repetition rates alone was considered unpractical.

PD signals from other high-voltage equipment than the cable system under test are considered as interference as well. This type of interference cannot be distinguished from PD signals by signal waveforms or repetition rates. However, if signals are synchronously detected at both cable ends, pulses originating within and outside the cable can be distinguished by examining the difference in time of arrival (DTOA).

The current measured at a termination flows in the opposite direction when a signal propagates towards the cable under test as compared to a signal that originates within the cable. In many situations in the Netherlands, a distribution transformer is connected to the RMU rail system by means of cables with a one-sided earth connection. The direction of a current pulse measured in the transformer cables does not depend on the origin of the signal. It was shown that the direction of arrival (DOA) of signals can be determined by examining the currents in the two paths, which offers an additional technique to distinguish PD signals from interferences.

The exact signal model parameters depend on the specific cable connection under test. In Chapter 4 methods were presented that enable parameter estimation by excitation of the cable system with a known signal. The proposed methods rely on the extraction of signals that are reflected on impedance transitions within the cable system under test. Consequently, the injected and reflected signals must be separable, since parameter estimation from mixtures is generally not feasible. It was shown that under this condition, the properties of the individual sections can be estimated. Although accurate measurement principles were elaborated, the procedures may not always be applicable in practice. Nevertheless, average propagation parameters can be obtained by considering the system as a uniform propagation path, as was shown by experiments. The estimates obtained from this simplification are still very valuable, since in many cases cable connections are composed of similar cable sections.

Accurate knowledge of the channel delay and propagation velocity is essential for the purpose of discharge location. In an on-line situation, these parameters can only be estimated if either a reflection on the far cable end can be extracted or if the measurements are synchronized with a reference, e.g. the global positioning system (GPS). From both a practical and an economical point of view, application of GPS is not preferred. However, as was shown by experiments, far-end reflections may not always be detectable. Nevertheless, this problem can be overcome by temporarily disconnecting the cable and performing propagation measurements on the off-line system.

Generally, existing extraction techniques for partial discharge signals only partially exploit a priori knowledge on signals and interference. Based on the signal model and the noise power spectral distribution, matched filters can be designed specifically for PD signals originating from the cable system under test. In Chapter 5, this approach to PD signal extraction was studied. The proposed methods are applicable to both on-line and off-line PD detection. Discharging insulation defects can be present at any location along the cable length, resulting in a variety of signal waveforms at the sensor. However, PD pulse shapes do not differ appreciably for closely spaced defect sites, especially when the propagation distance is large. As a consequence, a finite set of signal templates is sufficient to match every possible PD waveshape from the cable system, resulting in a matched filter bank. As a first step towards semi-continuous PD signal analysis, an efficient matched filter bank implementation was presented.

Besides signal extraction, application of matched filters to PD signal magnitude and arrival time estimation is proposed. These parameters are essential for the purpose of defect location and classification. In addition, theoretical lower bounds on the parameter estimation quality were derived. Since time of arrival (TOA) estimation using matched filters is bounded to the sampling grid, interpolation schemes were applied to increase estimation accuracy. The proposed methods were validated using data generated by computer simulations.

Location of discharging defects is of crucial importance for the mapping of degraded components in power cable systems. In case of off-line PD detection, the measurement equipment is generally connected to a single cable-end, while the other end is left open. For this reason, time-domain reflectometry (TDR) can generally be applied. In case of on-line detection, the cable is connected to the grid, and the quality of reflected signals is generally very low, implying that sensors at both cable ends are required. Apart from imprecise knowledge of the cable length, accurate location is impeded by dispersion and by the presence of multiple cable sections with different properties. In Chapter 6, maximum-likelihood (ML) location estimators were derived, that apply to both off-line and on-line PD location. In addition, a method was proposed that enables location using one sensor, i.e. based only on the waveshape of a detected PD pulse. Although the method is appealing, it was shown that locations can only be crudely estimated.

Accurate PD location relies on DTOA estimation of PD signals originating from the same discharge, which was accomplished by means of matched filters. In addition, methods were presented that correct for location estimation bias due to dispersion. A two-sided measurement topology requires synchronization of the measurement equipment. One method, already successfully applied in off-line PD measurements, utilizes the GPS to synchronize two-sided measurements, which is a patented solution. Another option to achieve time-base alignment is by injection of synchronization pulses.

The method of injection is also patented. Synchronization pulses can be utilized to correct for linear time-base wander that can occur when large data blocks are recorded. The proposed methods were validated using data generated by computer simulations.

In Chapter 7, a measurement system was proposed for on-line partial discharge detection in MV cable connections, based on the research results presented in this thesis and in [Wie05]. A two-sided measurement system was developed consisting of equipment that is installed in the RMUs at both cable ends. A distributed software architecture was proposed, which enables remote retrieval of results and flexible integration of additional monitoring and notification functionalities.

The system can operate in two measurement modes. In the identification mode, pulses are sequentially injected at the cable ends, and the cable responses are measured, from which model parameters are estimated. In the PD detection mode, synchronized measurements are conducted at each cable end, and PD signals are extracted using an MFB based on the cable model. The system prototype offers two possibilities for the purpose of time-base alignment. One utilizes the GPS for time-base alignment, the other is based on injection of synchronization pulses. The aligned extraction results are combined to pairs of which the DTOA is smaller than the cable propagation delay and the discharge location is estimated using the cable model. In order to reject finite-energy disturbances, expert-rules are applied, which are based on signal DOA and DTOA discrimination, as well as waveshape and polarity checks.

The conceptual design was validated by means of measurements on an experimental set-up, consisting of two cable sections with a total length of approximately 300 m. The cable connection was terminated to RMUs, representing a field situation. In a first set of experiments, transients were injected into the cable joint that interconnects the two sections. It was demonstrated that the proposed measurement system enables accurate location of the origin of the detected signals. Moreover, in the experiments, time-base alignment using pulse synchronization outperformed GPS-based synchronization.

Within the cable joint, a defect was created, such that discharges occurred when the experimental set-up was energized. It was shown that the proposed measurement system precisely located this defect and other discharge sources in the on-line situation. In addition, the measurement system offers the ability to monitor the evolution of discharge activity. The results of a 7 hours long experiment demonstrate that the occurrence of partial discharges is time-varying. Off-line reference measurements were conducted with conventional 0.1 Hz equipment. Comparison of the on-line and off-line results show a number of dissimilarities, which were mainly attributed to the different measurement methods as well as time variations in discharge generating processes. Another cable was terminated to one of the RMUs. PD signals originating from this cable propagate through the cable under test and are considered as interferences. The effectiveness of the proposed disturbance rejection techniques was demonstrated by experiments.

Although measurements were conducted in a controlled environment, the experimental results represent actual field situations, and demonstrate that practical application of the proposed system is indeed promising. In conclusion, the signal analysis methods presented in this thesis enable automated detection, location and monitoring of discharging defects in on-line cable systems. The proposed techniques open the way to continuous on-line cable diagnostics and consecutively a new field of research.

8.2 Recommendations for Future Research

PD signal extraction techniques presented in this thesis utilize matched filter templates derived from a signal model, which is specific to the cable connection under test. Instead of this approach, another strategy to obtain filter templates can be based on the measured signals themselves. Starting from a generic cable model, PD signals are extracted at both cable ends. If the combination of extracted signals with high SNR results in a location estimate within the cable under test, the original filter templates can be adapted to produce a better match to the actually measured waveshapes. Such a iterative structure then improves the extraction of signals with low SNR.

In some measurement situations, reflections on the far-end cable termination or on impedance transitions within the cable may be extractable at the near end. The DTOA between a PD signal and a corresponding reflection is bounded by some maximum that can be determined from cable system identification measurements. This a priori knowledge can be embedded in an additional expert rule for finite-energy disturbance rejection.

The measurement system prototype was primarily intended as a proof of concept. For this reason, system requirements related to aspects such as efficiency and robustness were not addressed. Evidently, personal computers are not the best choice for processing large amounts of measurement data. For the purpose of developing commercial apparatus, more efficient realizations may be of interest. For example, the proposed matched filtering algorithms can be implemented using field programmable gate arrays (FPGAs). Since the filters lengths are generally small, real-time processing may even be feasible. Moreover, if a lower performance in terms of accuracy is acceptable, data can be acquired at a lower sampling rate and less filters can be applied, thus reducing the computational complexity. The presence of small discharges is inherent to aged PILC cables, while merely large discharges provide valuable information on the insulation condition. In order to reduce the communication channel load, a threshold can be applied such that only significant extraction results are transferred.

Over time, the measurement system will produce large amounts of detection results when installed in an on-line cable connection. In order to reduce the necessary storage capacity, clustering algorithms can be used for lossy data compression, which are applied to e.g. vector quantization (see e.g. [Moo99]). Clearly, the interpretation of results for the purpose of defect characterization is an important topic for further research. Clustering results can serve as an input for automated diagnostic decision and notification systems based on pattern recognition.

Appendix A

Propagation Channels of Three-Phase Belted Cables

The multi-conductor transmission line equations are given by

$$\frac{\partial}{\partial z}\begin{pmatrix} \underline{V}(z,\omega) \\ \underline{I}(z,\omega) \end{pmatrix} = -\begin{pmatrix} \mathbf{0} & \mathbf{Z}(\omega) \\ \mathbf{Y}(\omega) & \mathbf{0} \end{pmatrix}\begin{pmatrix} \underline{V}(z,\omega) \\ \underline{I}(z,\omega) \end{pmatrix} \tag{A.1}$$

where the phase voltage and current vectors equal $\underline{V}(z,\omega) = (V_1, V_2, V_3)^t(z,\omega)$ and $\underline{I}(z,\omega) = (I_1, I_2, I_3)^t(z,\omega)$. Decoupling of the system is achieved by introducing a transformation that simultaneously diagonalizes the line parameter matrices, see e.g. [DZ93, Pau94]. A three-phase belted cable has both rotation-symmetric and reflection-symmetric structure since the configuration does not change under permutation of the conductors. As a consequence the impedance and admittance matrix are circulant and symmetric,

$$\mathbf{Z}(\omega) = \begin{pmatrix} Z_1(\omega) & Z_2(\omega) & Z_2(\omega) \\ Z_2(\omega) & Z_1(\omega) & Z_2(\omega) \\ Z_2(\omega) & Z_2(\omega) & Z_1(\omega) \end{pmatrix} \tag{A.2}$$

and

$$\mathbf{Y}(\omega) = \begin{pmatrix} Y_1(\omega) & Y_2(\omega) & Y_2(\omega) \\ Y_2(\omega) & Y_1(\omega) & Y_2(\omega) \\ Y_2(\omega) & Y_2(\omega) & Y_1(\omega) \end{pmatrix} . \tag{A.3}$$

Circulant matrices are diagonalized by the discrete Fourier transform [Dav79]. In this case the transformation matrix equals

$$\mathbf{F} = \frac{1}{\sqrt{3}}\begin{pmatrix} 1 & 1 & 1 \\ 1 & e^{-j2\pi/3} & e^{-j4\pi/3} \\ 1 & e^{-j4\pi/3} & e^{-j2\pi/3} \end{pmatrix} . \tag{A.4}$$

A change of variables

$$\begin{aligned} \underline{\tilde{V}}(z,\omega) &= \mathbf{F}\underline{V}(z,\omega) \\ \underline{\tilde{I}}(z,\omega) &= \mathbf{F}\underline{I}(z,\omega) \end{aligned} \tag{A.5}$$

results in partial decoupling of the system (A.1),

$$\frac{\partial}{\partial z}\begin{pmatrix} \underline{\tilde{V}}(z,\omega) \\ \underline{\tilde{I}}(z,\omega) \end{pmatrix} = -\begin{pmatrix} \mathbf{0} & \tilde{\mathbf{Z}}(\omega) \\ \tilde{\mathbf{Y}}(\omega) & \mathbf{0} \end{pmatrix}\begin{pmatrix} \underline{\tilde{V}}(z,\omega) \\ \underline{\tilde{I}}(z,\omega) \end{pmatrix} , \tag{A.6}$$

where $\tilde{\mathbf{Z}}(\omega)$ and $\tilde{\mathbf{Y}}(\omega)$ are diagonal matrices that contain the eigenvalues of $\mathbf{Z}(\omega)$ and $\mathbf{Y}(\omega)$, respectively. The transformed equations (A.6) incorporate three mutually uncoupled systems, each of which characterizes a propagation channel that can be interpreted as a two-conductor transmission line. Because of the symmetric structure of a cable cross-section there are two repeated eigenvalues, and thus only two distinct propagation channels exist. The shield-to-phase (SP) channel is parameterized by its propagation factor and characteristic impedance

$$\gamma_{\mathrm{SP}}(\omega) = \sqrt{(Y_1(\omega)+2Y_2(\omega))(Z_1(\omega)+2Z_2(\omega))}\,, \tag{A.7a}$$

$$Z_{\mathrm{c_{SP}}}(\omega) = \sqrt{\frac{Z_1(\omega)+2Z_2(\omega)}{Y_1(\omega)+2Y_2(\omega)}}\,. \tag{A.7b}$$

The two phase-to-phase (PP) channels, corresponding to the repeated eigenvalues, are characterized by

$$\gamma_{\mathrm{PP}}(\omega) = \sqrt{(Y_1(\omega)-Y_2(\omega))(Z_1(\omega)-Z_2(\omega))}\,, \tag{A.8a}$$

$$Z_{\mathrm{c_{PP}}}(\omega) = \sqrt{\frac{Z_1(\omega)-Z_2(\omega)}{Y_1(\omega)-Y_2(\omega)}}\,. \tag{A.8b}$$

Considering a forward travelling wave, the propagation of the phase voltages and currents can now be described in terms of the SP and PP parameters. For instance, the phase currents at location z are expressed as

$$\begin{aligned}\underline{I}^{+}(z,\omega) &= \mathbf{F}^{*}\begin{pmatrix} e^{-\gamma_{\mathrm{SP}}(\omega)z} & 0 & 0\\ 0 & e^{-\gamma_{\mathrm{PP}}(\omega)z} & 0\\ 0 & 0 & e^{-\gamma_{\mathrm{PP}}(\omega)z}\end{pmatrix}\mathbf{F}\underline{I}^{+}(0,\omega) \qquad \text{(A.9)}\\ &= \frac{1}{3}\left[e^{-\gamma_{\mathrm{SP}}(\omega)z}\begin{pmatrix}1&1&1\\1&1&1\\1&1&1\end{pmatrix}+e^{-\gamma_{\mathrm{PP}}(\omega)z}\begin{pmatrix}2&-1&-1\\-1&2&-1\\-1&-1&2\end{pmatrix}\right]\underline{I}^{+}(0,\omega)\end{aligned}$$

where $\underline{I}^{+}(z,\omega) = (I_1^{+}, I_2^{+}, I_3^{+})^t(z,\omega)$. Evidently, a similar relation holds for the phase voltages. The forward travelling wave of some initial SP voltage and current vector is expressed as

$$\begin{pmatrix} V_1^{+}+V_2^{+}+V_3^{+} \\ I_1^{+}+I_2^{+}+I_3^{+}\end{pmatrix}(z,\omega) = e^{-\gamma_{\mathrm{SP}}(\omega)z}\begin{pmatrix} V_1^{+}+V_2^{+}+V_3^{+} \\ I_1^{+}+I_2^{+}+I_3^{+}\end{pmatrix}(0,\omega)\,. \tag{A.10}$$

Propagation of the difference between two phase voltages and currents is parameterized by $\gamma_{\mathrm{PP}}(\omega)$ and $Z_{\mathrm{c_{PP}}}(\omega)$, which explains the term PP channel, e.g.

$$\begin{pmatrix} V_1^{+}-V_2^{+} \\ I_1^{+}-I_2^{+}\end{pmatrix}(z,\omega) = e^{-\gamma_{\mathrm{PP}}(\omega)z}\begin{pmatrix} V_1^{+}-V_2^{+} \\ I_1^{+}-I_2^{+}\end{pmatrix}(0,\omega)\,. \tag{A.11}$$

It should be noted that the phase difference signals are not orthogonal, whereas the transformed signals (A.5) are orthogonal.

Appendix B

Cable Propagation Measurements

Network Analyzer Propagation Measurements

As any linear system, a propagation channel can be represented by a generic two-port, which is completely parameterized by its input and output impedances and transfer functions. Alternatively, a two-port can be characterized by scattering parameters or S-parameters, as frequently applied in microwave network analysis. For a lossy unmatched transmission line of length l, with propagation factor $\gamma(\omega)$ and characteristic impedance $Z_{\mathrm{c}}(\omega)$, the scattering matrix obtained by a Z_0 measuring system equals [Gup81]

$$\mathbf{S}(\omega) = \frac{1}{D_s(\omega)} \begin{pmatrix} (Z_{\mathrm{c}}^2(\omega) - Z_0^2)\sinh\gamma(\omega)l & 2Z_{\mathrm{c}}(\omega)Z_0 \\ 2Z_{\mathrm{c}}(\omega)Z_0 & (Z_{\mathrm{c}}^2(\omega) - Z_0^2)\sinh\gamma(\omega)l \end{pmatrix} \tag{B.1}$$

where $D_s(\omega) = (2Z_{\mathrm{c}}(\omega)Z_0\cosh\gamma(\omega)l + (Z_{\mathrm{c}}^2(\omega) + Z_0^2)\sinh\gamma(\omega)l)$. Extracting $\gamma(\omega)$ and $Z_{\mathrm{c}}(\omega)$ from the expression yields [Eis92] [Car00]

$$\cosh\gamma(\omega)l = \frac{1 - S_{11}^2(\omega) + S_{12}^2(\omega)}{2S_{12}(\omega)} \tag{B.2a}$$

$$Z_{\mathrm{c}}(\omega) = Z_0\sqrt{\frac{(1 + S_{11}(\omega))^2 - S_{12}^2(\omega)}{(1 - S_{11}(\omega))^2 - S_{12}^2(\omega)}}\,. \tag{B.2b}$$

A network analyzer (HP8753C) combined with S-parameter set (HP85047A) is used to determine the S-parameters of a test cable propagation channel over a wide frequency range. Clearly, the method can only be applied to uninstalled cables, since each cable end must be connected to the measuring apparatus.

Using a coaxial approximation of the shield-to-phase (SP) propagation channel, the complex relative dielectric constant is determined from the network analyzer propagation measurements by

$$\varepsilon_r(\omega) \approx \frac{\gamma_{\mathrm{SP}}(\omega)}{Z_{\mathrm{c_{SP}}}(\omega)j\omega 2\pi\epsilon_0}\ln\frac{r_{\mathrm{s}}}{r_{\mathrm{c}}} \tag{B.3}$$

where r_{c} and r_{s} are the core radius and screen inner radius.

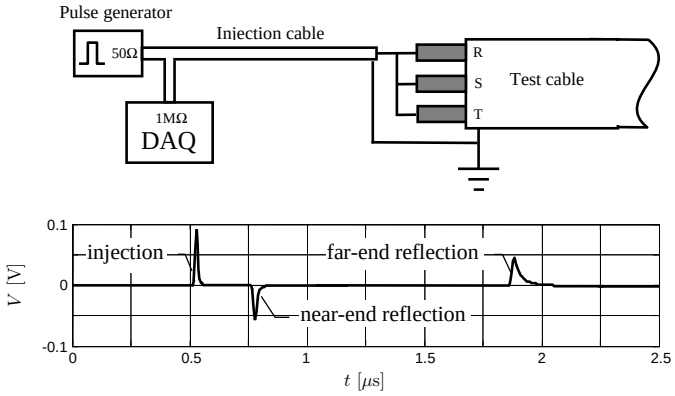

Figure B.1 *Pulse propagation measurement on the SP-channel of the cable under test. The channel propagation parameters are estimated by evaluating the transfer functions between the injection and the near-end reflection, and between the injection and the far-end reflection.*

Propagation Measurements by Pulse Response Analysis

Channel propagation properties in a three-phase belted cable can be determined by applying a wide-band pulse on one cable end, and evaluating the resulting reflection at the other end. A pulse response analysis method requires connection to a single cable end; therefore the method can be applied to cables installed in the field. The pulse injection set-up consists of a pulse generator and a digitizer, connected closely together, and a relatively long injection cable. The injection cable is connected to the appropriate channel of the three-phase belted cable under test. When a pulse is injected, a first reflection occurs at the interface of the injection and the test cable, and a second reflection occurs at the test cable far end, which is left open. Since both the injection and the test cable are long, the recorded injection and reflections are separable in the time domain (see Fig. B.1), and the transfer functions $H_1(\omega)$ and $H_2(\omega)$ between the injection and the reflections are obtained.

In order to eliminate the influence of the injection set-up, a calibration measurement is performed. During the calibration, the propagation path is deliberately shorted at the injection and test cable interface. The calibration transfer function $H_{\mathrm{cal}}(\omega)$ is obtained from the injection and the first reflection. Now from the first reflection transfer function $H_1(\omega)$, the reflection coefficient $R(\omega)$ at the injection cable and test cable interface is obtained,

$$R(\omega) = -\frac{H_1(\omega)}{H_{\mathrm{cal}}(\omega)} \; . \tag{B.4}$$

Assuming that the wave impedance Z_0 of the injection cable is approximately constant in the frequency range of interest, the test cable characteristic impedance equals

$$Z_{\mathrm{c}}(\omega) = Z_0 \frac{1 + R(\omega)}{1 - R(\omega)} \; . \tag{B.5}$$

Note that this measurement method is not limited to cables, but can also be applied to determine the wave impedance of some other test object.

From the second reflection transfer function $H_2(\omega)$, the test cable propagation factor is obtained, since

$$\frac{H_2(\omega)}{H_{\mathrm{cal}}(\omega)} = -e^{-\gamma(\omega)2l}(1 - R(\omega))(1 + R(\omega)) \; . \tag{B.6}$$

where l equals the length of the cable under test. Generally, the measurement noise is white Gaussian under laboratory conditions; therefore the accuracy of the estimates is improved by averaging the results of multiple propagation measurements.

Phase-to-Phase Channel Propagation Properties

In a field measurement situation, there always exists a strong capacitive coupling of the cable screen with the earth. As a consequence, the propagation properties of the phase-to-phase (PP) channel can only be measured directly using a differential pulse generator, which enables balanced signal injection and measurement. Here, an alternative method is presented that can be applied without the use of special equipment.

The injection cable is connected to one of the phase conductors of the three-phase belted cable under test, with the other two conductors floating, which is referred to as shield-to-single-phase (SSP) injection. When a pulse is injected, the signal arriving at the injection and test cable interface, is distributed among the orthogonal propagation channels of the test cable. As a consequence, the measured cable response to SSP injection is determined by the propagation properties of both the SP and PP channel.

At the injection and test cable interface, the forward propagating phase voltages $\underline{V}^+(z,\omega) = (V_1^+, V_2^+, V_3^+)^t(z,\omega)$ and currents $\underline{I}^+(z,\omega) = (I_1^+, I_2^+, I_3^+)^t(z,\omega)$ are related by the impedance matrix $\mathbf{Z}_{\mathrm{c}}(\omega)$ of the cable under test. By inverse transformation of the characteristic impedance matrix $\tilde{\mathbf{Z}}_{\mathrm{c}}(\omega)$ that relates the voltages and currents in the orthogonal propagation channels, the elements of $\mathbf{Z}_{\mathrm{c}}(\omega)$ are obtained, viz.

$$\mathbf{Z}_{\mathrm{c}}(\omega) = \mathbf{F}^* \tilde{\mathbf{Z}}_{\mathrm{c}}(\omega) \mathbf{F} \tag{B.7}$$

where

$$\tilde{\mathbf{Z}}_{\mathrm{c}}(\omega) = \begin{pmatrix} Z_{\mathrm{c_{SP}}}(\omega) & 0 & 0 \\ 0 & Z_{\mathrm{c_{PP}}}(\omega) & 0 \\ 0 & 0 & Z_{\mathrm{c_{PP}}}(\omega) \end{pmatrix} \; . \tag{B.8}$$

As a result of the configuration symmetries, all diagonal elements of $\mathbf{Z}_{\mathrm{c}}(\omega)$ are equal, and so are the off-diagonal elements. Initially, i.e. at the impedance transition from the injection cable to the cable under test, the currents in the floating phase conductors are zero. Consequently, each diagonal element of $\mathbf{Z}_{\mathrm{c}}(\omega)$ equals the impedance of the test cable at the injection and test-cable interface, i.e.

$$Z_{\mathrm{c_{SSP}}}(\omega) = \tfrac{1}{3}(Z_{\mathrm{c_{SP}}}(\omega) + 2Z_{\mathrm{c_{PP}}}(\omega)) \; , \tag{B.9}$$

from which the PP characteristic impedance is obtained.

The distribution of the applied signal among the propagation channels is determined by the impedance matrix $\mathbf{Z}_{\mathrm{c}}(\omega)$. For instance, when the signal is injected into the first phase conductor, the forward travelling voltages that are transmitted to the cable under test, equal

$$\underline{V}^+(0,\omega) = \mathbf{Z}_c(\omega)\, \underline{I}^+(0,\omega) = (1, K, K)^t \; V_1^+(0,\omega) \tag{B.10}$$

where $V_1^+(0,\omega)$ is determined by the injected signal, the injection cable transfer, and the transmission coefficient at the injection and test cable interface. The off-diagonal elements of $\mathbf{Z}_\mathrm{c}(\omega)$ equal $\frac{1}{3}(Z_{\mathrm{c_{SP}}}(\omega) - Z_{\mathrm{c_{PP}}}(\omega))$, thus the factor K becomes

$$K = \frac{Z_{\mathrm{c_{SP}}}(\omega) - Z_{\mathrm{c_{PP}}}(\omega)}{Z_{\mathrm{c_{SP}}}(\omega) + 2Z_{\mathrm{c_{PP}}}(\omega)} \; . \tag{B.11}$$

Now, using Eq. A.9, propagation of the signal on one of the phase conductors can be expressed as a function of the SP and PP channel properties. Equivalent to Eq. B.6, the transfer between the injected signal and the far-end reflection can be obtained, where the following expression is substituted

$$e^{2\gamma(\omega)l} = \tfrac{1}{3}\left((1+2K)e^{2\gamma_{\mathrm{SP}}(\omega)l} + 2(1-K)e^{2\gamma_{\mathrm{PP}}(\omega)l}\right) \; . \tag{B.12}$$

Consequently, the PP propagation properties can be obtained from the SP and SSP propagation measurements.

Appendix C

Theoretical Bounds on PD Signal Parameter Estimation Variance

Scaling Factor Estimation Variance

The variance of the maximum filter response $y_{\max}$ to a measurement $x(kT_\mathrm{s}) = As(kT_\mathrm{s}) + n(kT_\mathrm{s})$ can be expressed as

$$\begin{aligned}
\mathrm{var}\,(y_{\max}) &= E\{y_{\max} - E\{y_{\max}\}\}^2 \\
&= E\left\{\left|\Delta f \sum_{i=0}^{B-1} \frac{N(i\Delta f)S^*(i\Delta f)}{P_N(i\Delta f)}\right|^2\right\} \\
&= (\Delta f)^2 E\left\{\left(\sum_{i=0}^{B-1} \frac{N(i\Delta f)S^*(i\Delta f)}{P_N(i\Delta f)}\right)^* \left(\sum_{j=0}^{B-1} \frac{N(j\Delta f)S^*(j\Delta f)}{P_N(j\Delta f)}\right)\right\} \\
&= (\Delta f)^2 \sum_{i=0}^{B-1}\sum_{j=0}^{B-1} \frac{E\left\{S(i\Delta f)N^*(i\Delta f)N(j\Delta f)S^*(j\Delta f)\right\}}{P_N(i\Delta f)P_N(j\Delta f)} \qquad \text{(C.1)}
\end{aligned}$$

Since the Fourier coefficients of a stationary noise process are mutually uncorrelated, the summation is only nonzero for $j = i$, thus

$$\begin{aligned}
\mathrm{var}\,(y_{\max}) &= (\Delta f)^2 \sum_{i=0}^{B-1} \frac{|S(i\Delta f)|^2 E\left\{|N(i\Delta f)|^2\right\}}{P_N^2(i\Delta f)} \\
&= \Delta f \sum_{i=0}^{B-1} \frac{|S(i\Delta f)|^2}{P_N(i\Delta f)}\,, \qquad \text{(C.2)}
\end{aligned}$$

which follows from the Wiener-Khinchin theorem, see e.g. [Kay88]. Now with $\mathrm{var}\,(C\,y_{\max}) = C^2\mathrm{var}\,(y_{\max})$,

$$\frac{\mathrm{var}\,(\hat{A})}{A^2} = \frac{T_\mathrm{s}}{T_0}\left(\frac{1}{B}\sum_{i=0}^{B-1} \mathrm{SNR}(i\Delta f)\right)^{-1}. \qquad \text{(C.3)}$$

where

$$\mathrm{SNR}(i\Delta f) = \frac{|A\,S(i\Delta f)|^2}{T_0 P_N(i\Delta f)}\,.$$

Time of Arrival Estimation Variance

In the frequency domain, the scaled log-likelihood function (see e.g. [Tre68]) of a measured PD signal $x(kT_\mathrm{s}) = As(kT_\mathrm{s} - \tau) + n(kT_\mathrm{s})$ is expressed as

$$L(\underline{\theta}) = \Delta f \sum_{i=0}^{B-1} -\frac{|X(i\Delta f) - AS(i\Delta f)e^{-j2\pi i\Delta f\tau}|^2}{2P_N(i\Delta f)} \;, \tag{C.4}$$

assuming zero-mean Gaussian noise. The function expresses the likelihood of the PD signal parameter vector $\theta = (A,\, \tau)^t$ given the observation $x(kT_\mathrm{s})$ and the signal waveform $s(kT_\mathrm{s})$. The Cramer-Rao bound on the estimation variance for a vector of unbiased estimators $\underline{\hat{\theta}} = (\hat{A}\,, \hat{\tau})^t$ equals (see e.g. [Tre68])

$$E\{(\underline{\hat{\theta}} - \underline{\theta})(\underline{\hat{\theta}} - \underline{\theta})^t\} \geq \mathbf{J}^{-1}(\underline{\theta}) \;,$$

where $\mathbf{J}(\underline{\theta})$ is the Fisher information matrix of which the elements equal

$$J_{ij}(\underline{\theta}) = E\left\{\frac{\partial L}{\partial \theta_i}\frac{\partial L}{\partial \theta_j}\right\} = -E\left\{\frac{\partial^2 L}{\partial \theta_i \partial \theta_j}\right\} \;. \tag{C.5}$$

The first derivatives of the likelihood function with respect to the parameters equal

$$\begin{aligned}
\frac{\partial L}{\partial \tau} &= -\Delta f \sum_{i=0}^{B-1} \frac{j(2\pi i\Delta f)X^*(i\Delta f)AS(i\Delta f)e^{-j2\pi i\Delta f\tau}}{2P_N(i\Delta f)} \\
&\quad +\Delta f \sum_{i=0}^{B-1} \frac{j(2\pi i\Delta f)X(i\Delta f)AS^*(i\Delta f)e^{j2\pi i\Delta f\tau}}{2P_N(i\Delta f)} \;, \\
\frac{\partial L}{\partial A} &= \Delta f \sum_{i=0}^{B-1} \frac{-A|S(i\Delta f)|^2 + \mathrm{Re}\left\{X^*(i\Delta f)S(i\Delta f)e^{-j2\pi i\Delta f\tau}\right\}}{P_N(i\Delta f)} \;.
\end{aligned} \tag{C.6}$$

Now the lower bound on the time of arrival estimation variance equals

$$\begin{aligned}
\mathrm{var}(\hat{\tau}) \geq J_{22}^{-1}(\underline{\theta}) &= \left(\Delta f \sum_{i=0}^{B-1} \frac{(2\pi i\Delta f)^2|AS(i\Delta f)|^2}{P_N(i\Delta f)}\right)^{-1} \\
&= \frac{T_\mathrm{s}}{T_0}\left(\frac{1}{B}\sum_{i=0}^{B-1}(2\pi i\Delta f)^2 \mathrm{SNR}(i\Delta f)\right)^{-1} \;,
\end{aligned} \tag{C.7}$$

since only the diagonal elements of the information matrix equal non-zero. Likewise

$$\mathrm{var}(\hat{A}) \geq J_{11}^{-1}(\underline{\theta}) = \left(\Delta f \sum_{i=0}^{B-1} \frac{|S(i\Delta f)|^2}{P_N(i\Delta f)}\right)^{-1} \;, \tag{C.8}$$

which is equivalent to Eq. C.3.

Appendix D

Theoretical Bounds on PD Source Location Variance

General Solution

Again assuming zero-mean Gaussian noise, the scaled log-likelihood function of a measured PD signal $x(kT_\mathrm{s}) = As(kT_\mathrm{s} - \tau) + n(kT_\mathrm{s})$ is expressed as

$$L(\underline{\theta}) = \Delta f \sum_{i=0}^{B-1} -\frac{|X(i\Delta f) - AS(i\Delta f, z)e^{-j2\pi i\Delta f(\tau - t_s)}|^2}{2P_N(i\Delta f)} \,, \tag{D.1}$$

where the PD origin z is introduced as another unknown parameter, thus $\underline{\theta} = (A, \tau, z)^t$. In order to determine the CRLB for all parameters, the 3×3 Fisher matrix must be obtained. Regardless of the relation between the signal spectrum and the location, the first derivative of $L(\underline{\theta})$ to z can be expressed as

$$\begin{aligned}\frac{\partial L(\underline{\theta})}{\partial z} &= -\Delta f \sum_{i=0}^{B-1} \frac{A^2(S^*(i\Delta f, z)\partial S(i\Delta f, z)/\partial z + S(i\Delta f, z)\partial S^*(i\Delta f, z)/\partial z)}{2P_N} - \\ &\quad \frac{A(X^*(i\Delta f)e^{-j2\pi i\Delta f\tau}\partial S(i\Delta f, z)/\partial z + X(i\Delta f)e^{+j2\pi i\Delta f\tau}\partial S^*(i\Delta f, z)/\partial z)}{2P_N}\end{aligned}$$

The expectations of the second derivatives equal

$$\begin{aligned}E\left\{\frac{\partial^2 L(\underline{\theta})}{\partial z^2}\right\} &= -\Delta f \sum_{i=0}^{B-1} \frac{A^2\,\partial S^*(i\Delta f, z)/\partial z\;\partial S(i\Delta f, z)/\partial z}{P_N(i\Delta f)} \,, \\ E\left\{\frac{\partial^2 L(\underline{\theta})}{\partial z \partial A}\right\} &= -\Delta f \sum_{i=0}^{B-1} \frac{A\mathrm{Re}\{S^*(i\Delta f, z)\,\partial S(i\Delta f, z)/\partial z\}}{P_N(i\Delta f)} \,, \\ E\left\{\frac{\partial^2 L(\underline{\theta})}{\partial z \partial \tau}\right\} &= \Delta f \sum_{i=0}^{B-1} \frac{A^2(2\pi i\Delta f)\mathrm{Im}\{S^*(i\Delta f, z)\,\partial S(i\Delta f, z)/\partial z\}}{P_N(i\Delta f)} \,.\end{aligned} \tag{D.2}$$

Using Cramer's rule, the estimation variance of parameter θ_i is expressed as

$$\mathrm{var}(\hat{\theta}_i) = \frac{C_{ii}}{\det(\mathbf{J}(\underline{\theta}))} \tag{D.3}$$

where C_{ii} equals the co-factor of J_{ii}. The determinant of the information matrix equals

$$\begin{aligned}\det(\mathbf{J}(\underline{\theta})) &= -E\left\{\frac{\partial^2 L(\underline{\theta})}{\partial A^2}\right\} E\left\{\frac{\partial^2 L(\underline{\theta})}{\partial \tau^2}\right\} E\left\{\frac{\partial^2 L(\underline{\theta})}{\partial z^2}\right\} \\ &\quad +E\left\{\frac{\partial^2 L(\underline{\theta})}{\partial A^2}\right\}\left(E\left\{\frac{\partial^2 L(\underline{\theta})}{\partial z \partial \tau}\right\}\right)^2 \\ &\quad +E\left\{\frac{\partial^2 L(\underline{\theta})}{\partial \tau^2}\right\}\left(E\left\{\frac{\partial^2 L(\underline{\theta})}{\partial z \partial A}\right\}\right)^2 , \end{aligned} \tag{D.4}$$

and the co-factor corresponding to the location z equals

$$C_{33} = E\left\{\frac{\partial^2 L(\underline{\theta})}{\partial A^2}\right\} E\left\{\frac{\partial^2 L(\underline{\theta})}{\partial \tau^2}\right\} . \tag{D.5}$$

Subsequently, the location estimation variance is expressed as

$$\mathrm{var}(\hat{z}) \geq \left(-E\left\{\frac{\partial^2 L(\underline{\theta})}{\partial z^2}\right\} + \frac{\left(E\left\{\frac{\partial^2 L(\underline{\theta})}{\partial z \partial \tau}\right\}\right)^2}{E\left\{\frac{\partial^2 L(\underline{\theta})}{\partial \tau^2}\right\}} + \frac{\left(E\left\{\frac{\partial^2 L(\underline{\theta})}{\partial z \partial A}\right\}\right)^2}{E\left\{\frac{\partial^2 L(\underline{\theta})}{\partial A^2}\right\}} \right)^{-1} \tag{D.6}$$

where $E\left\{\frac{\partial^2 L(\underline{\theta})}{\partial \tau^2}\right\}$ and $E\left\{\frac{\partial^2 L(\underline{\theta})}{\partial A^2}\right\}$ follow from Eq. C.6.

Single-Pulse-Based Location

For a uniform cable system the signal spectrum of a PD signal originating z meters from the sensor can be expressed as

$$S(i\Delta f, z) = Z_{\mathrm{t}}(i\Delta f) H_{\mathrm{s}}(i\Delta f) T(i\Delta f) e^{-\gamma(i\Delta f)z} . \tag{D.7}$$

Now with

$$\frac{\partial S(i\Delta f, z)}{\partial z} = -\gamma(i\Delta f) Z_{\mathrm{t}}(i\Delta f) H_{\mathrm{s}}(i\Delta f) T(i\Delta f) e^{-\gamma(i\Delta f)z} \tag{D.8}$$

it follows that

$$\begin{aligned}\mathrm{var}(\hat{z}) \geq \frac{T_{\mathrm{s}}}{T_0} \Bigg(& \frac{1}{B}\sum_{i=0}^{B-1} |\gamma(i\Delta f)|^2 \mathrm{SNR}(i\Delta f) - \frac{1}{B}\frac{\left(\sum_{i=0}^{B-1}(2\pi i\Delta f)\beta(i\Delta f)\mathrm{SNR}(i\Delta f)\right)^2}{\sum_{i=0}^{B-1}(2\pi i\Delta f)^2 \mathrm{SNR}(i\Delta f)} \\ & -\frac{1}{B}\frac{\left(\sum_{i=0}^{B-1}\alpha(i\Delta f)\mathrm{SNR}(i\Delta f)\right)^2}{\sum_{i=0}^{B-1}\mathrm{SNR}(i\Delta f)} \Bigg)^{-1} . \end{aligned} \tag{D.9}$$

One-Sided Double-Pulse-Based Location

For a uniform cable system the signal spectrum of a PD signal originating z meters from the sensor and the reflection on the far-end terminal equals

$$S(i\Delta f, z) = S_1(i\Delta f, z) + S_2(i\Delta f, z) \tag{D.10}$$

with

$$\begin{aligned} S_1(i\Delta f, z) &= Z_\mathrm{t}(i\Delta f) H_\mathrm{s}(i\Delta f) T_1(i\Delta f) e^{-\gamma(i\Delta f)z} , \\ S_2(i\Delta f, z) &= S_1(i\Delta f, z) R_2(i\Delta f) e^{-\gamma(i\Delta f)2(l-z)} \end{aligned}$$

where l is the cable length, $T_1(i\Delta f)$ is the near-end transmission coefficient, and $R_2(i\Delta f)$ is the reflection coefficient at the far cable end. Now with

$$\frac{\partial S(i\Delta f, z)}{\partial z} = -\gamma(i\Delta f) \left(S_1(i\Delta f, z) - S_2(i\Delta f, z) \right)$$

it follows that

$$\mathrm{var}(\hat{z}) \geq \frac{T_\mathrm{s}}{T_0} \left(\frac{1}{B} \sum_{i=0}^{B-1} a - \frac{1}{B} \frac{\left(\sum_{i=0}^{B-1} (2\pi i \Delta f)\, b \right)^2}{\sum_{i=0}^{B-1} (2\pi i \Delta f)^2 \mathrm{SNR}(i\Delta f)} - \frac{1}{B} \frac{\left(\sum_{i=0}^{B-1} c \right)^2}{\sum_{i=0}^{B-1} \mathrm{SNR}(i\Delta f)} \right)^{-1} \tag{D.11}$$

where

$$\begin{aligned} a &= A^2 |\gamma(i\Delta f)|^2 \frac{|S_1(i\Delta f, z)|^2 + |S_2(i\Delta f, z)|^2 - 2\mathrm{Re}\left\{ S_1^*(i\Delta f, z) S_2(i\Delta f, z) \right\}}{P_N(i\Delta f)} , \\ b &= A^2 \frac{\beta(i\Delta f)(|S_2(i\Delta f, z)|^2 - |S_1(i\Delta f, z)|^2) + 2\alpha(i\Delta f)\mathrm{Im}\left\{ S_1^*(i\Delta f, z) S_2(i\Delta f, z) \right\}}{P_N(i\Delta f)} , \\ c &= A^2 \frac{\alpha(i\Delta f)(|S_2(i\Delta f, z)|^2 - |S_1(i\Delta f, z)|^2) + 2\beta(i\Delta f)\mathrm{Im}\left\{ S_1^*(i\Delta f, z) S_2(i\Delta f, z) \right\}}{P_N(i\Delta f)} . \end{aligned}$$

Since

$$\Delta f \sum_{i=0}^{B-1} S_1^*(i\Delta f, z) S_2(i\Delta f, z)$$

equals the time-domain correlation coefficient of the first pulse and reflection at lag zero, i.e. the product of $s_1(kT_\mathrm{s})$ and $s_2(kT_\mathrm{s})$. Evidently, the direct pulse and reflected pulse overlap only for a small region of locations very close to the far-end termination; therefore the following approximations hold for almost the entire cable length

$$\begin{aligned} a &= |\gamma(i\Delta f)|^2 (\mathrm{SNR}_1(i\Delta f) + \mathrm{SNR}_2(i\Delta f)) , \\ b &= \beta(i\Delta f)(\mathrm{SNR}_1(i\Delta f) - \mathrm{SNR}_2(i\Delta f)) , \\ c &= \alpha(i\Delta f)(\mathrm{SNR}_1(i\Delta f) - \mathrm{SNR}_2(i\Delta f)) \end{aligned} \tag{D.12}$$

where $\mathrm{SNR}_1(i\Delta f)$ and $\mathrm{SNR}_2(i\Delta f)$ equal the SNRs of the first arriving pulse and the reflection, respectively.

Two-Sided Location

Assuming mutually uncorrelated and zero-mean Gaussian noise processes, the combined a posteriori likelihood function of the signal model is expressed as

$$L(\underline{\theta}) = \Delta f \sum_{i=0}^{B-1} \sum_{q=1}^{2} -\frac{|X_q(i\Delta f) - AS_q(i\Delta f, z)e^{-j2\pi i\Delta f t_0}|^2}{2P_{N_q}(i\Delta f)} \,, \tag{D.13}$$

given the sensor signals $x_1(kT_\mathrm{s}) = As_1(kT_\mathrm{s} - t_0) + n_1(kT_\mathrm{s})$ and $x_2(kT_\mathrm{s}) = As_2(kT_\mathrm{s} - t_0) + n_2(kT_\mathrm{s})$ measured at both cable ends. Now analogue to the derivations shown earlier the location estimation variance is expressed as

$$\mathrm{var}(\hat{z}) \geq \left(-E\left\{ \frac{\partial^2 L(\underline{\theta})}{\partial z^2} \right\} + \frac{\left(E\left\{ \frac{\partial^2 L(\underline{\theta})}{\partial z \partial t_0} \right\} \right)^2}{E\left\{ \frac{\partial^2 L(\underline{\theta})}{\partial t_0^2} \right\}} + \frac{\left(E\left\{ \frac{\partial^2 L(\underline{\theta})}{\partial z \partial A} \right\} \right)^2}{E\left\{ \frac{\partial^2 L(\underline{\theta})}{\partial A^2} \right\}} \right)^{-1} \tag{D.14}$$

where

$$\begin{aligned}
E\left\{ \frac{\partial^2 L(\underline{\theta})}{\partial z^2} \right\} &= -\Delta f \sum_{i=0}^{B-1} \sum_{q=1}^{2} \frac{A^2\, \partial S_q^*(i\Delta f, z)/\partial z \; \partial S_q(i\Delta f, z)/\partial z}{P_{N_q}(i\Delta f)} \,, \\
E\left\{ \frac{\partial^2 L(\underline{\theta})}{\partial z \partial A} \right\} &= -\Delta f \sum_{i=0}^{B-1} \sum_{q=1}^{2} \frac{A\mathrm{Re}\{ S_q^*(i\Delta f, z)\, \partial S_q(i\Delta f, z)/\partial z \}}{P_{N_q}(i\Delta f)} \,, \\
E\left\{ \frac{\partial^2 L(\underline{\theta})}{\partial z \partial t_0} \right\} &= \Delta f \sum_{i=0}^{B-1} \sum_{q=1}^{2} \frac{A^2(2\pi i\Delta f)\mathrm{Im}\{ S_q^*(i\Delta f, z)\, \partial S_q(i\Delta f, z)/\partial z \}}{P_{N_q}(i\Delta f)} \,.
\end{aligned}$$

For a uniform cable system, the sensor signals equal

$$\begin{aligned}
S_1(i\Delta f, z) &= Z_\mathrm{t}(i\Delta f) H_{\mathrm{s},1}(i\Delta f) T_1(i\Delta f) e^{-\gamma(i\Delta f)z} \,, \\
S_2(i\Delta f, z) &= Z_\mathrm{t}(i\Delta f) H_{\mathrm{s},2}(i\Delta f) T_2(i\Delta f) e^{-\gamma(i\Delta f)(l-z)} \,,
\end{aligned}$$

and subsequently the CRLB on the PD location estimation variance is expressed as

$$\begin{aligned}
\mathrm{var}(\hat{z}) \geq \quad & \frac{T_\mathrm{s}}{T_0} \left(\frac{1}{B} \sum_{i=0}^{B-1} |\gamma(i\Delta f)|^2 (\mathrm{SNR}_1(i\Delta f) + \mathrm{SNR}_2(i\Delta f)) \right. \\
& - \frac{1}{B} \frac{\left(\sum_{i=0}^{B-1} (2\pi i\Delta f)\beta(i\Delta f)(\mathrm{SNR}_1(i\Delta f) - \mathrm{SNR}_2(i\Delta f)) \right)^2}{\sum_{i=0}^{B-1} (2\pi i\Delta f)^2 (\mathrm{SNR}_1(i\Delta f) + \mathrm{SNR}_2(i\Delta f))} \\
& \left. - \frac{1}{B} \frac{\left(\sum_{i=0}^{B-1} \alpha(i\Delta f)(\mathrm{SNR}_1(i\Delta f) - \mathrm{SNR}_2(i\Delta f)) \right)^2}{\sum_{i=0}^{B-1} (\mathrm{SNR}_1(i\Delta f) + \mathrm{SNR}_2(i\Delta f))} \right)^{-1}
\end{aligned} \tag{D.15}$$

where $\mathrm{SNR}_1(i\Delta f)$ and $\mathrm{SNR}_2(i\Delta f)$ equal the SNRs of the pulses arriving at the cable near-end and far-end, respectively.

Bibliography

[Aar98] D. M. v. Aartrijk, "Method and device for detecting and locating irregularities in a dielectric", Int. Patent No. PCT/NL1998/00111, KEMA, the Netherlands, Feb. 1998.

[Ahm98a] N. H. Ahmed and N. N. Srinivas, "The noise effect in conducting on-line partial discharge testing in distribution-class cables", *Annual Report of the Conference on Electrical Insulation and Dielectric Phenomena (CEIDP)*, vol. 1, pp. 319–322, 1998.

[Ahm98b] N. H. Ahmed and N. N. Srinivas, "On-line partial discharge detection in cables", *IEEE Transactions on Dielectrics and Electrical Insulation*, vol. 5, no. 2, pp. 181–188, Apr. 1998.

[Ahm01] N. H. Ahmed and N. N. Srinivas, "On-line partial discharge diagnostic system in power cable system", *Proceedings of the IEEE/PES Transmission and Distribution Conference and Exposition*, vol. 2, pp. 853 –858, Oct. 2001.

[Bar00] R. Bartnikas and K. D. Srivastava, *Power and communication cables*, McGraw-Hill, London, UK, 2000.

[Bog96] S. A. Boggs, A. Pathak, and P. Walker, "Partial discharge XXII: High frequency attenuation in shielded solid dielectric power cable and implications thereof for PD location", *IEEE Electrical Insulation Magazine*, vol. 12, no. 1, pp. 9–16, Jan./Feb. 1996.

[Bog00] S. A. Boggs and J. Densley, "Fundamentals of partial discharge in the context of field cable testing", *IEEE Electrical Insulation Magazine*, vol. 16, no. 5, pp. 13–18, Sept./Oct. 2000.

[Bor92] H. Borsi, "Digital location of partial discharges in HV cables", *IEEE Transactions on Electrical Insulation*, vol. 27, no. 1, pp. 28–36, Feb. 1992.

[Bor95] H. Borsi, E. Gockenbach, and D. Wenzel, "Separation of partial discharges from pulse shaped noise signals with the help of neural networks", *IEE Proceedings on Science, Measurement and Technology*, vol. 142, no. 1, pp. 69–74, Jan. 1995.

[Buc96] H. Buchalla, T. Flohr, and W. Pfeiffer, "Digital signal processing methods for interference recognition in partial discharge measurement - a comparison", *Proceedings of the IEEE International Symposium on Electrical Insulation (ISEI)*, pp. 393–396, Montreal, Canada, June 1996.

[Cac95] M. Cacciari, A. Contin, G. Rabach, and G. C. Montanari, "An approach to partial discharge investigation by height-distribution analysis", *IEE Proceedings on Science, Measurement and Technology*, vol. 142, no. 1, pp. 102–108, Jan. 1995.

[Car00] J. F. Carpentier, S. Gellida, D. Gloria, G. Morin, and H. Jaouen, "Comparison between s-parameter measurements and 2d electromagnetic simulations for microstrip transmission lines on bicmos process", *Proceedings of the 2000 International Conference on Microelectronic Test Structures (ICMTS)*, pp. 235–240, Mar. 2000.

[Cla62] F. M. Clark, *Insulating materials for design and engineering practice*, Wiley, London, UK, 1962.

[Con65] T. E. Constandinou, "Relation between moisture content and low-voltage electrical properties of oil-impregnated, resin-couted and unimpregnated papers", *IEE Proceedings*, vol. 112, no. 9, pp. 1783–1794, Sept. 1965.

[Cri89] G. C. Crichton, P. W. Karlsson, and A. Pedersen, "Partial discharges in ellipsoidal and spheroidal voids", *IEEE Transactions on Electrical Insulation*, vol. 24, no. 2, pp. 335–342, Apr. 1989.

[Dav79] P. Davis, *Circulant Matrices*, Wiley-Interscience, Chichester, UK, 1979.

[Du94a] Z. Du and M. S. Mashikian, "Self-learning digital filter for the field location of partial discharge in cables", *Proceedings of the IEEE International Symposium on Electrical Insulation (ISEI)*, pp. 245–248, Pittsburgh, USA, June 1994.

[Du94b] Z. Du, M. S. Mashikian, and F. Palmieri, "Partial discharge propagation model and location estimate", *Proceedings of the IEEE International Symposium on Electrical Insulation (ISEI)*, pp. 99–102, Pittsburgh, USA, June 1994.

[DZ93] D. De Zutter, F. Olyslager, and N. Fache, *Electromagnetic and circuit modelling of multiconductor transmission lines*, Clarendon Press, Oxford, UK, 1993.

[Eis92] W. R. Eisenstadt and Y. Eo, "S-parameter-based ic interconnect transmission line characterization", *IEEE Transactions on Components, Hybrids, and Manufacturing Technology*, vol. 15, no. 4, pp. 483–490, Aug. 1992.

[Fuk91] K. Fukunaga, M. Tan, H. Takehana, T. Takahashi, and S. Yoshida, "New partial discharge detection method for live power cable systems", *Conference Record of the 3^{rd} International Conference on Properties and Applications of Dielectric Materials (ICPADM)*, vol. 2, pp. 1218–1220, Tokyo, Japan, July 1991.

[Gul98] E. Gulski, J. J. Smit, P. N. Seitz, and J. C. Smit, "PD measurement on site using oscillating wave test system", *Conference Record of the IEEE International Symposium on Electrical Insulation (ISEI)*, vol. 2, pp. 420–423, Arlington, USA, June 1998.

[Gul03] E. Gulski, E. Lemke, M. Gamlin, E. Gockenbach, W. Hauschild, and E. Pultrum, "Experience in partial discharge detection of distribution power cable systems", *Electra*, pp. 34–43, June 2003.

[Gup81] K. C. Gupta, R. Garg, and R. Chadha, *Computer-aided design of microwave circuits*, Artech House, Dedham, USA, 1981.

[Ham01] B. R. Hamerling, F. J. Wester, E. Gulski, J. J. Smit, and E. R. S. Groot, "Fundamental aspects of on-line PD measurements on distribution power cables", *Proceedings of the 7^{th} IEEE International Conference on Solid Dielectrics (ICSD)*, pp. 408–411, Eindhoven, the Netherlands, June 2001.

[Har96] A. Hariri, Z. Du, D. Sui, M. S. Mashikian, and D. Jordan, "Field location of partial discharge in power cables using an adpative noise mitigating system", *Proceedings of the IEEE International Symposium on Electrical Insulation (ISEI)*, pp. 121–125, Montreal, Canada, June 1996.

[Hen96] C. G. Henningsen, K. Polster, B. A. Fruth, and D. W. Gross, "Experience with an on-line monitoring system for 400kV XLPE cables", *Proceedings of the IEEE Transmission and Distribution Conference*, pp. 515–520, Los Angeles, USA, 1996.

[Hes99] M. W. J. v. Hest, *Multi-resolution analysis of partial discharge signals*, Master's thesis, Technical University of Eindhoven, Eindhoven, the Netherlands, Apr. 1999.

[IEC87] IEC60885, *Electrical test methods for electric cables*, 1 ed., International Electrical Commision (IEC), Geneva, Switzerland, 1987.

[IEC00] IEC60270, *High-voltage test techniques - Partial discharge measurements*, 13 ed., International Electrical Commision (IEC), Geneva, Switzerland, 2000.

[Kad59] H. Kaden, *Wirbelströme und Schirmung in der Nachrichtentechnik*, Springer-Verlag, Berlin/Göttingen/Heidelberg, Germany, 1959.

[Kay88] S. M. Kay, *Modern spectral estimation: theory and application*, Prentice Hall, Englewoord Cliffs, UK, 1988.

[Kna90] C. H. Knapp, R. Bansal, M. S. Mashikian, and R. B. Northdrop, "Signal processing techniques for partial discharge site location in shielded cable", *IEEE Transactions on Power delivery*, vol. 5, no. 2, pp. 859–865, Apr. 1990.

[Köp95] U. Köpf and K. Feser, "Rejection of narrow-band noise and repetitve pulses in on-site PD measurements", *IEEE Transactions on Dielectrics and Electrical Insulation*, vol. 2, no. 6, pp. 1180–1191, Dec. 1995.

[Kre64] F. H. Kreuger, *Partial discharge detection in high voltage equipment*, Heywood, London, UK, 1964.

[Kre93a] F. H. Kreuger, E. Gulski, and A. Krivda, "Classification of partial discharges", *IEEE Trans. on Electrical Insulation*, vol. 28, no. 6, pp. 917–931, Dec. 1993.

[Kre93b] F. H. Kreuger, M. G. Wezelenburg, A. G. Wiemer, and W. A. Sonneveld, "Partial discharge XVIII: Errors in the location of partial discharges in high voltage solid dielectric cables", *IEEE EI Magazine*, vol. 9, no. 6, pp. 15–24, Nov./Dec. 1993.

[Lem95] E. Lemke and P. Schmiegel, "Complex discharge analysing (CDA) - an alternative procedure for diagnosis tests on HV power apparatus of extremely high capacity", *Proceedings of the 9^{th} International Symposium on High Voltage Engineering (ISH)*, vol. 5, pp. 617/1–617/4, Graz, Austria, Aug. 1995.

[LP03] V. Latva-Pukkila and P. Pakonen, "Disturbances occuring in on-site partial discharge measurements", *Conference Record of the Nordic Insulation Symposium (NORDIS)*, pp. 11–19, Tampere, Finland, June 2003.

[Lun92] L. E. Lundgaard, "Partial discharge. xiii. acoustic partial discharge detection - fundamental considerations", *IEEE Electrical Insulation Magazine*, vol. 8, no. 5, pp. 34–43, Sept./Oct. 1992.

[Lun98] L. E. Lundgaard and W. Hansen, "Acoustic method for quality control and in-service periodic monitoring of medium voltage cable terminations", *Conference Record of IEEE International Symposium on Electrical Insulation (ISEI)*, pp. 130–133, Arlington, USA, June 1998.

[Mac98] R. R. Mackinlay and C. Walton, "Some advances in PD monitoring for high voltage cables", *IEE Collection on Medium Voltage Paper Cables: Asset or Liability? (Digest No. 1998/290)*, pp. 6/1–6/5, 1998.

[Mas90] M. S. Mashikian, R. Bansal, and R. Northdrop, "Location and characterization of partial discharges sites in shielded power cables", *IEEE Transactions on Power Delivery*, vol. 5, pp. 833–839, Apr. 1990.

[Mas92] M. S. Mashikian, F. Palmieri, R. Bansal, and R. Northdrop, "Location of partial discharges in shielded cables in the presence of high noise", *IEEE Transactions on Electrical Insulation*, vol. 27, no. 1, pp. 37–43, Feb. 1992.

[Mas00] M. S. Mashikian, "Partial discharge location as a diagnostic tool for power cables", *Proceedings of the IEEE Power Engineering Society Winter Meeting*, vol. 3, pp. 1604–1608, Jan. 2000.

[Mic03] M. Michel, "Moving towards a complete on-line condition monitoring solution", *Proceedings of the 17^{th} International Conference on Electricity Distribution (CIRED)*, Barcelona, Spain, May 2003.

[Mit98] S. K. Mitra, *Digital signal processing: A computer-based approach*, McGraw-Hill, New York, USA, 1998.

[Moo99] T. K. Moon and W. C. Stirling, *Mathematical methods and algorithms for signal processing*, Prentice Hall, Upper saddle river, USA, 1999.

[Mor99] R. Morin, R. Bartnikas, and G. Lessard, "In-service location of partial discharge sites in polymeric distribution class cables using capacitive and inductive probes", *Proceedings of the IEEE Transmission and Distribution Conference*, vol. 1, pp. 120–127, Barcelona, Spain, Apr. 1999.

[Nag93] V. Nagesh and B. I. Gururaj, "Evaluation of digital filters for rejecting discrete spectral interference in on-site PD measurements", *IEEE Transactions on Electrical Insulation*, vol. 28, no. 1, pp. 73–85, Feb. 1993.

[Nag94] V. Nagesh and B. I. Gururaj, "Automatic detection and elimination of periodic pulse shaped interference in partial discharge measurements", *IEE Proceedings on Science, Measurement and Technology*, vol. 141, no. 5, pp. 335–342, Sept. 1994.

[Par72] T. Parks and J. McClellan, "Chebyshev approximation for nonrecursive digital filters with linear phase", *IEEE Trans. on Circuits and Systems*, vol. 19, no. 2, pp. 189–194, Mar. 1972.

[Pau94] C. R. Paul, *Analysis of multiconductor transmission lines*, John Wiley, New York, USA, 1994.

[Pla99] R. Plath, U. Herrmann, K. Polster, J. Spiegelberg, and P. Coors, "After laying tests of 400 kV XLPE cable systems for Bewag Berlin", *Proceedings of the 11^{th} International Symposium on High Voltage Engineering (ISH)*, vol. 5, pp. 276–279, London, UK, Aug. 1999.

[Pre92] W. H. Press, S. A. Teukolsky, W. T. Vetterling, and B. P. Flannery, *Numerical recipes in C : the art of scientific computing*, Cambridge university press, Cambridge, UK, 1992.

[Pul95] E. Pultrum and M. J. M. v. Riet, "HF partial discharge detection in HV extruded cable accessories", *Proceedings of the 3^{rd} International Conference on Insulated Power Cables (JICABLE)*, pp. 662–665, Versailles, France, June 1995.

[Sat03] L. Satish and B. Nazneen, "Wavelet-based denoising of partial discharge signals buried in excessive noise and interference", *IEEE Transactions on Dielectrics and Electrical Insulation*, vol. 10, no. 2, pp. 354–367, Apr. 2003.

[Sch94a] U. Schichler, H. Borsi, and E. Gockenbach, "Application of digital filters for on-site partial discharge detection on high voltage cables", *Proceedings of the 4^{th} International Conference on Properties and Applications of Dielectric Materials (ICPADM)*, pp. 618–621, Brisbane, Australia, July 1994.

[Sch94b] U. Schichler, H. Borsi, and E. Gockenbach, "Problems and new solutions for partial discharge measurement on high voltage cables under noisy conditions", *Proceedings of the IEEE International Symposium on Electrical Insulation (ISEI)*, pp. 66–69, Pittsburgh, USA, June 1994.

[Sch99a] N. v. Schaik, W. Boone, E. Hetzel, and B. J. Grotenhuis, "MV cable maintenance, practices and results", *Proceedings of the International Conference on Insulated Power Cables (JICABLE)*, Versailles, France, June 1999.

[Sch99b] K. Schon, "Intercomparison of PD calibrators and PD instruments", *Proceedings of the IEE High Voltage Engineering Symposium*, 467, Amsterdam, The Netherlands, August 1999.

[Sch00] N. v. Schaik, O. J. G. M. Groen, and E. Hetzel, "Medium voltage cable diagnostics; experience and results; extension to transformer tails, very long lengths and branched cable circuits", *Proceedings of the 13th Conference of the Electricity Power Supply Industry (CEPSI)*, Manila, Philippines, October 2000.

[Sch03] N. v. Schaik, E. F. Steennis, D. M. v. Aartrijk, R. H. Rieksen, and R. Ross, "Cable diagnostics to serve CBM on power cable systems", *Proceedings of the 13^{th} International Symposium on High Voltage Engineering (ISH)*, Delft, the Netherlands, August 2003.

[Shi00] I. Shim, J. J. Soraghan, and W. H. Siew, "Digital signal processing applied to the detection of partial discharge: An overview", *IEEE Electrical Insulation Magazine*, vol. 16, no. 3, pp. 6–12, May/June 2000.

[Shi01] I. Shim, J. J. Soraghan, and W. H. Siew, "Detection of PD utilizing digital signal processing methods part 3: open-loop noise reduction", *IEEE Electrical Insulation Magazine*, vol. 17, no. 1, pp. 6–13, Jan./Feb. 2001.

[Sil73] R. W. Sillars, *Electrical insulation materials and their application*, Peregrinus, London, UK, 1973.

[Ste91] E. F. Steennis, E. Hetzel, and C. W. J. Verhoeven, "Diagnostic medium voltage cable test at 0.1Hz", *Proceedings of the 3^{rd} International Conference on Insulated Power Cables (JICABLE)*, pp. 408–414, Versailles, France, June 1991.

[Ste92] J. P. Steiner, P. H. Reynold, and W. L. Weeks, "Estimating the location of partial discharges in cables", *IEEE Transactions on Electrical Insulation*, vol. 27, no. 1, pp. 44–59, Feb. 1992.

[Ste01] E. F. Steennis, R. Ross, N. v. Schaik, W. Boone, and D. M. v. Aartrijk, "Partial discharge diagnostics of long and branched medium voltage cables", *Proceedings of the 7^{th} IEEE International Conference on Solid Dielectrics (ICSD)*, pp. 27–30, Eindhoven, the Netherlands, June 2001.

[Ste02a] E. F. Steennis, P. A. A. F. Wouters, P. C. J. M. van der Wielen, and J. Veen, "Method and system for transmitting an information signal over a power cable", Int. Patent No. WO 2004/013642, June 2002.

[Ste02b] E. F. Steennis, P. A. A. F. Wouters, P. C. J. M. van der Wielen, and J. Veen, "Werkwijze en systeem voor het overbrengen van een informatiesignaal over een vermogenskabel", Dutch Patent No. NL 1020925, June 2002.

[Ste03] E. F. Steennis, P. C. J. M. v. d. Wielen, J. Veen, and P. A. A. F. Wouters, "Aspects and implications of on-line PD detection and localization of MV cable systems", *Conference Record of the International Conference on Insulated Power Cables (JICABLE)*, pp. 666–671, Versailles, France, June 2003.

[Ste04] E. F. Steennis, *KEMA course on power cables*, KEMA Transmission and Distribution (T&D) Testing Services, Arnhem, The Netherlands, 2004.

[Sto82] G. Stone and S. Boggs, "Propagation of partial discharge pulses in shielded power cable", *Annual report of the conference on electrical insulation and dielectric phenomena*, pp. 275–280, Washington, USA, 1982.

[Su94] Q. Su, "Application of digital signal processing techniques for noise suppression in PD measurements", *Proceedings of the 4^{th} International Conference on Properties and Applications of Dielectric Materials (ICPADM)*, Brisbane, Australia, July 1994.

[Su01] Q. Su and K. Sack, "New techniques for on-line partial discharge measurements", *Proceedings of the IEEE International Multi Topic Conference on Technology for the 21^{st} Century*, pp. 49 –53, Dec. 2001.

[Tal04] M. Talbi, *De puls injector*, Master's thesis, Avance, Breda, The Netherlands, 2004.

[Tan83] T. Tanaka and A. Greenwood, *Advanced power cable technology*, vol. 1, CRC press, Boca Raton, Florida, 1983.

[Tan95] T. Tanaka, "Partial discharge pulse distribution pattern analysis", *IEE Proceedings on Science, Measurement and Technology*, vol. 142, no. 1, pp. 534–539, Jan. 1995.

[Tre68] H. L. Trees, *Detection, estimation and modulation theory*, Wiley, London, UK, 1968.

[Vee02a] J. Veen, "Frequency domain fractional delay estimator for noisy channels", *Proceedings of ProRISC*, pp. 516–519, Veldhoven, The Netherlands, Nov. 2002.

[Vee02b] J. Veen, P. C. J. M. van der Wielen, and E. F. Steennis, "Propagation characteristics of three-phase belted paper cable for on-line PD detection", *Conference Record of the IEEE International Symposium on Electrical Insulation (ISEI)*, pp. 96–99, Boston, USA, June 2002.

[Vee03a] J. Veen and P. C. J. M. van der Wielen, "Online partial discharge detection in power cables using matched filters", *Proceedings of the 18^{th} Nordic Symposium on Electrical Insulation (NORDIS)*, pp. 71–78, Tampere, Finland, June 2003.

[Vee03b] J. Veen and P. C. J. M. van der Wielen, "Partial discharge detection and localization using matched filters", *IEEE Electrical Insulation Magazine*, vol. 19, no. 5, pp. 20–26, Sept./Oct. 2003.

[Vee04a] J. Veen and P. C. J. M. van der Wielen, "PD location in power cables using parametric models", *Proceedings of the 8^{th} IEEE International Conference on Solid Dielectrics (ICSD)*, pp. 711–714, Toulouse, France, July 2004.

[Vee04b] J. Veen, P. C. J. M. van der Wielen, and E. F. Steennis, "Cancellation of continuous periodic interference for PD detection", *Proceedings of the 8^{th} IEEE International Conference on Solid Dielectrics (ICSD)*, pp. 707–710, Toulouse, France, July 2004.

[Wag03] P. Wagenaars, "Modeling a substation for pulse injection and detection", Tech. Rep., Technical University of Eindhoven, Eindhoven, the Netherlands, Aug. 2003.

[Wai62] L. A. Wainstein and V. D. Zubakov, *Extraction of signals from noise*, Prentice-Hall, Englewood Cliffs, UK, 1962.

[Wal95] R. A. Walling, R. D. Melchior, and B. A. McDermott, "Measurement of cable switching transients in underground distribution systems", *IEEE Trans. on Power Delivery*, vol. 10, no. 1, pp. 534–539, Jan. 1995.

[Wal01] C. Walton, "Detecting and locating MV failure before it occurs", *Proceedings of the 16^{th} International Conference on Electricity Distribution (CIRED)*, 482, Amsterdam, The Netherlands, June 2001.

[Wid85] B. Widrow and S. D. Stearns, *Adaptive signal processing*, Prentice-Hall, London, UK, 1985.

[Wie02] P. C. J. M. v. d. Wielen, P. A. A. F. Wouters, and E. F. Steennis, "Signal interpretation of partial discharges in three-phase medium voltage cable systems measured on-line", *Conference Record of the IEEE International Symposium on Electrical Insulation (ISEI)*, pp. 542–545, Boston, USA, June 2002.

[Wie03a] P. C. J. M. v. d. Wielen, E. F. Steennis, and P. A. A. F. Wouters, "Fundamental aspects of excitation and propagation of on-line partial discharge signals in three-phase medium voltage cable systems", *IEEE Transactions on Dielectrics and Electrical Insulation*, vol. 10, no. 4, pp. 678–688, Aug. 2003.

[Wie03b] P. C. J. M. v. d. Wielen, J. Veen, and P. A. A. F. Wouters, "Evaluation of different types of sensors and their positioning for on-line PD detection and localisation in distribution cables", *Conference Record of the Nordic Insulation Symposium (NORDIS)*, pp. 367–374, Tampere, Finland, June 2003.

[Wie03c] P. C. J. M. v. d. Wielen, J. Veen, P. A. A. F. Wouters, and E. F. Steennis, "Sensors for on-line PD detection in MV power cables and their locations in substations", *Conference Record of the 7^{th} International Conference on Properties and Applications of Dielectric Materials (ICPADM)*, pp. 215–219, Nagayo, Japan, June 2003.

[Wie03d] P. C. J. M. v. d. Wielen, P. A. A. F. Wouters, J. Veen, and D. M. v. Aartrijk, "Synchronization of on-line PD detection and localization setups using pulse injection", *Conference Record of the 7^{th} International Conference on Properties and Applications of Dielectric Materials (ICPADM)*, pp. 327–330, Nagayo, Japan, June 2003.

[Wie04a] P. C. J. M. v. d. Wielen, J. Veen, P. Wagenaars, and P. A. A. F. Wouters, "Determination of substation model for correct interpretation of on-line measured PD signals from MV cable systems", *Conference Record of the International Conference on Solid Dielectrics (ICSD)*, pp. 747–750, Toulouse, France, July 2004.

[Wie04b] P. C. J. M. v. d. Wielen, J. Veen, P. A. A. F. Wouters, and E. F. Steennis, "Time-base alignment of PD signals measured at multiple cable-ends", *Conference Record of the International Conference on Solid Dielectrics (ICSD)*, pp. 648–651, Toulouse, France, July 2004.

[Wie05] P. C. J. M. v. d. Wielen, *On-line detection and location of partial discharges in medium voltage power cables*, Ph.D. thesis, Eindhoven University of Technology, Eindhoven, the Netherlands, 2005.

[Wlo94] R. Wlodek, Z. Florkowski, and P. Zydron, "Improvement of signal to noise ratio in partial dischrge measurements", *Proceedings of the 4^{th} International Conference on Properties and Applications of Dielectric Materials (ICPADM)*, pp. 590–593, Brisbane, Australia, July 1994.

[Wol04] J. A. Wolse, W. T. J. Hulshorst, G. A. Bloemhof, and I. P. Peters, "Betrouwbaarheid van electriciteitsnetten in nederland in 2003", Tech. Rep., KEMA Transmission and Distribution (T&D) Consulting, Arnhem, the Netherlands, May 2004.

[Wou] P. A. A. F. Wouters, P. C. J. M. v. d. Wielen, J. Veen, P. Wagenaars, and E. F. Steennis, "Effect of cable load impedance on coupling schemes for MV power line communication", *To be published in IEEE Transactions on Power Delivery.*

[Wou91] P. A. A. F. Wouters, W. J. S. Bollen, P. C. T. v. d. Laan, and E. F. Steennis, "Lokalisatie van partiële ontladingen in XLPE kabels", Tech. Rep. EHC/RAP/91/011, Eindhoven University of Technology, Eindhoven, The Netherlands, 1991.

[Wou03a] P. A. A. F. Wouters and P. C. J. M. v. d. Wielen, "Effect of cable load impedance on coupling schemes for MV power line communication", *Proceedings of the IEEE Bologna Power Tech Conference*, Bologna, Italy, June 2003.

[Wou03b] P. A. A. F. Wouters, P. C. J. M. v. d. Wielen, J. Veen, and E. F. Steennis, "On-line PD measuring system for MV cables: some practical aspects and implications", *Proceedings of the 13^{th} International Symposium on High Voltage Engineering (ISH)*, Delft, the Netherlands, August 2003.

[Wou03c] P. A. A. F. Wouters, P. C. J. M. v. d. Wielen, and E. F. Steennis, "Challenges related to development of an on-line PD detection and localisation system", *Conference Record of the Nordic Insulation Symposium (NORDIS)*, pp. 3–10, Tampere, Finland, June 2003.

[Zae03] W. S. Zaengl, "Dielectric spectroscopy in time and frequency domain for hv power equipment. i. theoretical considerations", *IEEE Electrical Insulation Magazine*, vol. 19, no. 5, pp. 5–19, Sept./Oct. 2003.

Glossary

Accessory	Generic term for components within a cable system other than cables, viz. joints or splices, and terminations.
Cable section	Uniform cable with accessories only at the cable ends.
Cable system	Cascade of cable sections that are interconnected by joints.
Calibration	Determination of the relationship between the physical variable measurement input and the system output of some part of the measurement system.
Detection	The combined process of measurement and analysis of partial discharge signals.
Estimation	Determination of signal or model parameter values from indirect or disturbed observations.
Excitation	Partial discharge and its consequent induced charges in nearby conductors.
Extraction	Recovery of partial discharge signals from measurements.
Interference	(Disturbance) Any signal originating from outside the cable under test.
Joint	(Splice) Connection device between two cables.
Location	Pinpointing the origin of partial discharge within a cable system.
Measurement	Conversion of an electrical or electromagnetic signal into a form that is suitable for analyzing.
On-line	Energized by the power grid.
Partial discharge	Local breakdown of the electric field that only partially bridges the insulation between the conductors.
Partial discharge signal	Current or voltage that results from a partial discharge within the cable system under test.
Ring main unit (RMU)	Junction of cable terminations and other high-voltage equipment located in a common housing.
Rotating field	Electrical or magnetic field with rotating direction.
Signal analysis	The combined process of interference rejection, signal extraction, and parameter estimation from measurements.
Synchronization	(Time-base alignment) Performing simultaneous starting or correction of the time-base difference between multiple measurements.
Termination	Electrical and mechanical reliable end-device of a cable that allows interconnection of other high-voltage equipment to the cable system.

Abbreviations

AM	Amplitude modulation
CM	Common mode
CRLB	Cramer-Rao lower bound
CT	Current transformer
DAQ	Data acquisition
DC	Direct current
DFT	Discrete Fourier transform
DOA	Direction of arrival
DTOA	Difference in time of arrival
DM	Differential mode
FFT	Fast Fourier transform
FIR	Finite impulse response
GPS	Global positioning system
HV	High voltage
IDFT	Inverse discrete Fourier transform
IIR	Infinite impulse response
MFB	Matched filter bank
ML	Maximum likelihood
MM	Measurement manager
MSPS	Million of samples per second
MU	Measurement unit
MV	Medium voltage
PC	Personal computer
PD	Partial discharge
PILC	Paper insulated lead covered
PP	Phase to phase
PSDF	Power spectral density function
RMU	Ring main unit
SPIAR	Signal to periodic interference amplitude ratio
SNR	Signal to noise ratio
SP	Shield to phase
SSP	Shield to single phase
TDR	Time domain reflectometry
TOA	Time of arrival
TU/e	Eindhoven University of Technology
XLPE	Cross-linked polyethylene

Notation and Symbols

General Notations

$x(t)$	Scalar in the time domain, continuous time signal
$X(\omega)$	Phasor in the frequency domain, Fourier transform of $x(t)$
$x(kT_\mathrm{s})$	Sampled signal
$X(i\Delta f)$	Discrete Fourier transform of $x(kT_\mathrm{s})$
$\mathrm{Re}\{X\}$	Real part of X
$\mathrm{Im}\{X\}$	Imaginary part of X
X^*	Complex conjugate of X
$\lvert X\rvert$	Absolute value of X
$\angle X$	Angle of X
$\underline{X}$	Vector
X_i	Vector element on the i-th row of $\underline{X}$
$\mathbf{X}$	Matrix
X_{ij}	Matrix element on the i-th row and j-th column of $\mathbf{X}$
$\underline{X}^t, \mathbf{X}^t$	Transpose of $\underline{X}$, $\mathbf{X}$
$X^{-1}, \mathbf{X}^{-1}$	Inverse of X, $\mathbf{X}$
$\det(\mathbf{X})$	Determinant of $\mathbf{X}$
$E\{x\}$	Expected value of x
$\mathrm{var}(x)$	Variance of x
$\mathrm{std}(x)$	Standard deviation of x
$p(x)$	Probability of x
$L(x)$	Likelihood of x
$\hat{x}$	Estimated value of x

Symbols

Symbol	Meaning	Unit
α	Attenuation	Np/m
β	Phase shift	rad/m
γ	Propagation factor	Np/m
Δf	Frequency domain resolution	Hz
$\Delta\tau$	Difference in time of arrival	s
τ	Time of arrival or time delay	s
ω	Angular frequency	rad/s
A	Scaling factor	
B	Discrete Fourier transform length	
f	Frequency	Hz
H	Transfer function	
I	Current	A
j	Imaginary unit	
l	cable length	m
N	Additive noise	V
P_{N}	Noise power spectral density function	V^2/Hz
Q	Charge	C
R	Reflection coefficient	
S	Partial discharge signal	V
t	Continuous time	s
T	Transmission coefficient	
T_0	Observation interval	s
T_{s}	Sampling period	s
V	Voltage	V
v_{p}	Phase velocity	m/s
X	Measured partial discharge signal	V
Y	Admittance	Ω^{-1}
z	Discharge location	m
Z_{c}	Characteristic wave impedance	Ω
Z_{l}	Propagation channel load impedance	Ω
Z_{t}	Transfer impedance	Ω

Acknowledgment

I am especially grateful to my promotors, prof. Jan Bergmans and prof. Fred Steennis, for their enthusiastic support and guidance. Also I would like to thank my copromotor dr. Peter Wouters, for his advice and comments; and dr. Martin Bastiaans, my supervisor. Special thanks to my colleague Peter van der Wielen for the fruitful corporation and the many discussions we have had that contributed to this thesis.

I would like to thank everyone at the Distribution Testing Services department of KEMA in Arnhem. In particular I owe much gratitude to Dick van Aartrijk and Osrick Anita for their support and technical assistance during the many experiments we conducted. I would like to acknowledge Marko Kruithof (Eneco) and Maarten van Riet (Continuon) for making available parts of the distribution grid for measurements and providing the experimental set-up. Also many thanks to Pim Jacobs for his help with the experiments. Thanks to everyone at the Signal Processing Systems group of the Eindhoven University of Technology for their support, in particular Jakob van de Laar and Emanuël Habets.

My deepest gratitude goes to my parents and my brother for their profound love and support. Many thanks to all my friends, especially to Henk de Bruin, who has encouraged and inspired me all the time. Above all, I would like to thank Rinske Brummelman for her endless support and endurance.

Curriculum Vitae

Jeroen Veen was born in Dordrecht, the Netherlands, on September 20, 1977. In 1994 he finished secondary school in Veenendaal, the Netherlands. He received the B.Eng. degree in Telematics from the University of Professional Education, Utrecht, the Netherlands, in 1998. In 2001 he obtained the M.Sc. degree (cum laude) in Electrical Engineering from the Eindhoven University of Technology (TU/e), Eindhoven, the Netherlands. From 2001 to 2005, he worked as a researcher in the Signal Processing Systems (SPS) group of the TU/e, and in the Transmission and Distribution Testing Services department (TDT) of KEMA, Arnhem, the Netherlands, where he carried out the work reported in this thesis.

1. Automatische signaalanalyse is onontbeerlijk voor de interpretatie van on-line partiële ontladingsmetingen.
   Automated signal analysis is essential for the interpretation of on-line partial discharge measurements.
   (Dit proefschrift)

2. On-line karakterisering van kabel- en onderstationparameters is mogelijk d.m.v. inductieve pulsinjectie.
   On-line characterization of cable and substation parameters is possible by means of inductive pulse injection.
   (Dit proefschrift, hoofdstuk 4)

3. Karakterisering van de kwaliteit van een kabeldiagnostiek door een enkele waarde voor gevoeligheid en voor lokalisatie-nauwkeurigheid, is misleidend.
   Characterization of the quality of a cable diagnostic by a single value for sensitivity and location accuracy is misleading.
   (Dit proefschrift, hoofdstuk 5 en 6)

4. Liberalisatie van publieke voorzieningen draagt niet bij tot het liberaliseren van het publiek.
   Liberalization of public facilities does not contribute to liberalizing the public.

5. De mens verkiest zekerheid boven vrijheid.
   Man prefers security above liberty.

6. Het opleggen van democratie getuigt van weinig inzicht in haar grondbeginselen.
   Enforcing democracy shows little insight into democratic principles.

7. Beschaving blijkt niet uit een ontwikkelde wetgeving, maar uit het gedrag van de mens bij het ontbreken van wetten.
   Civilization is not characterized by a developed legislation, but by human behavior in the absence of laws.

8. Het Kyoto-protocol leidt tot een moderne aflatenhandel.
   The Kyoto-protocol leads to a modern form of indulgence trading.

9. In navolging van populaire televisieshows, zou het mogelijk moeten zijn parlementariërs weg te stemmen, om de algemene interesse voor politiek te vergroten.
   Following popular television shows, it should be possible to vote out members of parliament, in order to expand the general interest in politics.

10. Het kleine aantal politici met een bèta opleiding verklaart dat logica in de politiek geen belangrijke plaats inneemt.
    The small number of politicians with an education in the exact sciences explains why logic does not figure prominently in politics.

11. Het streven naar perfectie is verre van optimaal.
    The pursuit of perfection is far from optimal.
    (Bron : Voltaire, Dictionnaire Philosophique)